AEROACOUSTIC MEASUREMENT AND ANALYSIS OF TRANSIENT SUPERSONIC HOT NOZZLE FLOWS

by

DANIEL ROBERT KIRK

Bachelor of Science in Mechanical Engineering
Rensselaer Polytechnic Institute, 1997

Submitted to the Department of Aeronautics and Astronautics
in partial fulfillment of the requirements for the degree of

MASTER OF SCIENCE
in
AERONAUTICS AND ASTRONAUTICS

at the

MASSACHUSETTS INSTITUTE OF TECHNOLOGY

June 1999

Author: _____
Department of Aeronautics and Astronautics
May 25, 1999

Certified by: _____
Professor Ian A. Waitz
Associate Professor of Aeronautics and Astronautics
Thesis Supervisor

Accepted by: _____
Professor Jaime Peraire
Associate Professor of Aeronautics and Astronautics
Chairman, Departmental Graduate Committee

Aeroacoustic Measurement and Analysis of Transient Supersonic Hot Nozzle Flows

by

Daniel Robert Kirk

Submitted to the Department of Aeronautics and Astronautics
on May 25, 1999, in partial fulfillment of the requirements for the degree of

Master of Science

Abstract

A transient testing technique for the study of jet noise was investigated and assessed. A shock tunnel facility was utilized to produce short duration, 10-20 millisecond, underexpanded supersonic hot air jets from a series of scaled nozzles. The primary purpose of the facility is to investigate noise suppressor nozzle concepts relevant to supersonic civil transport aircraft applications.

The shock tube has many strengths; it is mechanically simple, versatile, has low operating costs, and can generate fluid dynamic jet conditions that are comparable to aircraft gas turbine engine exhausts. Further, as a result of shock heating, the total temperature and pressure profiles at the nozzle inlet are uniform, eliminating the noise associated with entropy non-uniformities that are often present in steady-state, vitiated air facilities. The primary drawback to transient testing is the brief duration of useful test time. Sufficient time must be allowed for the nozzle flow and free jet to reach a quasi-steady-state before acoustic measurements can be made. However, if this constraint is met, the short run times become advantageous. The test articles are only exposed to the high temperature flow for a fraction of a second, and can be constructed of relatively inexpensive stereo-lithography or cast aluminum.

A comparison between shock tunnel transient noise data and steady-state data is presented to ascertain the usefulness of the technique to make acoustic measurements on scaled nozzles. Three types of nozzles are compared in the assessment effort: (1) a series of 0.64 - 1.9 cm exit diameter small-scale round nozzles that can be operated at transient *and* cold-flow steady-state conditions at the MIT facility for in-house comparison, (2) a series of 5.1 - 10.2 cm exit diameter ASME standard axisymmetric nozzles, and (3) a $1/12^{th}$ scale version of a modern mixer-ejector nozzle. Scaled versions of nozzles (2) and (3) were tested at Boeing's steady-state low speed aeroacoustic facility for comparison to the transient shock tube noise data. The assessment establishes the uncertainty bounds on sound pressure level measurements over the range of frequency bands, nozzle pressure ratios (1.5 - 4.0), total temperature ratios (1.5 - 3.5), and nozzle scales for which the facility can be employed as a substitute and/or as a complimentary mode of investigation to steady-state hot-flow test facilities.

Far-field narrowband spectra were obtained at directivity angles from 65 to 145 degrees and the data were extrapolated to full-scale flight conditions consistent with FAR-36 regulations. Nozzle pressure ratio and total temperature ratio were repeatable to within ± 1 percent of desired conditions. The constraint of short test duration is shown to be alleviated through the use of multiple runs to reduce the uncertainty associated with making transient acoustic measurements. Sound pressure level versus frequency trends with nozzle pressure ratio and directivity angle are shown to be comparable between the steady-state and transient noise data for all three nozzle types. The small scale nozzles exhibited agreement to within ± 1 - 2 dB over a full-scale frequency range of 50 - 1250 Hz. The ASME nozzle results demonstrated that the transient noise data replicates the Boeing steady-state data to within ± 2 - 3 dB on SPL versus full-scale frequency from 250 - 6300 Hz, as well as OASPL and PNL versus directivity angle. The magnitude of EPNL values are shown to agree to within 1 - 3 dB depending on test condition and nozzle scale. The mixer-ejector model exhibited agreement with the steady-state noise data to within 2 - 5 dB over a frequency range of 500 - 6300 Hz for all directivity angles. OASPL and PNL versus directivity angle noise data exhibited agreement with magnitude to within 1 - 4 dB. Steady-state trends with MAR, azimuthal angle, and EPNL were also present in the transient noise data.

Thesis Supervisor: Professor Ian A. Waitz
Title: Associate Professor of Aeronautics and Astronautics

Acknowledgments

Praise be to the God and Father of our Lord Jesus Christ, who has blessed us in the heavenly realms with every spiritual blessing in Christ. For he chose us in him before the creation of the world to be holy and blameless in his sight. In love he predestined us to be adopted as his sons through Jesus Christ, in accordance with his pleasure and will - to the praise of his glorious grace, which he has freely given in the One he loves. In him we have redemption through his blood, the forgiveness of sins, in accordance with the riches of God's grace that he lavished on us with all wisdom and understanding.

Ephesians 1:3-8

All glory and praise to my Father

The completion of this thesis is the result of assistance and advice from a number of individuals. Foremost, I would like to thank my thesis advisor Prof. **Ian A. Waitz**. In May of 1997, before I committed to attending MIT, Prof. Waitz told me, "My job is to provide as many opportunities as possible for you to shine." Those words rang true over the course of this research, and for those opportunities I am grateful. I am sincerely appreciative of his guidance and genuine advice, not only on this project, but with course work, the doctoral qualifying examination, as well as in many other aspects of graduate education. I look forward to continuing to work under the tutelage of Prof. Waitz during my doctoral studies at MIT.

I consider myself fortunate to have worked on this project with **Doug Creviston**. Through the course of over 1000 shock tunnel shots and re-coating the acoustic chamber with fiber glass absorber in smoldering heat, our friendship was always present. My prayers are with you as you continue beyond the confines of the shock tunnel. A special thanks to **James Bridges**, for answering numerous questions concerning aeroacoustics, providing countless hours of help mastering the ever enigmatic DADS and for always taking the time to review and make sense of the results. Also thanks to **David Forsyth** for help with the steady-state data and LSAF. Thanks to **Edward Kawecki**, **Brad Leland**, **Kamran Fouladi**, and **Alfred Stern** for their support and valuable technical advice throughout the course of this project.

I would also like to express my thanks and appreciation for one of my best pals, **Chris Spadaccini**. I have shared numerous memorable experiences with my friend, studying for the Ph.D. qualifiers, getting jacked at the gym, managing our top-notch fantasy baseball squad, escorting disgruntled Red Sox fans out of Fenway after the Yankees clinched the A.L. East in 1998 and the general goofing around we do on a daily basis. Thanks for getting my back at MIT and for playing an outstanding shortstop. I would also like to thank **Kevin Lohner**, for being an extraordinary friend to me. I will always remember the numerous graduate school experiences we shared together, from class work to playing softball. Other friends that have made my GTL experience that much more memorable include the **Protz** brothers, **Mez Polad**, **Tony Chobot**, **Jeff Freedman**, **Amit Mehra**, **Luc Frechette**, **Adam London**, **Rory Keogh**, **Brian Schuler**, **Margarita Brito**, **Ken Gordon**, **Dave Underwood**, **Jinwoo Bae**, **Stephen Lukachko** and my office-mates **John Chi** and **Asif Khalak**. Also within the GTL, a very special thanks to **Lori Martinez**, **Diana Park**, **Paul Warren**, **Victor Dubrowski** and **Jimmy Letendre**. Also, thanks to **Frank** 'Hey there he is... you never know... hey, how about those Red Sox' **Rogers**.

Serdecznie dziekuje dla mojej mamy i taty za wychowanie mnie w wierze i dla pracy w Jezusie Chrytisie. Dziekuje bardzo za wasza milosc i cierpliwosc, moje ciazka prace poswiecelem dla was. Unbound thanks to my dear parents for years of love and guidance.

This thesis is dedicated to Mahdad Koosh. An altruist, who through his trying experiences, was able to enrich the lives of many. I was privileged to whiteness this firsthand. My life was enriched through our years of friendship. I miss my friend.

This material is based upon work supported under a National Science Foundation Graduate Fellowship. Any opinions, findings, conclusions, or recommendations expressed by the author do not necessarily reflect the views of the NSF. This work was supported by Pratt & Whittney PO F760652 from NASA HSCT/CPC Prime Contract NAS3-27235.

Table of Contents

3. Shock Tube Gas Dynamics

4. Acoustic Theory and Generation of the Supersonic Scaled Jet

List of Figures

List of Tables

Nomenclature

Roman

A	Cross-sectional area, m^2
D	Diameter, m
EPNL	Effective Perceived Noise Level, EPNdB
K	Kinematic momentum
M	Mach number
MAR	Exit to primary throat area ratio
Ms	Incident shock wave Mach number
NPR	Nozzle Pressure Ratio, P5/P0
OASPL	Overall Sound Pressure Level, dB
PNL	Perceived Noise Level, dB
Pr	Prandtl number
Re	Reynolds number
$\mathbf{Re_t}$	Transition Reynolds number
$\mathbf{R_{mic}}$	Distance from nozzle exit to microphones, m
SPL	Sound Pressure Level, dB
St	Strouhal number
T	Static temperature, K
Tr	Adiabatic recovery temperature, K
Tt	Total temperature, K
TTR	Total temperature ratio
a	Local speed of sound, m/s
cs	Incident shock wave speed, m/s
dB	Decibel, re 20 μPa
f	Frequency, Hz
l	Length, m
$\mathbf{l_{jet}}$	Jet length, m
$\mathbf{l_{pc}}$	Potential core length, m
$\mathbf{m_p}$	Primary nozzle mass flow, kg/s
p	Static pressure, Pa
pt	Total pressure, Pa

$\mathbf{t_{exg}}$	Exhaustion of test gas time scale, ms
$\mathbf{t_{jet}}$	Jet development time scale, ms
$\mathbf{t_{nozzle}}$	Nozzle starting time scale, ms
$\mathbf{t_{wave}}$	Reflected wave test time limit, ms
u	Velocity, m/s
x	Axial distance, m

Greek

χ**He**	Helium mass fraction, %
γ	Ratio of specific heats
ρ	Density, kg/m^3
μ	Viscosity,
δ	Boundary layer thickness, m
δ^*	Boundary layer displacement thickness, m
ε_o	Virtual kinematic viscosity
τ_x	Wall shear force, N
τ	Time, s
θ	Boundary layer momentum thickness
Ψ	Directivty angle, degrees
ν	Kinematic viscosity
ζ	Boundary layer similarity parameter

Subscripts

dn	Driven section
dr	Driver section
e	Exit
o	Conditions behind the incident shock wave
p	Primary stream
r	Reflected shock
s	Secondary stream
st	Shock tube

t	Total or stagnation quantities
w	Wall
0	Ambient conditions
1-5	Conditions in the shock tube

Superscripts

*	Primary nozzle throat
‘	Relative frame

Chapter 1
Introduction

1.1 Background

Current projections of the demand for air transportation indicate that the market is expected to undergo significant growth, particularly in trans-Pacific operation. In Boeing's *1996 Current Market Outlook*, air traffic was predicted to increase 5.1% per year worldwide and 7.1% per year in Asia during the period from 1996 to 2015. Such a substantial increase in the demand for air transportation has rekindled an interest in developing a supersonic commercial transport for trans-ocean operation. Currently, NASA and United States aerospace industry leaders, such as Boeing, Pratt & Whitney and General Electric Aircraft Engines, are participating in a joint research initiative to explore technologies to expedite the inception of such an aircraft. This new aircraft which has been designated the High Speed Civil Transport (HSCT) is shown in Figure 1-1.

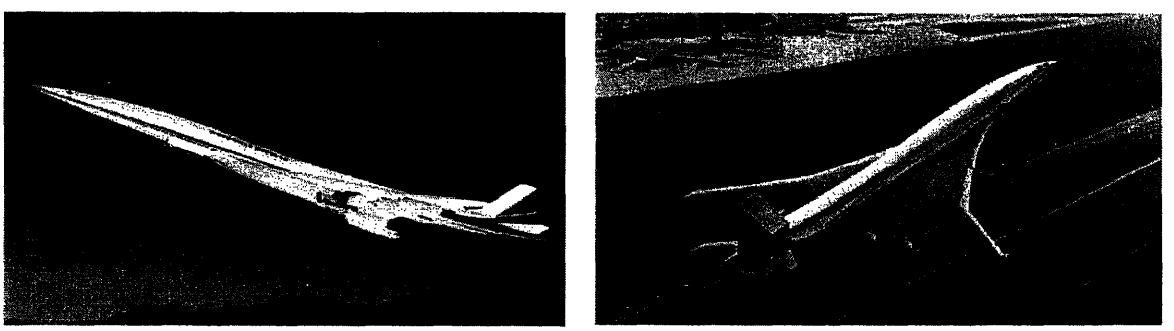

Figure 1-1: Artist conception of the High Speed Civil Transport, [58]

Realistic specifications for the new HSCT call for a Mach 2.4, 300 passenger, 5,500 nautical mile range aircraft. A more detailed schematic of the proposed design is shown in Figure 1-2. Because of its speed, a trip from Los Angeles to Tokyo, for example, would take just over four hours instead of the typical 10 hour flight time for a subsonic aircraft. The total cost of research and development is estimated at $15 - 20 billion with an actual development period of around 7 - 10 years. Surveys indicate that 50% of passengers would accept an average 25% surcharge over subsonic fares, while a 30 - 40% surcharge seems to be more pragmatic for an adequately profitable HSCT. The estimated market need of about 550 units by the year 2020 justifies a satisfactory return on investment of around 12% for only one

manufacturer. The unit cost of each HSCT is projected at 1.8 times that of the Boeing 747-400 in order to generate satisfactory profit for both airlines and manufacturers. However, before a supersonic HSCT takes to the skies, the technology to meet environmental compatibility and operational requirements for such an aircraft must be investigated and developed, [43].

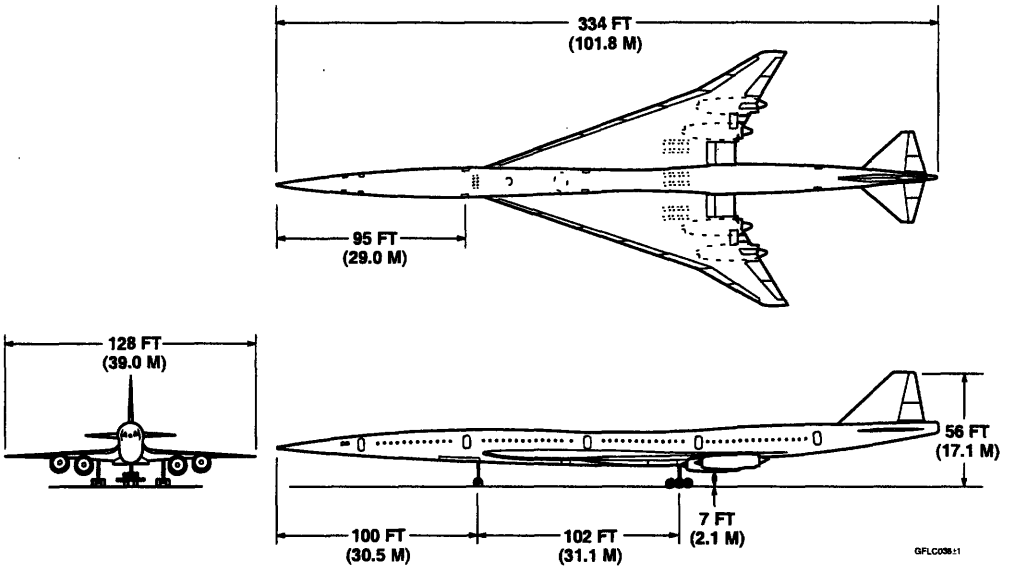

Figure 1-2: General arrangement of HSCT Model 2.4-7A, [61]

Aircraft noise is currently one of the most significant environmental concerns facing air carriers, as well as one of the most difficult engineering challenges associated with HSCT viability. Furthermore, with an anticipated population density increase within the vicinity of airports, noise abatement is of increasing consequence in the design of aircraft engines. The current supersonic transport, the Concorde, fails to meet the FAR 36 Stage III noise regulations, and must receive a special exemption to operate at U.S. airports, [48]. A future supersonic transport will have to meet the same stringent airport noise regulations that apply to subsonic transports. Hence, NASA's High Speed Research Program has instituted an effort to develop a jet noise suppressor for use on the proposed HSCT aircraft, [58].

The dominant noise source for aircraft at take-off and landing is the high speed exhaust jet that exits from the engine. A significant reduction in jet velocity during this phase of the aircraft's operation is widely regarded as one of the most promising means to curtail jet noise, [14]. Current efforts to develop such a technology have primarily focused on acoustically-lined mixer-ejectors. A schematic of a such a design is shown in Figure 1-3.

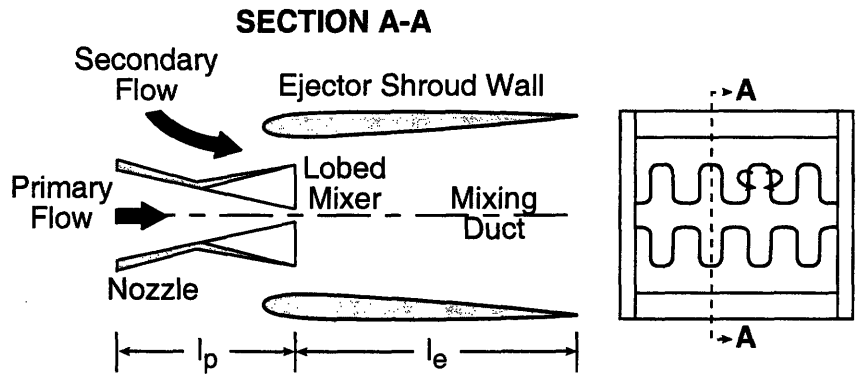

Figure 1-3: Conceptual HSCT mixer-ejector noise suppression system: Section and rear view, [28]

The underlying concept behind these nozzles is to make use of deployable chutes to mix ambient air with engine exhaust inside an acoustically-treated ejector duct. This reduces the jet exit velocity and, correspondingly, the turbulent intensity of the free jet and the associated radiated noise. With such an arrangement, thrust loss and the additional weight of the mixer-ejector are of critical importance in the design process. For this concept to be practically viable, a noise reduction of at least 4 EPNdB per percent of thrust loss will be required, while at the same time adding less than 20% to the total engine weight. It is therefore essential to mix the streams as rapidly as possible to reduce the required ejector length, and to perform the mixing of the two co-flowing streams with minimal fluid mechanic losses, [43], [52].

Research has demonstrated that a fixed geometry, passive lobed mixing device can be employed to rapidly mix co-flowing streams with relatively low losses. A schematic of a lobed mixer is shown in Figure 1-4. The augmented mixing that results from use of such a device is linked to the geometry of the mechanism and to the strain field associated with the generation of embedded streamwise and transverse vorticity along the interface between the co-flowing streams. Specifically, three distinct features of this lobed mixer design augment the mixing process:

1. Increased interfacial area between the two intermixing streams due to the convoluted trailing edge.
2. The presence of counter-rotating streamwise vortices on the interface between the two streams stretches the interface, further increasing interfacial area and increasing local gradients in fluid properties which provide the driving potential for mixing.
3. When the freestream velocities on either side of the lobe are not equal, as is most often the case in practical devices, vorticity components parallel to the trailing edge are present, resulting in Kelvin-Helmholtz or transverse vorticity, which further enhances the mixing process.

Items 2 and 3 are shown schematically in Figure 1-5.

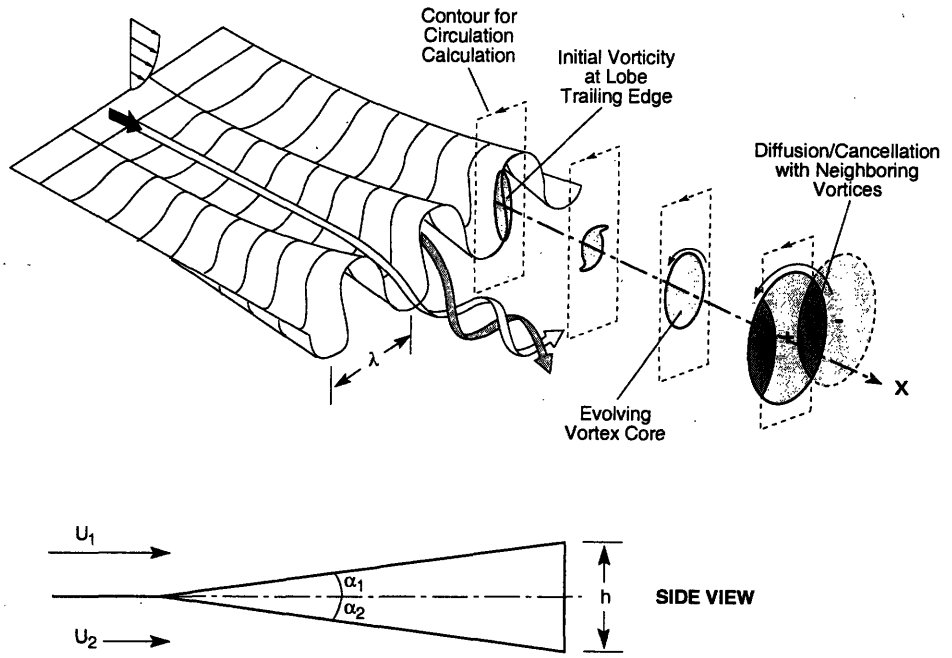

Figure 1-4: Isometric and side view of a typical lobed mixer

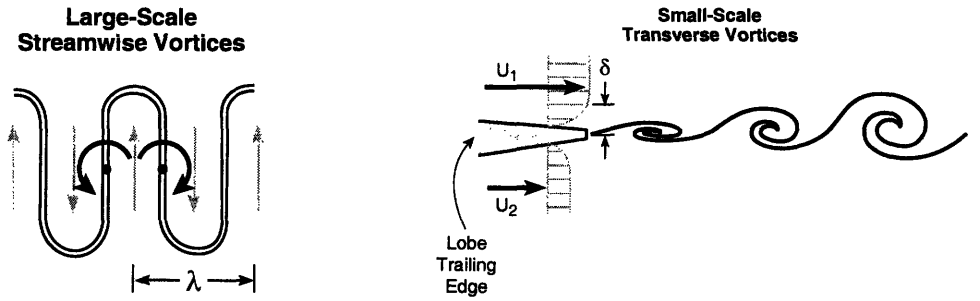

Figure 1-5: Streamwise and transverse vorticity details

Enhanced mixing rates are crucial to performance, where one pound of ejector weight can add more than 10 pounds to the gross take-off weight of a four engine HSCT aircraft. Thus far, experiments and analytical predictions indicate that advanced mixer-ejector nozzles can suppress jet noise to one-quarter of today's Concorde. Additionally, advanced high-lift aerodynamic devices combined with new operating procedures for take-off, climb-out, and landing could cut noise levels even more substantially, [28], [52].

1.2 Motivation

In order to elucidate the links between the dominant flow structures and acoustic radiation of hot turbulent supersonic jets, as well as to facilitate development of simplified acoustic models, carefully controlled experiments must be conducted. Conventional steady-flow combustion or electric-arc-heated facilities are

currently employed as the primary means of acquiring fluid mechanic and acoustic data used to investigate noise suppressor nozzle concepts. Typical sub-scale nozzles cost more than $100,000 and require several months to design and fabricate. Such time and fiscal constraints impose practical limits on the number of nozzle concepts and geometries that can be investigated and provide motivation for the development of more flexible and efficient testing techniques for the study of noise suppressor nozzles.

One concept, the shock tube, is mechanically simple, has minimal operating and maintenance costs, and can generate flows with a wide range of total pressures and total temperatures comparable to steady-state facilities. Furthermore, as a result of shock heating, the total temperature and pressure profiles at the nozzle inlet are uniform, eliminating the noise associated with entropy non-uniformities that are often present in steady-state, vitiated-air facilities. The compromise made for mechanical simplicity and versatility is the brief duration of useful test time. Sufficient time must be allowed for the nozzle flow and free-jet to reach a quasi-steady-state before measurements can be made. However, if this constraint is met, the short run times become advantageous. The test nozzles are exposed to high temperature flow for only a fraction of a second, thus relatively inexpensive stereo-lithography or cast aluminum nozzles ($2,000 - $50,000 each), can be tested at realistic flow conditions. Conversely, nozzles for steady-state facilities are typically an order of magnitude more expensive since they must be robust enough to withstand pressures at elevated temperatures for extended periods of time.

1.3 Shock Tunnel Facility Overview

The shock tunnel is a research facility operating within MIT's Gas Turbine Laboratory and the Aero-Environmental Research Laboratory. A detailed design and analysis of the facility was performed by Kerwin [22].

The shock tube consists of a 7.3 m driven section and an 8.4 m driver, both constructed from 30 cm diameter steel pipe. The shock tube is suspended on rollers to provide access to the diaphragms and allow repositioning of the test nozzles with respect to the microphones. Figure 1-6 provides a simple schematic of the shock tube's modular parts, as well as the roller assembly onto which it is mounted.

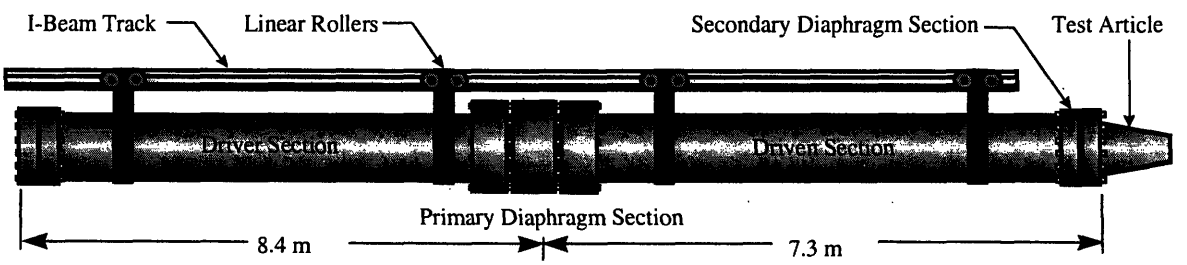

Figure 1-6: Schematic of MIT shock tube and associated roller assembly

The nozzles exhaust into an 8.3 m x 9.8 m x 3.7 m anechoic test chamber treated with a 10 cm thick fiberglass acoustic absorber, which results in 10 to 20 dB reduction in reflected acoustic intensity for frequencies above 500 Hz. Fluid mechanic and acoustic data acquisition systems are located in the control room adjacent to the test chamber. The filling and firing of the shock tunnel is completely automated and computer controlled once the desired fluid jet conditions have been specified. Turnaround time for the facility varies depending on the jet conditions being investigated, but is typically around 30 - 40 minutes, making 8 - 10 shock tunnel tests per day viable. A more detailed description of the facility is contained in Chapter 2, and in Reference [22].

1.4 Objective

The objective of the research described in this thesis is to assess whether or not a transient shock tunnel facility can be utilized to produce useful fluid mechanic and acoustic measurements of hot supersonic jets and nozzle flows.

1.5 Approach

In order to achieve this objective,

1. A series of experiments involving an acoustic point source, a small round nozzle operating in steady-state, and small round nozzle operating transiently were conducted to assess and validate the internal consistency and repeatability of the facility. A comparison between steady-state and transient acoustic data on a small round nozzle, both tested within the shock tunnel facility, was made.
2. An assessment of the acoustic performance of three sizes of reference conic ASME (American Society of Mechanical Engineers) nozzles was performed over a range of operating conditions relevant to an HSCT application. A comparison between steady-state acoustic data obtained from Boeing's LSAF (Low Speed Aeroacoustic Facility, [60]) and transient data obtained from the MIT shock tunnel was performed.
3. Facility repeatability on a run-to-run basis and day-to-day basis, determination of useful test times and a comparison to an analytical prediction were performed.
4. An assessment of whether multiple transient shock tunnel shots could be combined to reduce the uncertainty associated with making transient acoustic measurement, was performed.
5. An investigation of the acoustic performance of model mixer-ejector, similar to that shown in Figure 1.3 and shown in more detail in Figures 2-6 and 2-7, was performed over a range of operating

conditions relevant to HSCT application. A comparison between steady-state acoustic data obtained from Boeing's LSAF and transient data obtained from the MIT shock tunnel was performed.

6. An assessment to establish the uncertainty bounds on sound pressure level measurements over the range of frequency bands, nozzle pressure ratios, total temperature ratios, and nozzle scales for which the facility can be successfully utilized as a substitute and/or as a complimentary mode of investigation to steady-state hot-flow test facilities, was completed.

1.6 Thesis Overview

This thesis describes an effort to assess whether or not a shock tunnel facility can be utilized to produce useful fluid mechanic and acoustic measurements on hot supersonic jets and nozzle flows. The resolution of this objective is brought to fruition through the course of the next four Chapters. Chapter 2 presents an overview and discussion of the MIT shock tunnel facility, as well as a brief overview of the steady-state facility where the acoustic data used in the comparison effort was obtained. Chapter 3 presents an overview of shock tube wave phenomena and physics in order to develop a 1-D inviscid ideal gas model to predict the flow properties across the nozzle. Also included in this chapter is an analytical prediction of the useful test times that can be achieved with the facility, as well as an extension of the 1-D model to include viscous effects associated with the unsteady turbulent boundary layer behind the incident shock wave. Chapter 4 continues with theoretical development of the acoustics associated with the supersonic scaled-jet. Chapter 5 presents the acoustic results obtained from a series of nozzles that were tested, as well as how the transient acoustic data performs with respect to steady-state measurements. The thesis is concluded with Chapter 6, which presents an overview of two other diagnostics that can be performed on scaled-nozzles using the shock tunnel facility: mixing measurements and thrust diagnostics.

Chapter 2

Experimental Facility and Instrumentation

This chapter describes the MIT shock tunnel facility and its accompanying support instrumentation used to make fluid mechanic and acoustic measurements on scaled-nozzle flows. A description of the test articles used in the investigation is presented along with a summary of facility performance and range of operation. The chapter also presents a description of the fluid mechanic data processing and gives an overview of the acoustic data system (Digital Acoustic Data System, DADS) located at NASA Lewis Research Center, which was used to process both the transient shock tunnel data as well as the steady-state data obtained at Boeing's Low Speed Aeroacoustics Facility, LSAF.

2.1 Facility Overview, Test Articles and Performance Capability

The shock tunnel is a research facility that operates within MIT's Gas Turbine Laboratory and the Aero-Environmental Research Laboratory. A detailed design and analysis of the facility was performed by Kerwin [22].

2.1.1 Shock Tunnel Facility Description

The MIT shock tube consists of a 7.3 m driven section and an 8.4 m driver section, both constructed from 30 cm diameter steel pipe. A schematic of the shock tunnel facility is shown in Figure 2-1. More details of the facility are contained in Reference 22.

The shock tube is suspended on rollers to provide access to the diaphragms and allow repositioning of the nozzles with respect to the microphones. The nozzles exhaust into an 8.3 m x 9.8 m x 3.7 m anechoic test chamber treated with a 10 cm thick fiberglass acoustic absorber, which results in 10 to 20 dB reduction in reflected acoustic intensity for frequencies above 500 Hz. This precaution is taken to avoid reflection of the jet noise during the test and to eliminate reverberations of the high amplitude noise associated with the initiation of jet flow into the test chamber. The shock tunnel is equipped with a system that flushes the residual helium from the driver section after each test, ensuring subsequent tests are not tainted by extraneous helium. Helium introduced to the test chamber after a test is removed via an exhaust fan located within the test chamber.

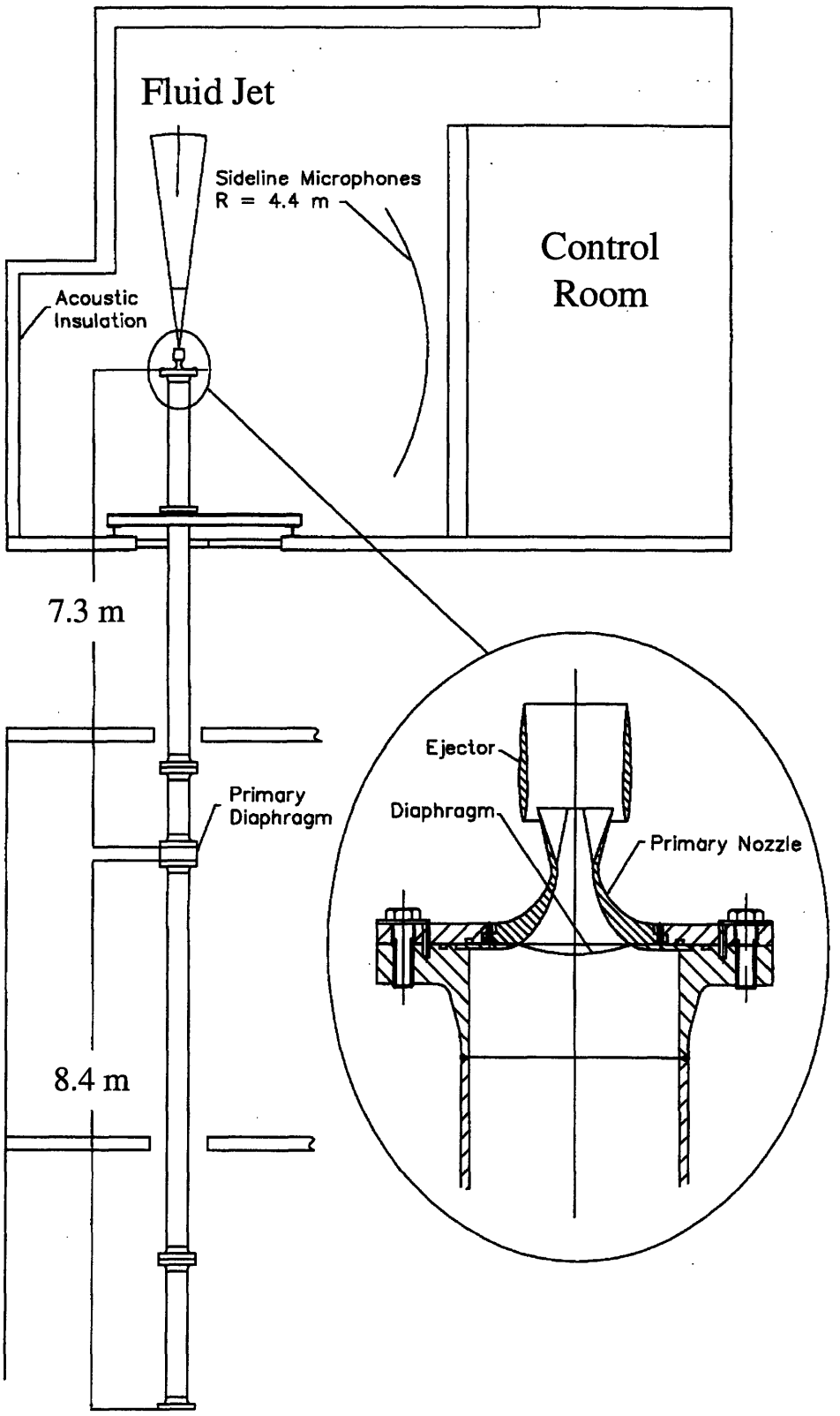

Figure 2-1: MIT shock tunnel facility schematic

A view of the acoustic chamber and 1/20th scale nozzle is shown in Figure, 2-2.

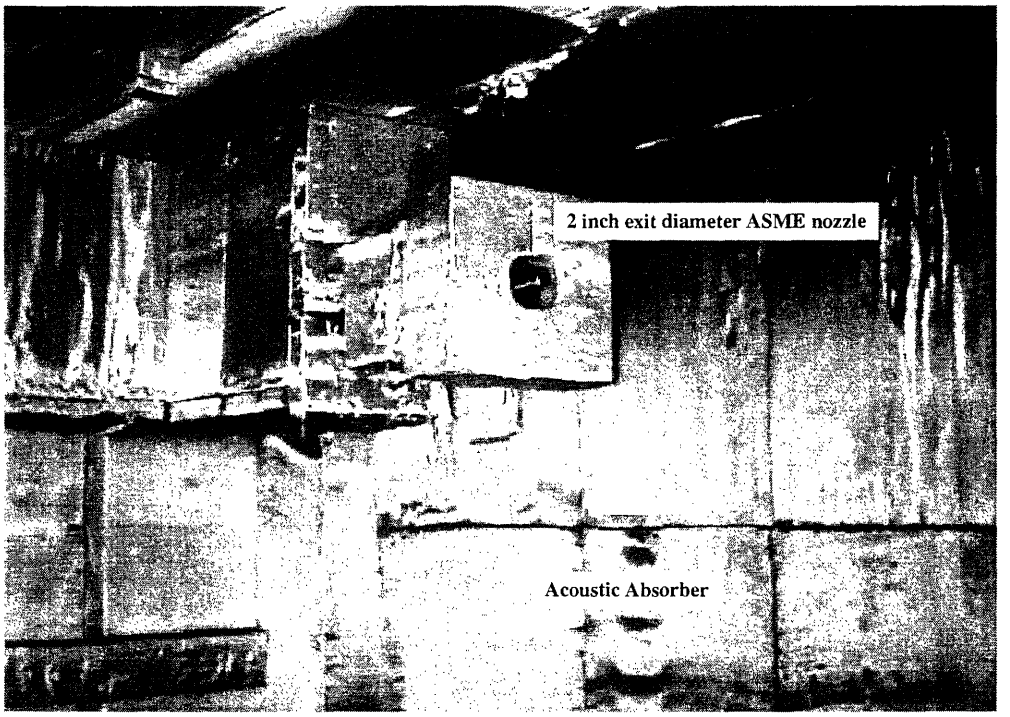

Figure 2-2: View of 1/20th scale ASME nozzle within the acoustic chamber

The control room is shown in Figure 2-3.

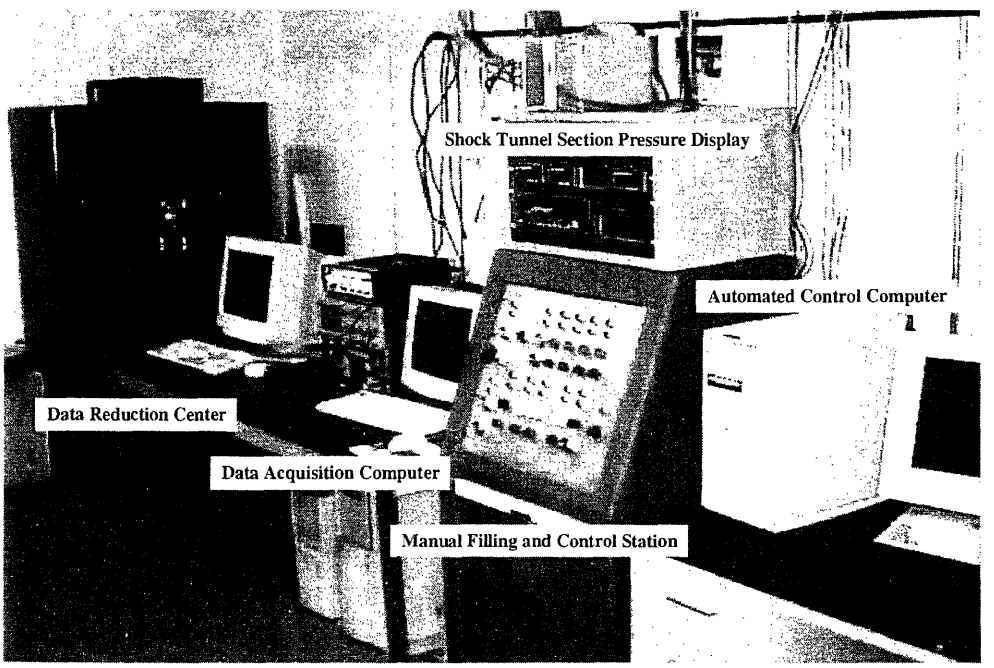

Figure 2-3: Shock tunnel facility control room

For a transient facility that acquires only 10-20 ms of data per test to be practical, the turn-around time from test-to-test should be such that 8-10 tests can be completed per day. The run-to-run turn-around time for this facility was found to be 30-45 minutes depending on the desired set conditions, i.e. the high NPR condition takes longer to fill the driver section than a low NPR condition.

2.1.2 Test Articles

The primary test articles used in the experiments to assess the performance of the MIT shock tunnel facility are three sizes of ASME standard axis-symmetric nozzles and a Large Scale Model Similitude (LSMS) mixer-ejector model. Furthermore, to compliment the investigation, a series of small exit diameter nozzles were fabricated to fit onto the end of the 1/20th scale ASME nozzle. This section provides a brief description of the nozzle geometries.

2.1.2.1 Small-Scale Nozzles

A series of small scale nozzles, ¼, ½, and ¾ inch exit diameter were fabricated to take advantage of the compressed air tunnel flushing system. Nozzles of this small size can be run at steady-state as well as under transient conditions to provide an 'in-house' comparison between transient and steady-state acoustic data. A picture of two of the small scale nozzles is shown in Figure 2-4.[1]

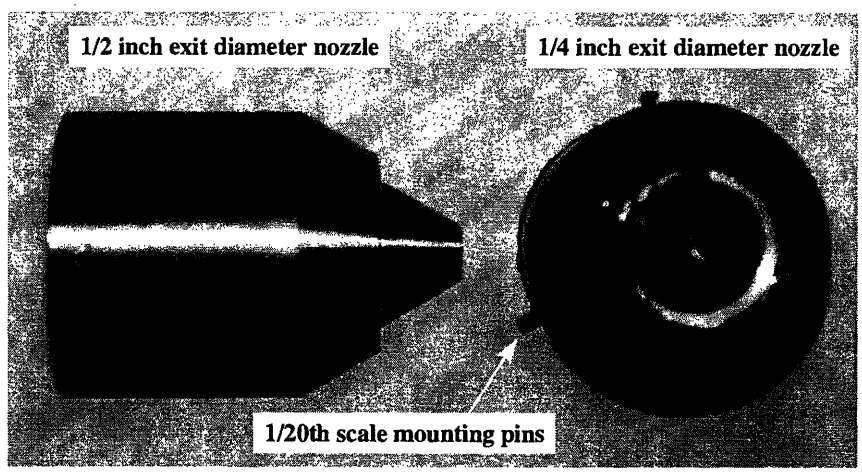

Figure 2-4: Small-scale round nozzles

The small-scale nozzles are attached to the 5.1 inch exit diameter (1/20th scale) ASME nozzle using three mounting pins located 120 degrees apart, as shown in the figure. Additionally, a bead of silicon is placed around the base of the nozzle to ensure a good seal between the two nozzles.

[1] The dark discoloration shown on the nozzle of Figure 2-4 is black spray-paint that was applied to the nozzle to minimize glare during video diagnostics, which are discussed in Section 6.1.2.1.

2.1.2.2. ASME Conic Nozzles

The sizes of the three ASME standard axisymmetric nozzles used on the shock tube to assess facility performance, as well as the ASME nozzle used to acquire steady-state acoustic data, are summarized in Table 2.1.

Table 2.1: Summary of ASME conic nozzle geometry

Nozzle Description	Nozzle Scale	Exit Diameter	Exit Area, A^*	Lp
Transient (Small)	$1/20^{th}$	2 inches / 5.1 cm	3.14 in^2 / 20.43 cm^2	7.5 in / 19.1 cm
Transient (Medium)	$1/15^{th}$	2.67 inches / 6.8 cm	5.6 in^2 / 36.32 cm^2	10 in / 25.4 cm
Transient (Large)	$1/10^{th}$	4 inches / 10.2 cm	12.57 in^2 / 81.71 cm^2	14 in / 35.6 cm
Steady-State	$1/8^{th}$	5 inches / 12.7 cm	19.63 in^2 / 126.67 cm^2	17.5 in / 44.5 cm
Full-Scale Comparison	1	40 inches / 101.6 cm	1248 in^2 / 8051.6 cm^2	140 in / 355.6 cm

A picture of the $1/15^{th}$ Scale ASME nozzle is shown in Figure 2-5a, and the $1/20^{th}$ scale ASME nozzle mounted on the driven end of the shock tube is shown in Figure 2-5b.

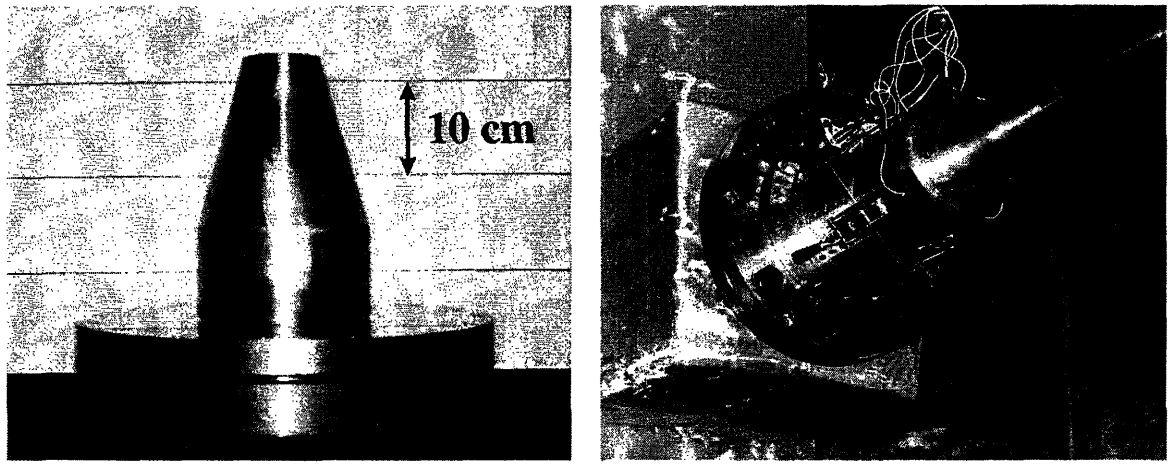

Figure 2-5: ASME Nozzles (a) $1/15^{th}$ scale ASME conic nozzle, (b) $1/20^{th}$ scale ASME conic nozzle mounted on the driven end of the shock tube

2.1.2.3. LSMS Mixer-Ejector Model

The geometry of the LSMS mixer-ejector nozzle is limited rights exclusive (LER), so no explicit definitions of the geometry of the model can be portrayed in this thesis. Figure 1-3 of Chapter 1 provided a conceptual design of a mixer-ejector similar to the one investigated using the shock tunnel. The model is a $1/12^{th}$ scale version of the full-size, with an overall length of the model being slightly larger than the $1/10^{th}$ scale ASME nozzle. Figure 2-6 shows the shell of the mixer-ejector, as well as some of the features of the model. Figure 2-7 shows a top view of the model, specifically depicting the location of the Kulite pressure transducers. The chute racks tested in the LSMS model are made of either cast aluminum or plastic stereo-lithography, SLA. The aluminum chute rack was cast from an SLA model.

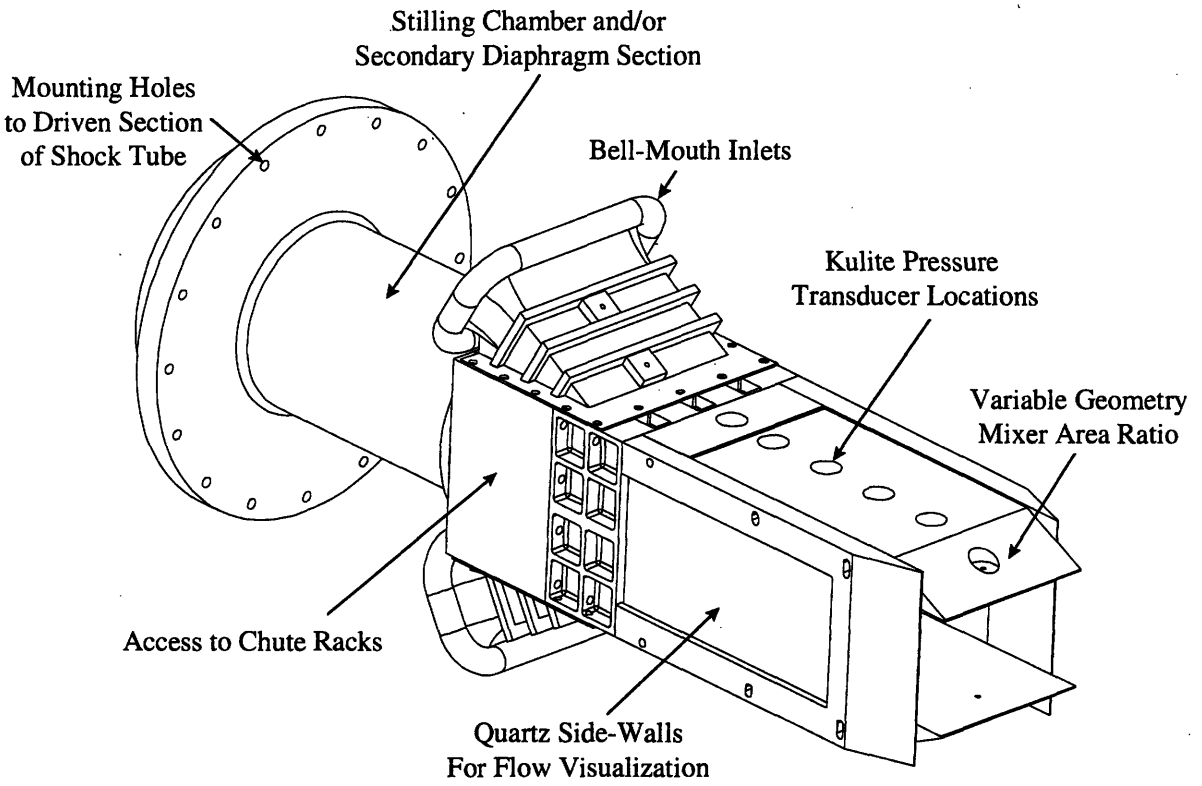

Figure 2-6: 1/12th scale LSMS model and associated features

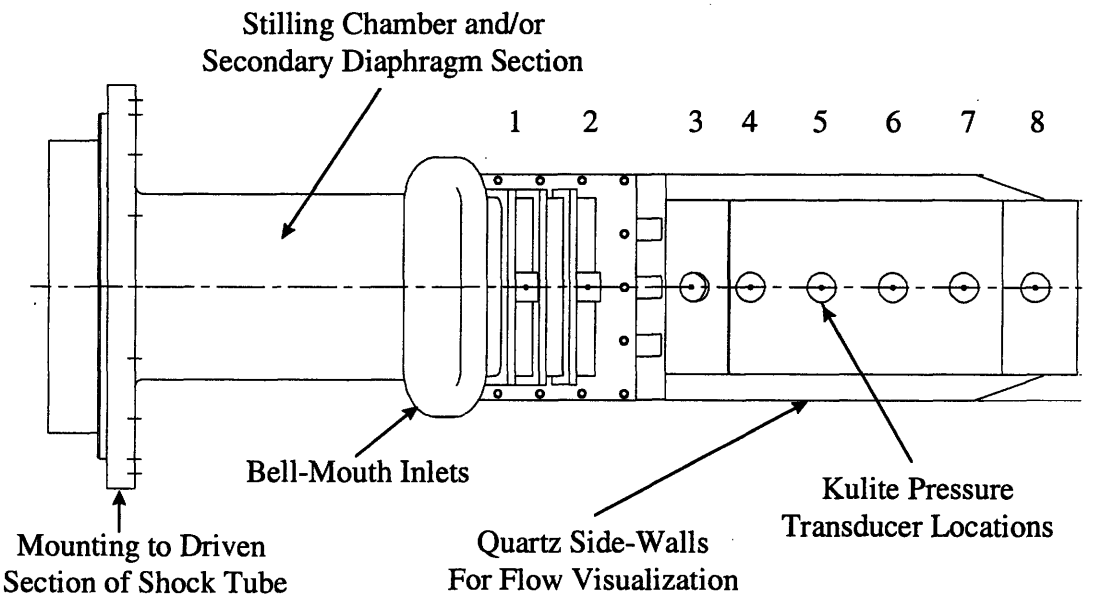

Figure 2-7: Top view of LSMS model and Kulite pressure transducer locations

The LSMS model also features an additional five Kulite pressure transducers (9 - 13) located on the bottom of the mixing duct, with transducer number 9 located directly below transducer number 8, and transducer 13 located in the lower bell-mouth assembly. Pressure signatures from these transducers will be shown in Section 4.5. Some digital photos of the LSMS model mounted in the shock tunnel facility are shown in Figures 2-8 - 2-10.

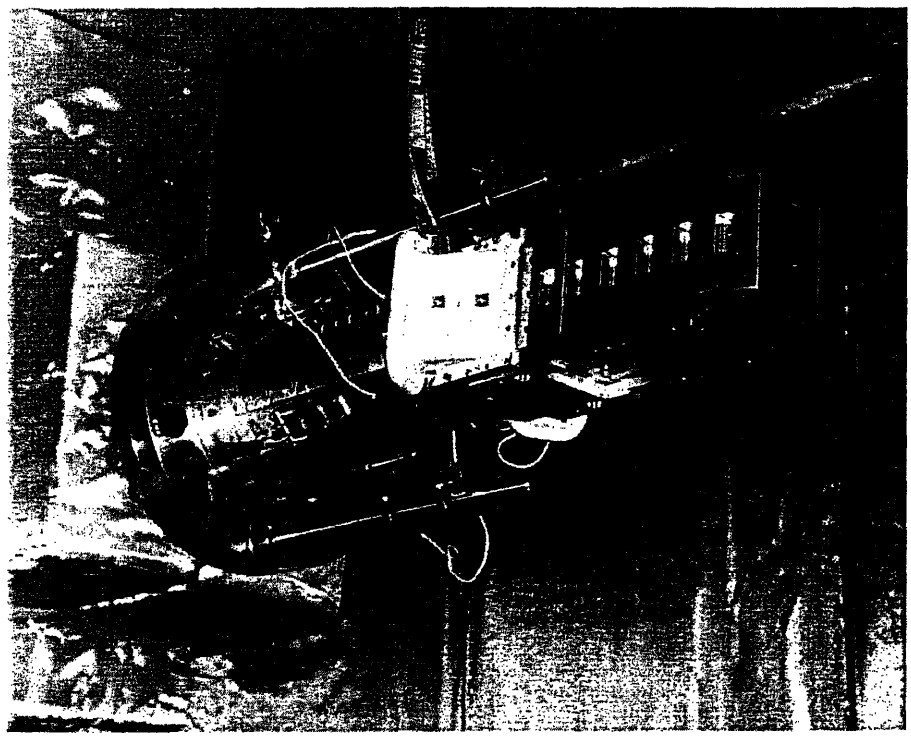

Figure 2-8: Isometric view of LSMS model mounted onto driven section of shock tunnel

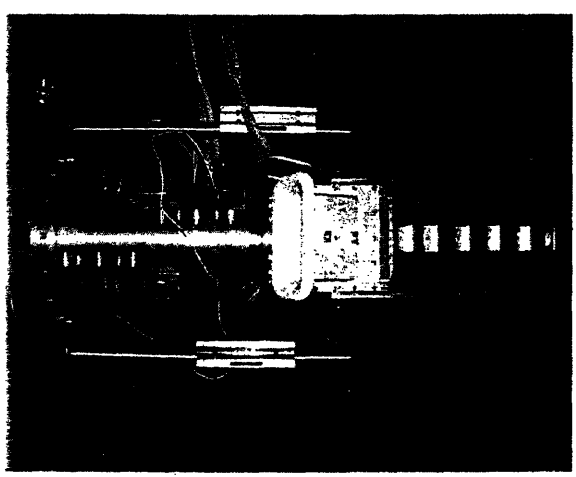

Figure 2-9: Top view of LSMS model

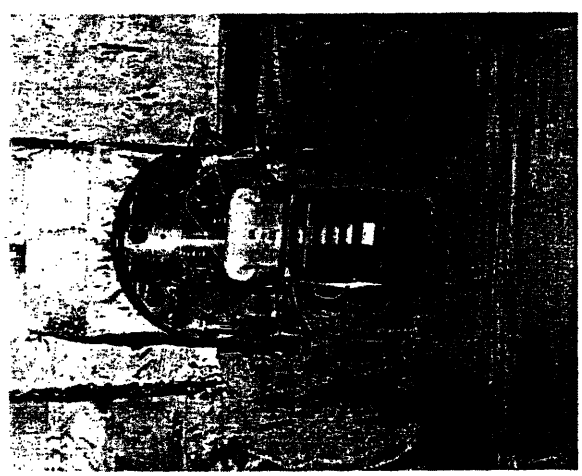

Figure 2-10: Far isometric view of LSMS model

2.1.3 Facility Performance and Range of Operation

The shock tunnel range of performance for the experiments presented in this thesis is summarized in Table 2.2. The shock tube is rated to 100 psi, corresponding to potentially achievable nozzle pressure ratios and total temperature ratios significantly higher than those presented in Table 2.2.

Table 2.2: Summary of shock tunnel facility performance capability

Parameter of Interest	Range of Operation
Nozzle Pressure Ratio, NPR	1.5 - 4.0
Total Temperature Ratio, TTR	1.2 - 3.5
Steady-State Nozzle Capability	¼, ½, and ¾ inch exit diameters
ASME Nozzles	2, 2.56, and 4 inch exit diameters
Mixer-Ejector Size	similar to ASME nozzles
Minimum R_{mic}/De for Steady-State Nozzles	600
Minimum R_{mic}/De for ASME Nozzles	40 (4 inch nozzle, worst case)
Minimum R_{mic}/De for LSMS	~ 40
Full Scale Frequency Range (B&K 4135)	100 Hz - 8 kHz
Full Scale Frequency Range (B&K 4136)	100 Hz - 6 kHz

Also presented in the summary are the microphone location constraints due to the size of the test chamber (as well as the constraining radius divided by the nozzle exit diameter), and the frequency range which can be measured using the microphones.

2.2 Fluid Mechanic and Acoustic Instrumentation and Measurement

This section presents an overview of the instrumentation and measurement tools used in the facility to make pressure measurements within the tube and in the test chamber.

2.2.1 Fluid Mechanic and Ambient Condition Measurement Instrumentation

Three Sensotec STJE 0-2000 kPa transducers accurate to ± 690 Pa are mounted in the driver, diaphragm, and driven sections of the shock tube. These transducers are used to display the set pressures of the three sections of the shock tube before each test. Four Kulite XT-190 0-670 kPa dynamic pressure transducers are flush-mounted on the wall of the driven section. These four transducers are used to measure the nozzle pressure, shock speed, and test time (duration of the uniform pressure region). A Paroscientific 0-2000 kPa transducer accurate to ± 207 Pa is used to calibrate the Sensotec control and Kulite dynamic pressure transducers. Additionally, two MKS mass flow controllers are employed to control the filling of the driver section of the tube with the helium-air mixture. Ambient conditions are measured just prior to each test

using a Paroscientific model 740 pressure transducer and Vaisala HMP231 temperature and humidity sensor. Ambient conditions are measured just prior to each test using a Paroscientific model 740 pressure transducer and Vaisala HMP231 temperature and humidity sensor.

2.2.2 Acoustic Instrumentation

This section presents a brief overview of the acoustic instrumentation used in the facility, a description of the microphones and associated support hardware, as well as procedures used to calibrate the microphones.

2.2.2.1 Microphones and Accompanying Support Instrumentation

Acoustic data were acquired using 6 Brüel & Kjær 4135, ¼ inch free-field microphones positioned on a constant radius arc 3.7 m from the nozzle exit at zero degrees incidence; locations are shown in Figure 2-11.

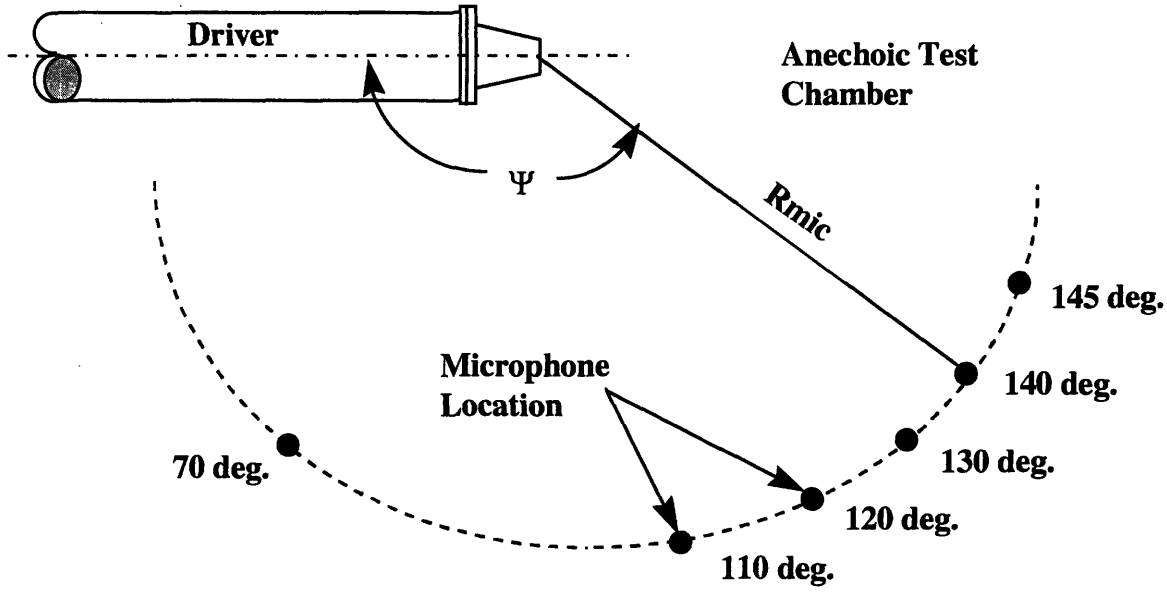

Figure 2-11: Microphone locations at constant radius for ASME conic nozzle testing

For an appropriate comparison between the transient and steady-state data, the microphones were located at directivity angles comparable to the steady-state facility. The six microphones were placed at directivity angles: 70, 110, 120, 130, 140, and 145 degrees, as measured from the inlet axis. To ensure that far-field behavior of the jet noise is captured, the microphones were located at greater than 30 exit diameters away from the nozzle exit. For the 10.2, 6.8 and 5.1 cm exit diameter nozzles, the microphones were located at 39, 57 and 76 exit diameters away, respectively. For the LSMS mixer-ejector model testing the

microphones were located at slightly different directivity angles[2] and the microphones were no longer placed at constant radius to take advantage of room geometry and ease of aziumuthal angle measurement. [3]

The microphones used in the experiment are Brüel & Kjær 4135, ¼ inch free-field microphones. Some important properties of the B&K 4135 are summarized in Table 2.3.

Table 2.3: Description of B&K 4135 ¼ inch microphone, [8]

Microphone Property	Description / Value
Frequency Response Characteristic	Free-Field 0° Incidence and Random Incidence
Open Circuit Frequency Response	4 Hz to 100 kHz
Open Circuit Sensitivity mV/Pa	4
Lower Limiting Frequency (-3 dB)	0.3 Hz to 3 Hz
Cartridge Thermal Noise (dB)	29.5
Resonance Frequency	100 kHz
Polarization Voltage	200 V

Condenser microphones require an electric field to be present between the backplate and the diaphragm when being used. The 4135 is an externally polarized microphone that obtains the charge for the electric field from a DC power supply[4] connected to the microphone via the preamplifier. Charge build-up on the backplate is not instantaneous, due to the high charge resistance of the preamplifier. Therefore externally polarized microphones reach the correct working voltage after about one minute. Before this time a microphone may not be within specifications. Also, during production, the microphone cartridges are subjected to a high temperature (150 °C) forced aging process which ensures long term stability. The predicted long-term stability is of the order of 1 dB over several hundred years at room temperature.

A sample calibration chart for one of the B&K microphones is shown in Figure 2-12. The upper curve is the open circuit free field characteristic, valid for the microphone cartridge without protection grid, for 0° sound incidence. The middle curve is the open circuit random incidence response, valid for the microphone with protection grid DD0023. The lower curve is the open circuit pressure response recorded with an electrostatic actuator. As can be seen from Figure 2-12, the response of the 4135 microphone rapidly rolls-off after around 100 kHz.

[2] Peak noise for ASME nozzles is around 130-140 degrees as measured by the convention shown in Figure 2-11. For mixer-ejector tests, the peak noise is expected to be located around 110-120 degrees, hence the microphones for LSMS testing were clustered more tightly around this region.
[3] Azimuthal angle geometry is described in Figure 2-19 within Section 2.3.
[4] This DC power is provided by the Microphone Multiplexer Type 2822.

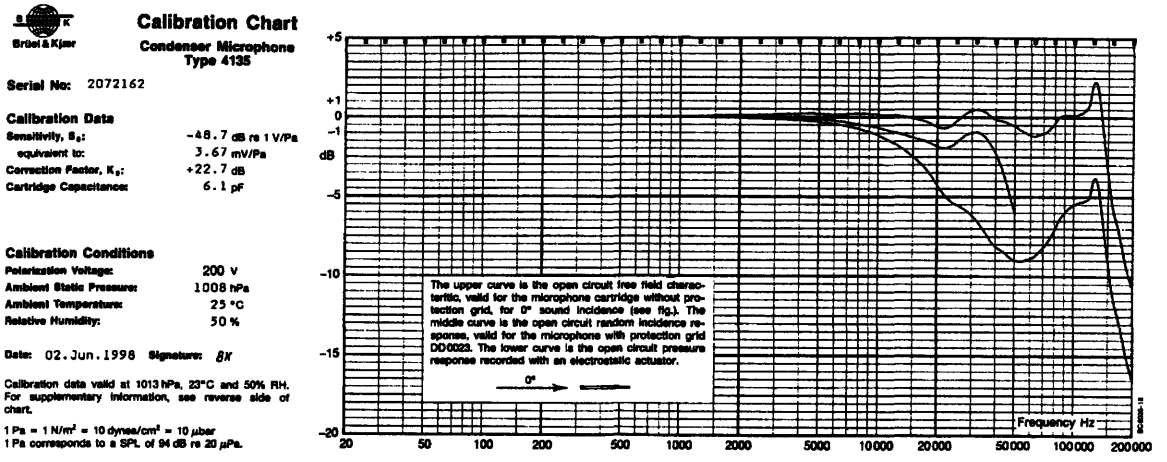

Figure 2-12: Typical calibration chart for B&K 4135 ¼ inch microphone. SN: 2072162 shown, [9]

When using a free-field response microphone such as the 4135, the microphone should be pointed towards the source. Figure 2-13 shows the free-field corrections for the B&K 4135 microphone with incidence angle.

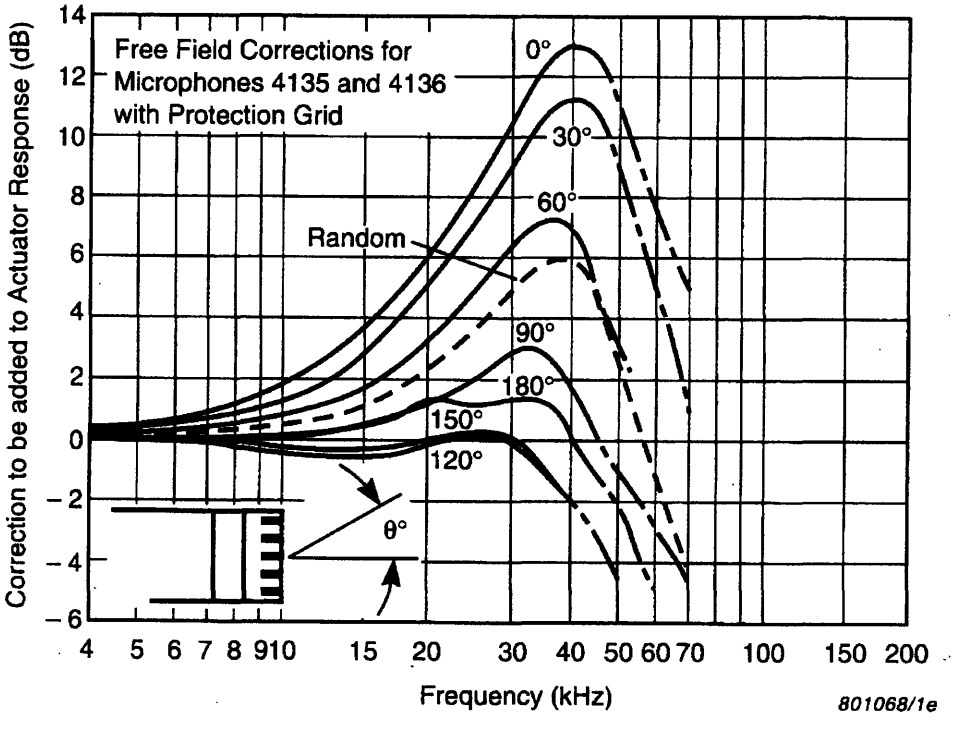

Figure 2-13: Free-field corrections for microphones 4135 with protection grid, [8]

For all experiments conducted in this thesis, the microphones were oriented at zero degrees incidence to the source[5] and grid caps were left on. The calibration curves shown in figures 2-12 and 2-13 were taken into account in the acoustic data processing, which will be further discussed in Section 2.3.

The microphones are connected to a ½ inch B&K preamplifier Type 2669 using a UA 0035 ¼ to ½ inch adapter. The preamplifier has a very high input impedance presenting virtually no load to the microphone, [9]. The high output voltage, together with an extremely low inherent noise level, gives a wide dynamic range, with a frequency response of ± 0.5 dB between 3 Hz to 200 kHz. The preamplifiers are then connected to cable 2669 B, which in turn connects to B&K Microphone Multiplexer 2822 using a coaxial extension cable AO 0038. The purpose of the multiplexer is to power the pre-amplifiers and to convert the output to a BNC cable which connects to a set of variable gain Pacific amplifiers. From the amplifiers the output is fed into the data acquisition system that is described in Section 2.2.3. A schematic of the microphone assembly and associated support instruments is shown in Figure 2-14.

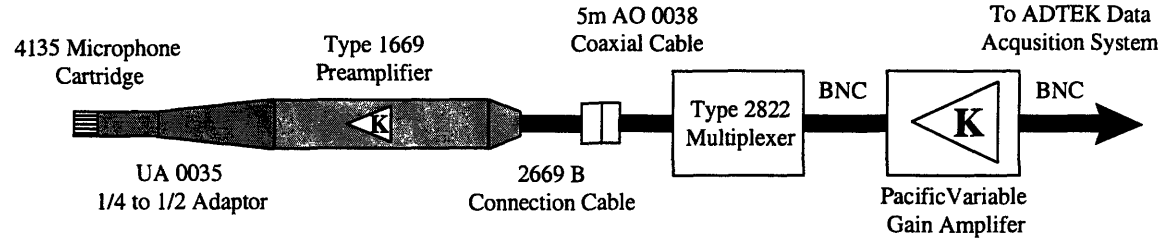

Figure 2-14: Microphone system schematic and associated components

2.2.2.2 Microphone Calibration

Calibration coefficients for each microphone were obtained with a B&K Pistonphone type 4228 using the procedure described in this section, [11]. The sound pressure level given on the calibration chart for the piston phone is only for the reference conditions stated there. However, ambient conditions will affect the SPL and give rise to a number of corrections. These should, therefore, be taken into account. Ambient condition corrections for pressure, load volume and relative humidity were taken into account during the calibration process to comply with class 1L laboratory requirements, equation 2.1. For improved calibration, a class 0L standard should be used, which is presented in equation 2.2.

Class 1L $$actualSPL = statedSPL + \Delta L_p + \Delta L_v \quad (2.1)$$

Class 0L $$actualSPL = statedSPL + \Delta L_p + \Delta L_v + \Delta L_H \quad (2.2)$$

[5] The source location was taken to be the exit plane of the nozzle. This assumption is further discussed in Chapter 4.

The most significant factor affecting the Pistonphone SPL is the ambient pressure. Generally, the pressure correction, ΔL_p, can be derived as:

$$\Delta L_p = 20\log\left(\frac{P_a}{1013hPa}\right)dB \qquad 2.3$$

When the Pistonphone Type 4228 is used as a class 1 calibrator, the correction for ambient pressure can be obtained in a faster and simpler way using Correction Barometer UZ0004. For ambient pressure within the range from 650 hPa to 1080 hPa, the correction for ΔL_p in dB can be read directly from the barometer scale.

The factory calibration is valid for an effective load volume of 1.333cm^3. However, different microphones represent different load volumes. The microphone load volume correction is given by:

$$\Delta L_v = -20\log\left(\frac{V_{load} + 18.400cm^3}{19.733cm^3}\right)dB \qquad 2.4$$

V_{load} is the actual effective load volume (the sum of the front volume and the microphone equivalent volume). For the B&K 4135 ¼ inch free-field microphones used in all experiments described herein, the correction for load volume is 0.0.

Humidity changes inside the coupler cavity affect the SPL produced by the Pistonphone. The humidity correction is a function of both temperature, relative humidity and atmospheric pressure. To find the correction for humidity, ΔL_H, the following formula is used:

$$\Delta L_H = 20\log\left(\frac{1013hPa}{P_a}\right)\Delta L + 0.0064dB \qquad 2.5$$

Pa is the actual atmospheric pressure, and ΔL is the correction obtained from the standard influence of humidity on SPL curve shown in Figure 2-15. More details associated with calibration of microphones using a pistonphone can be found in Reference [11].

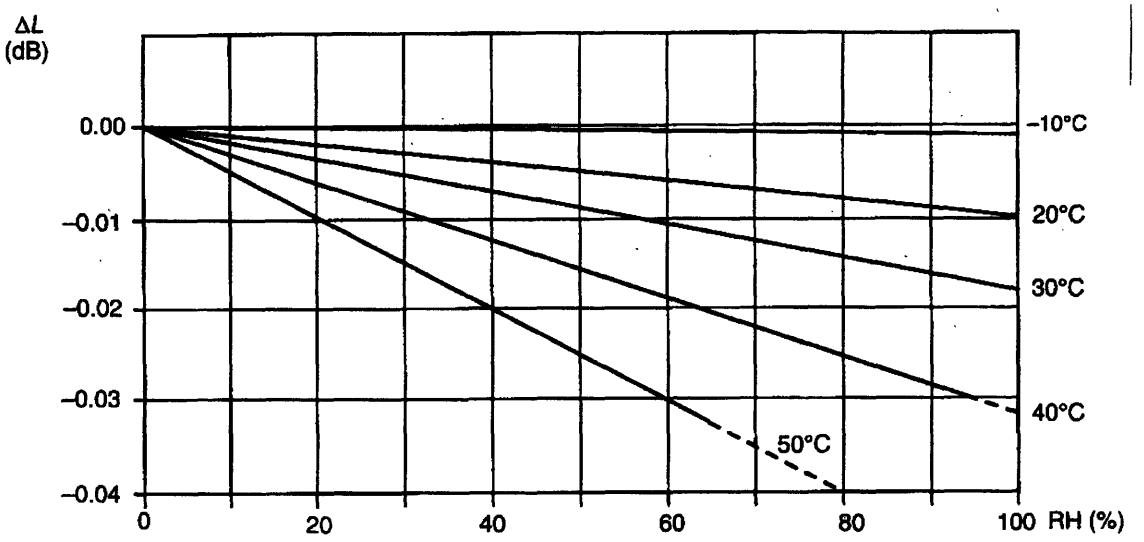

Figure 2-15: Influence of humidity on the SPL produced by Pistonphone Type 4228, [11]

The factory calibration coefficients for the six B&K 4135 microphones used in the experiments within this thesis are summarized in Table 2.4. Also listed in the table are the measured calibration coefficients using the techniques described in this section.

Table 2.4: Summary of B&K 4135 microphone calibration coefficients, factory versus measured

Serial Number	Sensitivity	Correctio n Factor	Cartridge Capacitance	Factory Calibration Coefficient	Measured Calibration Coefficient
2072154	-48.8 dB	+ 22.8 dB	6.3 pF	3.63 mV/Pa	3.239 mV/Pa
2072155	-48.0 dB	+ 22.0 dB	6.1 pF	3.98 mV/Pa	3.547 mV/Pa
2072156	-48.5 dB	+ 22.5 dB	6.4 pF	3.76 mV/Pa	3.259 mV/Pa
2072157	-47.9 dB	+ 21.9 dB	6.4 pF	4.03 mV/Pa	3.526 mV/Pa
2072158	-48.6 dB	+ 22.6 dB	6.4 pF	3.72 mV/Pa	3.271 mV/Pa
2072159	-49.0 dB	+ 23.0 dB	6.2 pF	3.55 mV/Pa	3.173 mV/Pa

The microphones were calibrated approximately once every 6 weeks. The drift of the microphone calibration coefficients was seen to be less than 1 percent over the course of this investigation corresponding to less than 0.1 dB of variation in SPL.

2.2.3 Data Acquisition, Location of the Quasi-Steady Pressure Region and Nozzle Pressure Ratio and Total Temperature Ratio Calculation

Two computers are used to control the operation of the facility and acquire the pressure and noise signals. One computer is used to control the sequence of 13 solenoid valves and 2 mass flow controllers necessary to fill and fire the tube, as well as to acquire and save the dynamic pressure data obtained from four wall-mounted pressure transducers in the shock tube. The second of the two computers is used to record and

save the microphone data. This computer is configured with two ADTEK AD830 high-speed data acquisition boards which enable it to simultaneously sample 16 channels at 12 bits, 333 kHz, [1]. The data acquisition is automatically triggered by the evacuation of the diaphragm section, signaling the initiation of the test. Pre-processing codes were developed to locate and parse both the uniform pressure region occurring after the reflected shock and the corresponding acoustic data for input to the data processing system.

NPR can either be calculated from the shock speed or by dividing the value of the static pressure during the quasi-steady region by the ambient pressure. A sample of how the pressure transducer data is analyzed is shown in Figure 2-16. TTR is completely a function of shock speed,[6] which is measured from the four pressure transducers located in the driven section. An example of TTR calculation from the incident shock passage over the pressure transducer is shown in Figure 2-17. Knowing the time that the incident shock wave passes each transducer, and knowing the physical transducer separation, the shock speed can be calculated from a simple distance equals speed multiplied by time equation. Using all four transducers, the uncertainty in the measurement can be reduced by taking the average speed over several distance and transducer location combinations.

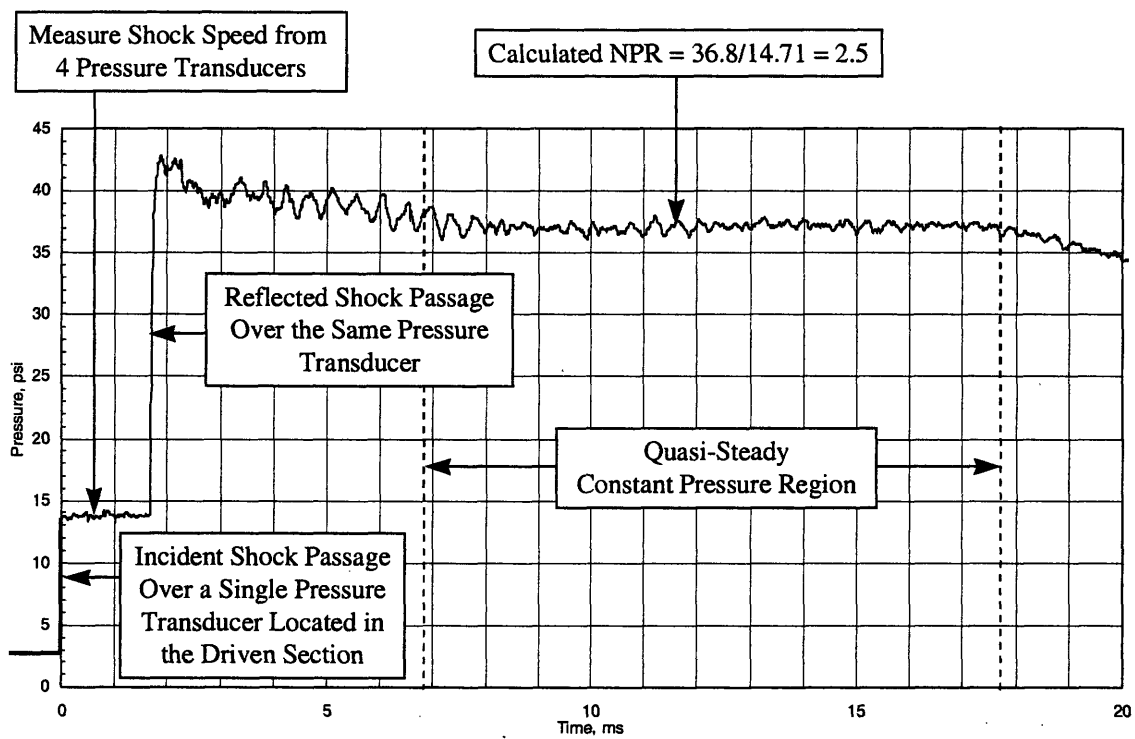

Figure 2-16: Example of location of the steady-state pressure region and NPR calculation

[6] The governing equations for the calculation of TTR from the shock speed will be presented in Chapter 3 when the 1-D model for shock tube flows is developed.

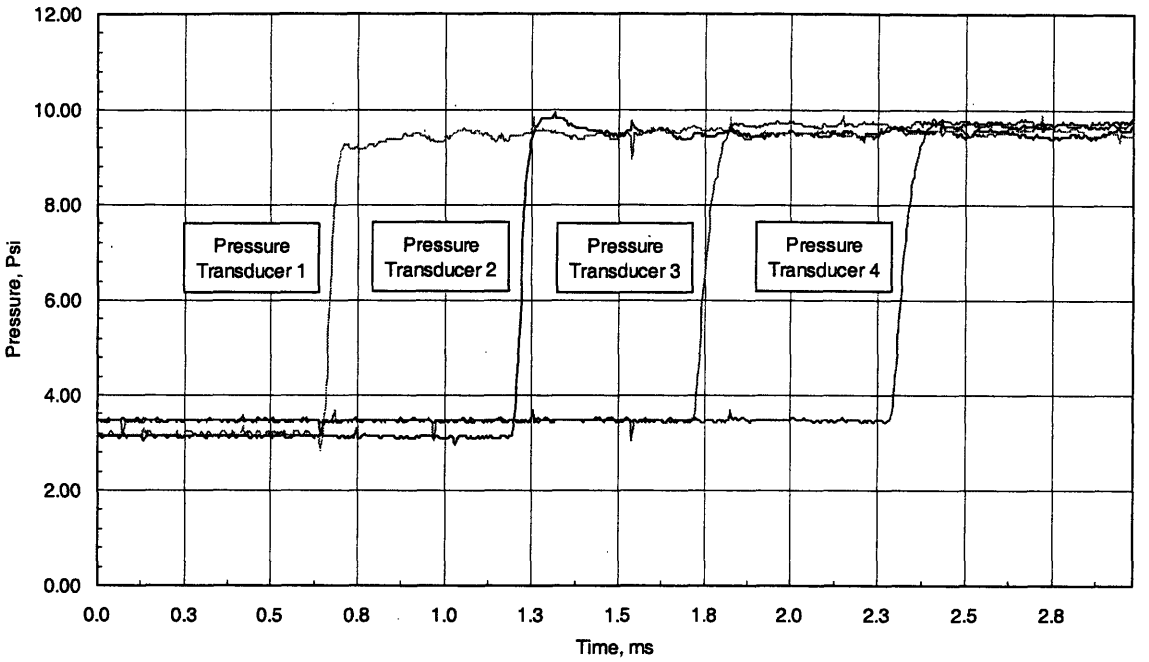

Figure 2-17: Calculation of TTR from incident shock passage over the four transducers located in the driven section of the shock tube

Using this instrumentation, NPR can be determined with an uncertainty on the order of 0.1%. TTR is determined with an uncertainty on the order of 0.1% through measurement of the incident shock speed and use of the shock tube equations. The sensitivity of the acoustic measurements to uncertainties in microphone calibration coefficient (± 1%), temperature (± 2 °F), relative humidity (± 2%), nozzle area (± 1%), and microphone location (± 5 cm) were also investigated and found to be small relative to the importance of measuring jet conditions accurately. The overall uncertainty in SPL, taking all these factors into account, was approximately ± 0.5 dB.

2.3 Acoustic Data Processing

Acoustic data were processed using the NASA Lewis Research Center Digital Acoustic Data System (DADS) as follows: the input was subdivided and converted into pressure versus time records, which were then processed to obtain spectra; the data were then processed to a one foot loss-less scenario taking into account instrument corrections and atmospheric attenuation, and then a fly-over transformation was performed, [6]. Frequency response characteristics and free-field corrections for microphone incidence angle were also incorporated into DADS. Steady-state SPL vs. frequency data were also processed using

DADS over the same frequency range as the transient data to ensure that the comparison presented was not influenced by the processing scheme.

For an appropriate comparison to be made with steady-state results, the acquired data are compared at a 'full-scale' diameter of 101.6 cm and over a simulated flight path where the noise is over an observer at a distance of 496.5 m. The noise data are extrapolated over a range of polar angles between 50 and 160 degrees. A schematic of the extrapolation used for the ASME nozzles is shown in Figure 2-18. A schematic showing the azimuthal angles and distances used in the extrapolation for the LSMS mixer-ejector model is shown in Figure 2-19.

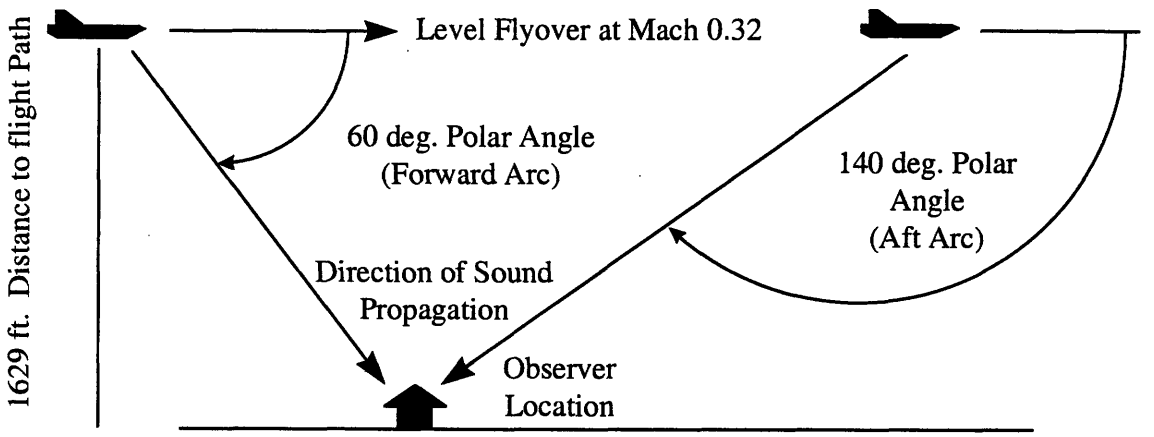

Figure 2-18: Free-field level flyover geometry at 1629 ft. used in extrapolation of model-scale noise data to full-scale conditions

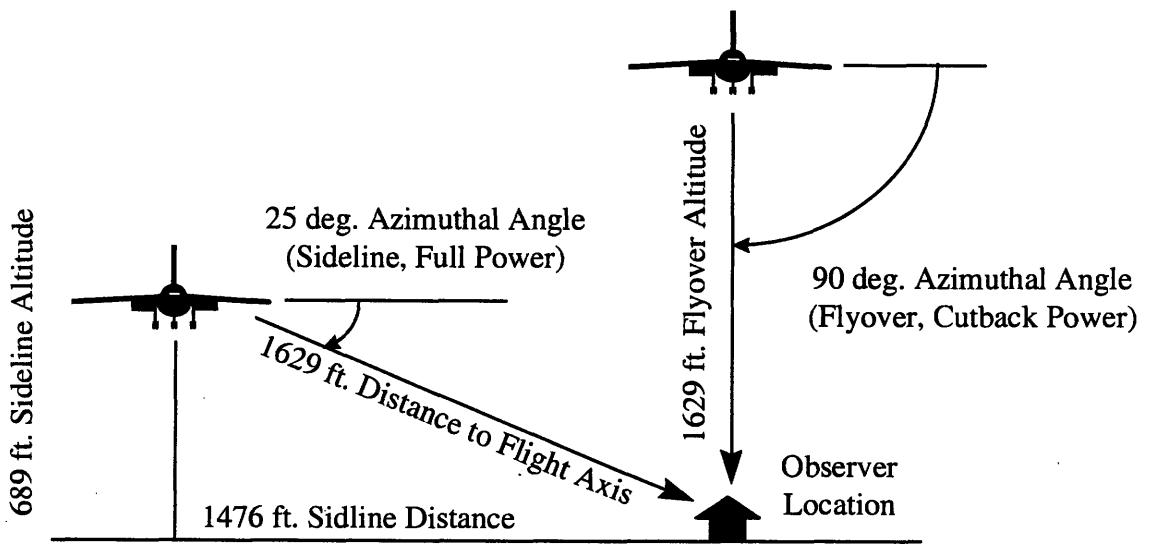

Figure 2-19:Azimuthal flight geometry used in extrapolation of model scale noise data

Information beyond the range of polar angles measured is created by extrapolating the last angle's source spectrum to the new angle's propagation distance while taking into account atmospheric absorption, [6]. Furthermore, each set of data is also corrected to standard day ambient conditions. The extrapolation generates SPL vs. frequency data for each of the polar angles, and the two data sets can be examined for agreement in magnitude of SPL over the full-scale frequency range, which corresponds to 250-4000 Hz for the 5.1 cm nozzle, 300-5300 Hz for the 6.8 cm nozzle and 500-6000 Hz for the 10.2 cm nozzle. Overall Sound Pressure Level (OASPL) and Perceived Noise Level (PNL) at each polar angle are also calculated and compared to assess the directivity behavior of the transient and steady-state noise data.

The resulting files from the DADS processing system are summarized in Table 2.5, as well as a statement as to how each of these files may be used:

Table 2.5: Summary of DADS output files

Output File	File Description and Relevance
C*	Instrument corrected as-measured spectra, useful to quality check the spectra
L*	1 ft loss-less narrowband data at model scale
T*	Level fly-over at full-scale, standard day, useful to compare to steady-state

2.3.1 Atmospheric Attenuation and Data Scaling

References [2], [40], [46], [49] explain the effects of atmospheric attenuation on propagating high frequency acoustic waves, as well as the process for correcting test data for this effect. Atmospheric attenuation correction of the static acoustic data is performed on narrow band spectra. Atmospheric attenuation is a linear phenomenon, so it is not dependent upon SPL level. Sheilds and Bass' correction is for attenuation at a particular frequency and ambient condition and tends to be nonlinear in frequency. Attenuation is calculated at the center frequency for each relatively small band in the constant bandwidth spectrum, and since the difference in attenuation across the narrowband is less small, the approximation is justified.

Within the LeRC DADS package, atmospheric attenuation is corrected for in the following way: The acoustic energy that was lost, when the acoustic waves propagated from the source to the microphone, is added to the measured data using the values for atmospheric attenuation, based on static temperature and humidity of the test chamber. The data is moved to any desired extrapolation distance by subtracting the appropriate atmospheric attenuation values. However, this correction is done for atmospheric attenuation values based on a standard day. In this fashion, various types of data (steady-state, transient, or full-scale fly-over) can be corrected to a standard day and then be comparable to each other, [6].

Since the high frequency data gathered at the shock tunnel facility is acquired using various nozzle scales, it is desirable to scale the data to an equivalent full-scale size. To apply the scaling laws properly, with regard to atmospheric attenuation, the data must be scaled after the test chamber

atmospheric attenuation corrections have been added to the model-scale data. In this fashion, the attenuation that occurred at high frequency on the test day is removed and the attenuation that would have applied to the full-scale acoustic lower frequency waves on the standard day are taken into account.

2.3.2 Background Noise Considerations

When making acoustic measurements there is always a potential for background noise contamination, [2]. As with the broadband electrical noise, the background noise during different hours of operation was measured and documented. The source of interest, i.e., the acoustic jet or the point source was turned off, but the other test parameters that may have produced background noise were left on, such as acoustic instrumentation, water pumps, mass flow controllers, and other hardware. Multiple background noise measurements were taken at various pre-amplifier gains to ensure that the acoustic measurements were not contaminated. Furthermore, a repeatability check on the background noise was performed at various times during data collection since the MIT shock tunnel facility is located next to other experimental facilities which produce varying amounts of noise depending on their level of operation.

The correction process for background noise is to compare the levels of background noise to the levels of each test measurement, and subtract the background noise from the test data if the difference between the test data and background noise levels are larger than a certain permissible dB tolerance level, ΔdB_{min}. If the difference between the background and test data levels are less than this permissible amount, the data should be considered contaminated. The value ΔdB_{min} is based on the repeatability of the background noise measurements. The more repeatable the background noise measurement, the smaller ΔdB_{min} can be for a given correction accuracy, [2].

Once an estimate for ΔdB_{min} has been established, the amount of noise contamination ΔdB_{contam} is determined from:

$$\Delta dB_{contam} = -10\log\left(1-10^{-\Delta dB_{min}/10}\right) \qquad 2.6$$

This equation can be interpreted as providing an estimate of the level of corruption to test data as a function of the separation between the data and the background noise.

For the MIT facility, on average, the acoustic data was 20 dB above the background noise, which corresponds to less than 0.1 dB of contamination. From this estimate it was taken that the background noise level was sufficiently low that no background noise subtraction would be necessary. However, if background noise contamination were to become an issue in the future, a background noise file could be created and subtracted from the acoustic measurements. The method of performing this subtraction is summarized briefly here, and discussed in detail in Reference [2].

When subtracting background noise levels from test measurement levels, the subtraction is performed using linear squared units. This subtraction assumes that the source of interest and the source of background noise are not coherent with each other and are not standing wave phenomena. In this case their acoustic power would add together instead of their pressures. When subtracting levels that are ΔdB_{min} apart, the higher level is always reduced by a fixed dB amount, independent of the absolute values (all levels are assumed positive).

If the background noise has a combined repeatability/error of $\pm \Delta dB_{err}$, then the accuracy of the background noise subtraction can be determined from:

$$\Delta dB_{bgcorr} = 10\log\left(1-10^{-\Delta dB_{min}/10}\right) - 10\log\left(1-10^{-\Delta dB_{min}+\Delta dB_{err}/10}\right) \qquad 2.7$$

For a series of different values of ΔdB_{err}, ΔdB_{min} can be determined based on ΔdB_{err} and the desired accuracy for the background noise subtraction, ΔdB_{bgcorr}. For example, if the repeatability of the background noise is $\pm$ 0.5 dB, and the required accuracy for the background noise subtraction is $\pm$ 0.5 dB, then the background noise may be subtracted from the test data as long as it is at least 3.2 dB below the data. Equations 2.6 and 2.7 are plotted in Figures 2-20 and 2-21, respectively.

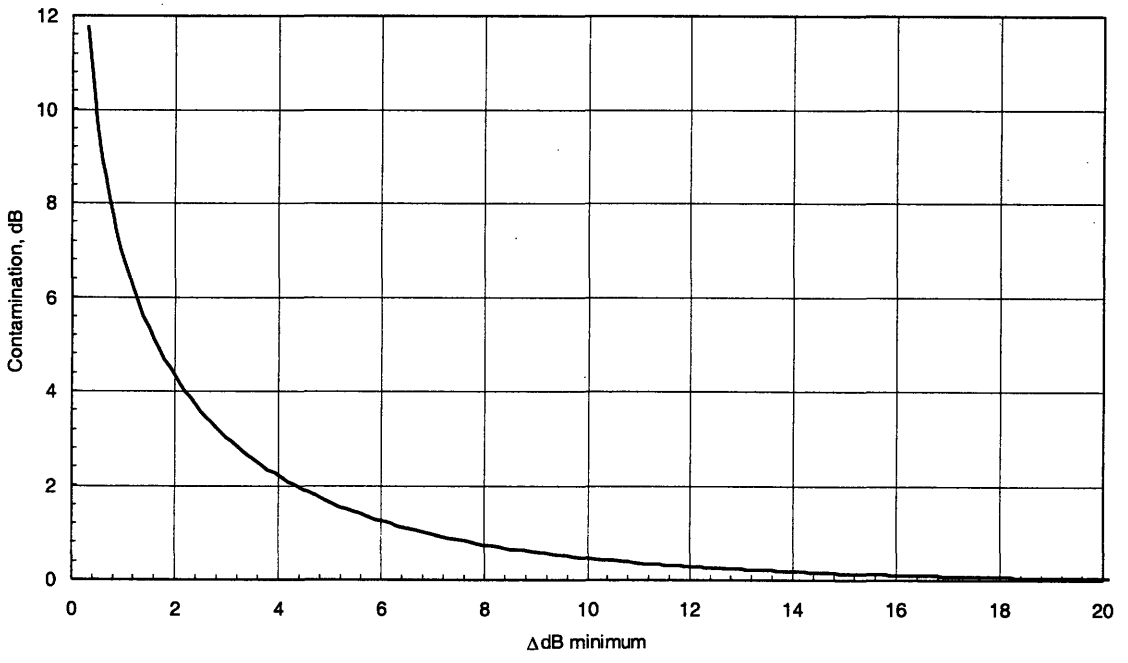

Figure 2-20: Amount of data contamination as a function of the separation between background noise and data measurement, [2]

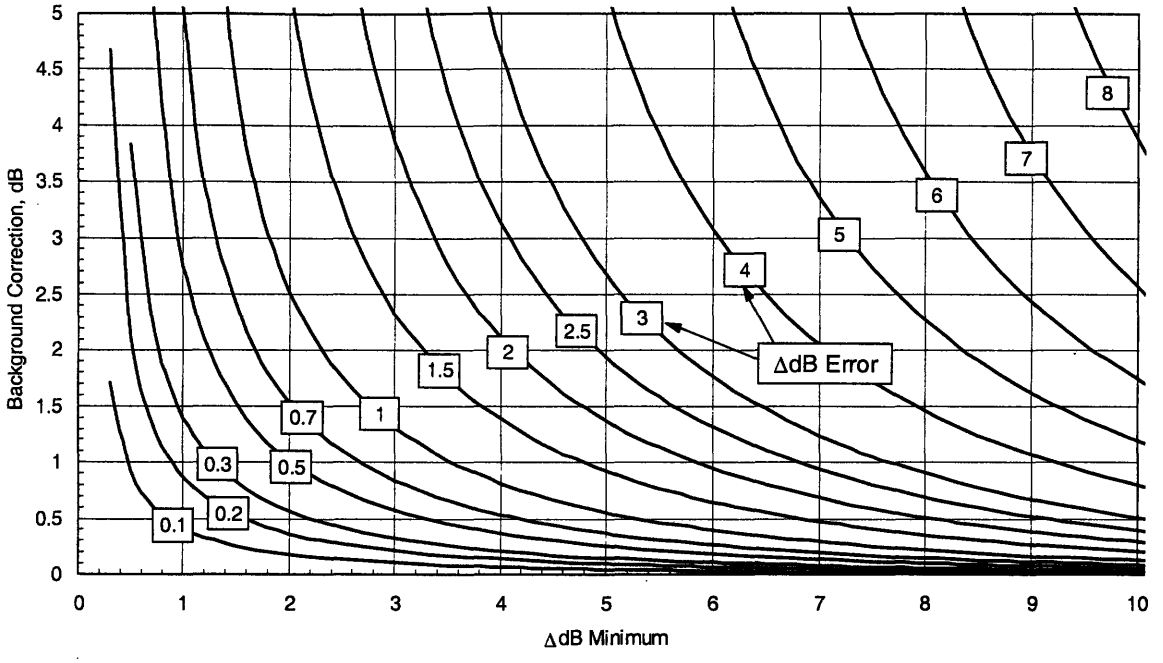

Figure 2-21: Accuracy of background noise correction as a function of background noise repeatability and minimum separation from data, [2]

Figure 2-22 shows as-measured SPL versus frequency for a low condition case of NPR = 1.51 and TTR = 1.82 taken on a 1/20th scale nozzle. Also plotted is the background noise measurement.

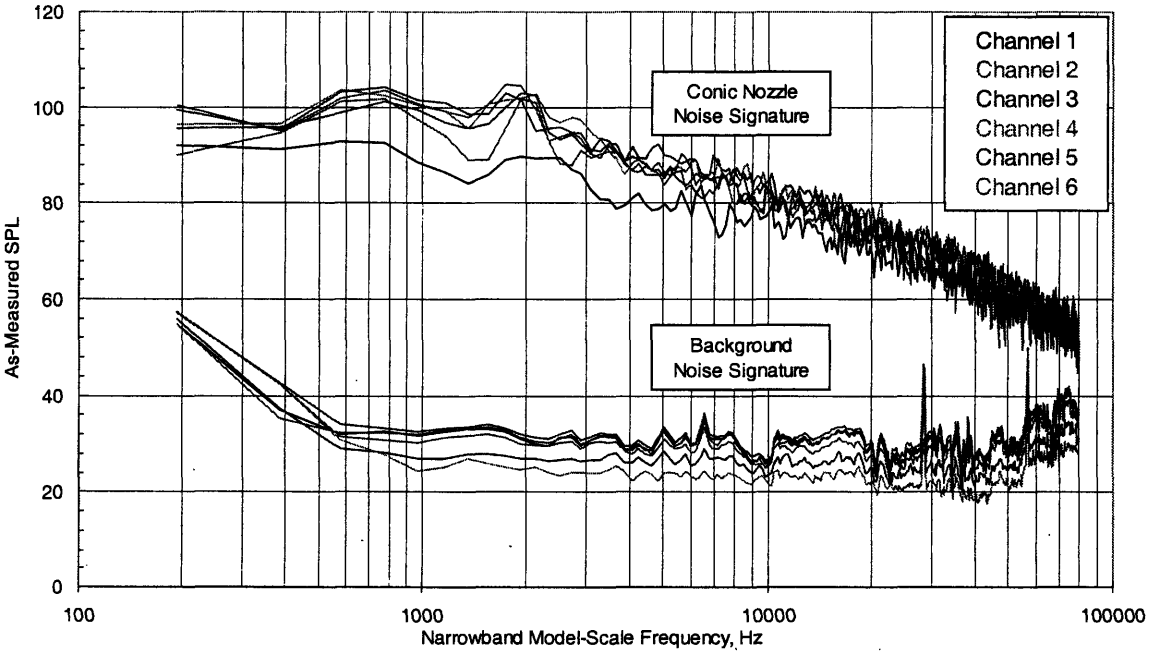

Figure 2-22: 1/20th Scale ASME nozzle NPR = 1.51, TTR = 1.82 SPL versus narrowband frequency showing background noise measurement

This represents the worst case scenario because this is data taken on the smallest nozzle at the lowest NPR condition. As can be seen from the figure, the background noise is approximately 20 dB below the measured data, which corresponds to approximately 0.2 dB of contamination. At 80 kHz[7] the separation between the background noise and the data is approximately 5 dB, which corresponds to about 1.5 dB of background noise contamination.

2.4 Facility Validation Using an Acoustic Point Source

The first step in validating the acoustic performance of the facility was to do some simple tests to make sure the chamber was anechoic over the frequency range of interest and to make sure that the microphone and processing system were working properly. To expedite this process, an acoustic point source was created to perform some initial diagnostic tests. The point source was made out of ½ inch rubber with a small speaker mounted within it. A simple schematic of the point source is shown in Figure 2-23. To test the point source a hand-held SPL meter was used and these results were compared to those obtained from each of the B&K 4135 ¼ inch microphones.

The hand-held SPL meter and microphones were located at distances from 2 to 64 inches away from the acoustic point source. The speaker was driven using a function generator at frequencies from 1 - 8 kHz and measurements of SPL were made on the hand-held meter using the appropriate 1/3-Octave band setting. Measurements were also made with the B&K 4135 microphones using the same data acquisition system as would be used for the shock tunnel tests. These sets of data were also input through the DADS acoustic data processing system. Two comparisons were made, 1) to ensure that a 6 dB drop for every doubling of distance was achieved, and 2) to make sure that there was relative agreement between the hand held meters and the microphones. A sample of the results for one microphone versus the hand held SPL meter is shown in Figure 2-24.

[7] For the 1/20th scale ASME nozzle, this corresponds to 4000 Hz full-scale.

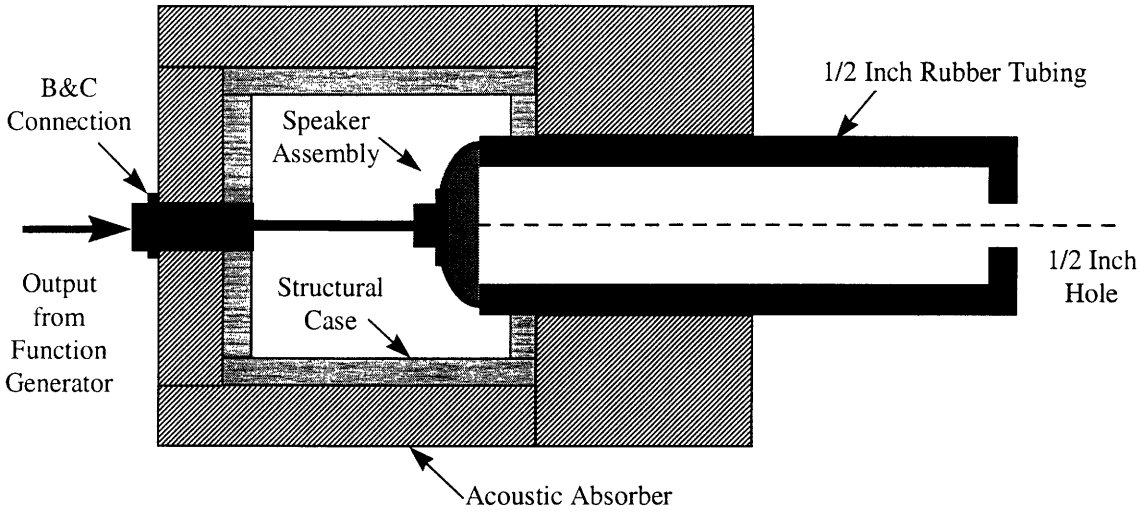

Figure 2-23: Point source schematic used in facility validation

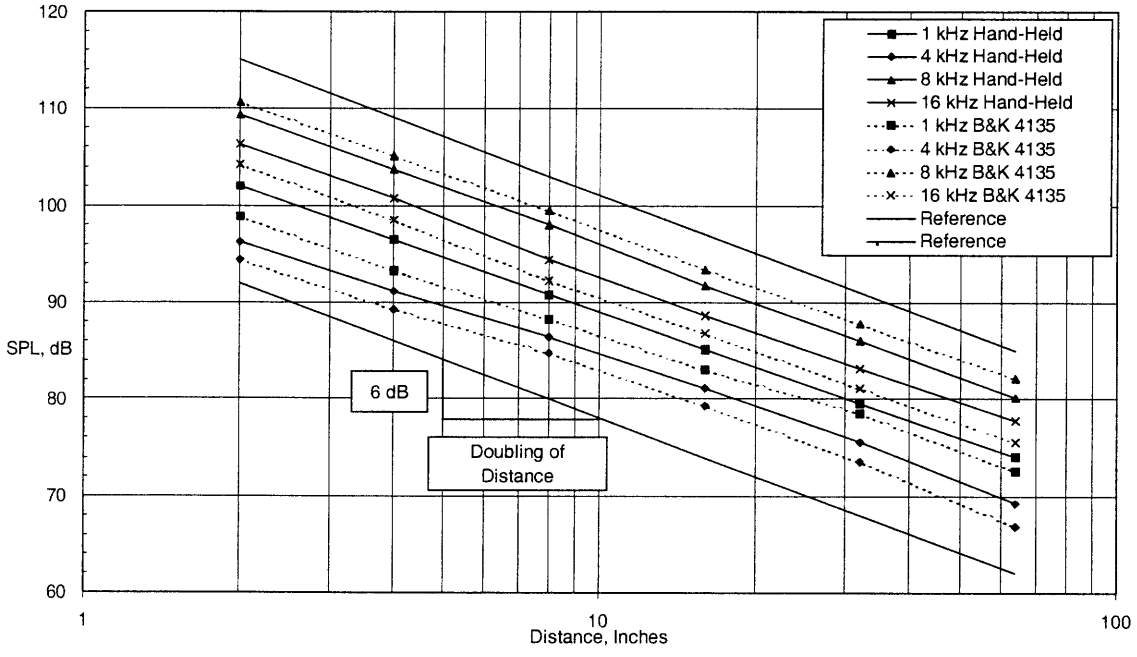

Figure 2-24: Decay of point source noise with distance for four frequencies showing a comparison between hand-held SPL meter and B&K 4135 microphones

As can be seen from the figure, there is approximately a 6 dB drop for each doubling of distance in both the hand-held meter and microphone readings. A possible explanation for the slight deviation is that it is difficult to ensure that both the microphone and SPL meter were located at precisely the same location. Furthermore, these tests were done on different days, where the ambient conditions within the test chamber may have been slightly different. However, the purpose of this diagnostic was to serve as a quick check that the 6 dB drop for each doubling of distance was observable over several frequency ranges, and to make sure the chamber had no extraneous reverberations.

2.5 Shock Tunnel Facility Operation

The purpose of this section is to provide a detailed account of the procedures to perform a single shock tube firing. The steps are summarized below.

1. Find set conditions for P_{dr}/P_{dn}, P_{dn}/P_{atm} and χHe, by choosing the desired NPR and TTR of the supersonic jet.[8] Due to viscous effects within the flow field, the set conditions calculated using 1-D inviscid shock tube equations, based on desired jet conditions, will not be correct. By performing some experimentation on the desired versus realized NPR and TTR, as well as some analytical predictions described in section 3.3 on the attenuating effects of the boundary-layer, it was found that the desired conditions are about 87% of the analytically predicted conditions for a tunnel with the geometry described above. The pressure ratios across various sections of the tube are calculated by employing the one-dimensional shock tube model that will be developed in Chapter 3.
2. If knife blades are used to rupture the diaphragms, the position of the blades with respect to the diaphragms must be calculated, and subsequently the blades moved to that position, such that the diaphragms will flex into the blades when the diaphragm section is evacuated to initiate a test. To facilitate this process, a correlation between diaphragm deflection for a series of aluminum diaphragms of varying thickness versus pressure was compiled. Using this technique, the knife blades can be properly placed to ensure that rupture occurs when desired. A second option that was employed to acquire the majority of the acoustic data presented in this thesis, was to eliminate the knife blades by scoring the diaphragms in an 'X' fashion, as shown in Figure 2-25, as well as some ruptured diaphragms from the primary and secondary diaphragm sections of the MIT facility. A detail of the secondary diaphragm section is shown in Figure 2-26. This method proved to work exceptionally well, with some practice, and it tended to eliminate any of the petals from tearing off the diaphragm and traveling down the driven section. Since the driven section is evacuated to sub-atmospheric pressure, a light-weight plastic disc is placed on the nozzle to act as a seal during the evacuation and subsequent filling of the driver section of the shock tube. The plastic disc is then jettisoned off the nozzle by the shock induced flow. The jettisoned plug concept is further discussed in Section 5.3, where the addition of a secondary diaphragm section, to replace the plastic disc, is discussed.

[8] Examples of these values will be shown in Section 3.2, when the 1-D shock tube model is derived.

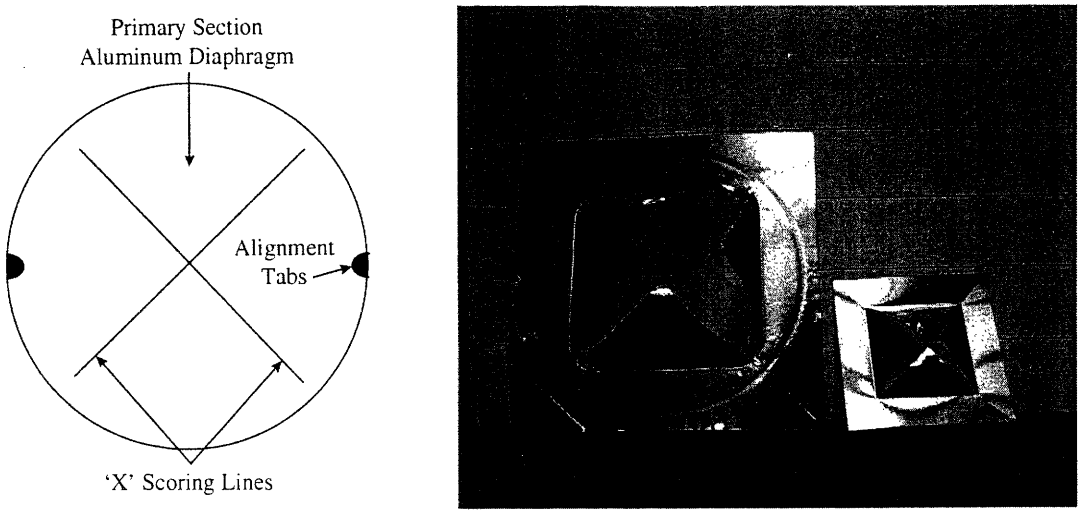

Figure 2-25: (a) Primary diaphragm scoring, and (b) Ruptured primary and secondary diaphragms

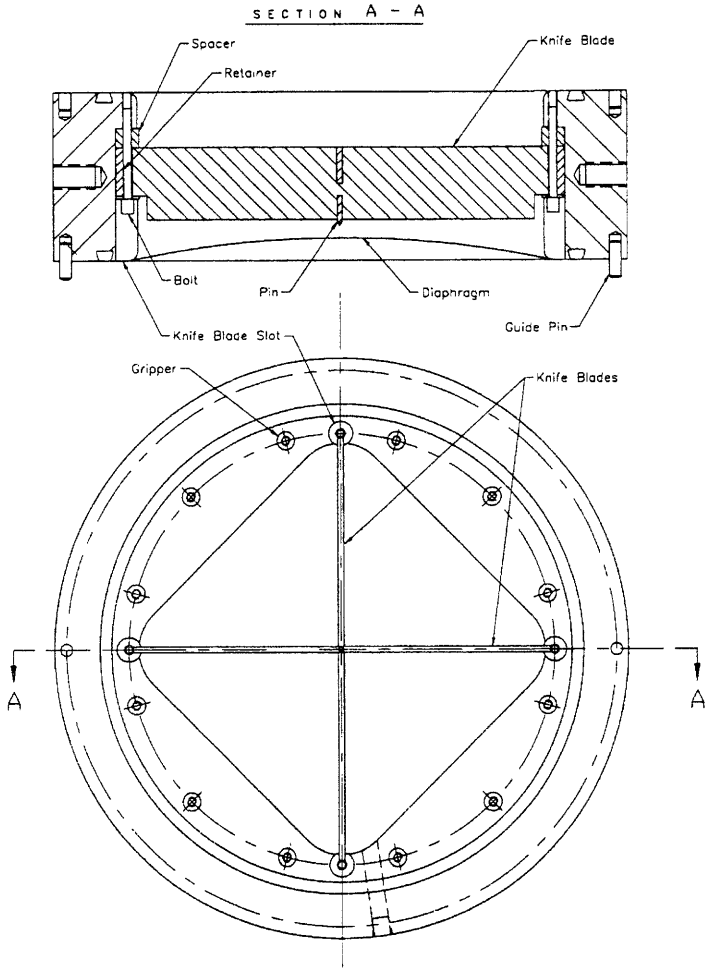

Figure 2-26: Detail of diaphragm section and knife blade configuration, [22]

3. Once the diaphragms have been installed in the tube, the test is ready to commence. A computer controlled system first evacuates the tube and then fills the various chambers. Figure 2-27 shows graphically the pressures in various parts of the tube as it is filled. To fire the tunnel the diaphragm section is evacuated and the increased pressure ruptures the diaphragm generating a shock wave. This process will be further discussed in Chapter 3. At this point ambient conditions within the test chamber are measured.
4. Once the test has concluded, the pressure signatures from the 4 pressure transducers (see section 2.2.1) are analyzed to determine what the actual jet conditions were. TTR is completely a function of the shock speed, and NPR can be similarly calculated from knowledge of the shock speed, or by determining the steady-state pressure plateau and dividing by the ambient pressure, as was described in section 2.2.3.

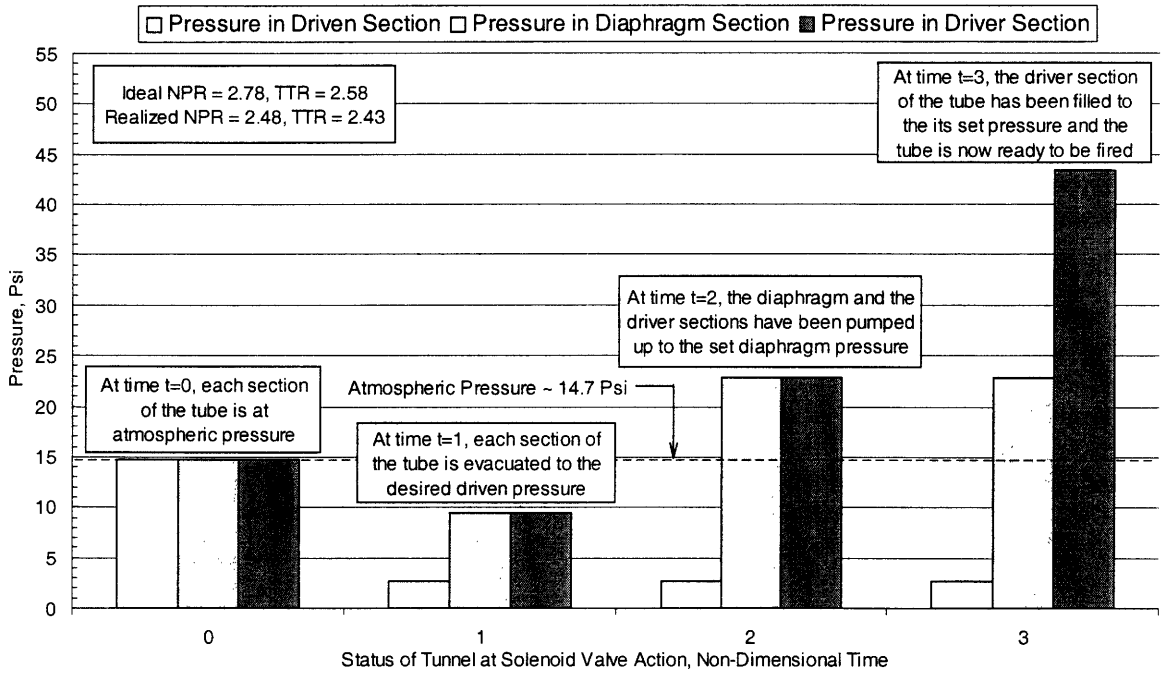

Figure 2-27: Shock tunnel filling history for NPR = 2.48 and TTR = 2.43

5. If the resultant jet conditions are within an acceptable level, the acoustic data from the test can then be processed with confidence that the jet conditions are as desired. However, often some iteration of steps 1 - 4 is necessary before the set conditions yield the desired jet conditions.
6. Flush the tube with compressed air to remove any residual helium, which was previously described in Section 2.1.1.

2.6 Steady-State Test Facility Description

The steady-state data used for comparison was obtained from a 14.5 cm exit diameter ASME nozzle, tested in the Boeing Low-Speed Aeroacoustic Facility (LSAF). LSAF combines a large (20 m long x 23 m wide x 10 m high) anechoic test chamber with a 2.7 m x 3.7 m free-jet wind tunnel. Acoustic instrumentation includes a traversing azimuthal microphone array at 4.6 m from the jet axis, with additional free-standing microphones to augment the array measurement. Additional information on LSAF can be found in Reference [60]. A few sample pictures of the facility are shown in Figures 2-28 and 2-29.

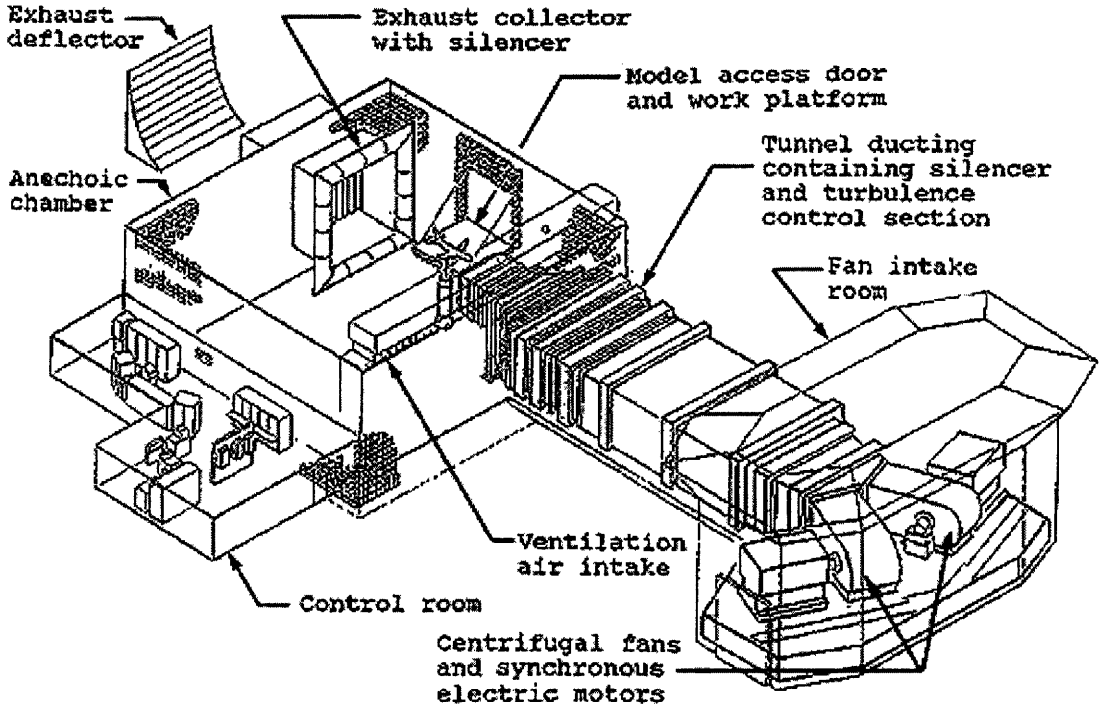

Figure 2-28: View of Low Speed Aeroacoustics Facility, LSAF, [60]

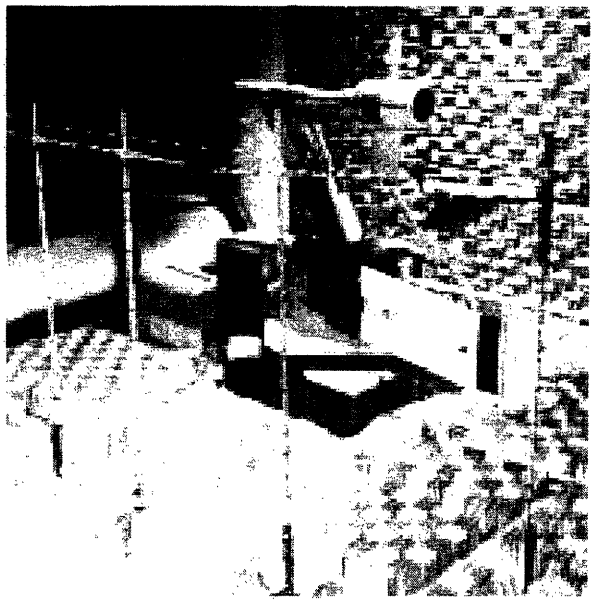

Figure 2-29: View of LSAF acoustic chamber where ASME and LSMS nozzles are tested, [60]

Figures 2-28 and 2-29 show the relative size and complexity of the steady-state facility as compared to the shock tunnel facility shown in Figures 1-6 and 2-1. Figure 2-30 shows a simple schematic of the azimuthal angle configuration and measurement apparatus at LSAF. The array shown in Figure 2-30 traverses in and out of the page.

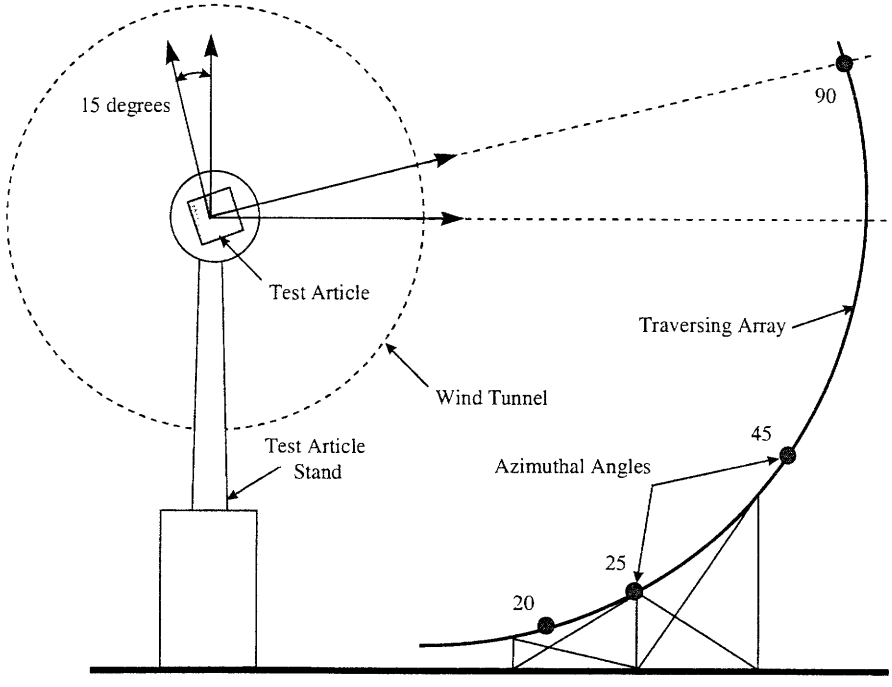

Figure 2-30: Schematic of LSAF azimuthal angle measurement configuration

2.7 Chapter Summary

This chapter described the MIT transient shock tunnel facility, associated instrumentation and data processing techniques. In Chapter 5 the transient acoustic data will be compared to steady-state data that was obtained at Boeing's LSAF described in Section 2.6. Both sets of noise data were processed using the methods described in Section 2.3. The chapter also provided an example of how the facility was validated using an acoustic point source to demonstrate that the acoustic measurements were repeatable and exhibited a 6 dB drop for every doubling of distance. The facility has been in operation for about two years as of the writing of this thesis, with approximately 1000 shock tunnel shots being fired over the course of the investigation presented herein.

Chapter 3

Shock Tube Gas Dynamics

The fundamental purpose of a shock tunnel is to generate a reservoir of high temperature, high pressure fluid that can be expanded through a nozzle or other test article, to create a hot supersonic jet. By employing different pressure ratios and gas mixtures, a wide range of conditions across the nozzle can be achieved, comparable to those generated using steady-state electric or arc-heated facilities. The compromise made for mechanical simplicity and the versatility of using a shock tube, is the brief duration of useful test time; the reservoir conditions typically remain constant for only 5 - 25 milliseconds. Sufficient time must be allowed for the nozzle flow and free-jet to reach a quasi-steady-state before measurements can be made. However, if this constraint is met, the short run times become advantageous. The test nozzles are exposed to high temperature flow for only a fraction of a second, thus relatively inexpensive stereo-lithography or cast aluminum nozzles can be tested at realistic flow conditions. Conversely, nozzles for steady-state facilities are typically an order of magnitude more expensive since they must be robust enough to withstand pressures at elevated temperatures for extended periods of time.

In this chapter the gas-dynamics and wave phenomena associated with shock tubes will be presented. An ideal one-dimensional fluid dynamic model is developed to establish the performance of the shock tube under various operating conditions. This model is then used to generate the initial set-conditions across the diaphragm, to generate desired jet conditions. An analytical prediction of the useful test time achievable from a shock tube is also developed. The one-dimensional fluid dynamic model is then extended to account for the viscous effect of the developing boundary-layer behind the incident shock wave.

3.1 Wave System in a Simple Reflection-Type Shock Tube

The simple shock tube considered here consists of a straight tube of uniform cross sectional area. Initially, the shock tube is separated into a driven section, denoted as region (1), and driver section, denoted as region (4), by two thin diaphragms, as shown in Figure 2-1a. [1]

[1] Many conventional shock tunnel facilities only employ a single diaphragm between the driver and driven section. The MIT facility includes two diaphragms so that the center region can be evacuated to initiate the test, and to provide two discontinuous steps in pressure while the tube is being filled with the test gas instead of a single pressure step.

A useful convention for referring to regions of the shock tube is summarized in Table 3.1.

Table 3.1: Summary of shock tunnel convention and notation

Region	Physical Description	Thermodynamic State Description
1	Driven Section: contains the test gas	Evacuated to sub-atmospheric pressure
2	State of the gas which has been traversed by the incident shock, located between the incident shock and contact surface	Generally still at sub-atmospheric pressure, the shock wave uniformly heats the flow
3	State of the gas which has been traversed by the expansion fan, located between the expansion fan and contact surface	The expansion fan decreases the pressure in the driver section and accelerates the flow in the direction of the nozzle
4	Driver Section: contains mixture of air and helium[2]	High pressure fluid, around 3 - 4 atmospheres, contains He for tailoring
5	Between Nozzle-End and Reflected Shock Wave	Stagnant, high-pressure, high-enthalpy air

The driven section contains the test gas, air for each test, and is typically evacuated to around $1/5^{th}$ of an atmosphere. Since the driven section is evacuated to sub-atmospheric pressures, a light-weight plastic diaphragm can be placed on the end of the nozzle as a seal from the ambient air. The driver section is evacuated and then filled with a mixture of helium and air to a pressure between 2 and 6 atmospheres, depending on the desired shock strength. Initially, the two gases are in thermal equilibrium. The shock tube affords a great deal of flexibility because the driver pressure and gas composition, as well as the test gas pressure can be accurately regulated to yield different stagnation temperatures and pressures behind the reflected shock.

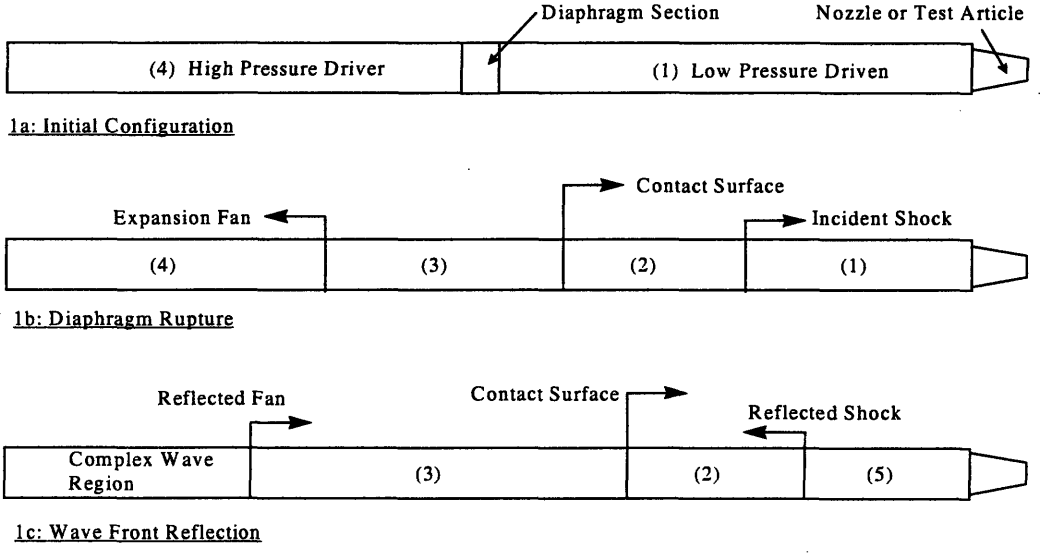

Figure 3-1: Schematic of wave system in a shock tube during the time of interest

[2] The motivation for including a well mixed, specified mass fraction of Helium in the driver section is discussed in Section 2.1.3

When the section of the tube between the two diaphragms is evacuated, the pressure difference causes the diaphragms to press against knife blades and rupture. The driver gas acts as an impulsively started piston initiating a series of converging compression waves, which move to the right in the figure, rapidly compressing the test gas. The compression fronts coalesce into a shock wave, propagating through the driven section, accelerating and heating the driven gas. Concurrently, a series of diverging expansion waves propagate through the driver gas mixture, decreasing the pressure and accelerating the fluid in the direction of the nozzle. The state of the gas which is traversed by the incident shock wave is denoted by region (2), and that of the gas traversed by the expansion fan is denoted as region (3), as depicted in Figure 3-1b. The interface, or contact surface, between regions (2) and (3), marks the boundary between the gases which were initially separated by the diaphragm. To first approximation, regions (2) and (3) can be assumed not to mix and to be perpetually separated by the contact surface, which is analogous to the face of the piston. The test is initiated when the incident shock wave reaches the nozzle-end of the tube, reflects from the nozzle-end-plate, and creates a region of stagnant, high-pressure, high-enthalpy air, denoted as region (5) in Figure 3-1c. This air can be expanded through a nozzle to the desired conditions. A more detailed mathematical description of the flow physics is presented in Appendix A.

Another insightful way to view the developing wave system within the shock tube, is through a wave diagram. Figure 3-2 shows the wave system in the shock tube using a wave diagram interpretation.

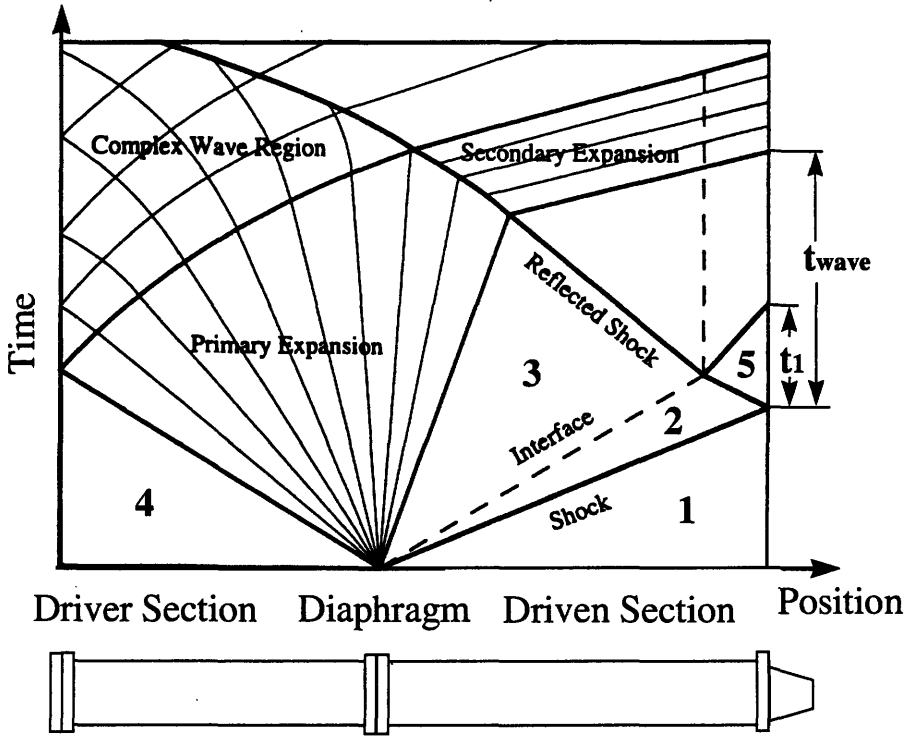

Figure 3-2: Wave system in a reflection type shock tube

The figure shows the time-distance history of the shock and expansion waves that will occur in the shock tube. As can be seen from the figure, the shock wave travels from the diaphragm through the driven section. The shock wave is trailed by the contact surface. The driver section of the tube is traversed by an expansion fan which accelerates the flow in the nozzle direction. The figure also shows two test times, denoted t_1 and t_{wave}. These time scales correspond to the limiting extremes of achievable test times using a shock tube. The details associated with test time limitations will be discussed in Section 3.3.

3.2 Ideal Shock Tube Modeling

The purpose of this section is develop a one-dimensional model for shock tube flows, and to specifically apply this model to the geometry associated with the MIT facility. It will be shown how this model can be employed to set initial conditions in the driver and driven sections and to predict the fluid and thermodynamic conditions of the resultant supersonic jet.

The ideal gas-dynamic model of the shock tube was derived using a number of simplifying assumptions. Most of these assumptions are valid for the temperature and pressure ranges that are employed in the MIT facility. Some of the non-ideal effects, however, are significant over the operating range of interest, so corrections can be made to the results from the ideal model. The ideal modeling assumptions are:

- The diaphragm removal is assumed to be instantaneous, resulting in a step discontinuity in pressure between the two sections at t=0. Any effects due to the diaphragm curvature of finite bursting time are neglected.[3]
- It was assumed that there is no mixing between the driver and driven gases such that distinct contact surface exists at the interface between the two regions.
- The flow was assumed to be inviscid,[4] except across the shock. This is generally a poor assumption so corrections for the boundary layer must be made to study effects such as shock attenuation and contact surface acceleration.
- One-dimensional flow was assumed throughout the tube.

[3] In actual shock tubes, the diaphragm bursting process is highly three-dimensional and requires a finite period of time for the diaphragm to burst and fold out of the ensuing flow field. As a result, there will not be a distinct shock front but rather an irregular distribution of compression waves. These waves, however, will overtake each other as they travel downstream, resulting in a steepening compression front. Within a few tube diameters, the waves coalesce into a distinct shock front and exhibit close agreement with the idealized one-dimensional model.

[4] This restriction is removed in Section 3.4.

- Real-gas effects were ignored and the ratio of specific heats was assumed to be constant for each of the driver and driven gases.

A description of this model can be found in Appendix A, with a more thorough derivation found in References [17], [22], [25].

3.2.1 The Shock Tube Equation

The gas dynamic behavior of a shock tube is typically characterized by any one of three dependent parameters: (1) the diaphragm pressure ratio, P4/P1, (2) the incident shock Mach number, Ms, and (3) the driver gas composition, χHe. Only the initial conditions of the two chambers, and the shock strength, are required for the calculation of the physical quantities of the flow.

The pressure ratio across the incident shock wave, P2/P1, can be found as a function of the initial conditions:

$$\frac{P1}{P4}=\frac{P1}{P2}\left[1-\left(\frac{P2}{P1}\right)\sqrt{\frac{\left((\gamma_4-1)/2\gamma_4\right)(C_vT)_1/(C_vT)_4}{(\gamma_1+1)/(\gamma_1-1)(P2/P1)+1}}\right]^{\frac{2\gamma_4}{(\gamma_4-1)}} \qquad 3.1$$

This equation indicates that the shock pressure ratio, P2/P1, is a function of the diaphragm pressure ratio, P4/P1, the internal energy ratio across the diaphragm, and the specific heat ratios of the gases in the driver and driven sections. For convenience, equation 3.1 can be re-cast as:

$$\frac{P4}{P1}=\frac{P2}{P1}\left[1-\frac{(\gamma_4-1)(a_1/a_4)(P2/P1-1)}{\sqrt{2\gamma_1}\sqrt{2\gamma_1+(\gamma_1+1)(P2/P1-1)}}\right]^{-\frac{2\gamma_4}{(\gamma_4-1)}} \qquad 3.2$$

The expansion strength can be obtained from:

$$\frac{P3}{P4}=\frac{(P2/P1)}{(P4/P1)} \qquad 3.3$$

Once the shock strength is determined, all other flow quantities can be calculated from normal shock relations, and thus the thermodynamic and fluid mechanic properties of the jet are predicted. Additional details of the derivation of equations 3.1 - 3.3 can be found in Appendix A and in References [17], [22].

The results of the shock tube modeling analysis can be used to determine the set condition of the shock tube to achieve the desired jet NPR and TTR. Table 3.2 summarizes the pressure ratios required over a range of conditions for which the shock tube is operated. P_{driver}/P_{driven} is the ratio of the pressures in the driver to the driven sections, P_{driven}/P_{atm} gives information of how far the driven section is to be evacuated below atmospheric, χ He is the mass fraction of helium to ensure contact surface tailoring[5] and P_{air}/P_{atm} is the ratio of the air pressure in the driver to the atmospheric pressure. [6]

Table 3.2 1-D gas dynamic model results for desired jet conditions

	Jet Conditions		Shock Tube Pressure Ratios for Input into Control Computer			
Nozzle Scale	TTR	NPR	P_{driver}/P_{driven}	P_{driven}/P_{atm}	χ He	P_{air}/P_{atm}
1/20	2.3	2.0	12.81	0.162	0.26	0.585
1/20	2.3	2.5	12.81	0.203	0.26	0.731
1/20	2.3	3.0	12.81	0.243	0.26	0.878
1/20	2.3	3.43	12.81	0.280	0.26	1.004
1/20	2.3	4.0	12.81	0.324	0.26	1.170
1/20	2.9	2.0	21.60	0.097	0.38	0.381
1/20	2.9	2.5	21.60	0.121	0.38	0.477
1/20	2.9	3.0	21.60	0.145	0.38	0.572
1/20	2.9	3.43	21.60	0.1661	0.38	0.654
1/20	2.9	4.0	21.60	0.1937	0.38	0.762
1/15	2.3	2.0	13.94	0.163	0.28	0.598
1/15	2.3	2.5	13.94	0.204	0.28	0.748
1/15	2.3	3.0	13.94	0.245	0.28	0.897
1/15	2.3	3.43	13.94	0.280	0.28	1.026
1/15	2.3	4.0	13.94	0.327	0.28	1.196
1/15	2.9	2.0	23.398	0.098	0.41	0.383
1/15	2.9	2.5	23.398	0.123	0.41	0.479
1/15	2.9	3.0	23.398	0.147	0.41	0.574
1/15	2.9	3.43	23.398	0.168	0.41	0.657
1/15	2.9	4.0	23.398	0.196	0.41	0.766
1/10	2.3	2.0	13.56	0.163	0.27	0.594
1/10	2.3	2.5	13.56	0.204	0.27	0.742
1/10	2.3	3.0	13.56	0.244	0.27	0.891
1/10	2.3	3.43	13.56	0.279	0.27	1.019
1/10	2.3	4.0	13.56	0.326	0.27	1.188
1/10	2.9	2.0	22.76	0.098	0.40	0.381
1/10	2.9	2.5	22.76	0.122	0.40	0.477
1/10	2.9	3.0	22.76	0.146	0.40	0.572
1/10	2.9	3.43	22.76	0.167	0.40	0.654
1/10	2.9	4.0	22.76	0.195	0.40	0.763

Several trends can be seen from Table 3.2. For a given TTR, the driver to driven pressure ratio is fixed, and the NPR is controlled by varying the driven to atmospheric pressure ratio. Furthermore, for a constant TTR, the helium mass fraction, χ He, also remains constant. If the last column, P_{air}/P_{atm}, is greater than

[5] Contact surface tailoring considerations are discussed in Section 3.2.3.
[6] The use of these pressure settings was discussed in Section 2.5, and shown schematically in Figure 2-27.

unity, which occurs for high NPR and low TTR conditions, additional compressed air must be introduced into the driver to meet the desired jet conditions.

3.2.2 Shock Reflection

This section describes the physics associated with the incident shock reflection, from the nozzle end of the driven section to create a region of hot stagnant fluid, denoted as region 5. This section considers two scenarios: reflection from a rigid end-plate, and reflection from an end-plate with a nozzle, as well as a justification of when the limiting form of the rigid end-plate assumption may be applied.

3.2.2.1 Reflection From a Rigid End-Plate

When the shock reaches the end-plate it will be reflected, leaving behind a region of high-temperature fluid at a well defined thermodynamic state which can be used as the test gas through the nozzle. Due to the short test duration, it is impractical to measure the reservoir temperature directly with any type of instrument, so it must be deduced from the incident shock speed. A method for calculating the incident shock speed, based on pressure transducer traces within the driven section, was presented in Section 2.2.3 and a sample of the pressure transducer traces for a typical shock tube run was shown in Figure 2-16. The pressure and temperature in the reservoir can then be related to the incident shock Mach number, M_s, by the following relations:

$$\frac{P5}{P1} = \left[\frac{2\gamma_1 M_s^2 - (\gamma_1 - 1)}{(\gamma_1 + 1)}\right]\left[\frac{(3\gamma_1 - 1)M_s^2 - 2(\gamma_1 - 1)}{(\gamma_1 - 1)M_s^2 + 2}\right] \qquad 3.4$$

$$\frac{T5}{T1} = \frac{\left[2(\gamma_1 - 1)M_s^2 + (3 - \gamma_1)\right]\left[(3\gamma_1 - 1)M_s^2 - 2(\gamma_1 - 1)\right]}{(\gamma_1 + 1)^2 M_s^2} \qquad 3.5$$

These conditions will remain constant until the arrival of a reflected disturbance. In the case of a solid end-plate,[7] the reservoir conditions can be found by assuming perfect shock relations. In this case the reflected shock Mach number is:

$$M_r = \frac{1}{M_{2(s)}} \qquad 3.6$$

[7] A shock reflecting from an end-plate with a small nozzle, will exhibit almost identical behavior to a perfect shock reflection, provided that the nozzle throat area is small compared to the tube cross sectional area. Typically if A^*/A_{st} is less than around 5%, a perfect shock reflection assumption is justifiable.

where M2' is the Mach number of the fluid in region 2 relative to the incident shock. Once again, additional details of these equations are provided in Appendix A and in References [17], [22].

3.2.2.2 Reflection From an End-Plate with a Nozzle

The presence of a significantly large nozzle can effect the conditions behind the reflected shock wave. Immediately after the shock reflects, there will be a complex system of unsteady rarefactions resulting from the nozzle starting process and the shock reflection from the curved nozzle geometry. This results in a distortion of the reflected wave and a highly three-dimensional flow arises. After the nozzle start-up process is complete, however, a steady-state pattern is approached which can be described by the simple one-dimensional model that is described in Appendix A.

In order to solve for the reflected shock strength, it is first necessary to establish the fluid Mach number in the reservoir. Using a one-dimensional analysis, it can be shown that the drift Mach number, M5, is only a function of the ratio of specific heats in region 1 and the nozzle area to shock tube area ratio:

$$M_5 = \left[1+\frac{\gamma-1}{2}\right]^{\frac{-(\gamma+1)}{2(\gamma-1)}}\left[\frac{\rho_{t5}}{\rho_5}\right]\left[\frac{T_{t5}}{T_5}\right]^{\frac{1}{2}}\left[\frac{A^*}{A_{st}}\right] \qquad 3.7$$

The reflected shock Mach number, Mr,[8] can now be found from the expression for the velocity change across a normal shock wave:

$$\frac{\Delta u}{a_2} = M_2 - M_5\left(\frac{a_5}{a_2}\right) = \frac{2}{\gamma+1}\left[M_r - \frac{1}{M_r}\right] \qquad 3.8$$

Figure 3-3 shows the effect of incomplete shock reflection for a typical operating condition as a function of the nozzle area ratio. The effect on reservoir pressure is of little consequence because it will be measured directly. Stagnation temperatures, on the other hand, are typically inferred from the incident shock speed as was discussed previously. If an ideal reflection is assumed for a large scale nozzle, the derived temperature will be significantly in error. This issue is another reason, other than the viscous effects of the boundary layer, that result in the need to arrive at an experimentation relationship between the ideal set conditions and the realized jet conditions, as was discussed in Section 2.5.

[8] Once again M_r is defined as the shock Mach number of the fluid in region 2 relative to the standing reflected shock wave.

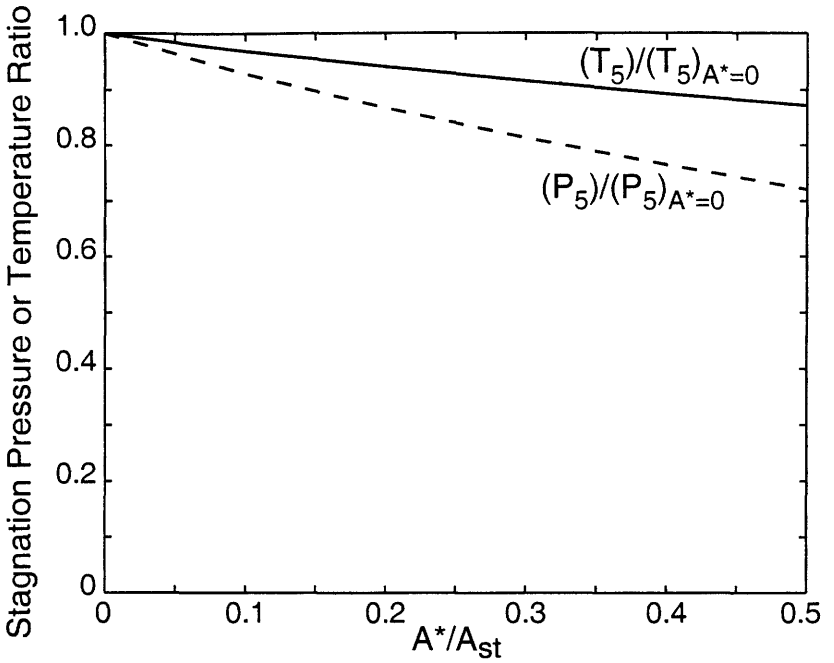

Figure 3-3: Incomplete shock reflection due to mass flow through the nozzle, [22]

3.2.3 Interface Tailoring

On either side of the contact surface it is essential that the speeds of sound between regions (2) and (3) are identical to prevent extraneous waves from the reflected shock as it passes through the contact surface. These waves may substantially limit the available test time, as will be discussed in Section 3.3. To ensure that this does not occur, the speed of sound is matched by choosing the appropriate composition of gases for the driver section, using the matching condition know as 'interface tailoring':

$$\frac{\gamma_2}{a_2^2}\left[(\gamma_2+1)\frac{p_5}{p_2}+\gamma_2-1\right]=\frac{\gamma_3}{a_3^2}\left[(\gamma_3+1)\frac{p_5}{p_2}+\gamma_3-1\right] \qquad 3.9$$

This equation can be satisfied if a mixture of helium and air is employed as the driver gas. This allows for a variable mass-averaged molecular weight in the driver, and, as a consequence a variable speed of sound. For any given reflected shock strength there will be a unique gas pressure and mixture composition that will satisfy the tailoring equation.

This relation assumes that the flow within the shock tube behaves ideally. As a result, the test conditions calculated using these equations are only approximate. In practice, tailoring in the MIT facility was achieved by systematically varying the shock speed and analyzing the reservoir pressure traces for the

duration of the quasi-steady pressure region. It is known that the tailoring condition has be satisfied when the trace shows a flat-topped plateau.[9]

3.3 Analytical Prediction of Useful Test Times

The principal constraint associated with using a shock tube for jet noise measurements is the short duration of the test time. This section contains a discussion of the limitations on test time and the development of expressions to predict the useful test times analytically.

The duration of constant conditions in the reservoir will be limited by one of two factors, the arrival of a reflected disturbance at the nozzle end of the tube or the exhaustion of the test gas. Within the regime of the reflected disturbance, we find that the three disturbances can be reflections from the contact surface, reflections from the primary expansion head or a disturbance from shock-expansion interaction. These cases are summarized in the flow chart shown in Figure 3-4.

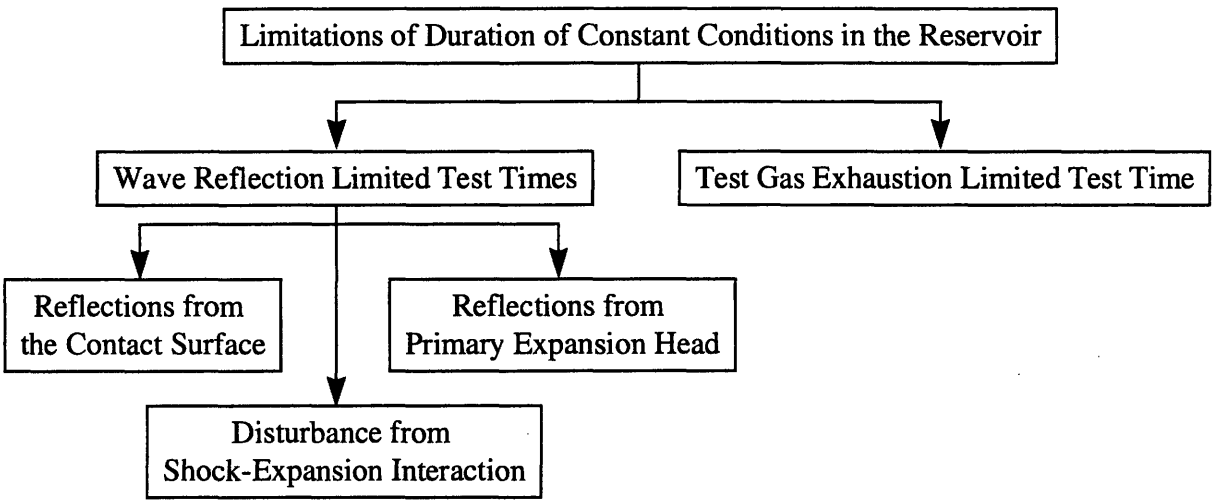

Figure 3-4: Flow chart summarizing test time limitations

In most cases in simple shock tubes, the arrival of a reflected disturbance will be limiting. However, for large area ratio nozzles or high reservoir temperatures, the volume of the test gas may be a greater constraint.

[9] It is important to note, however, that non-tailored operation can produce a similar signature. The multiple reflections between the contact surface and end-plate can result in a quasi-uniform region that is difficult to quantitatively distinguish from the tailored state. The measured reservoir pressures must therefore be checked against those predicted from the incident shock speed.

3.3.1 Wave Reflection Limited Test Times

Depending on the operating conditions and the relative lengths of the driver and driven sections, there are three different reflections that can result in the termination of the test. Wave diagrams for each of these conditions are shown in Figure 3-5. Each case is discussed below.

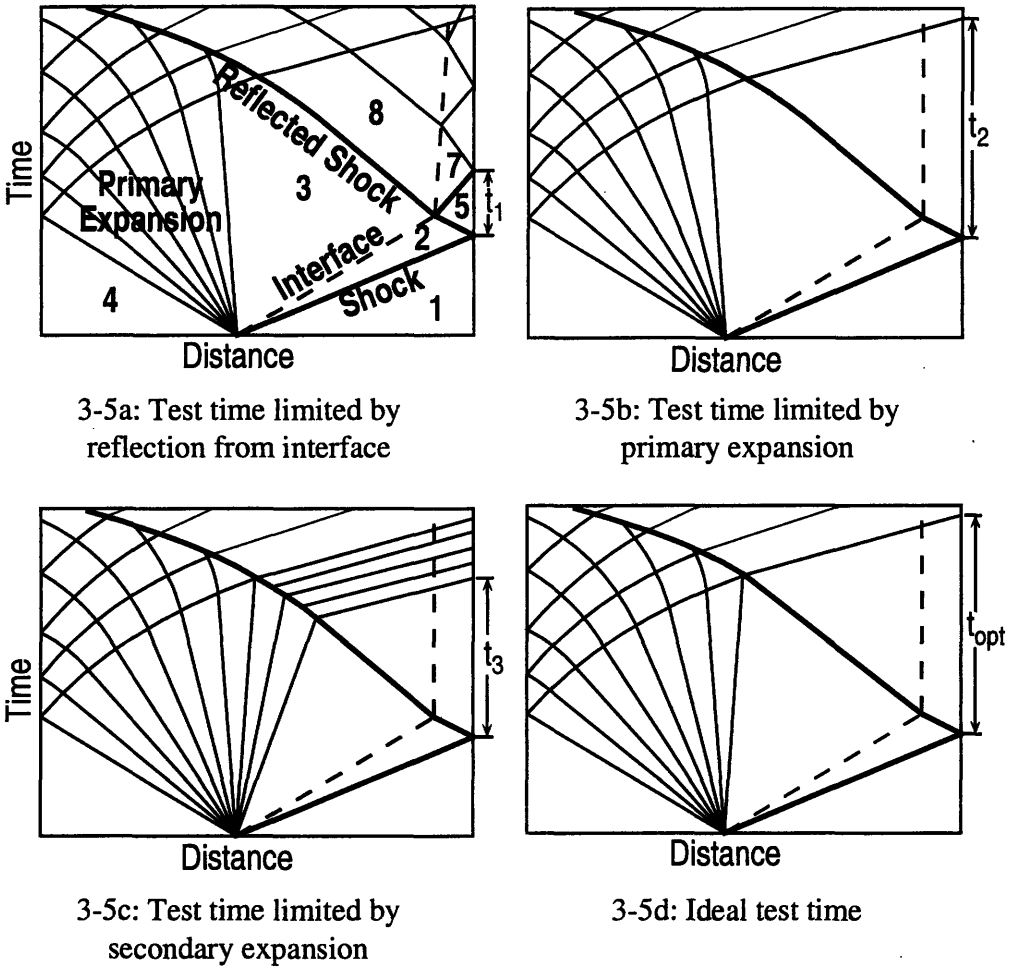

3-5a: Test time limited by reflection from interface

3-5b: Test time limited by primary expansion

3-5c: Test time limited by secondary expansion

3-5d: Ideal test time

Figure 3-5: Expansion wave limited test times

Reflections from the Contact Surface

The first disturbance that could potentially end a test, results from the interaction of the shock with the contact surface. This is shown schematically in Figure 3-5a. In this case, test times will typically be on the order of 3 - 5 milliseconds, which is insufficient for jet noise experiments on the scale of nozzles considered in the MIT facility, as the fluid jet will not have time to reach a quasi-steady state. Particularly in the case of mixer-ejector studies, a quasi-steady flow regime will not have sufficient time to be established. Therefore reflections from the contact surface must be curtailed through tailoring of the driver gas to match speeds of sound as was discussed in Section 3.2.3.

Reflections from The Primary Expansion Head

This situation is represented schematically in Figure 3-5b. The head of the primary expansion fan will travel the length of the driver section, reflect from the end-wall, and propagate back to the nozzle end of the shock tube. This is a strong wave and will rapidly reduce the reservoir pressure and temperature once it arrives from the far end of the tube. In this case, test times are in the range of 15-20 milliseconds as shown in the figure. The arrival of the expansion head can be delayed by careful design of the geometry of the shock tube. This was taken into account by Kerwin in the design of the MIT facility, [22]. The arrival of the expansion head was delayed by increasing the relative length of the driver section.

Disturbance from shock-Expansion Interaction

If the reflected shock overtakes the expansion tail, as shown in Figure 3-5c, a weak secondary expansion is created that will arrive at the nozzle ahead of the primary expansion. This generally occurs at high reservoir temperatures where stronger shocks are required to generate the necessary temperature rise. Figure 3-5d shows the ideal arrival times of the different reflected disturbances for the shock tube.

3.3.2 Test Gas Exhaustion Limited Test Times

In the case where there is a relatively high mass flow through the nozzle, the depletion of the test gas can also limit the useful testing time. This is generally the case when testing large scale nozzles ($A^*/A_{st} > 0.1$) or at high reservoir temperatures (T5/T0 > 3.0). An estimate of the time to exhaust the test gas was made by Kerwin, [22] and is summarized here for completeness. An estimate of the time to exhaust the test gas is given by:

$$t_{exg} = \frac{\rho_1 l_{dn} A_{st}}{\dot{m}_n} \tag{3.10}$$

where $\rho_1 l_{dn} A_{st}$ is the total mass of the test gas. Substituting in relations for the nozzle mass flow gives the expression:

$$texg = \left[1+\frac{\gamma_1-1}{2}\right]^{\frac{\gamma_1+1}{2(\gamma_1-1)}}\left[\frac{T_5}{T_1}\right]\left[\frac{P_5}{P_1}\right]^{-1}\left[\frac{A_*}{A_{st}}\right]^{-1}\left[\frac{Ldn}{a_5}\right] \tag{3.11}$$

It should be noted that P5/P1 and T5/T1 can be related by the basic shock tube equation, developed earlier in this chapter, so that the ideal test time to exhaust the test gas becomes a function of only the required reservoir temperature, T5, and the driven section geometry.

In practice, the contamination of the test gas with the cold driver fluid, will reduce the test gas exhaustion limited test times. Thus the above model provides only an upper bound for the test gas exhaustion limited test time. Three-dimensional effects during diaphragm bursting will result in a contact zone rather than a distinct contact surface. Similarly, when the shock impinges on the interface between the driver and driven gases, Richtmyer-Meshkov instabilities can result that will further mix the two gases. During the design of the MIT facility it was assumed that no more than 60% to 70% of the ideal test gas exhaustion time would be realized. The tube was then sized so that this conservative estimate for the test gas exhaustion time was roughly equal to the wave-limited test time.

3.3.3 Comparison of Analytical and Experimental Test Times

This Section presents a comparison of the analytically predicted test times with those actually achieved in the MIT facility for the ASME nozzles.

Tables 3.3 presents a summary of the analytically predicted test time, t_{net}, and realized test time, t_{act}, for eight combinations of nozzle size and jet condition for the ASME conic nozzles.

Table 3.3: Analytically predicted test times for ASME nozzles (ms)

D_e	NPR	TTR	t_{wave}	t_{exg}	t_{nozzle}	t_{jet}	t_{net}	t_{act}
5.1	1.51	1.82	25.9	568.2	2.1	1.5	22.3	20
5.1	2.48	2.43	23.6	259.0	1.9	1.4	20.3	17
5.1	3.43	2.91	20.4	137.7	1.7	1.2	17.5	15
6.8	2.48	2.43	23.6	127.1	2.4	1.8	19.4	17
6.8	3.43	2.91	20.4	71.4	2.2	1.6	16.7	14
10.2	1.51	1.82	25.9	131.2	4.1	2.9	18.9	15
10.2	2.48	2.43	23.6	64.7	3.8	2.7	17.1	14
10.2	3.43	2.91	20.4	31.4	3.4	2.4	14.6	11

The nomenclature used for the tests time constraints are summarized in Table 3.4.

Table 3.4: Test time limitation nomenclature

Time constraint	Description of phenomena
t_{wave}	test time limitation due to the reflected expansion wave[10]
t_{exg}	test time limited by the exhaustion of the test gas[11]
t_{nozzle}	nozzle starting time conservatively assumed that the nozzle can be considered started after three flow through times
t_{jet}	jet starting time
t_{net}	$t_{wave} - (t_{nozzle} + t_{jet})$
t_{act}	experimentally realized test time based on pressure transducer measurement

[10] See Reference Section 3.3.1 for more details on wave limited test times

[11] This is conservatively assumed that no more than 70% of the ideal test gas exhausted would actually be realized, due to interface mixing (regions 2 and 3), and Richtmyer-Meshkov instabilities that will further mix the two gases.

A comparison of the predicted and achieved test times for the mixer-ejector model will be delayed until Chapter 4, because a jet development model must be developed first.

3.4 Boundary Layer Modeling and Analysis

The fluid between the expansion head and the shock wave (region 2) has been accelerated from rest to a velocity U2. As a result, there will be an unsteady boundary layer growing in this region. The maximum boundary layer thickness will occur somewhere between the diaphragm section and the contact surface, and will be reduced to zero thickness ($\delta = 0$) at the expansion wave head and incident shock wave. The purpose of this section is to investigate the development of the boundary layer behind the incident shock wave. The generation of the boundary layer results in the attenuation of the shock, axial and transverse flow non-uniformities, acceleration of the contact surface, shock curvature, reflected shock bifurcation, and a general reduction in test time. Thus, understanding the development, and quantifying the boundary layer, are important to understanding the performance of the facility. In Section 3.5, the detrimental effect of the growing boundary layer on shock attenuation and contact surface acceleration will be addressed.

3.4.1 Boundary Layer Model

The boundary layer is rather difficult to analyze due to the unsteady nature of the flow. However, if a shock stationary reference frame is adopted, then the problem can be approximated as a steady boundary layer moving over a semi-infinite flat plate. This convention is shown schematically in Figure 3-6.

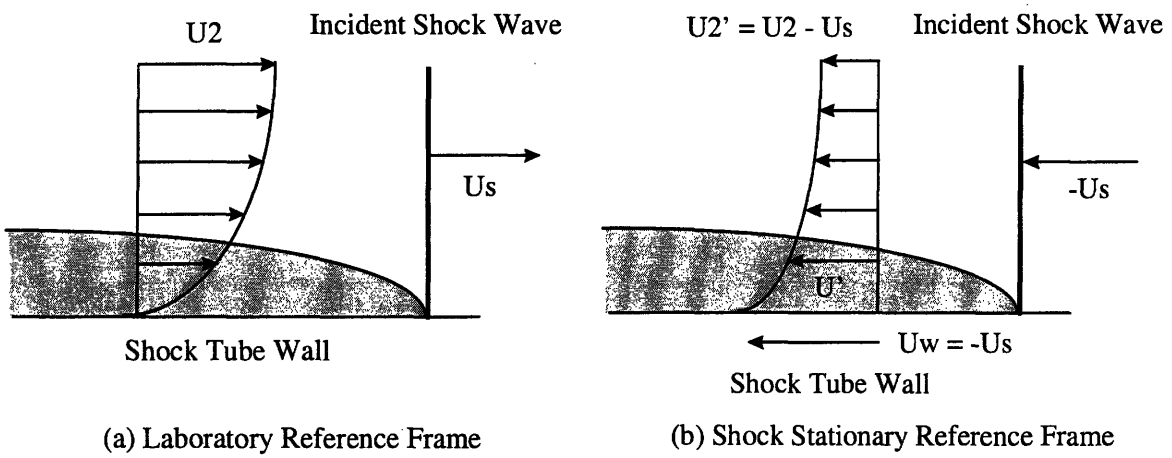

(a) Laboratory Reference Frame (b) Shock Stationary Reference Frame

Figure 3-6: Boundary layer approximated as steady flow over a semi-infinite flat plate through a change of reference frame, [22]

This model makes the following assumptions:

- The boundary layer is thin compared to the shock tube diameter, such that within the region of study the growing boundary layers do not attach.
- The pressure perturbations associated with the unsteady boundary layer growth can be ignored. [12]
- The shock attenuation can be neglected, and the inflow conditions can be assumed to be uniform.
- The free stream velocity is independent of position ($\delta^* << D_{st}$).
- Locally, the curved shock tube wall can be modeled as a flat plate.

Before the boundary layer can be analyzed, it is necessary to ascertain whether the boundary layer behind the incident shock wave can be described as wholly laminar or turbulent, or a combination of both, with transition occurring a significant distance behind the incident shock wave. One method to determine this is presented in the next section.

3.4.2 Prediction of Transition from Laminar to Turbulent Flow

Predicting transition from a laminar to a turbulent boundary-layer is more complex in the case of boundary-layer development behind a traveling shock wave than in the case of steady flow due to the unsteady nature of the problem. Reasonable estimates on transition distance and time, from a laminar to a turbulent boundary-layer, have been made by experimental studies using optical methods in conjunction with a thin film heat gauge. Figure 3-7 illustrates the concept of using a thin film heat gauge to measure the transition distance and time.

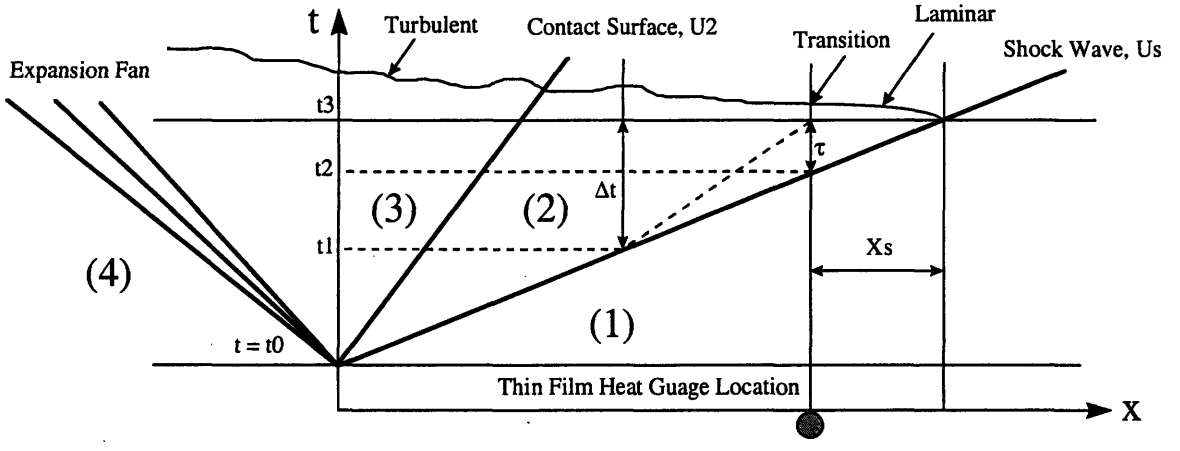

Figure 3-7: Illustration of the measurement of boundary layer transition with a thin film heat gauge

[12] This assumption will be removed in Section 3.5.

From Figure 3-7, τ is the time between the passage of the shock over the gauge and transition to turbulence, which is equal to t3-t2. This phenomenon moves along with a speed equal to the shock speed, Us. Δt is the total flow time of the particle which first goes turbulent on hitting the gauge, which is equal to $(V1/V2)\tau$, where V1 and V2 are in the shock attached coordinate system or (t3-t1). Xs is the distance behind the incident shock in which the boundary-layer reaches the transition distance, and L is the distance that the fluid has traveled since the passage of the shock, thus:

$$\Delta t = \frac{(l + Xs)}{Us} \tag{3.12}$$

and,

$$l = U2\Delta t = \frac{U2}{Us}(l + Xs) \tag{3.13}$$

$$\tau = \frac{Xs}{Us} \tag{3.14}$$

combining equations 3.12 - 3.14, and solving for l (making use of shock stationary coordinates) gives:

$$l = \frac{U2\tau}{\frac{Us - U2}{Us}} = U2\left(\frac{V1}{V2}\right)\tau \tag{3.15}$$

This provides the length term in the transition Reynolds number definition:

$$\mathrm{Re}_t = \frac{\rho U l}{\mu} = \frac{Ul}{\upsilon} = \frac{U2^2\left(\frac{V1}{V2}\right)\tau}{\upsilon_w} \tag{3.16}$$

This equation can now be solved for the transition time, which when multiplied by V1 (the wall velocity in the shock attached coordinate system) gives X_s:

$$\tau_t = \frac{\mathrm{Re}_t\,\mu_w}{\rho_w U2^2}\left(\frac{V2}{V1}\right) \tag{3.17}$$

$$Xs = V1\tau_t \tag{3.18}$$

For shock tube flows, transition Reynolds numbers have been observed in the range of $2.5x10^5$ - $2x10^6$ range, [17], [34]. The table below makes use of an inviscid shock tube model and equations 3.15 - 3.18 to calculate transition parameters over the range of conditions investigated at the MIT shock tunnel.

Table 3.5: Transition parameters over the TTR Range of interest to the MIT shock tunnel

Re(trans)	TTR	ν (m^2/s)	U2 (m/s)	V1 (m/s)	V2 (m/s)	τt (ms)	Xs (cm)
800000	1.82	0.0000151	287.287	558.958	271.671	.0711375	3.97
800000	2.43	0.0000151	431.528	691.0907	259.563	.024364	1.68
800000	2.91	0.0000151	523.1793	781.106	257.927	.014573	1.138

These calculations indicate that the boundary-layer will become turbulent a short distance behind the incident shock, therefore a fully turbulent boundary-layer model can be justified. However, it should be noted that if low tube pressures, p1 < 0.05 atm, and relatively weak shocks, Ms < 2.0, are used a substantial length of the boundary-layer will be laminar and the fully turbulent model will no longer be applicable.

3.4.3 Boundary Layer Analysis

For the transformed coordinates shown in Figure 3-6, we can write the conversation of mass and momentum as follows:

$$\int_0^\infty \rho_1 v_1 dy = \int_0^\infty \rho_2 v_2 dy \qquad 3.19$$

$$\int_0^x \tau_x dx = \int_0^\infty \rho_2 v_2^2 dy - \int_0^\infty \rho_1 v_1^2 dy \qquad 3.20$$

Substituting equation 3.19 into 3.20 and integrating with respect to x, gives an expression for the derivative of the momentum thickness with respect to the tube station, x, can be found:

$$\frac{\tau_x}{\rho_2 v_2^2} = \frac{\partial}{\partial x}\int_0^\infty \frac{\rho_1 v_1}{\rho_2 v_2}\left(1 - \frac{v_1}{v_2}\right) dy \equiv \frac{d\theta}{dx} \qquad 3.21$$

The velocity profile used in the boundary layer analysis was assumed to be a simple power-law distribution. Relative to the stationary shock, the velocities can be described as:

$$\left|\frac{v-v_1}{v_2-v_1}\right| = \left(\frac{y}{\delta}\right)^{1/n} = \zeta^{1/n} \qquad 0 \le \zeta \le 1 \qquad 3.22$$

$$\left|\frac{v-v_1}{v_2-v_1}\right| = 1 \qquad 1 \le \zeta \qquad 3.23$$

It has been found that n = 5 has produces the best correlation with experimental data for shock tube flows. The thermal boundary layer was defined using the Crocco-Busemann relation between temperature and velocity. Typically this relation is used for laminar flows, however, it is also a valid approximation for turbulent flows in the absence of a strong axial pressure gradient. This relation is written as:

$$\frac{T}{T_2} = \frac{T_w}{T_2} + \frac{T_r - T_w}{T_2}\left(\frac{u}{u_2}\right) - \frac{1}{2}P_r(1-\gamma)M_e^2\left(\frac{u}{u_2}\right)^2 \qquad 3.24$$

The displacement thickness, δ^*, and the momentum thickness, θ, can also be defined in the shock stationary coordinates:

$$\delta^* \equiv \int_0^\infty \left(1 - \frac{\rho v}{\rho_2 v_2}\right) dy \qquad 3.25$$

$$\theta \equiv \int_0^\infty \frac{\rho v}{\rho_2 v_2}\left(1 - \frac{v}{v_2}\right) dy \qquad 3.26$$

The boundary layer thickness and wall shear forces were found using the Blausius relation for compressible turbulent flow over a semi-infinite flat plate, which are given below:

$$\delta \approx (0.130)\left[\frac{\mu_m}{\mu_2}\right]^{1/4}\left[\frac{T_2}{\frac{1}{2}(T_w+T_2)+(0.22)(T_r-T_2)}\right]^{2/3}\left[\frac{1-\frac{v_1}{v_2}}{\frac{\theta}{\delta}}\right]^{3/4}\left|1-\frac{v_1}{v_2}\right|^{1/2}\left[\frac{v_2}{v_2 x}\right]^{1/4} x \qquad 3.27$$

$$\frac{\partial\theta}{\partial x}=\frac{\tau_x}{\rho_2 v_2^2}\approx(0.0488)\left(\frac{\mu_m}{\mu_2}\right)^{1/3}\left(\frac{T_2}{T_m}\right)^{2/3}\left(1-\frac{v_1}{v_2}\right)\left|1-\frac{v_1}{v_2}\right|^{2/3}\left(\frac{mu_2}{\rho_2 v_2\delta}\right)^{1/4} \qquad 3.28$$

The complete details of the boundary layer analysis are presented in Appendix B of Reference [22], with additional details of the boundary layer within the shock tube found in References [17], [32], [34], [41].

Results of these calculations are presented in Figures 3-8 through 3-10 for the geometry of the shock tunnel employed at the MIT facility. The boundary layer model has been demonstrated to agree with experimental data to within approximately 15% over the range of operation considered for the MIT facility. As a general trend, the boundary-layer effects will become more severe as the driver section pressure is reduced.[13]

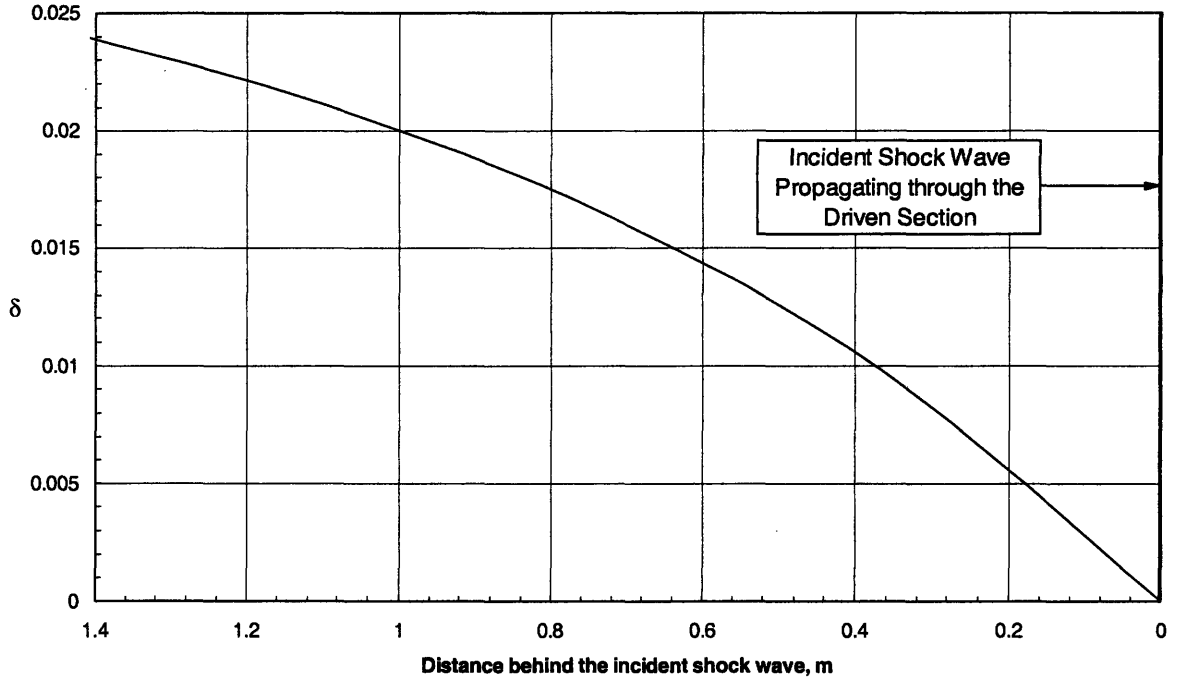

Figure 3-8: Boundary layer thickness versus shock tube station

[13] In general the boundary-layer effects will also become more severe as the length to diameter ratio of the shock tube is increased.

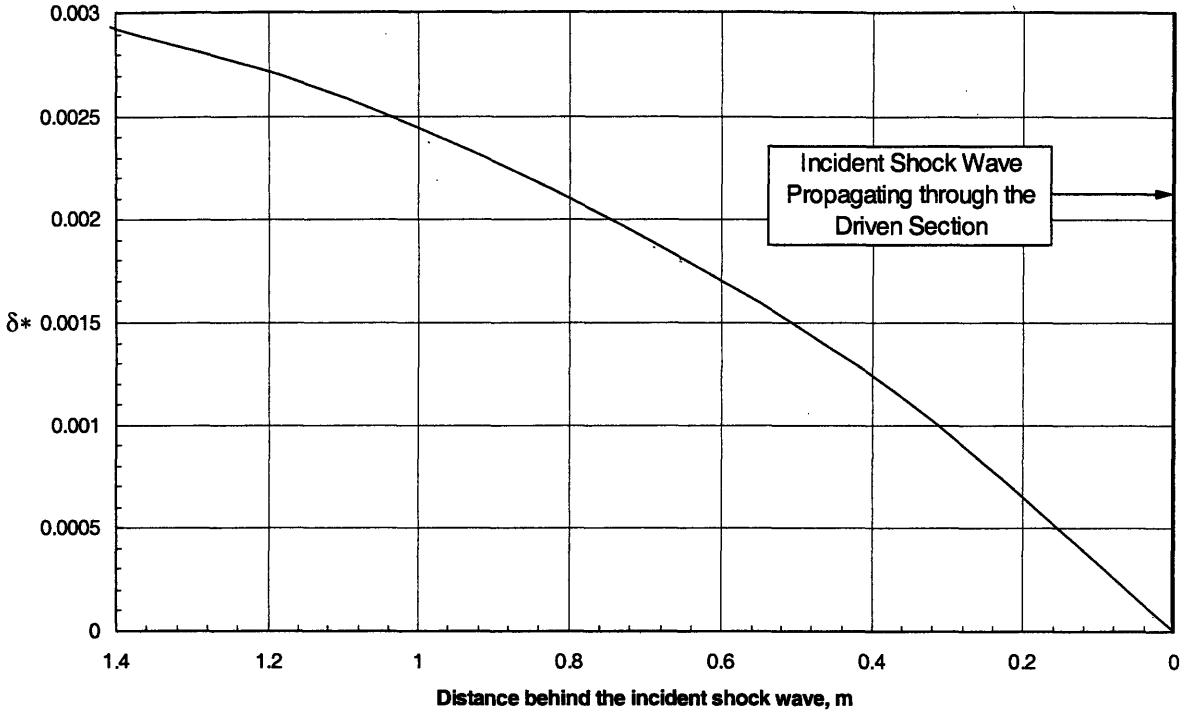

Figure 3-9: Displacement thickness versus shock tube station

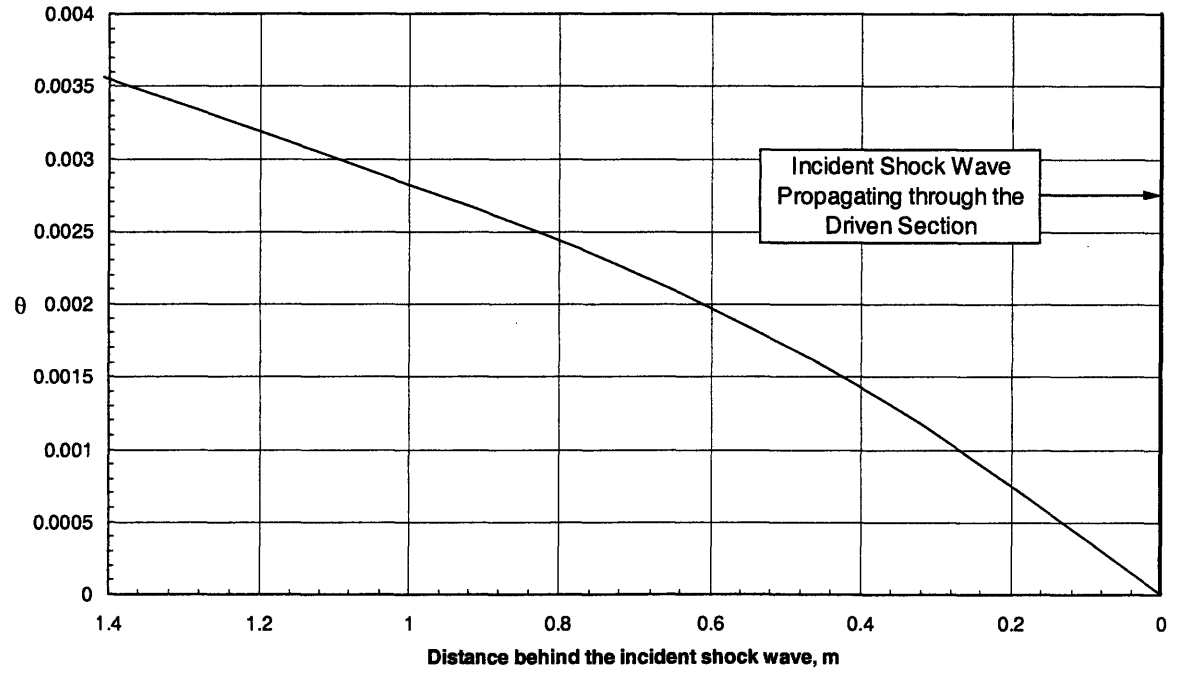

Figure 3-10: Momentum thickness versus shock tube station

3.5 Shock Wave Attenuation and Contact Surface Acceleration Modeling

This section develops an intuitive understanding of why shock wave attenuation occurs, and why it is an important phenomena to understand and quantify.

3.5.1. Overview and Importance of Shock Attenuation Calculations

The one-dimensional gas dynamic analysis of a perfect fluid is useful for providing a first estimate of shock tube performance and wave behavior. However, in real shock tubes there are viscous, thermal, and three dimensional effects that have a notable impact on performance. The most significant of these effects is the growth of an unsteady boundary-layer. There will be a negative velocity, v, in region (2) producing the same effect as if the tube diameter were widening, and similarly a positive velocity in region (3), which corresponds to the tube diameter shrinking. This generates weak pressure waves that overtake and attenuate the shock and accelerate the contact surface. This effect is portrayed in Figure 3-11.

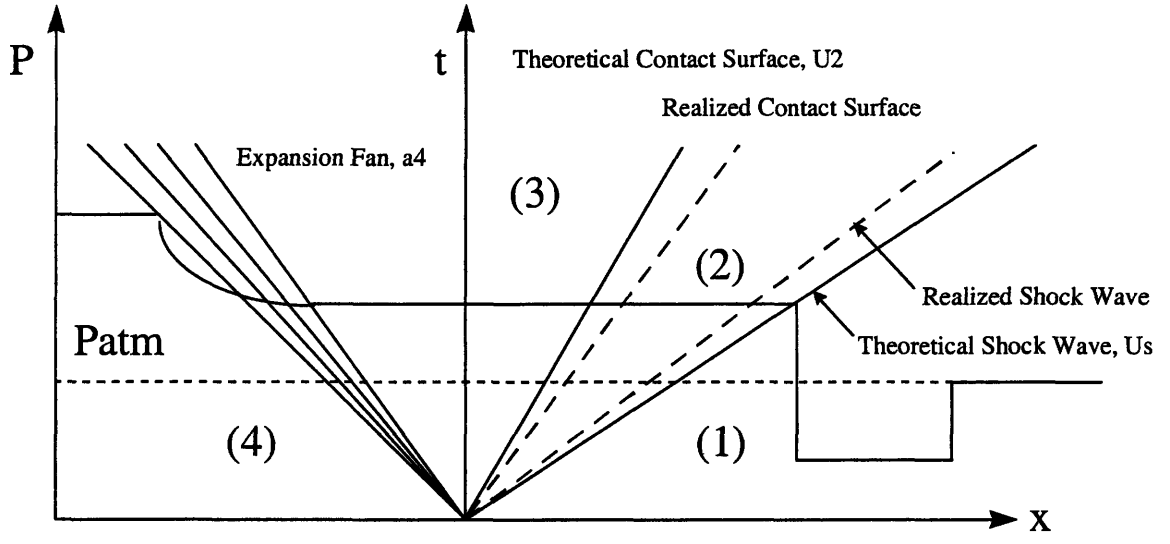

Figure 3-11: Wave diagram showing theoretical versus realized wave behavior

The developing boundary-layer continuously generates traveling compression and expansion waves. These pressure waves traverse the flow and alter its properties, as well as the speed of the incident shock wave and the contact surface. This implies that there are no uniform flow regions within the flow field and that all flow properties are a function of position and time. Although it is generally accepted that that unsteady-boundary-layer generates unsteady pressures waves, the mechanism by which these waves are produced is debatable. In Reference [33] the arguments of Trimpi and Cohen are presented. They suggest that the pressure waves are generated by skin friction and heat transfer effects. Their model is

shown to work reasonably well for thick boundary-layers or fully-turbulent pipe flow theory. Mirles, [33] has argued that the pressure waves are generated by the vertical velocity at the edge of the boundary layer, which is analogous to a piston-like effect. This theory is shown to work well for a thin boundary layer with an isentropic core, which is the fluid dynamic situation encountered in shock tube flow. Both theories predict an attenuation that varies with the flowing parameters:

1. Incident shock strength (P2/P1).
2. Distance the shock has traveled from the diaphragm.
3. Boundary-layer type (laminar or turbulent) and profile.
4. Tube cross-sectional geometry and dimension.

Calculation of the boundary-layer thickness in Section 3.4.3 demonstrated that the boundary-layer is indeed thin compared to the tube diameter, and therefore the methods developed and suggested by Mirels are utilized for the attenuation calculation.

Existing shock tubes with similar geometries to the MIT facility and operating conditions realize 90% to 95% of the ideal shock speed. The exact shock attenuation is not consequential in practice by virtue of the fact that driver pressure can be increased to account for the viscous effect. Nonetheless, it is a useful exercise to quantify the magnitude of the incident shock attenuation that occurs over the range of operating conditions and compare this effect to data obtained from the facility. An analytical model for predicting shock attenuation can be a useful tool for expediting convergence to the actual initial set conditions, as opposed to an exclusively "guess and check" method.

3.5.2 Calculation and Analysis Overview

The attenuation of the incident shock wave can be predicted by modeling the boundary-layer as a distribution of mass sources along the wall of the tube, as done by Mirels, [33]. It is assumed that the boundary-layer is thin relative to the tube diameter and induces one-dimensional longitudinal pressure waves whose strength are proportional to the vertical velocity at the edge of the boundary-layer. The pressure perturbations can then be integrated along characteristic lines to determine the variation in shock strength with position.

The effect of the vertical velocity, due to the developing turbulent boundary layer, is shown schematically in Figure 3-12. As can be seen in the figure, the positive velocity in region 3 generates compression waves which accelerate the contact surface. In region 2, the growing boundary layer produces a negative vertical velocity, which generates expansion waves, which attenuates the incident shock wave. These two phenomena were shown by the dashed lines in Figure 3-11. A more mathematically rigorous description of these compression and expansion waves is given in Appendix B, specifically shown in Figures B-2 and B-3 for the contact surface and shock wave, respectively.

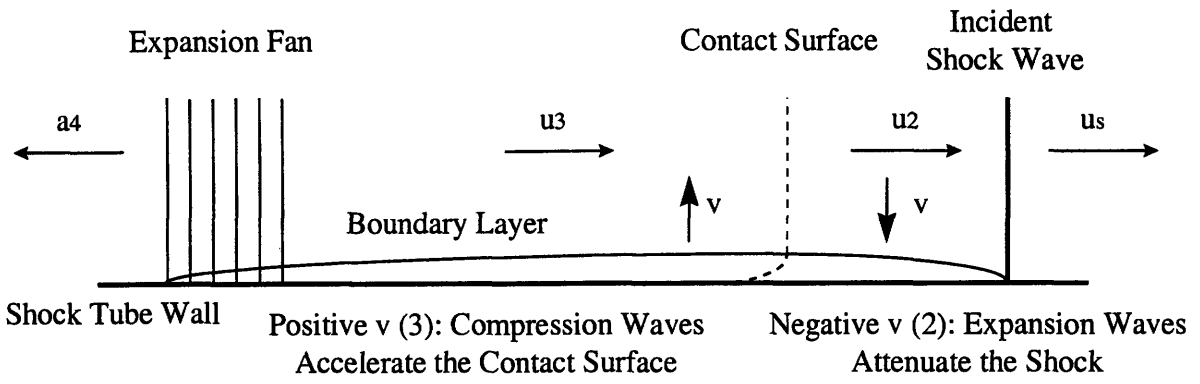

Figure 3-12: Vertical velocity due to the unsteady turbulent boundary layer

The various compression and expansion waves, which interact over the region from the incident shock wave to the contact surface, are shown in Figure 3-13.

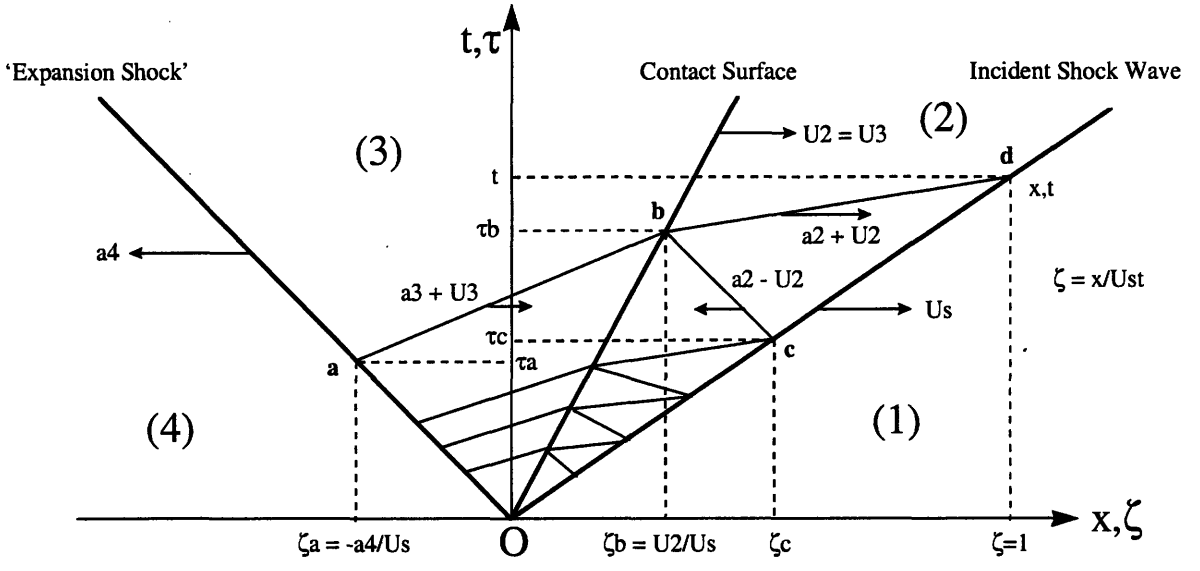

Figure 3-13: Characteristic lines of integration for shock wave attenuation, [33]

The figure shows the incident shock wave, the contact surface, and the expansion shock, with the interacting perturbation waves. The perturbation waves of interest, shown by lines, ab, bc, and db, are described in more detail in Reference [33], and summarized in Appendix B. The magnitude of the contribution of all other perturbation waves shown in Figure 3-13, is discussed in Reference [33].

The perturbation quantities behind the incident shock can be found from Mirel's [33], which is summarized in Appendix B, and the normal shock relations. These attenuation quantities for velocity, density, temperature, and incident shock Mach number, are summarized below:

$$\frac{\Delta U_{2,d}}{U_2} = \frac{2\gamma_1 M_s^2 - (\gamma_1 - 1)}{4\gamma_1 M_s^2}\left(\frac{M_s^2 + 1}{M_s^2 - 1}\right)\left(\frac{\Delta p_{2,d}}{p_2}\right) \tag{3.29}$$

$$\frac{\Delta \rho_{2,d}}{\rho_2} = \frac{2\gamma_1 M_s^2 - (\gamma_1 - 1)}{\gamma_1 M_s^2\left[(\gamma_1 - 1)M_s^2 + 2\right]}\left(\frac{\Delta p_{2,d}}{p_2}\right) \tag{3.30}$$

$$\frac{\Delta T_{2,d}}{T_2} = \left(\frac{\Delta p_{2,d}}{p_2}\right)\left(1 - \frac{2\gamma_1 M_s^2 - (\gamma_1 - 1)}{\gamma_1 M_s^2\left[(\gamma_1 - 1)M_s^2 + 2\right]}\right) \tag{3.31}$$

The resulting perturbation of the shock Mach number can also be found in terms of the net pressure perturbation behind the shock:

$$\frac{\Delta M_{s,d}}{M_s} = \frac{\gamma_1 + 1}{4\gamma_1}\frac{\left(p_2 / p_1\right)}{M_s^2} F\left(\frac{\Delta p_{2,d}^+}{p_2}\right) \tag{3.32}$$

Once again a complete derivation of the attenuation equations, a derivation of the magnitude of the vertical velocity in regions 2 and 3, as well as the boundary layer thickness in those regions, may be found in Appendix B.

3.5.3 Results and Discussion

It is interesting to note that these perturbations are not isentropic except for the limiting case where the incident shock Mach number approaches unity. This is understood because a perturbation of shock strength creates an entropy perturbation. An entropy wave moves with the speed of the background flow, and the acoustic disturbance that was introduced in the density perturbation moves at the sonic speed of the region relative to the background flow. In the one-dimensional isentropic core, there can be no vorticity disturbance. However, the vorticity disturbance within the boundary-layer is converted undisturbed at the speed of the background flow.

As was discussed above, the vertical velocity at the edge of the boundary-layer in region (2) is negative and introduces expansion waves (which attenuate the shock), whereas the vertical velocity in region (3) is positive and inroduces compression waves (which accelerate the shock). Dissipation and heat transfer modify these results. Table 3.6 presents a convinient way to summarize the importance of these effects, noting that the net result of these contributors is to attenuate the incident shock wave and accelerate the contact surface:

Table 3.6: Physical effect summary of heat transfer on boundary layer behavior

Physical Effect	Region (2) Consequence	Region (3) Consequence	Net Consequence
Dissipation	increase v	increase v	v less negative in region (2) v more possitive in region (3)
Heat transfer from Wall to BL (weak expansion)		increase v	Heat transfer generates compression waves which accelerate the incident shock wave
Heat transfer from BL to Wall (strong expansion)		increase v	Heat transfer generates expnasion waves which attenuate the incident shock wave
Heat transfer from BL to Wall	decrease v		Larger negative values of v2 and more shock attenuation

The condition where the wall temperature in region (2) is assumed to be equal to the intial temperature in the driven section corresponds to the case where the shock tube wall is a perfect conductor. This is in good agreement with the MIT shock tube, where the walls are made out of metal. For comparison, taking the temperature of the wall in region (2) equal to the adiabatic recovery temperature corresponds to the case where the shock tube can be modeled as a perfect conductor. Results for T2,w = T1 and T2,w = T2,r provide the upper and lower bounds of the consequences of heat transfer on shock attenuation. The attenuation is greater, by a factor of exactly the ratio of specific heats in region (1), when there is heat transfer as compared with the perfectly insulated case. These upper and lower bounds for the shock wave attenuation parameter are depicted in Figure 3-14.

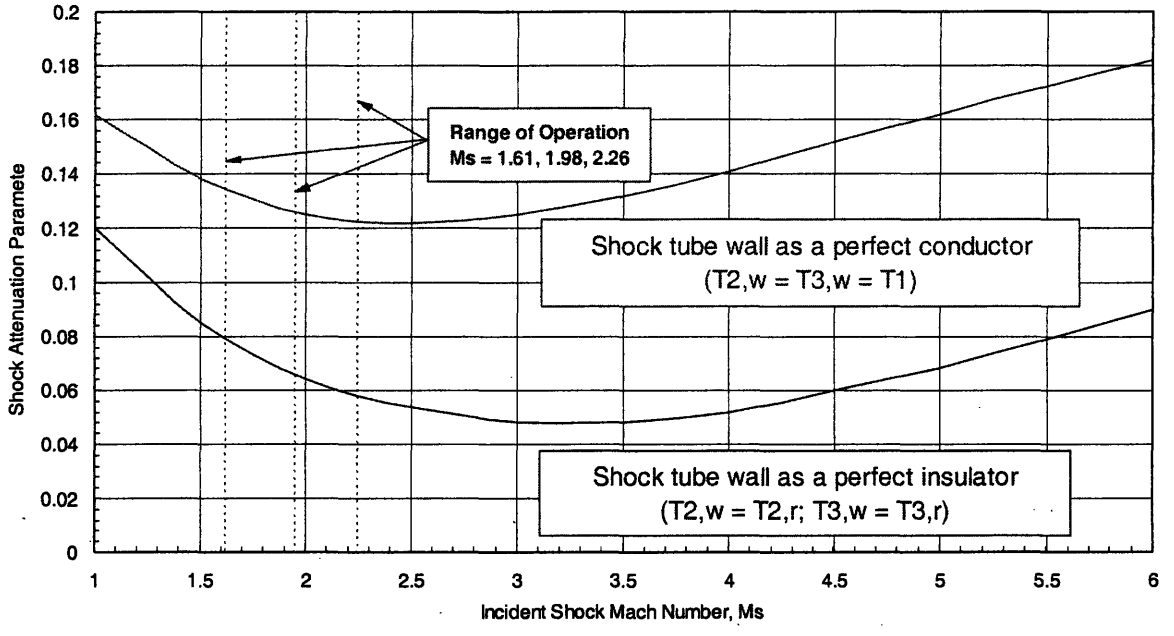

Figure 3-14: Incident shock wave attenuation parameter versus incident shock Mach number for turbulent boundary layer model

The relative contribution to the net attenuation of the various waves, shown in Figure 3-12, that interact between the expansion fan, contact surface, and the incident shock wave are shown in Figure 3-14. As can be seen for weak shocks, the major contribution to the shock attenuation comes from the integration along the characteristic line bd. With increasing incident shock Mach number, the contribution along characteristic line bc increases gradually to a value around 30% at an incident Mach shock number of 6.0. The integration along characteristic line ab leads to compression waves (which as aforementioned tends to accelerate the shock) and therefore is negative. The value decreases to around 35% at an incident shock Mach number of around 2.5 and then increases with increasing incident shock Mach number. It is important to note that the influence of characteristic line ab may be slightly overestimated in this analysis because of the modeling assumption of the expansion fan as an "expansion shock". The contribution of the remainder of the lines is small and a maximum of around 5% at an incident shock Mach number of 6.0. To neglect the remaider of the lines seems to be a satisfactory assumption for the range of operations considered in this analysis.

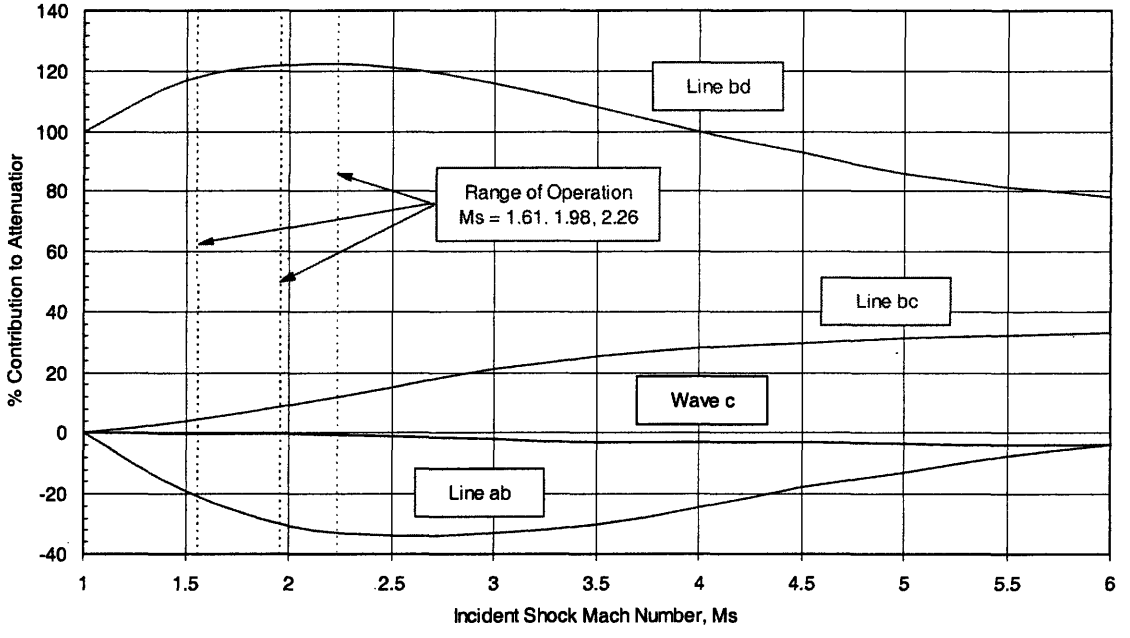

Figure 3-15: Percent contribution to shock attenuation of characteristic lines for turbulent model

Finally, Figure 3-16 shows the analyticaly predicted attenuation for three conditions that the MIT shock tube is operated at (NPR = 1.51, TTR = 1.81; NPR = 2.48, TTR = 2.43; NPR = 2.71, TTR = 3.43) as well as the measured shock speeds for those conditions.

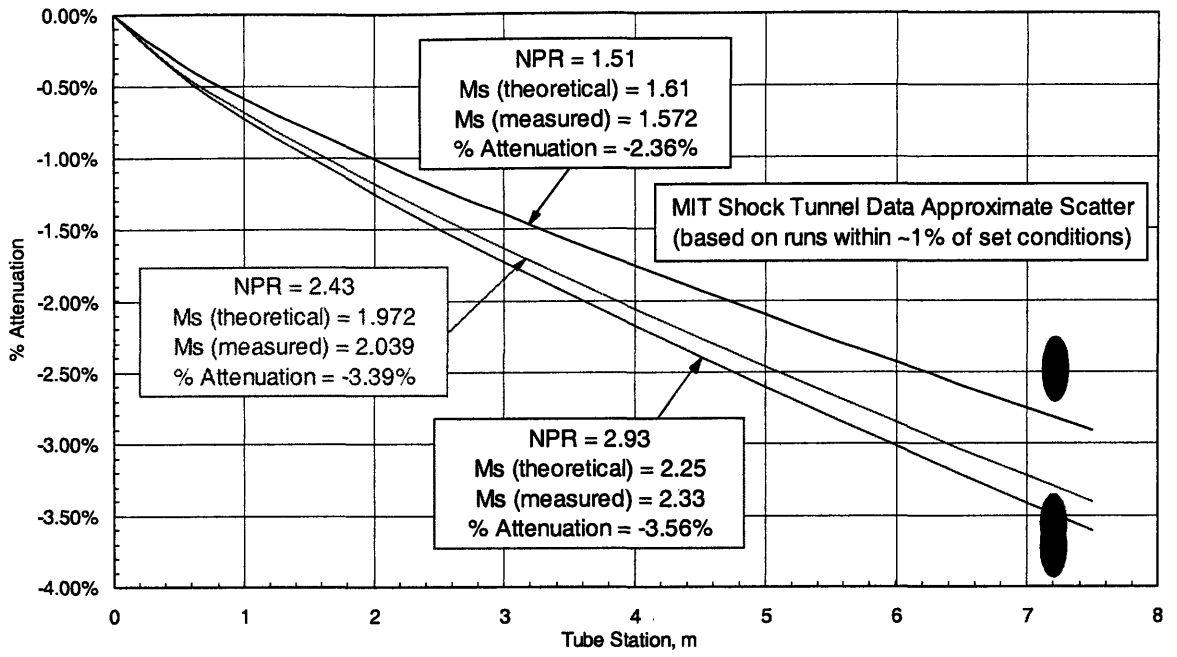

Figure 3-16: Percent incident shock wave attenuation versus shock tunnel station for MIT facility

As can be seen the attenuation agrees within 0.5 % with the analytically predicted values.

3.5.4. Discussion of Attenuation based on Generation of Pressure Waves by Wall Shear and Heat Addition

The generation of pressure waves by shear forces and heat sources in one-dimensional flow, was also investigated by Mirels [33], and the results are compared to the analytical result obtained from the theory that the pressure waves are proportional to the vertical velocity at the edge of the boundary-layer. The methods developed by Trimpi and Cohen do not give a complete representaiton of the wave phenomena in a shock tube induced by the wall boundary-layer. The discrepeancy is associated with the use of the wall shear stress in the prediction of the perturbation pressure waves generated by the wall boundary-layer. Reference [33] argues that, "it is well recognized that the effect of the boundary-layer on the external flow is directly related to the vertical velocity at the edge of the boundary layer." By analogy, consider the Rayleigh impulsively started flat plate problem for a compressible fluid. It shows that the boundary-layer generates pressure waves in the external flow which, are equivalent to those which are produced if the wall moves normal to itself with a velocity equal to the vertical velocity at the edge of the boundary-layer. The non-zero pressure gradient over a flat plate moving at high speeds (because of the finite displacement thickness of the boundary-layer) is an equivalent steady-flow pheonmena. Thus, a proper way to quantify the waves generated by the unsteady-boundary-layer in a shock tube is to correlate the calculation with the vertical velocity at the edge of the boundary-layer.

The numerical value of the magnitude of the vertical velocity depends on terms which are related to the boundary-layer velocity profile, dissipation, and heat transfer. However, Reference [33] shows that the velocity profile term in the equation for the vertical velocity has a sign opposite to that of the wall shear term for characteristic lines ab (compression wave) and bc (expansion wave). Thus, application of a similar approach to that developed in [33] would overestimate and underestimate, respectively, the contribution of these lines to the shock attenuation. Table 3.7 summarizes the differences between the two methods:

Table 3.7: Summary of perturbation quanities

		Perturbation on v			Perturbation on τw	
Region	v	ΔP+	ΔP-	τw	ΔP+	ΔP-
2	-	-	-	-	-	+
3	+	+	+	-	-	+

When heat transfer and dissipation are neglected, a perturbation solution based on the vertical velocity at the edge of the boundary layer differs from a perturbation based on the wall shear stress in regard to the sign of the Δp- waves in region (2) and the Δp+ waves in region (3). However, in the case where the incident shock Mach number appraoches unity, the contributions from lines ab and bc are small, thus the results between Mirles and Trimpi and Cohen are in good agreement for this limiting case. When the boundary layer is thin, the attenuation calculation should be based on the method presented in Reference [33]. If the viscous shear influences the entire flow crosssection, there is no longer a potenial core flow and the solution should be based on the methods suggested by Trimpi and Cohen, however, the wall shear stress and heat transfer should be based on unsteady pipe flow rather than thin boundary-layer theory.

3.5.5 Reflected Shock Boundary Layer Interaction

After the shock reflects from the end wall, it will encounter the unsteady boundary layer and no longer behave as a simple plane wave, [22], [31]. In laminar flows, a strong bifurcation of the shock has been observed in the region close to the shock tube walls as shown in Figure 3-17.

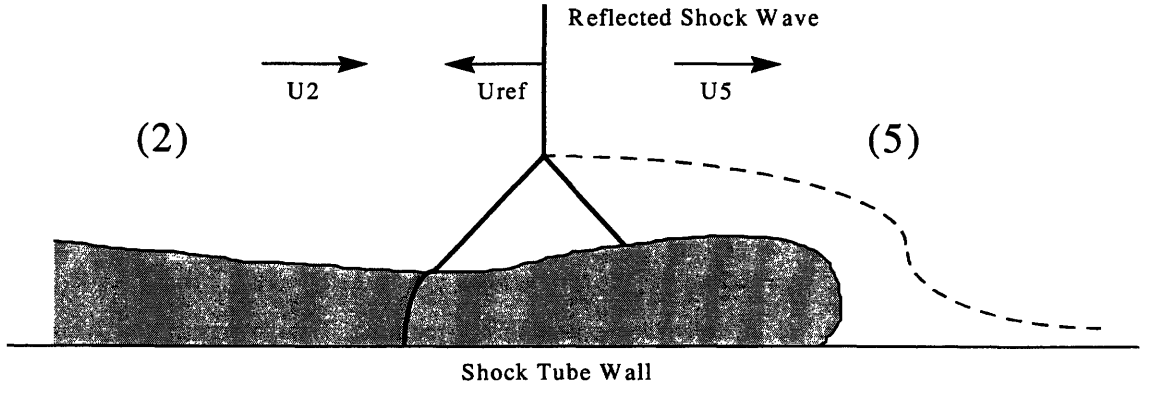

Figure 3-17: Shock bifurcation for reflected shock and laminar boundary layer interaction, [31]

This oblique shock structure leads to non-uniform heating across the test section and, more importantly, the mixing of the driver and driven gases as the shock crosses the contact surface. This contaminates the test gas with the cold driver fluid and reduces the total available test time.

In turbulent flows this effect is significantly less severe. The increased transport of energy from the main stream eliminates the conditions in the low-energy laminar boundary layer that lead to shock bifurcation. As a result, it is necessary to establish whether the reflected shock will be interacting with a laminar or turbulent boundary layer when it crosses the contact surface, [31]. Section 3.4.2 predicted that the boundary layer behind the incident shock wave turns turbulent a short distance behind the shock, for the range of operating conditions used in this investigation. During the investigation presented in Reference [31], it was shown that the highly turbulent boundary layer leads to minimized shock bifurcation.

3.6 Chapter Summary

This chapter presented a summary of the gas dynamic models used to predict the initial conditions across the diaphragm for shock tube operation. Test time limitations, due to reflected waves and test gas exhaustion, were presented, along with experimental methods that can be employed to maximize the duration of the quasi-steady pressure region, and hence maximizing the total test time. Prediction of the duration of the useful test time was based on the results of the 1-D inviscid shock tube gas dynamic model. Viscous effects, including the development and attenuating effect of the boundary layer, were explored. An analytical model developed in Reference [33] was presented, and the model was applied to the MIT facility to predict the magnitude of the incident shock wave attenuation over the range of facility operating conditions. Based on a knowledge of the expected incident shock wave attenuation, better initial estimates of the set conditions across the diaphragms can be made to more rapidly arrive at the initial conditions which produce the desired jet conditions.

Chapter 4

Acoustic Theory and Generation of the Supersonic Scaled Jet

The one dimensional gas-dynamic models presented in Chapter 3 can be used to relate shock tube geometry and operating condition to the duration of the constant pressure region behind the reflected shock wave. From these relations, the achievable test time, and hence the acoustic sampling period for a given operating condition, can be obtained. This chapter leaves behind the internal wave physics of the shock tube and explores the flow through the test articles, as well as the flow that issues into the test chamber, manifesting itself in the form of a supersonic jet. Within this chapter an overview of the theoretical background, which characterizes the behavior of a supersonic jet, is presented. Expressions for the time scales required for the jet to reach a quasi-steady state, and the sampling time required to accurately resolve the radiated acoustic signature into noise spectra, are developed. Nozzle sizing constraints are discussed and the methodology for sizing the LSMS mixer-ejector tested at the MIT facility is presented. Finally, the chapter presents a comparison between analytically predicted nozzle starting and jet development times with experimental starting time measurements.

4.1 Background

As far back as 1952, M.J. Lighthill established an analytical description of the fundamentals of aerodynamic noise generation, [26]. As a result of his seminal work, and numerous others that verified and extended his research, the physical origin of aerodynamic noise from a subsonic jet can now be regarded as reasonably well-understood, [27], [30], [56]. In a subsonic jet, noise is generated primarily by the turbulent mixing of the flow with the ambient fluid into which the jet exhausts. Lighthill explicated this source of acoustic radiation in terms of pressure fluctuations, which in turn produce pulsations in the fluid due to compressibility effects, and thus give rise to noise radiation, [29]. Furthermore, it was shown that at low Mach numbers, the overall sound power is proportional to the eighth power of the jet velocity.

$$P_j \approx \frac{\rho_o U^8 D_e}{a_o^5} \qquad 4.1$$

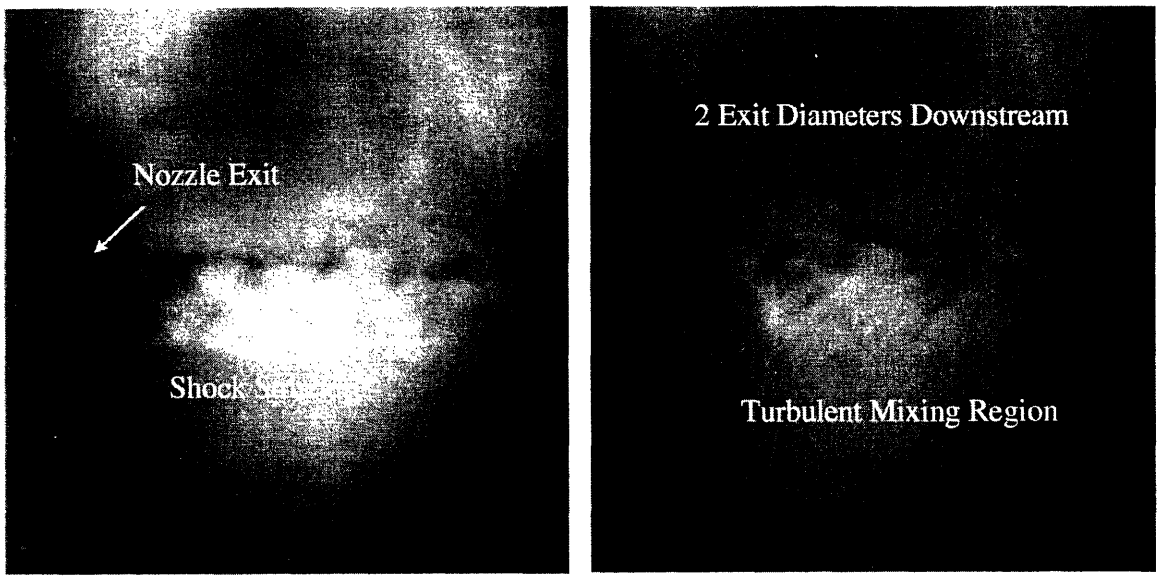

Figure 4-2: (a) Schlieren images of ¼ inch conic nozzle with view of the exit plane and (b) 2 exit diameters downstream in which the turbulent mixing region can be seen

As the jet exhausts into the ambient air it is subjected to a concentrated shearing action at its boundaries. A continuous exchange of momentum between the flow and the ambient air engenders the formation of the turbulent mixing region. When the supersonic core region of the jet, which is surrounded by the turbulent mixing region, becomes subsonic the flow transitions to a completely turbulent behavior, [29].

4.1.1.1 Description of the Mixing Region

The structure of the turbulent mixing region of a circular jet has been studied extensively, [26], [27], [50]. The initial mixing region, from about one to four diameters from the nozzle exit plane, is similar to the two-dimensional plane mixing layer since its overall thickness is small compared with the jet diameter, D_e. In the initial mixing region, if all upstream disturbances are absent, the mixing layer exhibits characteristics of laminar flow followed by transition to turbulence. Experimental evidence suggests that the vortex structures existing in the final stages of transition persevere into the fully turbulent flow regime. In addition, large vortex structures arise naturally in the turbulent flow, [44]. The importance of the collapse of vortex rings, vortex pairings and the resulting large localized pressure fluctuations as a source of intense noise radiation, has been studied in References [27], [44]. Unresolved issues still remain for jets at high Reynolds numbers, where the turbulent diffusion processes act to dampen peaks in the pressure fluctuations. At subsonic jet speeds, in fully turbulent flow, such noise mechanisms are small in amplitude compared with their supersonic counterparts.

Transition from laminar to turbulent flow is also a strong source of noise that occurs within the mixing region. Measurements of noise sources from jets at low Reynolds numbers, where the extent of laminar flow from the jet exit to transition covers many exit diameters downstream, do not follow the corresponding results for supersonic jets at higher Reynolds numbers. The turbulent structures within the

Since the mechanical power is proportional to the cube of the velocity, this law represents a net acoustic efficiency which is proportional to the fifth power of the velocity.[1]

4.1.1 Structure of the Supersonic Turbulent Jet

For a supersonic jet there is no simple explanation for the source of the aerodynamic noise. To foster an understanding of the physical processes which govern supersonic jet noise generation, the jet can be divided into three regions, which are summarized below and shown schematically in Figure 4-1.

1. **Supersonic Region:** The potential jet core where the flow is entirely supersonic with a complicated shock structure.
2. **Mixing Region:** Downstream of the supersonic region where the flow is subsonic and is characterized by strong turbulent mixing.
3. **Subsonic Region:** The jet broadens out and the flow is characterized by a gradual decay of large scale turbulent eddies.

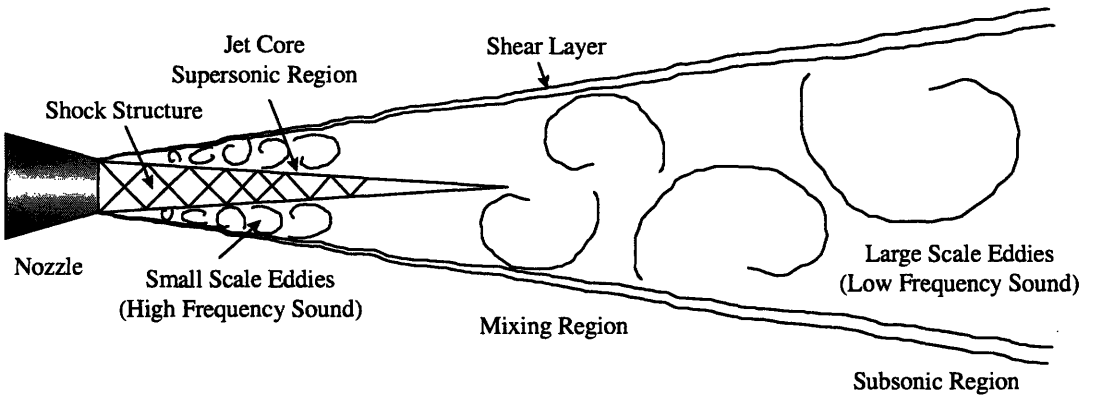

Figure 4-1: Supersonic turbulent jet structure schematic

Figure 4-2 shows Schlieren images taken at the MIT facility of a ¼ inch (0.64 cm) round jet at a nozzle pressure ratio and total temperature ratio of approximately 2.5 and 1.0, respectively. The first picture captures the nozzle exit plane in which the shock structure is visible. The second picture shows the Schlieren system moved two exit diameters downstream, in which the end of the potential core and the turbulent mixing region can be seen.

[1] In the supersonic case approximately half the overall acoustic power is generated by the initial supersonic mixing region, and the remainder comes from the wholly subsonic region downstream of the supersonic region.

jet at high Reynolds numbers are strongly non-uniform as a result of the spreading of the flow into the surrounding non-turbulent ambient fluid. The bounding surface of the mixing region is highly deformed by eddies that resemble the Helmholtz instability of a vortex sheet with a growth and decay cycle, [27].

4.1.1.2 The Large-Scale Structure of a Turbulent Jet

The large-scale structure of the turbulence within the mixing region of a jet has been observed to possess self-similar structures that are coherent and extend in the direction of flow convection. A model for the structure of the two-dimensional mixing region of a jet, based on the wave theory of turbulence, is described in Reference [26]. The amplitude of the unstable disturbances and their subharmonics initially grow exponentially with both time and space and are convected downstream with a phase speed of about 0.6 times the jet exit velocity. Eventually nonlinear and three-dimensional distortions dominate and the simple waveform of the most unstable wave becomes more broadband. The result is that the local flow develops into an eddy structure of many difference sizes, and the turbulence possesses a near a continuous spectral appearance.

As a result the width of the local mean flow grows with downstream distance. Accordingly the properties of the most unstable wave change and the largest eddy structures tend to dominate the flow regime. This condition is accommodated by a pairing of subsequent yet randomly formed upstream disturbances as they are convected in the flow direction. Some irregularity in the structures develops, and overall the new structures suffer a prominent instability due to the irregular, turbulent flow developing downstream. On average, the large-scale structures possess a coherent structure as they convect downstream. The main turbulence is smaller in scale but is also convected downstream along with the large-scale turbulence. The smaller-scale turbulence eventually decays through a Kolmogoroff cascade process to the smallest scales of turbulence at which viscous dissipation occurs. The irregularity in the large-scale structures becomes more prominent in the mixing region downstream of the potential core, but nevertheless such a large-scale structure appears to exist and acts to control both the local growth of the mean flow and the entrainment of the external irrotational ambient fluid into the jet, [26], [27], [50].

4.1.1.3 Entrainment Into the Jet

The growth of the width of a jet depends on the entrainment of the ambient fluid. Both the growth and the width of the jet are constrained by the equilibrium balance imposed by the conservation properties of jet flow and its boundary conditions. To elucidate, first consider the special case of incompressible flow, and let U_{ent} be the average entrainment velocity at the edge of the jet boundary. For flow in the jet far downstream of the potential core, it follows that U_{ent} is inversely proportional to downstream distance and is only weakly dependent on the velocity distribution across the jet. In the initial mixing layer, which can be assumed to be planar, the entrainment from the high-speed stream differs from that of the ambient

medium. Both entrainments are directed toward the mixing layer. The turbulent diffusion into the ambient medium is greater than that into the high-speed flow, [27].

Further study has established that in all regions of the jet the entrainment is a strong function of the velocity ratio and the density ratio of the jet to the ambient fluid, as well as jet Mach number. These parameters influence the structural properties of the jet, such as the spreading rate, the centerline velocity decay downstream of the potential core and the local turbulent intensity. At the MIT shock tunnel facility all jets are studied as they exhaust into a static atmosphere. Comparisons with steady-state data will also be made on supersonic jets that exited into a static environment. However, as can be ascertained from the above discussion, the flow structure of the jet on a full-scale aircraft jet engine in flight will differ significantly from that of a static model jet tested in the laboratory at ambient conditions, [16], [20], [48].

4.1.2 Supersonic Noise Generation Mechanisms

Supersonic jet noise generating mechanisms are still not well understood. Within the subsonic jet, where no complex phenomena such as shocks or eddy Mach waves exist, the noise is generated predominantly through turbulent mixing. In supersonic jet noise, there are cumulative effects of Mach wave radiation, nozzle lip radiation, shock turbulence interaction, shock unsteadiness, screech tones, refraction effects and turbulent mixing, as well as coupling these mechanisms. Some of the basic noise producing mechanisms associated with supersonic jet flows are summarized below and detailed descriptions of these attributes can be found in References [24], [26], [27], [29], [44], [45], [48], [50].

4.1.2.1 Mach Waves

Mach wave radiation is due to the eddies in the jet being convected supersonically relative to the ambient air. These Mach waves radiate sound in a highly directional peak and contribute to the formation of the directivity patterns associated with noise produced by the jet. They originate in a region of a few jet diameters from the nozzle exit and their existence has been confirmed by shadowgraphs and holographic techniques. Theoretical studies view these disturbances as eddies convecting within the shear layer, and/or as instability waves propagating within the shear layer, [29].

4.1.2.2 Shock Turbulence Interaction and Shock Unsteadiness

Noise associated with shock turbulence interaction is a major source of noise production within the supersonic region of the jet. The interaction of the strong shock patterns with the boundary of the jet causes the production of spherical waves which propagate in a radial direction away from the axis of the flow. The existence of this phenomena is also based on optical observations, which show spherical radiation centered at shock tips and propagating transverse to the jet axis. Their contribution to overall noise is not substantial, and influence with temperature is minimal. Turbulent interaction with shocks

results in three different perturbation modes: vorticity, entropy and acoustic. It is the acoustic mode which propagates outward.

4.1.2.3 Nozzle Lip Radiation

Nozzle lip radiation is associated with the turbulent flux exiting the nozzle and often is convected on the turbulent shear layer. This radiation has a dipole characteristic at low speed but monopole behavior at higher nozzle exit velocities. Screech noise is typically associated with a feedback instability[2] to the nozzle lip, which also impacts the structure of the shock cells, [29].

4.1.2.4 Turbulent Mixing and Refraction

Turbulent mixing, which dominates subsonic jet noise, is often modeled as the main supersonic jet noise mechanism. The noise associated within the mixing region is generated by the turbulent mixing of the flow, while the subsonic region emits considerably less noise. However, due to the existence of sufficiently large velocity, temperature and density gradients in the subsonic region, noise produced in other regions of the jet will be refracted and possibly trapped when passing through it. According to these theories, the dominant aerodynamic noise location is centered in a region approximately 20 diameters from the nozzle exit, where transition (M=1) to subsonic flow takes place, [26], [29]. Additionally, the refraction effects within the jet tend to bend the acoustic paths more than in subsonic jets. Refraction coupled with the convective effects give the jet the distinctive lobed shape as shown schematically in Figure 4-3.

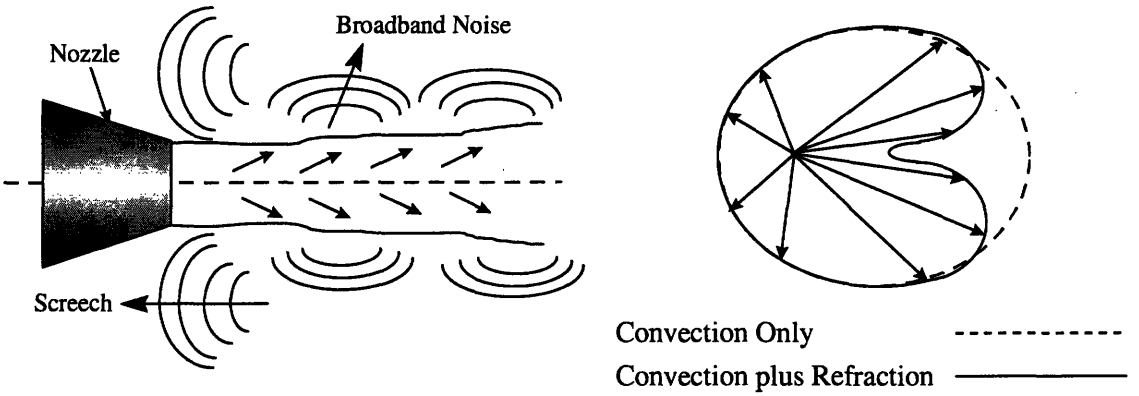

Figure 4-3: Schematic of outward refraction of sound rays by jet flow, [50]

For the mixer-ejector configuration studied in this thesis, the jet noise that is generated can be grouped into two primary sources: turbulent mixing and the interaction between turbulent structures and the shock cells.

[2] This is typically a subsonic outer flow.

Figure 4-4 shows where some of these structures are located within the jet exiting from and contained within the mixer-ejector.

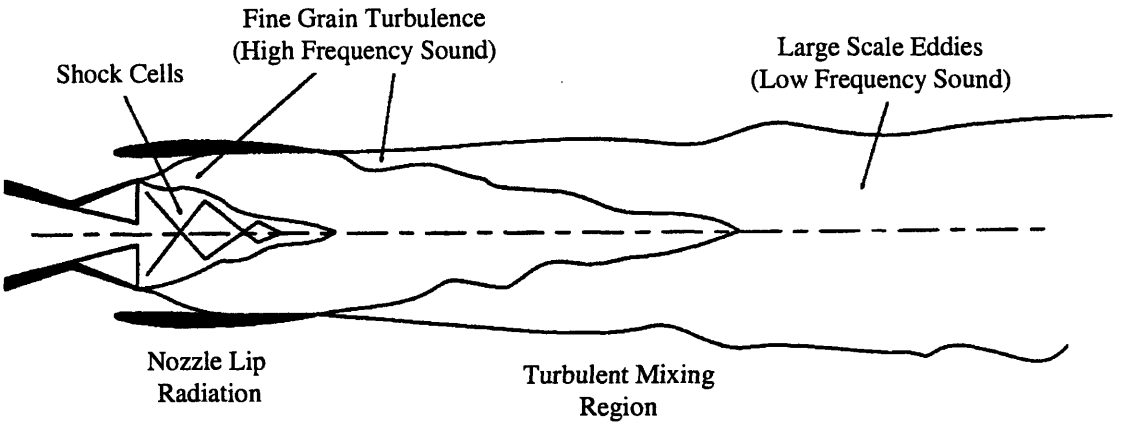

Figure 4-4: Mixer-ejector noise generation mechanisms and source locations, [22], [28]

The mixing noise will dominate at low frequencies and in the downstream direction. For mixer-ejectors this noise can be separated into two components based on the apparent source location of the noise:

1. **Internal Mixing Noise:** This component is associated with flow over the mixer lobes and tends to dominate at higher frequencies above $f = 500$ Hz full scale.
2. **External Mixing Noise:** The external noise is generated by larger scale turbulence resulting from the mixing between the jet and the free stream. It will dominate at lower frequencies of around $f = 50$ Hz to 500 Hz full scale.

Additionally, the HSCT nozzle may be imperfectly expanded at take-off, resulting in the shock associated noise sources and lip radiation as described in 4.1.2.3.

4.1.3 Effective Source Distribution

A useful non-dimensional parameter for relating the acoustics of varying nozzle scales is the Strouhal number:

$$St \equiv \frac{fD_e}{U_e} \qquad 4.2$$

For a constant jet velocity, the frequency is inversely proportional to the diameter of the nozzle. The frequency of mixing noise is a function of the turbulence scale and the convection speed. As a result, higher frequency sounds are generated by the fine grain turbulence near the nozzle exit, and lower

frequencies by the large-scale eddies that appear further downstream, [27]. In the cases of the mixer-ejector studies, there will be high frequency noise associated with the flow through the lobes and through the internal shock cells. These sources are contained within the mixing duct, and will have an apparent source location at the nozzle exit plane. However, the source of any given frequency will not be a discrete point, but rather a distribution over a finite volume of the jet, [22]. Figure 4-5 shows a typical source distribution for a subsonic jet.

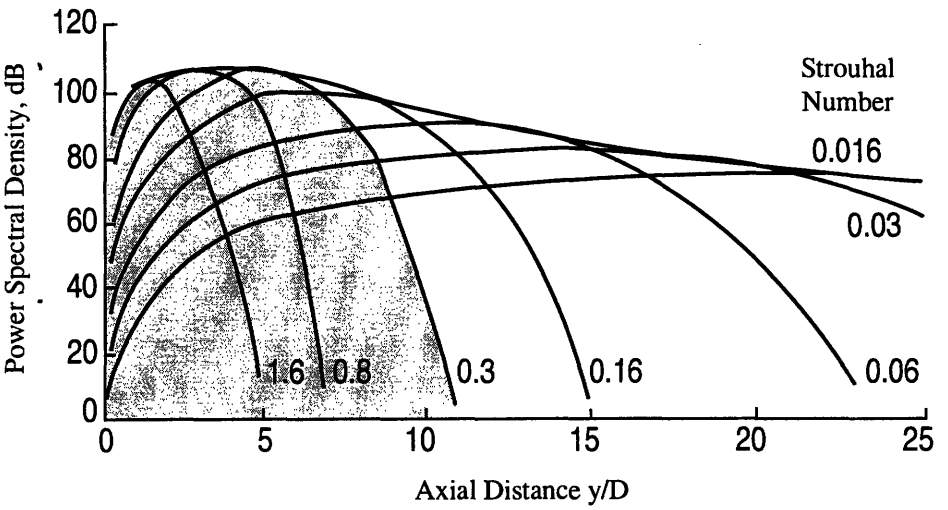

Figure 4-5: Jet noise source distributions at low Mach numbers for constant Strouhal number, [27]

To summarize Figure 4-5, it can be seen that the main contribution to the power spectral density for Strouhal numbers from 0.016 to 0.3 comes from the region y/D = 10 to 20, while for Strouhal numbers greater than 0.3 the region of greatest contribution stretches from y/D = 0 to 10. This later case corresponds to the shaded region in Figure 4-5. Although the low-frequency noise-generating region is spread over a very large region of the jet downstream of the potential core, its contribution to the total far-field noise power is relatively small, particularly when weighted for human noise response, [48]. The shaded portion of the figure also depicts the region critical to HSCT mixer-ejector noise signatures, roughly from the nozzle exit plane to 10 - 15 exit diameters downstream

4.2 Nozzle Starting and Jet Development Models

The duration of the constant reservoir conditions derived in Chapter 3 is not the actual amount of useful test time. A portion of this time will be required for the turbulent jet to reach quasi-steady state. For downstream mixing studies, the jet start-up time can be significant, with t_{start} being around 5 - 10

milliseconds. It is necessary to model this starting process in order to make a better estimate of the time available for making acoustic measurements. Figure 4-6 shows a schematic of the jet development and length scales that will be referred to into the next two sections.

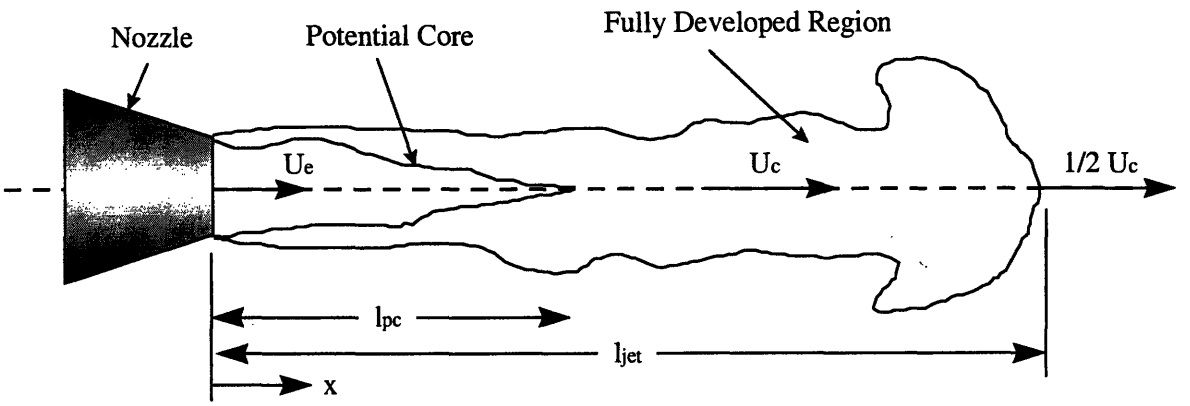

Figure 4-6: Schematic of jet starting and development with nomenclature, [22]

4.2.1 Jet Development Model

The jet development model can be found in Reference [22] and a summary of the details are presented here for completeness. The jet was assumed to develop at half the center line velocity, u_c, since this corresponds roughly to the convective speed of the structures responsible for generating the noise. In order to develop an expression for the jet development time, the jet was divided into two regions for this modeling calculation.

1. **Linear Growth Region:** A potential core in which $u_c = u_e$ and a linearly growing mixing region of lower velocity.
2. **Full-Developed Region:** Once the linearly growing mixing layer has reached the centerline, u_c, is assumed to decay with a 1/x dependence.

The centerline velocity in the fully-developed region of an axisymmetric, turbulent, free jet can be described by, [25]:

$$u_c = \frac{3K}{8\pi\varepsilon_o x} \qquad 4.3$$

where K, the kinematic momentum, is defined as:

$$K \equiv 2\pi\int_0^\infty u^2 r dr \qquad 4.4$$

Using conservation of momentum, K can be expressed in terms of the jet velocity:

$$K = K_e = u_e^2 \frac{\pi}{4} D_e^2 \tag{4.5}$$

The virtual kinematic viscosity, ε_o, is assumed to be constant over the entire jet and experimental correlation is approximately:

$$\varepsilon_o \approx 0.0161\sqrt{K} \tag{4.6}$$

Combining the above relations gives an expression for the centerline velocity as a function of downstream distance, x:

$$\frac{x}{D_e} \approx \frac{3u_e}{16\sqrt{\pi}(0.0161)u_c} \approx 6.57\frac{u_e}{u_c} \tag{4.7}$$

The beginning of the fully-developed region will be at the point $u_c = u_e$. This will also define the length of the potential core, l_{pc}:

$$\frac{l_{pc}}{D_e} = c \approx 6.57 \tag{4.8}$$

Having established the development speed of the jet in each region, the change in jet length is:

$$D_e d\left(\frac{x}{D_e}\right) = \frac{1}{2}u_c dt \tag{4.9}$$

Integrating each side gives:

$$\frac{t_{start}}{D_e} = \int_0^{l_{pc}/D_e} \frac{2}{U_c}\left(\frac{x}{D_e}\right) + \int_{l_{pc}/D_e}^{l_{jet}/D_e} \frac{2\left(\frac{x}{D_e}\right)}{cu_e} d\left(\frac{x}{D_e}\right) \tag{4.10}$$

The result is an expression for the jet starting time as a function of jet exit velocity, diameter, and the required jet length:

$$\frac{t_{start}u_e}{D_e} = 2\left(\frac{l_{pc}}{D_e}\right) + \left(\frac{D_e}{l_{pc}}\right)\left[\left(\frac{l_{jet}}{D_e}\right)^2 - \left(\frac{l_{pc}}{D_e}\right)^2\right] \tag{4.11}$$

Using the turbulent jet model, which is completely described in Reference [25], the time for the jet to develop to a length l_{jet} can be described in terms of the exit diameter, jet velocity, and potential core length.

$$\frac{t_{start}u_e}{D_e} = 2\left(\frac{l_{jet}}{D_e}\right) \qquad \frac{l_{jet}}{D_e} \le \frac{l_{pc}}{D_e} \qquad 4.12$$

$$\frac{t_{start}u_e}{D_e} = \left(\frac{l_{pc}}{D_e}\right)\left[\left(\frac{l_{jet}}{l_{pc}}\right)^2 + 1\right] \qquad \frac{l_{jet}}{D_e} \ge \frac{l_{pc}}{D_e} \qquad 4.13$$

Where the length of the potential core divided by the exit diameter, l_{pc}/D_e is approximately 6.57. For mixer-ejector studies a jet length of 7 to 15 exit diameters is sufficient to capture the pertinent noise sources. The results of these calculations are shown in Figure 4-7, as the nondimensional jet starting time as a function of the length of the jet normalized by the nozzle exit diameter.

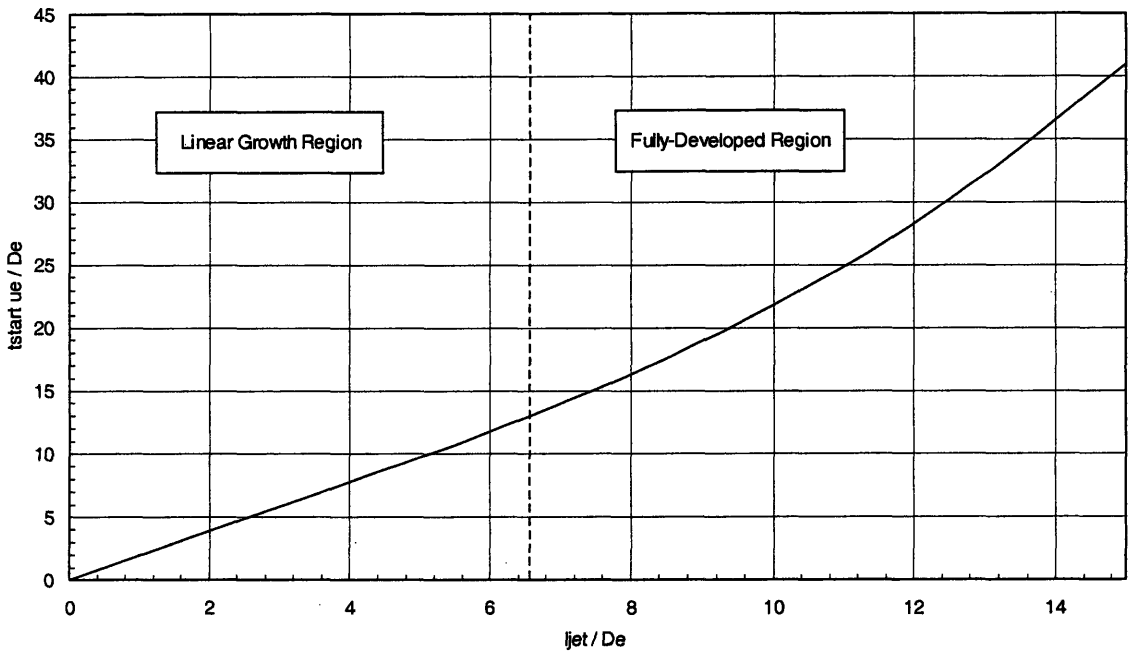

Figure 4-7: Non-dimensional jet starting time as a function of l_{jet}/D_e, [22]

4.2.2 Nozzle Starting Model

For mixer-ejector nozzles, the time for the nozzle to fully start can be a significant fraction of the total test time. In general, a nozzle can be considered started after about 3 flow through times. As a conservative

estimate, the average velocity in the primary nozzle was assumed to be the average of the primary and secondary nozzle flows.[3] The flow-though time scales for a sample mixer-ejector are summarized in Table 4.1, where the subscripts p and e refer to the primary and ejector portions of the nozzle, and l is the geometric length of the sections, shown in Figure 1-3.

Table 4.1: Approximate nozzle flow-through and start-up times for a typical mixer-ejector model[4]

NPR	l_p (cm)	l_e (cm)	t_p (ms)	t_e (ms)	t_{start} (ms)[5]
1.51	15.24	39.6	488	3740	12.7
2.48	15.24	39.6	360	3270	10.9
3.43	15.24	39.6	244	2802	9.1

The model predicts that the sample mixer-ejector will take approximately 13 milliseconds for the nozzle to be considered started at the 1.51 NPR condition. The results of these calculations can be added to those from the jet starting model, presented in Section 4.2.1, to give a conservative estimate of the total start-up time for the jet to be considered to be operating at quasi-steady state. These analytical predictions will be compared to experimentally realized test times for the ASME conic nozzles and the LSMS mixer-ejector nozzle in Section 4.5.

Another consideration when developing a starting time model for the acoustic jet is the start-up noise that will be introduced into the test chamber, [22]. A high amplitude acoustic impulse precedes the actual test, due to the unsteady mass addition associated with the starting of the test article. This noise is of a higher amplitude than the quasi-steady jet noise. As a result it is important to determine if reverberations of the noise from the acoustically treated walls of the chamber are strong enough and/or last long enough to influence the quasi-steady state acoustic measurements.

The pulse will contain a distribution of frequencies up to around f on the order of $1/\Delta t$, where Δt is the time for the mass flow to reach a quasi-steady state. At the initiation of each test, the shock wave will rupture the secondary diaphragm and propagate through the nozzle followed by the test gas. The time to induce flow in the nozzle, Δt, can be approximated as the time between the arrival of this shock wave and the test gas at the nozzle exit. For the $1/12^{th}$ scale LSMS model, Δt is on the order of 100 microseconds. This time is sufficiently small that the nozzle starting time completely dominates this effect. Since the steady-state pressure plateau, and hence the acoustic sampling period occurs significantly after this time,[6] it is assumed that reverberations introduced into the chamber, as a result of the introduction of the mass flow, can be neglected.

---

[3] The primary and secondary flows through the mixer-ejector are detailed in figures 1-3 and described in Section 1.1, with additional information in References [28], [51], [52].

[4] The geometry shown in Table 4.1 does not correspond to the geometry of the LSMS model.

[5] The nozzle was assumed to be started at $t_{start} = 3(t_p+t_e)$ where t_p is the residence time for the fluid in the primary nozzle and t_e for the ejector portion of the model.

[6] In subsequent sections it will be shown that this time can be on the order of 4 - 6 ms.

4.3 Required Acoustic Sampling Time

The short duration of the net test time, t_{net}, for the shock tube, makes it imperative to understand how much total test time will be required to produce results that are in good agreement with steady-state facility acoustic data. It will be shown that shock tubes are most useful for simulating jet noise in relatively high frequency bands since less time is required to accurately resolve the sound pressure level in the relatively broader (in terms of Hz) 1/3-Octave bands, [22].

To analytically predict the required test duration given a desired SPL confidence level, jet noise was statistically analyzed using the methods described by Hardin, [18]. The analysis illustrates the principal trade between resolution and measurement uncertainty. As the bandwidth of the measured noise spectrum is reduced, the uncertainty in the estimate of the sound amplitude in each band increases, [18], [36]. It was assumed that jet noise could be modeled as a chi-square random variable, S, with k degrees of freedom:

$$S = Y_1^2 + Y_2^2 + Y_3^2 + \ldots Y_k^2 = \sum_{i=1}^{k} Y_i^2 \qquad 4.14$$

where Y_i, i = 1,2,3...k, are independent, normally distributed random variables with zero mean and unity variance. The mean value of S is E(S), which is k, can be shown to be:

$$E(S) = \sum_{i=1}^{k} E\left(Y_i^2\right) = k \qquad 4.15$$

Similarly, the probability density function of the chi-square random variable is given by:

$$f_s(s;k) = \frac{1}{2^{k/2}\Gamma\left(\frac{k}{s}\right)} s^{k/2-1} e^{-s/2} \qquad 4.16$$

Using this relation, the variation of the chi-square variable around its mean can be investigated as a function of the number of degrees of freedom, k. Figure 4-8 shows this dependence for intervals about the mean containing 50% to 99% of the realizations. For example, 80% of the measured values of S/E(S) can be expected to fall between the lines marked 80.

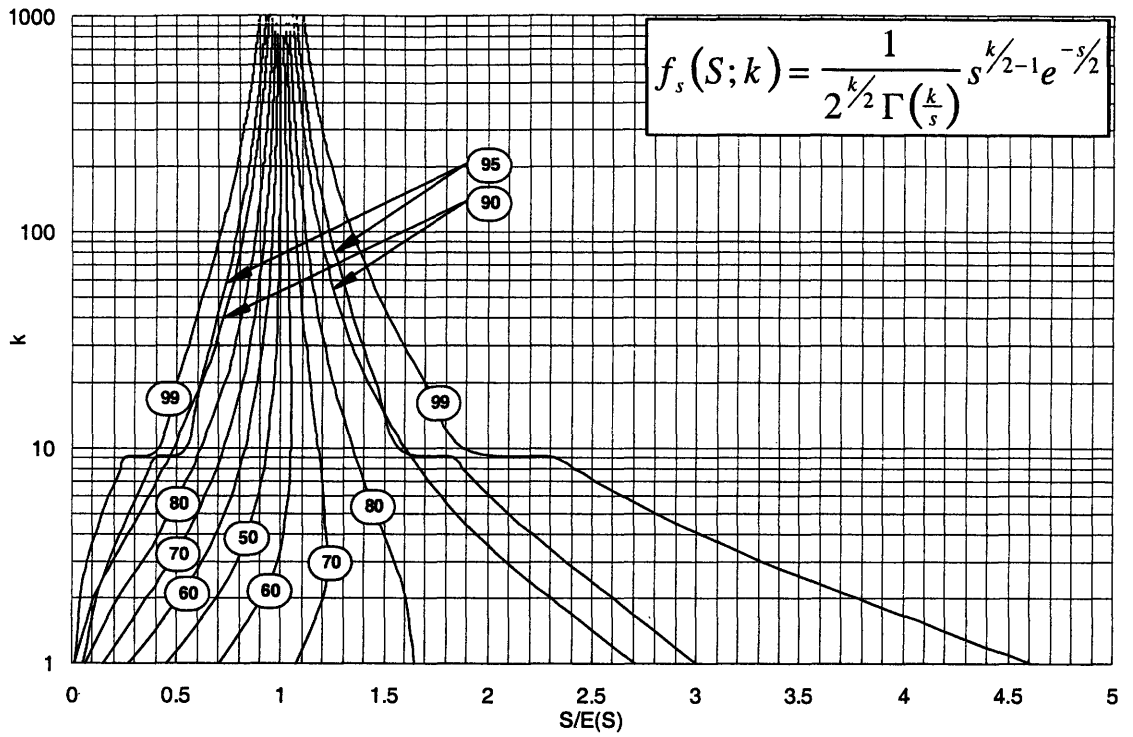

Figure 4-8: Variations of the chi-square variable about its mean, S/E(S), as a function of the number of degrees of freedom, k. Depicted are the boundaries for 99%, 95%, 90%, 80%, 70%, 60%, and 50% of the realizations

The number of degrees of freedom, k, the bandwidth, Δf, and the total test time, T, are related by:

$$k = 2T\Delta f \tag{4.17}$$

For example, if it is desired to resolve within 80% confidence the power spectrum levels to within ± 2 dB, with a bandwidth = 1 kHz, then k = 70, and 35 milliseconds of total test time is required. If 20 milliseconds of test time can be acquired for each shock tube shot, this then translated to two shock tube shots required to resolve the bandwidth frequency.

For jet noise experiments it is desirable to resolve the corresponding full-scale frequencies to 1/3-Octave bands since this bandwidth is the basis for the certification standard, [48]. Because each higher octave represents a doubling of frequency, the required bandwidth becomes larger with increased frequency, making higher frequency bands easier to resolve. The full-scale bandwidths, where f_c is the center frequency of the interval, can be written as:

$$\Delta f_{1/3} = \frac{2^{1/3} - 1}{2^{1/6}} f_c \tag{4.18}$$

As an example, consider resolving the corresponding full-scale frequencies starting at 1000 Hz into 1/3-Octave bands using a $1/12^{th}$ scale model. This corresponds to a bandwidth of $\Delta f_{1/12}$ = 2.8 kHz for the experiments. The higher the frequency of interest, the larger the bandwidth and correspondingly the fewer shock tube runs required. Table 4.2 presents a summary of these calculations along with the number of shock tube tests required.

Table 4.2: Summary of test matrix to determine whether multiple runs can be used to reduce the uncertainty associated with making transient acoustic measurements

80% Confidence Level				1/20th Scale			Required Full-Scale (ms/test)			Required 1/20th Scale (ms/test)		
± dB	k	Δf (Hz)	T (ms)	k	Δf (Hz)	T (ms)	10	15	20	10	15	20
1	300	200	750	300	928	162	75	50	38	17	11	9
1	300	500	300	300	2320	65	30	20	15	7	5	4
1	300	1000	150	300	4640	32	15	10	8	4	3	2
1	300	2000	75	300	9280	16	8	5	4	2	2	1
1	300	5000	30	300	23200	6	3	2	2	1	1	1
1	300	10000	15	300	46400	3	2	1	1	1	1	1
2	70	200	175	70	928	38	18	12	9	4	3	2
2	70	500	70	70	2320	15	7	5	4	2	1	1
2	70	1000	35	70	4640	8	4	3	2	1	1	1
2	70	5000	18	70	9280	4	2	2	1	1	1	1
2	70	10000	7	70	23200	2	1	1	1	1	1	1
90% Confidence Level				**1/20th Scale**			**Required Full-Scale (ms/test)**			**Required 1/20th Scale (ms/test)**		
± dB	k	Δf (Hz)	T (ms)	k	Δf (Hz)	T (ms)	10	15	20	10	15	20
1	500	200	1250	500	928	269	125	84	63	27	18	14
1	500	500	500	500	2320	108	50	34	25	11	8	6
1	500	1000	250	500	4640	54	25	17	13	6	4	3
1	500	2000	125	500	9280	27	13	9	7	3	2	2
1	500	5000	50	500	23200	11	5	4	3	2	1	1
1	500	10000	25	500	46400	5	3	2	2	1	1	1
2	120	200	300	120	928	65	30	20	15	7	5	4
2	120	500	120	120	2320	26	12	8	6	3	2	2
2	120	1000	60	120	4640	13	6	4	3	2	1	1
2	120	2000	30	120	9280	6	3	2	2	1	1	1
2	120	5000	12	120	23200	3	2	1	1	1	1	1
2	120	10000	6	120	46400	1	1	1	1	1	1	1

The table shows that as the required confidence level is decreased, the number of shock tube shots required to resolve the sound spectrum decreases. Furthermore, as the desired frequency band to be resolved increases, the number of required shock tube shots also decreases. For example, if it is desired to resolve the 5000 Hz band at 90% confidence using the 20^{th} scale ASME nozzle and more than 10

milliseconds of acoustic data can be captured per shot, only one shock tube shot would be required to resolve the acoustic signature to the desired confidence level.

Figure 4-9 provides the results of the statistical analysis, i.e. how the confidence bands are to be applied, for a series of 12 milliseconds test runs at 90% confidence for the 6.8 and 10.2 cm exit diameter nozzles ($1/15^{th}$ and $1/10^{th}$ scale) at full-scale dB vs. frequency. If multiple runs can be averaged together to increase the effective test time, convergence around the steady-state data within the boundaries shown in Figure 4-9, is expected. The convergence can be limited however, if systematic and run-to-run repeatability errors become significant.

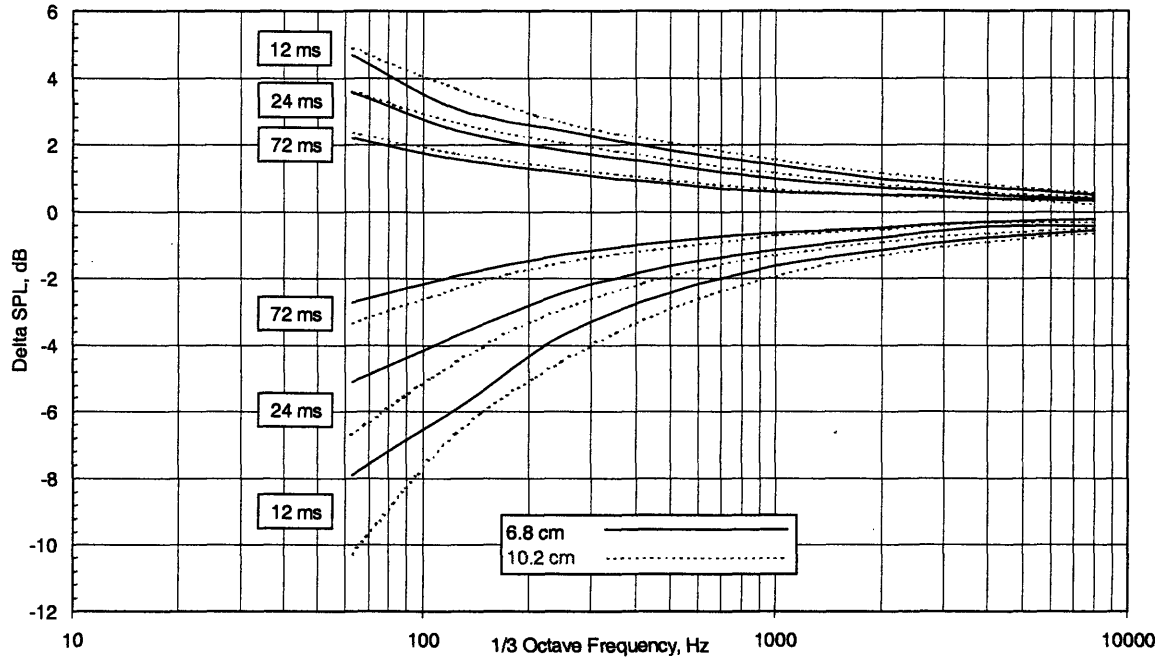

Figure 4-9: Δ dB resolution vs. frequency for 90% confidence for 6.8 and 10.2 cm nozzles

Figure 4-9 shows that in order to obtain measurements of full-scale frequencies greater than 2 kHz (30 kHz, 6.8 cm diameter), that are within ± 1 dB at 90% confidence, only one 12 millisecond test is needed. To resolve the spectra within ± 1 dB at 90% confidence for frequencies greater than 500Hz (7.5 kHz, 6.8 cm diameter), 72 milliseconds of total test time (6, 12 millisecond runs) is needed. More test time is needed, as nozzle exit diameter increases, to achieve the same level of confidence within a certain dB tolerance at a given full-scale frequency. The same confidence bands are also applied to the steady-state data in Section 5.2.2.2, for a comparison of the transient with steady-state noise data. After the confidence bands were applied to the 1/3-Octave steady-state data, the acoustic data was then re-processed through

DADS[7] to provide confidence bands on OASPL and PNL versus directivity angle plots, as well as bounding EPNL values.[8]

4.4 Nozzle Sizing Considerations

As a complimentary mode of investigation to steady-state combustion heated facilities, the shock tunnel facility can be used to test scaled-engine nozzles at elevated temperatures and highly uniform enthalpy conditions. However, the size of the test article is tightly constrained by the limited volume of test gas contained within the driven section and the acoustic measurement time requirements. If there is a high mass flow through the nozzle, the test gas (air) will be depleted rapidly, limiting the total available test time, [22]. In addition, the size of the test cell limits how far the microphones can be placed from the nozzle exit. If the nozzle diameter is large compared with the distance to the microphones, such that $R_{mic}/D_e < 30$, then the fluid jet will exhibit near-field acoustic behavior, making the noise measurements difficult to interpret and compare to steady-state far-field acoustic data.

The relevant acoustic range is a critical parameter for the sizing of the test nozzles. The frequency of the radiated noise varies inversely with the nozzle diameter as shown in equation 4.2. As a result, small-scale nozzles may produce frequencies that are beyond the range that can be measured using standard microphones.[9] As the scale of the nozzle is reduced, the sound pressure spectrum level maintains a similar shape but is offset to a higher frequency. Therefore, the frequency range of interest for the $1/20^{th}$ scale nozzle will be 20 times higher than that of the full scale version. The highest full-scale frequency of interest will dictate the smallest size of nozzle that can be investigated.

Another disadvantage of making the nozzles small, particularly in the case of mixer-ejector models, is that it is difficult to fabricate the lobe trailing edges such that the model is a scaled duplicate of the full-size prototype. Reynolds number matching is of importance between the two models, so the lobe trailing edges must replicate the full-size with regard to overall scaling. For structural robustness, the trailing edges of the lobes may have to be slightly thicker to ensure that the shock wave induced flow does not destroy or damage the SLA structure.[10] The scale of the nozzle is therefore a tradeoff between these constraints.

When the MIT facility was being designed, these trade-offs were taken into account to decide whether to build an 8 inch diameter vertical or a 12 inch diameter horizontal facility, [22]. The 12 inch

---

[7] The NASA Lewis Research Center Digital Acoustic Data System, DADS, was described in Section 2.3.
[8] A brief overview of the PNL and EPNL metrics are contained within this Chapter in Section 4.4.1.
[9] The B&K 4135 ¼ inch free-field microphones used in this experiment have an upper frequency limit of 100 kHz. Some special application microphones such as the B&K 4138 $1/8^{th}$ inch pressure-field and random incidence microphones have a resonance frequency as high as 160 kHz.

diameter facility was chosen because its primary advantage would lie in the fact that a single nozzle size could be used to investigate far-field behavior of both internal and external noise sources. The test cell geometry enables the microphones to be placed far enough from the exit plane to ensure that far-field behavior of the jet noise is captured, for frequencies above approximately f = 200 Hz model scale, for nozzles as large as 5 inches (12.7 cm) in diameter.

4.4.1 The Perceived Noise Scale

The facility was optimized to test mixer-ejectors at conditions comparable to HSCT applications. The nozzles must be sized so that the important frequency ranges relevant to noise abatement considerations are captured. The FAA regulates aircraft noise from 50 Hz - 11 kHz. However, due to the frequency weighting for the human auditory response, the 100 Hz - 5 kHz range is of primary importance for jet noise. Within this range the 1 - 4 kHz band is most heavily weighted and is considered critical for mixer-ejector performance. The development of metrics that can be used to quantify this response is discussed below.

Annoyance response curves characteristic of the human aural system were first constructed in the 1950's by conducting audiometric tests. These tests covered a range of discrete (single frequency) and broadband (multiple frequencies) spectral characteristics. These included the use of real aircraft sounds to provide a framework for the first perceived noise level scale (PNL), [48]. A typical response curve for the human auditory system is shown in Figure 4-10.

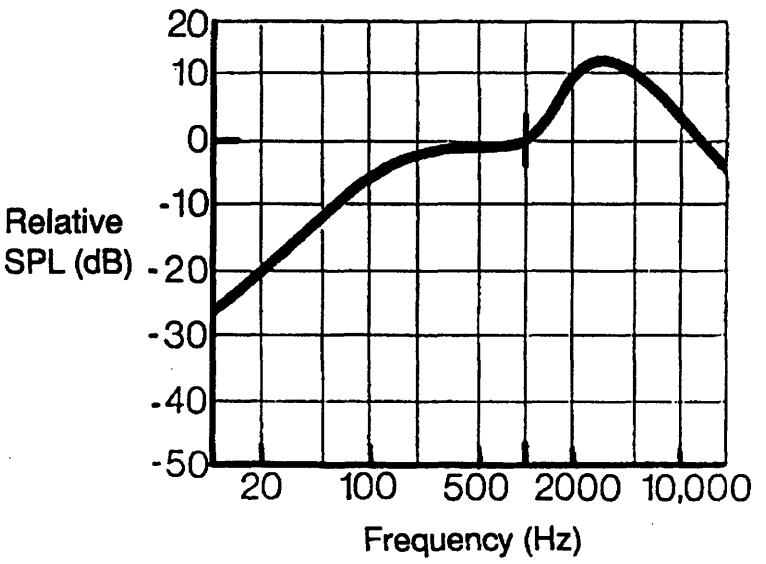

Figure 4-10: Human auditory response to sounds of constant intensity across the audible range, [48]

[10] Reference Section 7.3 for more details.

These first studies were not representative of a general cross section of the population since only young college students were used as the test subjects. It was found that on average, the students tended to have more acute hearing than the general populous. Upon subsequent reevaluation, making use of a more representative cross-section of the population, the high-frequency weighting was reduced to the level that now appears on the PNL noise scale.

Figure 4-11 shows how the average observed response of the test audience was expressed in terms of both level and frequency response. This response is identified numerically as the Noy Scale. The PNdB unit and its associated scale (PNL) make it possible to classify sound in terms of human response or annoyance. Because the human aural system is particularly sensitive to mid to high frequencies, the same physical overall sound pressure level (OASPL) can result in a variation of up to 20 PNdB as the frequency distribution is altered.

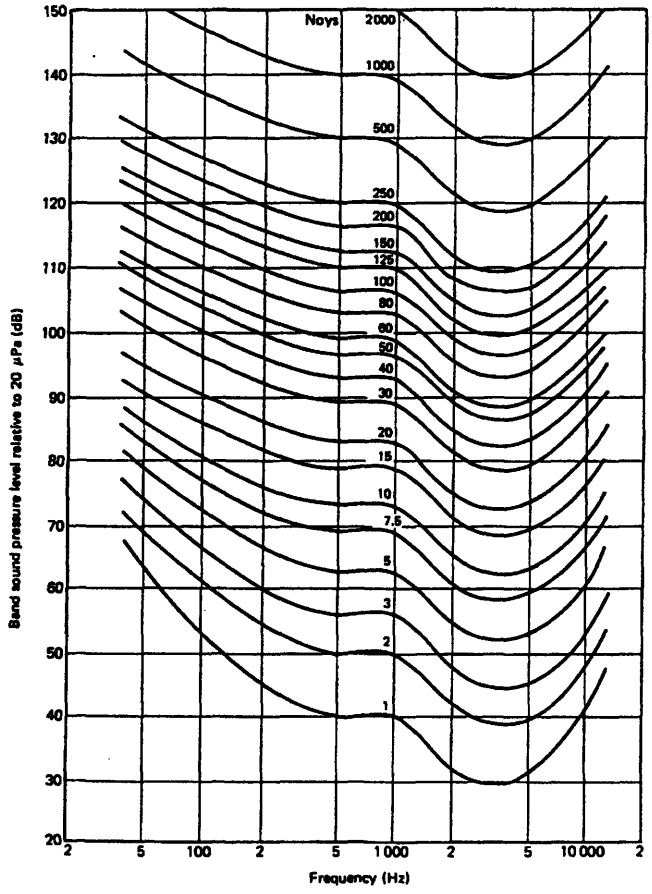

Figure 4-11: Contours of equal noisiness (Noy values), [48]

An integrated measure of the PNL is the Effective Perceived Noise Level, or EPNL, which is one of the metrics that will be used to compare the steady-state jet noise with the transient shock tube results. This

metric takes into account the human auditory response to the aircraft noise, and hence is one of the most common numbers used for the evaluation of aircraft noisiness.

4.5 Comparison of Analytical and Experimental Test Times

With the considerations of this chapter taken into account, a series of three ASME nozzles[11] were chosen at $1/20^{th}$, $1/15^{th}$, and $1/10^{th}$ scale to facilitate the assessment of facility performance and to examine internal nozzle-to-nozzle scaling consistency. The ASME nozzles were tested over a range of nozzle pressure and total temperature ratios relevant to the HSCT mixer-ejector development program, and a summary of the analytical estimates for achievable test times for the nozzle sizes, as well as the experimentally realized test times obtained in the facility, were presented in Section 3.3.4. Table 3.2 is repeated here as Table 4.3, so that these resultant ASME nozzle test times can be compared to the LSMS test time constraints. The test time limitation nomenclature described in Section 3.3.4. is shown in Table 4.4.

Table 4.3: Analytically predicted and experimentally realized test times for ASME nozzles (ms)

Scale	NPR	TTR	t_{wave}	t_{exg}	t_{nozzle}	t_{jet}	t_{net}	t_{act}
1/20	1.51	1.82	25.9	568.2	2.1	1.5	22.3	20
1/20	2.48	2.43	23.6	259.0	1.9	1.4	20.3	17
1/20	3.43	2.91	20.4	137.7	1.7	1.2	17.5	15
1/15	2.48	2.43	23.6	127.1	2.4	1.8	19.4	17
1/15	3.43	2.91	20.4	71.4	2.2	1.6	16.7	14
1/10	1.51	1.82	25.9	131.2	4.1	2.9	18.9	15
1/10	2.48	2.43	23.6	64.7	3.8	2.7	17.1	14
1/10	3.43	2.91	20.4	31.4	3.4	2.4	14.6	11

Table 4.4: Test time limitation nomenclature

Time constraint	Description of phenomena
t_{wave}	test time limitation due to the reflected expansion wave[12]
t_{exg}	test time limited by the exhaustion of the test gas[13]
t_{nozzle}	nozzle starting time conservatively assumed that the nozzle can be considered started after three flow through times
t_{jet}	jet starting time
t_{net}	$t_{wave} - (t_{nozzle} + t_{jet})$
t_{act}	experimentally realized test time based on pressure transducer measurement

[11] A complete description of these nozzles was presented in Section 2.1.2.

[12] Reference Section 3.3.1. for more details on wave limited test times.

[13] This is conservatively assumed that no more than 70% of the ideal test gas exhausted would actually be realized due to interface mixing (regions 2 and 3) and Richtmyer-Meshkov instabilities that will further mix the two gases.

To ensure that the LSMS nozzle was starting properly, a comparison between the steady-state pressure data within the ejector portion of the nozzle was compared to transient pressure data within the ejector at the same locations.[14] These comparisons are shown on a non-dimensional basis in Figures 4-12 and 4-13 for two conditions corresponding to a LOW and HIGH NPR condition, both at HIGH MAR values.[15] The plots show pressure at a given transducer location normalized by the ambient pressure versus non-dimensional axial location along the ejector duct.

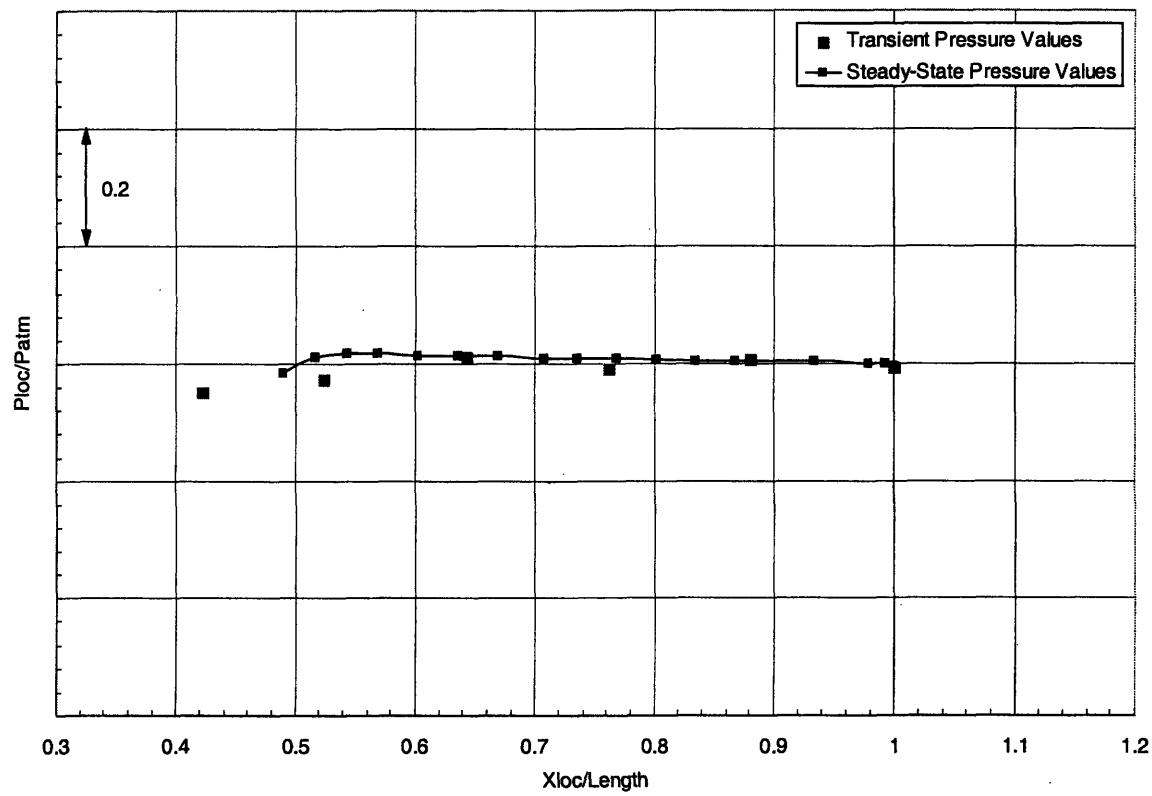

Figure 4-12: Pressure comparison between steady-state and transient within the ejector duct for LOW NPR and HIGH MAR condition

From this figure it can be seen that the transient and steady-state pressure tracers are in general agreement. Figure 4-13 shows the same type of plot as Figure 4-12, but at the HIGH NPR and MAR condition. The agreement of the steady-state and transient ejector duct pressures, to within about 0.1 P_{loc}/P_{atm}, suggests that the nozzle is started and the fluid mechanics occurring within the scaled-model are representative of the phenomena occurring during steady-state testing of the larger model.

[14] The location of the pressure transducers in the LSMS model tested at the transient facility are shown in Figure 2-7.

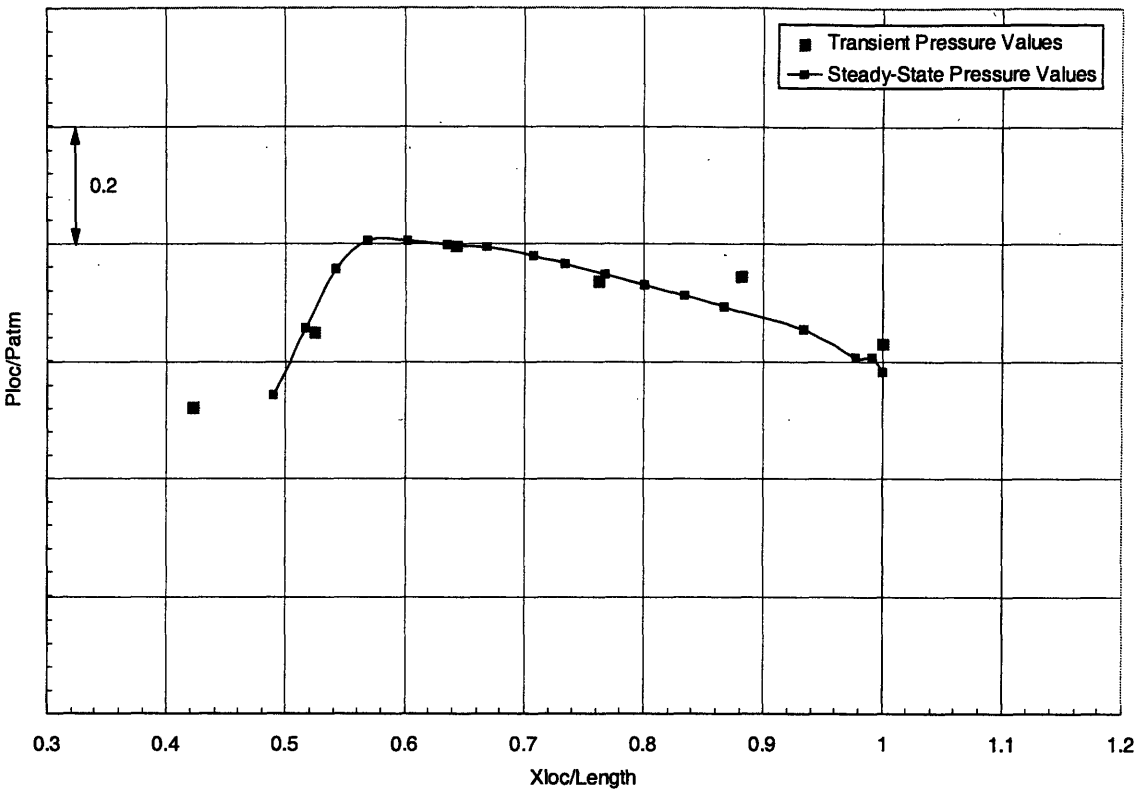

Figure 4-13: Pressure comparison between steady-state and transient within the ejector duct for HIGH NPR and HIGH MAR condition

To investigate the experimental nozzle starting time, figures 4-14 through 4-16 show the driven section and ejector pressure traces for low, mid and high condition shock tube shots using the LSMS model. The top pressure trace on each plot is taken from the second pressure transducer located 3 ft (91 cm) from the nozzle end of the driven section. Once again it is from this trace that NPR is determined, and similarly TTR is ascertained from measuring the shock speed using all four driven section pressure transducers, as was outlined in Section 2.2.3. The lower pressure signature on each plot is a trace from one of the transducers located approximately in the middle of the ejector portion of the LSMS model. As can be seen from the three plots of increasing nozzle pressure ratio, the static pressure decreases with increasing exit velocity. The data shown in these plots is classified as limited exclusive rights, therefore the values on the pressure axis are left off the plot. Nonetheless, the description of how the relevant portion of test time is determined is not sacrificed whatsoever by this restriction.

Each plot also shows what would be considered the quasi-steady state region based on the driven section pressure trace, which is identified by 'Test Time Based on Static Pressure Trace.' Furthermore, the

[15] The HIGH NPR and HIGH MAR conditions will be explained in Section 5.4. The purpose of presenting the pressure data in this section is to demonstrate nozzle starting.

plots also show the realized test time, which now takes into account the nozzle starting process, and is identified by the moniker, 'Test Time Based on Ejector Pressure Trace.'

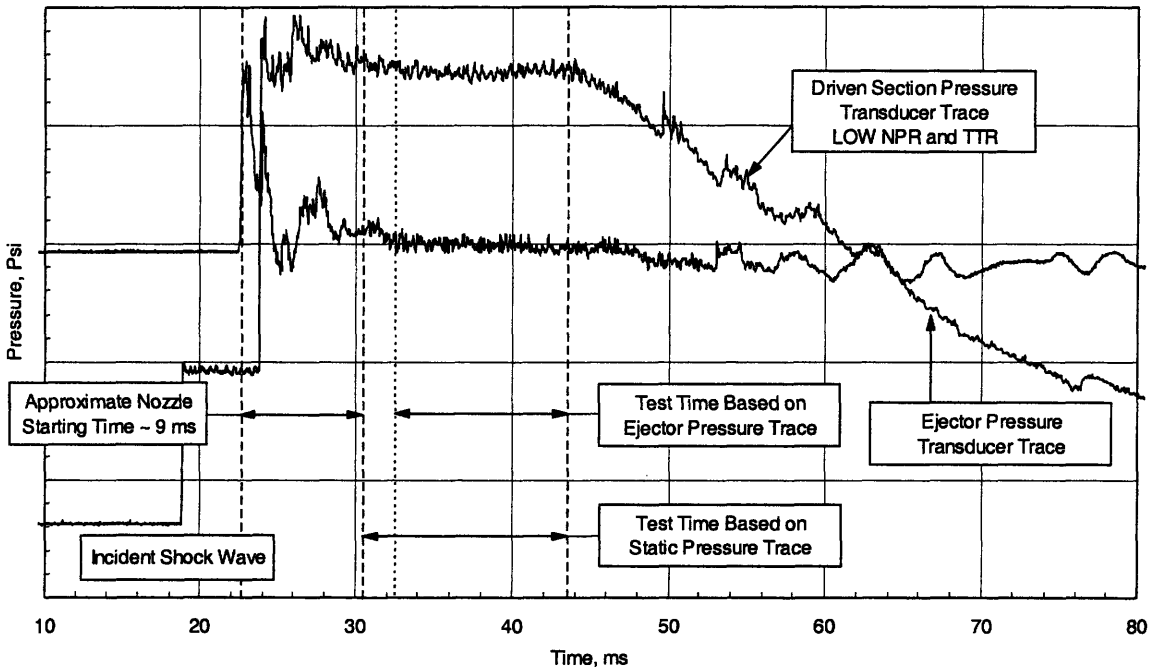

Figure 4-14: Driven section and ejector pressure traces for LSMS model: LOW NPR condition

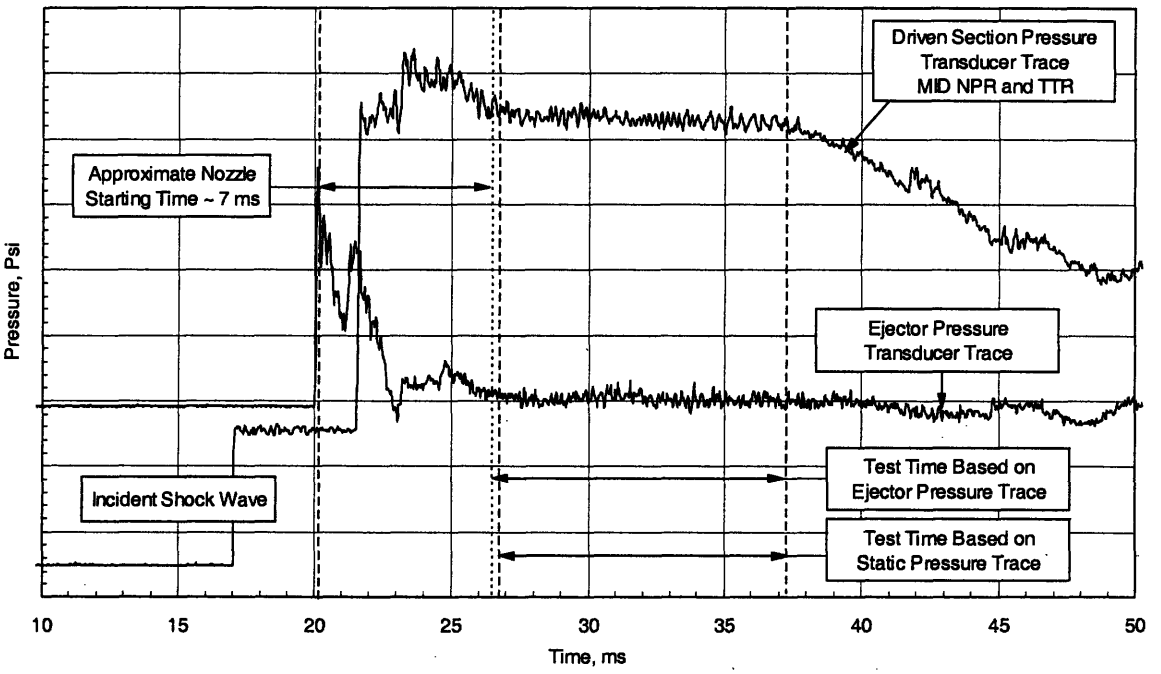

Figure 4-15: Driven section and ejector pressure traces for LSMS model: MID NPR condition

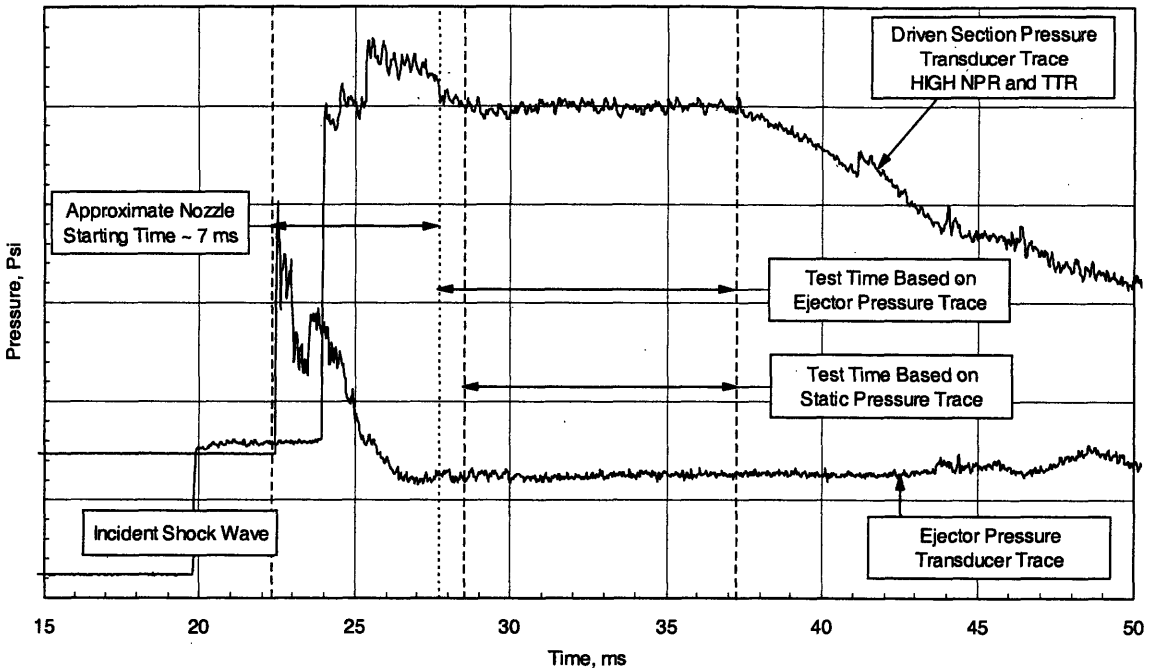

Figure 4-16: Driven section and ejector pressure traces for LSMS model: HIGH NPR condition

Several features are readily identifiable from plots 4-14 through 4-16, and the main points are:

- The nozzle starting process, which was identified as three flow-through times, begins approximately 3 - 4 milliseconds before the reflected shock wave reaches the same driven section pressure transducer. This is advantageous because flow is being introduced through the nozzle during the formation of the quasi-steady pressure plateau as the reflected shock travels through the driven gas. As a result of this earlier nozzle flow-through starting, the actual nozzle start up time, which overlaps into the quasi-steady pressure region, is *effectively* shorter than the predicted time by 3 - 4 milliseconds.[16]
- Nozzle starting time decreases with increasing nozzle pressure ratio.
- The low condition is most severely limited by the nozzle starting time, which curtails the duration of the quasi-steady pressure region on the order of 5 milliseconds.
- For the mid and high cases, the nozzle starting time poses no additional time constraints on the duration of the quasi-steady pressure region. The duration of the acoustic sampling time is completely

[16] The nozzle start-up time considered in the model presented in Section 4.2.2 were assumed to completely overlap the quasi-steady pressure region. In other words, the nozzle start-up time prediction was subtracted from the duration of the temporal length of the quasi steady-state pressure region, thus giving a worst case estimate.

governed by the formation of the steady pressure region within the driven section of the shock tube and is roughly on the order of an ASME nozzle of the same scale.

- Since the nozzle starting time is on average twice as long as the predicted jet development time, the duration and location of the acoustic sample period can be completely categorized by examining the two pressure traces shown as examples in Figures 4-14 through 4-16. It is assumed that jet development time commences after one flow-through time of the nozzle.
- Each driven section pressure trace shows a marked pressure overshoot and then a rapid decay to the quasi-steady pressure set condition. This feature was responsible for limiting the front end of the quasi-steady pressure region for the ASME nozzles, and also plays a significant role in limiting test time for the LSMS model. For most cases the nozzle starting and jet development times are shorter than this decay process. Details of this overshoot and decay phenomena are addressed in Reference [39].

The LSMS nozzle tested at the transient facility was selected to be a $1/12^{th}$ scale version of the full-size model. Table 4.5 presents a summary of the analytically predicted LSMS test times for the three jet conditions of interest. Actual test times, t_{act}, are displayed in the last column using the methods shown in Figures 4-14 through 4-16.

Table 4.5: Analytically predicted and experimentally realized test times for LSMS nozzle (ms)

Scale	NPR	Ue (m/s)	twave	texg	tnozzle	tjet	tnet	tact
1/12	LOW	462	25.9	64.7	8.9	4.9	12.1	~ 15
1/12	MID	523	23.6	42.2	7.6	4.7	11.3	~ 13
1/12	HIGH	587	21.1	37.7	6.8	4.5	10.8	~ 12

In general the experimental test time was found to be longer by approximately 2 - 3 milliseconds because of the initiation of flow through the nozzle while the reflected shock continued to heat the driven gas. The analytical prediction of the realized test time was somewhat conservative in that the nozzle starting time was subtracted from the beginning of the quasi-steady pressure region. Conversely, the model also did not take into account the overshoot of the pressure trace, and the subsequent decay to the set pressure of the test gas. Consequently, for the MID and HIGH jet conditions, the duration of the acoustic sampling period is governed by this decay, which is longer than both the jet development and nozzle starting time scales.

4.6 Chapter Summary

Chapters 3 and 4 of this thesis serve to provide physical background on the internal and external flows, respectively, that are pertinent to shock tube facility operation and jet noise generation. Whereas Chapter 3 was concerned with the flow and wave physics that takes place within the shock tube, Chapter 4 described the flow through the nozzle and the evolution of the supersonic jet that issues into the test chamber. A background of the mechanisms that are attributable to supersonic jet noise was presented, including a description of the three primary regions of a supersonic jet: the supersonic region, mixing region, and subsonic region.

Analytical models for nozzle starting and jet development time scales were derived. A discussion of how much total test time is required for a transient facility to produce results, within a given confidence level, that are analogous to steady-state noise data was also presented. With the additional test time considerations presented from the nozzle starting and jet development models, as well as the constraint of test time acquisition requirements taken into account, a nozzle sizing survey was presented with a rational justification for the nozzle scales selected to be tested in the MIT facility. It was shown that a $1/12^{th}$ scale LSMS nozzle would be of adequate size to capture all frequencies of interest to the HSCT mixer-ejector development program. Finally a comparison between the analytically predicted test times for both the ASME and LSMS nozzles versus experimentally measured test times was presented. It was shown that the analytical estimates were somewhat conservative over the experimental test times.

Chapter 5

Acoustic Results and Analysis of Transient Nozzle Flows

This chapter assesses the potential for using a transient testing technique to acquire jet noise from scaled-nozzles. Acoustic results obtained from transient shock tunnel tests on a series of ASME conic nozzles and a large-scale model similitude, LSMS, mixer-ejector nozzle, which might be typical of a HSCT application, are presented. The usefulness and quality of the transient noise data is evaluated by comparing with steady-state noise measurements obtained at Boeing LSAF, as was described in Section 2.6. The performance assessment is made by comparing SPL versus full-scale frequency, OASPL and PNL versus directivity angle, and EPNL values between the results of the two testing techniques. The chapter concludes with an establishment of the uncertainty bounds on sound pressure level measurements over the range of frequencies, nozzle pressure ratios, total temperature ratios, and nozzle scales for which the transient shock tunnel facility may be employed as a substitute and/or complementary mode of investigation to steady-flow heated facilities.

5.1 Small-Scale Round Nozzle Acoustic Evaluation

The purpose of this section is to begin to formulate an answer to the thesis question, which can be restated as follows: Can a transient shock tunnel test facility be utilized to acquire acoustic measurements on scaled nozzles that are in agreement with steady-state results? The acoustic signatures from the $1/10^{th}$, $1/15^{th}$, and $1/20^{th}$ scale ASME and $1/12^{th}$ scale LSMS mixer-ejector nozzles will be compared to results obtained from a steady-state facility for the definitive answer. However, before carrying out this comparison, it was advantageous to perform "in-house" tests, both transient *and* steady-state, at the MIT shock tunnel facility. Such experiments were beneficial in order to learn about the noise features associated with a supersonic round jet, to ensure that the facility and instrumentation exhibited repeatable acoustic results on a test-to-test and day-to-day basis, to examine which features of circular jet noise were captured using transient testing, and finally to determine how well those features compared to steady-state noise data taken at similar jet conditions.

5.1.1 Steady-State Tests Using a Round Nozzle

The flushing air system that is used to rid the tunnel of residual helium after each test, as described in section 3.2.3, provides a means by which to run steady-state cold flow tests on appropriately sized nozzles. A series of three small nozzles at ¼, ½, and ¾ inch exit diameter were designed and fabricated such that they could be attached to the end of the larger 2 inch exit diameter (1/20th scale) ASME nozzle.[1] By running the flushing air through the shock tube, a reservoir of high pressure air drives flow through the small nozzles at the sonic exit, choked flow condition. For a given nozzle exit diameter, the NPR can be monitored using the four Kulite pressure transducers located within the driven section of the shock tube. Since no heat transfer occurs in this process, the total temperature ratio for each of the steady-state tests is essentially unity. A sample of as-measured steady-state acoustic data obtained on the ¼ inch exit diameter nozzle, at constant microphone radius, R_{mic}, is shown in figure 5-1.

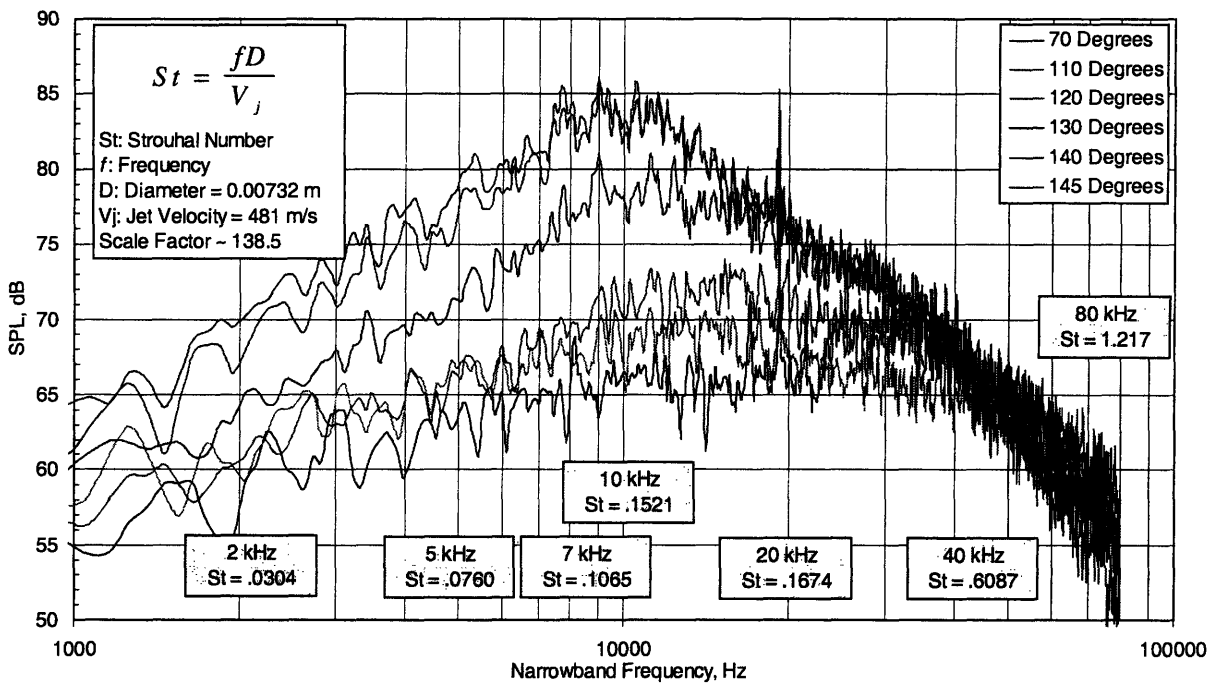

Figure 5-1: SPL versus model-scale frequency for ¼ inch exit diameter round nozzle operating at steady-state conditions, NPR = 2.5 and TTR = 1.0. As-measured acoustic data at constant microphone radius with Strouhal number shown at 2, 5, 7, 10, 20, 40, and 80 kHz

The figure provides a first check to ensure that the microphones are capable of acquiring important acoustic characteristics from round nozzle steady-state flows.

[1] The steady-state flushing air does not provide enough mass flow through the shock tube to generate a pressure plenum that would allow for supersonic steady-flow through even the smallest 1/20th scale ASME nozzle. Both the small round nozzles and the ASME conic nozzles were described in Section 2.1.2.

Several features are readily identifiable from the steady-state noise data shown in Figure 5-1.

- The peak noise for the round jet is concentrated around 130 - 145 degrees in directivity and is a maximum at Strouhal numbers of around 0.15 for round jet.
- The peak frequency is displaced to higher frequencies as the directivity angles become more forward.
- The acoustic signature of the aft directivity angles crosses over the forward directivity angles with increasing frequency.
- The spikes indicate that the microphones are picking up shock associated noise and tones. [2]

These features are typical of jet noise signatures described in References [6], [26], [27], [30], [42], [50], [56].

The small nozzles operating at steady-state conditions also served to verify test-to-test and day-to-day repeatability of the acoustic measurements. Additionally, the small nozzles were used to ensure that there was no variation in the acoustic signature with azimuthal angle, perhaps due to room acoustics or interference with the structural pillar shown in Figure 2-1. Test-to-test repeatability for the small nozzles operating at steady-state at the same nozzle pressure ratio was found to be better than ± 0.2 dB. On a day-to-day basis, the repeatability was on the order of ± 0.5 - 1.0 dB.[3] To ensure that the acoustic signature did not vary with azimuthal angle, three of the microphones were placed at different azimuthal angles circumferentially around the jet at a 140 degree directivity angle. Steady-state acoustic results indicated that circumferential variations of the jet noise were on the order of ± 1.0 dB on both a test-to-test and day-to-day basis. Deviations with azimuthal angle will be further discussed in Section 5.2.2.1.

5.1.2 Transient Tests on Small-Scale Nozzles and Comparison with Steady-State

After a series of steady-state measurements, as described in the preceding section, were acquired and the nozzle pressure ratio and total temperature ratio across the nozzle determined, transient shock tube tests using the same nozzles and similar operating conditions were performed. Given the NPR across the nozzle during steady-state operation, as well as the nozzle exit diameter,[4] the methods of Section 3.2 were used to determine the initial conditions across the diaphragm for the transient tests. Figure 5-2 shows two of the directivity angles, 63 and 143 degrees, for both the transient and steady-state tests, compared on an as-measured plot at constant radius.[5]

---

[2] The shock structure of the ¼ inch round jet is visible in Figure 4-2 of Chapter 4.

[3] Even a small change in relative humidity can be very significant to the high frequency radiation emitted from these small scale nozzles, see Section 2.3.1 for an example of the atmospheric attenuation effect. Therefore repeatability is always determined after the as-measured data is extrapolated to full-scale standard day conditions.

[4] The nozzle exit diameter is important based on the discussion in Section 3.2.2.2.

[5] The transient and steady-state tests were performed back-to-back, such that the ambient conditions

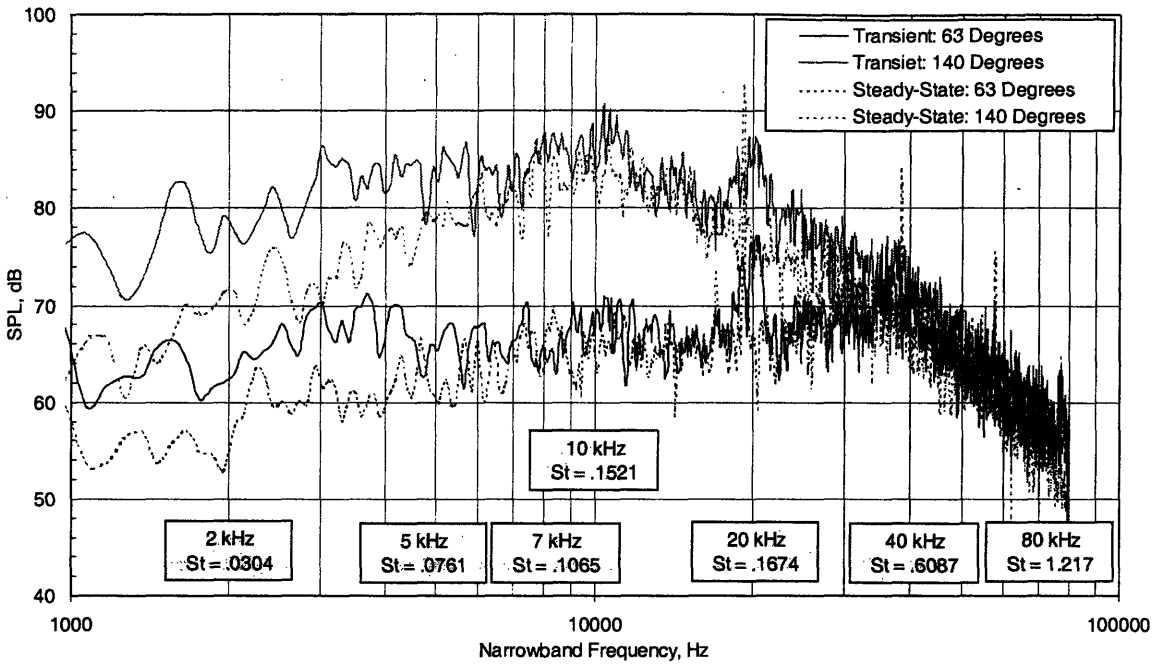

Figure 5-2: ¼ inch nozzle narrowband comparison of as-measured transient versus steady-state acoustic data. Both sets of data are acquired at the MIT facility at NPR = 2.5 and TTR ~ 1.0

The steady-state and the transient data exhibit agreement with frequency for f > 8 kHz, which corresponds to approximately 60 Hz full-scale for the ¼ inch nozzle. For frequencies below around 8 kHz, the steady-state data exhibits the same pattern shown in Figure 1, and the transient data deviates from the steady-state due to insufficient test duration. The figure shows 20 milliseconds of data for a nozzle which is approximately 1/138th scale. Using the methods that were described in Section 4.3., it can be shown that 20 milliseconds is insufficient to resolve the lower frequencies shown in Figure 5-2. Concentrating on the region above 8 kHz, the steady-state and transient data exhibit agreement to within ± 1-2 dB. Figure 5-2 also shows the corresponding Strouhal numbers at several frequencies.

Figure 5-3 shows two additional directivity angles from the same steady-state and transient tests. The comparison is shown on 1/3-Octave bands, with the corresponding Strouhal numbers. This plot compares the aft 110 and 145 degree angles, and once again the agreement between steady-state and transient data is on the order of ± 1-2 dB over the frequency range shown.

Figures 5-2 and 5-3 only showed 2 directivity angles each for clarity, however, it should be noted that all six directivity angles exhibited the ± 1-2 dB agreement over the 8 - 80 kHz nozzle-scale frequency range.

---

within the test chamber, namely relative humidity and temperature, remained constant over the tests.

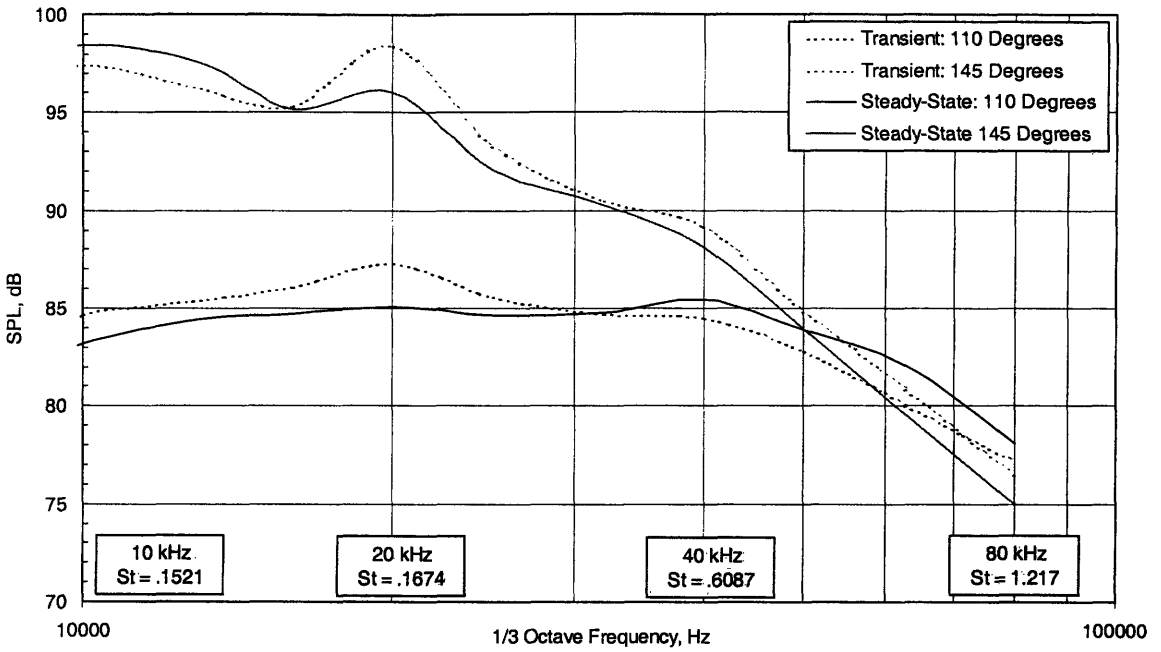

Figure 5-3: 1/3-Octave comparison of as-measured transient versus steady-state noise data. Both data sets were acquired at the MIT facility at NPR ~ 2.5 and TTR ~ 1.0

In general, all three of the small round nozzles exhibited agreement on the order shown in Figures 5-2 and 5-3, when compared on a transient versus steady-state per nozzle basis. With the tunnel flushing air system operating at a fixed volumetric flow rate, the NPR across the various sizes of nozzles could not be matched at steady-state conditions. However, transient shock tunnel shots could be compared on two different nozzle sizes under the same NPR and TTR conditions. The ¼ and ½ inch nozzles were tested under the same transient conditions at NPR = 2.3 and TTR = 1.4. The results of the comparison demonstrated agreement to within ± 2-3 dB on all directivity angles within a full-scale frequency range of 63 - 1250 Hz.[6] Furthermore, it was demonstrated that the frequency of the radiated noise from the nozzles, scaled with the primary length dimension, D_e. The peak frequency for the ½ inch nozzle, for a given directivity angle, was observed to occur at a Strouhal number twice as large as the ¼ inch nozzle, in accordance with equation 4.2.[7] Such in-house comparisons provided the first evidence that shock tube transient testing techniques could capture the same acoustic signature as steady-state testing. However, these nozzles were of relatively small scale; too small to make HSCT relevant acoustic measurements.[8]

[6] Variation of the steady-state TTR of 1.0 and transient TTR of 1.4 may also be responsible for some of the deviation between the two tests.

[7] Since both the ¼ and ½ inch nozzles are choked and TTR = 1, u_e is equal to the ambient speed of sound.

[8] Nozzle sizing considerations for the MIT facility were presented in Section 4.4.

After confirming agreement between noise data from transient and steady-state measurements of these small nozzles, several questions remained:

1. Can the facility be used to acquire transient acoustic measurements on ASME conic nozzles that are sized such as to produce frequencies of interest[9] to the HSCT development program?[10]
2. If so, can multiple runs be used to decrease the uncertainty associated with making transient acoustic measurements?
3. Can the facility be used to acquire transient acoustic measurements on nozzles with more complicated geometries, such as the LSMS mixer-ejector nozzle, that are of practical interest to HSCT applications?
4. Subsequently, can a less expensive plastic stereo-lithography chute rack survive the impulsively shock-induced flow and give acoustic results that are comparable to the cast aluminum chute rack, as well as to the steady-state noise data?

The remainder of this chapter is devoted to answering these questions.

5.2 ASME Conic Nozzle Acoustic Tests and Results

Sections 5.2 and 5.4 present the culmination of this thesis investigation, in that within these two sections the usefulness of the facility is ascertained through a comparison between transient and steady-state ASME and LSMS nozzle noise data over a range of operating conditions relevant to HSCT operation.

5.2.1 Summary of Steady-State ASME Nozzle Acoustic Data

This section presents a summary of the ASME steady-state acoustic data obtained at Boeing's LSAF facility, which was described in Section 3.4. The steady-state ASME acoustic data was measured at 11 directivity angles and 4 azimuthal angles simultaneously.[11] The steady-state data is not measured at constant radius, although all azimuthal angles are at the same distance from the source. Table 5.1 summarizes the directivity angles measured at the steady-state facility, with the angles matched at the MIT transient shock tunnel facility shown with a check mark.

---

[9] The small-scale nozzles described in Section 5.1 produces frequencies of interest to the HSCT program, however, such high model-scale frequencies are above those which can be captured using standard microphones, such as the B&K 4135 which has a frequency limit of 100 kHz.

[10] Frequency scaling is not the only reason to test larger scale nozzles. Reynolds number matching, particularly with the trailing edges of the LSMS chute racks, is essential, as well as manufacturing and robustness issues associated with the nozzles.

Table 5.1: Summary of steady-state microphone directivity angles

Microphone	Steady-state directivity angle	Transient
1	52.3°	
2	68.1°	✔
3	73.3°	
4	83.7°	
5	93.7°	
6	103.5°	✔
7	113.2°	✔
8	122.7°	
9	132.1°	✔
10	141.5°	✔
11	146.2°	✔

Figures 5-4 - 5-7 show full-scale extrapolated SPL versus frequency for directivity angles of 70, 90, 120 and 140 degrees at the LOW (NPR = 1.51, TTR = 1.82), MID (NPR = 2.48, TTR = 2.43) and HIGH (NPR = 3.43, TTR = 2.91) NPR and TTR jet conditions.

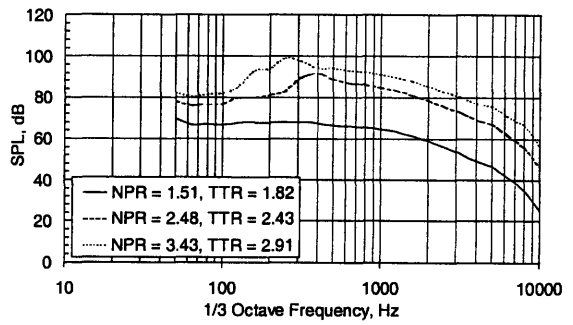

Figure 5-4: Steady-state ASME data: 70 degrees

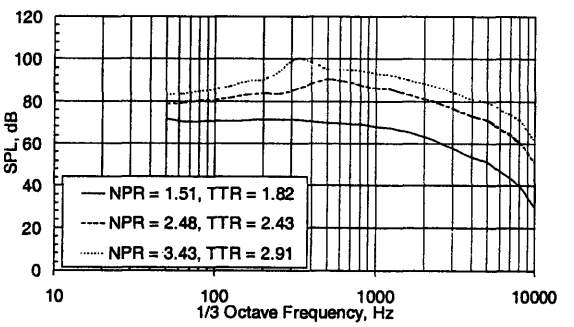

Figure 5-5: Steady-state ASME data: 90 degrees

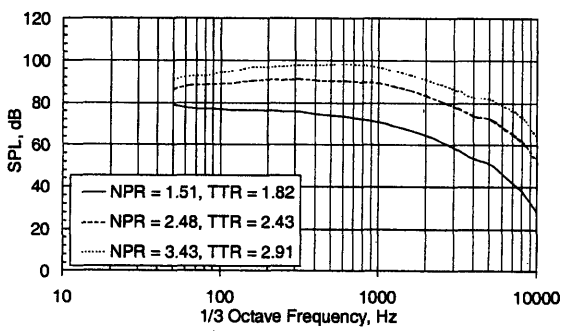

Figure 5-6: Steady-state ASME data: 120 degrees

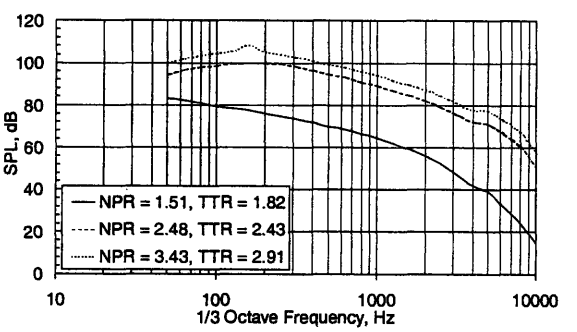

Figure 5-7: Steady-state ASME data: 140 degrees

The figures show the steady-state data at 1/3-Octave frequency bands from 50 to 10000 Hz.[12]

[11] Directivity and azimuthal angle definitions can be found in Figures 2-11, 2-19, and 2-30 of Chapter 2.
[12] This steady-state acoustic data, when used to compare to the transient data obtained from the MIT shock tube facility, will be processed over the same frequency bands as was discussed in Section 2.3.

From Figures 5-4 - 5-7, several features associated with the jet noise can be identified. The magnitude of the SPL values increase with increasing nozzle pressure ratio. Whereas the 120 degree directivity angle remains relatively constant in shape, the peaking of the noise signature at the other three directivity angles becomes more pronounced with increasing NPR. Also, as was observed in Figures 5-1 through 5-3, the spectra roll-off with increasing frequency.

Another way to examine this data is to investigate variations in the spectra with directivity angle. Figures 5-8 - 5-10, show the same data as plotted in Figures 5-4 - 5-7. Instead of holding the directivity angle constant, the jet NPR and TTR are held constant and the variation in directivity pattern for the 70, 90, 120 and 140 degree angles is exemplified. The three figures are plotted for the three NPR and TTR jet conditions, low, MID and high.

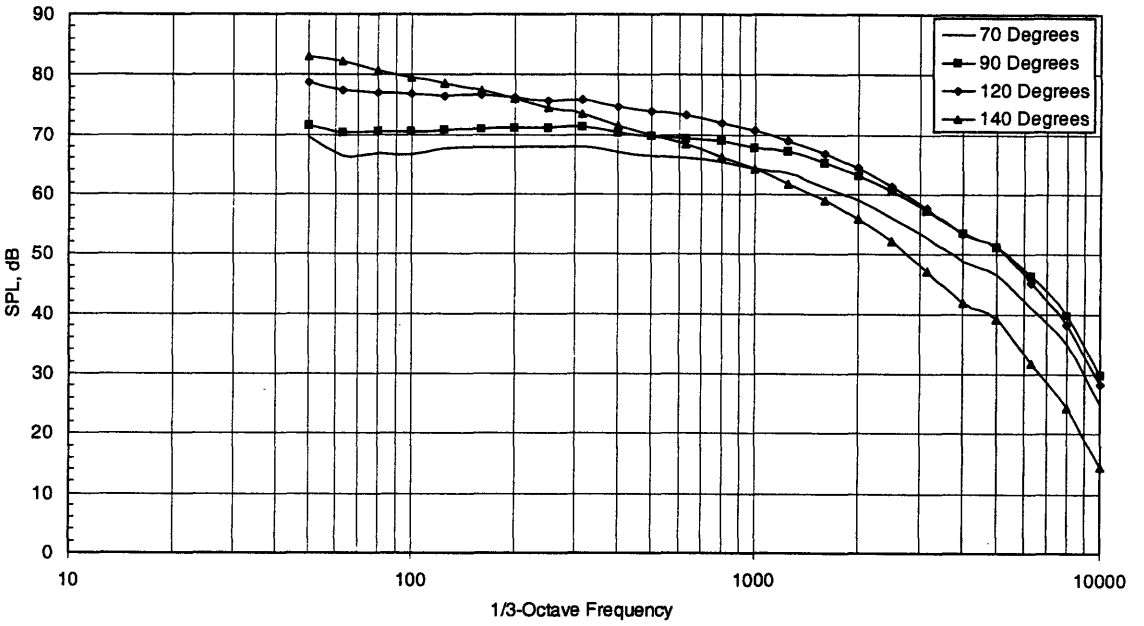

Figure 5-8: SPL versus 1/3-Octave Frequency for 70°, 90°, 120° and 140° angles, LOW condition

At the LOW condition, some of the features identified from Figure 5-1 can be observed, such as the roll-off with increasing frequency at each directivity angle, the cross-over of the more aft directivity angles with increasing frequency, and the peaking of the more aft directivity angles at lower frequency.

Figures 5-9 and 5-10 exhibit similar trends as those described in Figure 5-8. At these MID and HIGH conditions the peaking of the directivity angles is more pronounced. It should also be observed that the variation of the signature with directivity is most pronounced in the LOW frequency range, f = 50 - 3000 Hz.

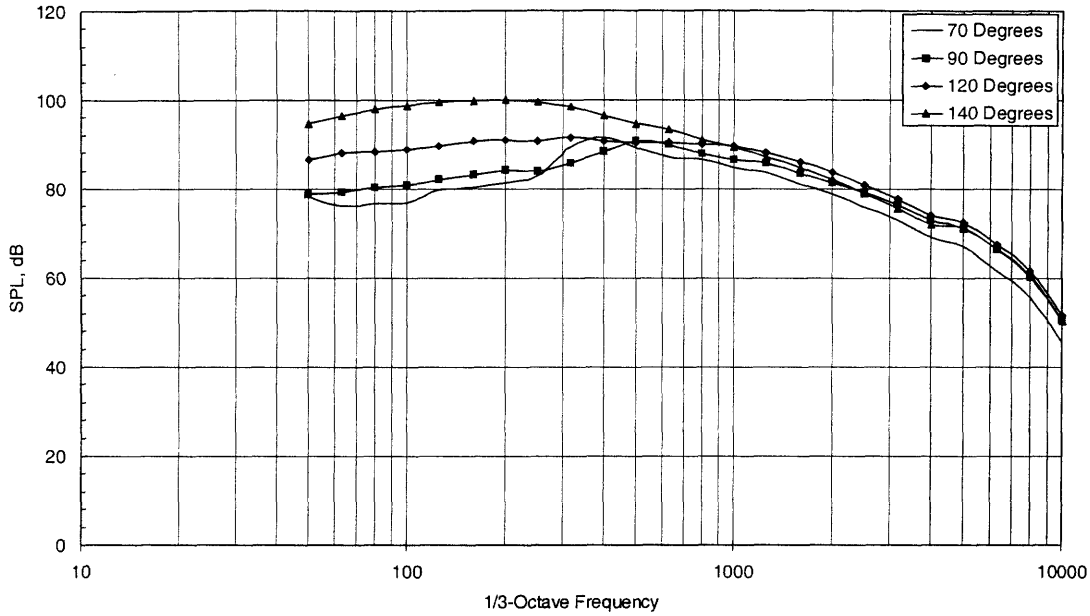

Figure 5-9: SPL versus 1/3-Octave Frequency for 70°, 90°, 120° and 140° angles, MID condition

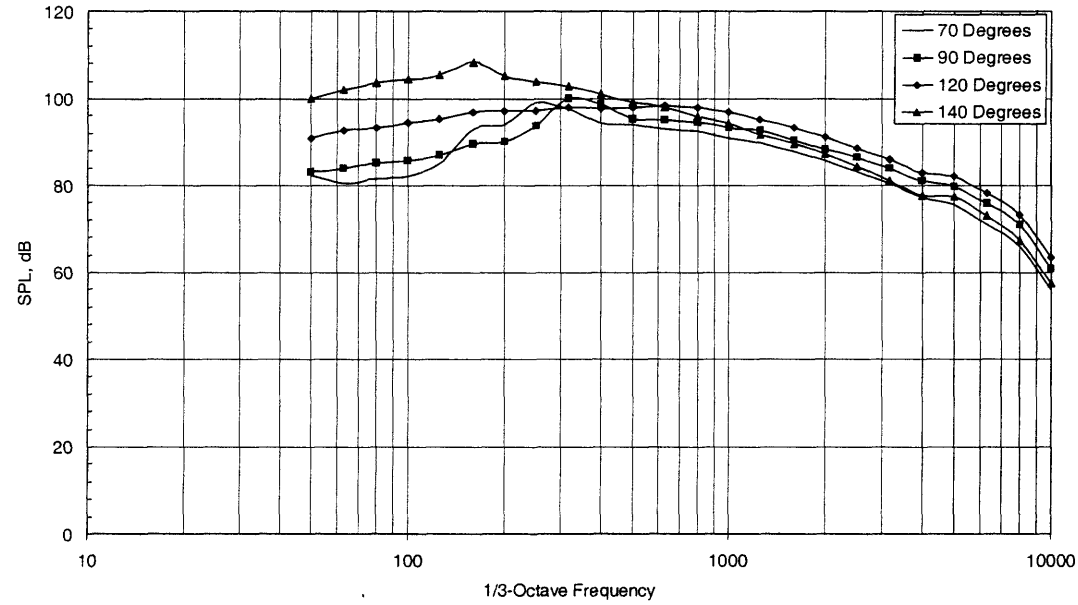

Figure 5-10: SPL versus 1/3-Octave Frequency for 70°, 90°, 120° and 140° angles, HIGH condition

Figure 5-11 shows OASPL and PNL versus directivity angle for the steady-state ASME data at the full-scale fly-over conditions.

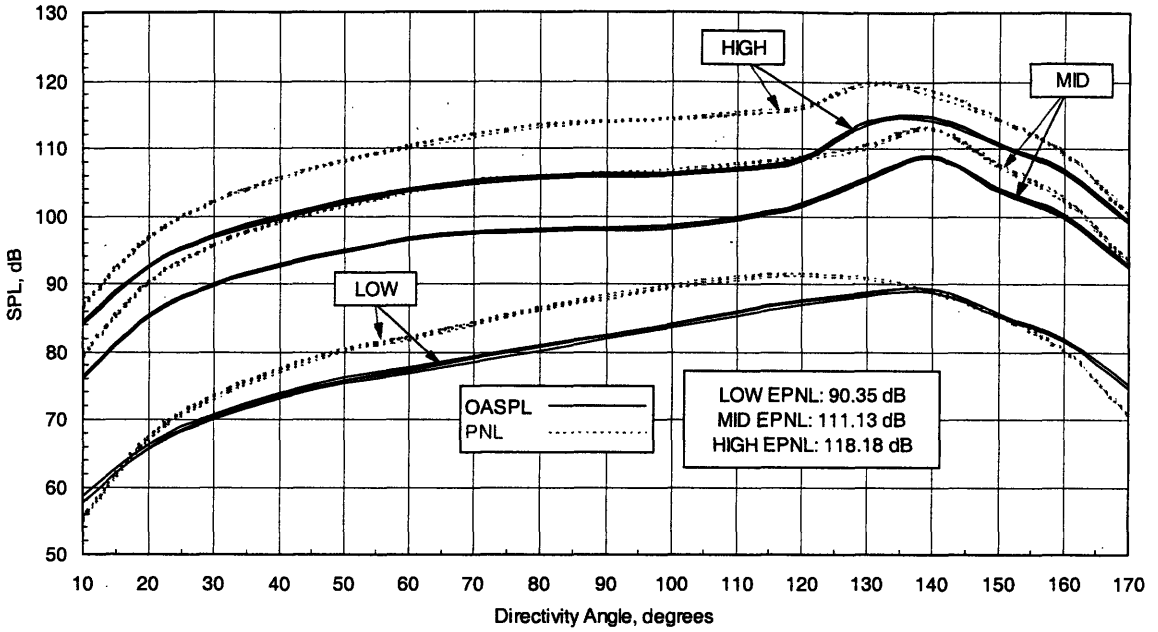

Figure 5-11: OASPL and PNL versus directivity angle for steady-state ASME nozzle data

The plot shows four lines plotted for each NPR and TTR combination, corresponding to the four azimuthal angles that were measured at the steady-state facility. The slight variations with azimuthal angle are discussed in the next sub-section.

As can be seen from Figure 5-11, the peak noise occurs at a directivity angle of around 120-140 degrees for the ASME conic nozzles.[13] The noise peak is also more pronounced and tends to sharpen with increasing NPR, and the signature exhibits a rapid drop-off at extreme forward and aft directivity angles. The location of this peak noise provides the motivation for clustering the microphones at the transient facility around the 110-145 degree directivity angles as summarized in Table 5.1. The figure also shows the Effective Perceived Noise Level, or EPNL, for each of the cases, which varies from 90.35 dB to 118.18 dB at the LOW and HIGH cases, respectively.

5.2.1.1 EPNL Summary and Variation with Azimuthal Angle

The steady-state ASME nozzle noise data was measured over four azimuthal angles, 20, 25, 45, and 90 degrees. A schematic describing the azimuthal angle configuration at LSAF is depicted in Figure 2-19 of Chapter 2. At the steady-state facility all azimuthal angle measurements are sampled simultaneously. Table 5.2 presents a summary of the Effective Perceived Noise Level, EPNL, values obtained from the steady-state tests.

[13] In Section 5.4.1 it will be shown that the peak noise for the LSMS mixer-ejector model occurs at directivity angles around 110-120 degrees.

Table 5.2: Summary of EPNL values for ASME nozzle tests and azimuthal angle variation

NPR	TTR	Azimuthal Angle	EPNL (dB)
1.52	1.81	20°	90.35
1.52	1.81	25°	90.41
1.52	1.81	45°	90.44
1.52	1.81	90°	90.02
2.48	2.43	20°	111.13
2.48	2.43	25°	111.24
2.48	2.43	45°	111.13
2.48	2.43	90°	110.79
3.43	2.91	20°	118.18
3.43	2.91	25°	118.23
3.43	2.91	45°	117.94
3.43	2.91	90°	117.94

Variations with azimuthal angle tend to be less than ± 0.5 dB on SPL versus frequency, and less than 0.5 EPNdB variation on EPNL for the steady-state noise data. Section 5.1.1 showed that steady-state nozzles operating within the MIT facility exhibited deviation with azimuthal angle on this order. The reason for the slight variation in directivity is not precisely known for either facility, although judging from Figure 5-11, the variations are exceedingly small compared to the variations between the three NPR and TTR combinations that will be investigated using the ASME conic nozzles. A possible explanation for the variation within the MIT facility is that the microphones may not have been located at precisely the same directivity angle or precisely the same distance from the nozzle exit plane.[14] Due to the high frequency noise emitted from these small nozzles, even small deviations in distance are consequential due to atmospheric attenuation and absorption.

5.2.2 ASME Nozzle Results

The purpose of the previous section was to make the reader conversant with some of the predominant acoustic features associated with conic jet noise data, and thus to provide a guide for what type of features to look for in the transient data. This section contains the results of the transient ASME nozzle tests and a comparison with the steady-state noise data.

5.2.2.1 Comparison Test Matrix for ASME Nozzles

A summary of the jet noise data acquired and used in the comparison between transient and steady-state is presented in Table 3. Three conditions, which are referred to as LOW (NPR = 1.51; TTR = 1.82), MID (NPR = 2.48; TTR = 2.43), and HIGH (NPR = 3.43; TTR = 2.91) for convenience, were acquired with three nozzle sizes in the transient investigation and with one nozzle size in the steady-state experiment. Table 5.3 also presents the nozzle pressure ratios and total temperature ratios achieved in the transient

[14] Furthermore, since the directivity angle chosen was 140 degrees for the azimuthal angle study, the noise signature is very sensitive to variations in directivity, near the noise peak, for the round jet.

tests and the corresponding multiple run total test time, with the steady-state target jet conditions shown in bold face. The NPR and TTR of the transient tests were typically within ± 1% of the steady-state values, which is within the data acquisition "drift" tolerances typically set by steady-state facilities, and the standard deviation of NPR within each run set (multiple runs at the same condition) was on the order of 0.05.

Table 5.3: Summary of acquired ASME conic nozzle data

		LOW			Mid			High		
Test Type	**D_e**	**NPR**	**TTR**	**Test Time**	**NPR**	**TTR**	**Test Time**	**NPR**	**TTR**	**Test Time**
Steady-State	14.2	**1.51**	**1.82**	1 sec/angle	**2.48**	**2.43**	1 sec/angle	**3.43**	**2.91**	1 sec/angle
Transient	10.2	1.51	1.81	80 ms	2.45	2.43	80 ms	3.45	2.96	50 ms
Transient	6.8	N/A	N/A	N/A	2.50	2.44	65 ms	3.51	2.93	50 ms
Transient	5.1	1.53	1.82	75 ms	2.57	2.45	60 ms	3.48	2.93	50 ms

Figure 5-12 shows a typical steady-state facility drift tolerance plot.

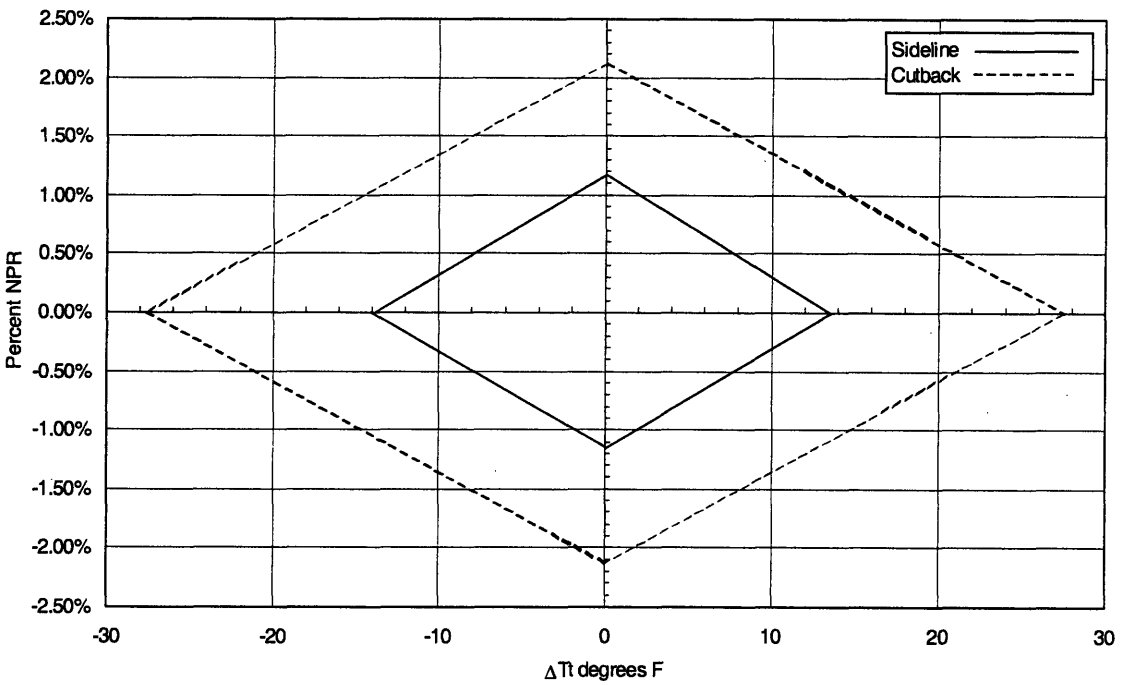

Figure 5-12: Steady-state data acquisition drift tolerance, [16]

To be within ± 0.2 dB on EPNL, the resultant NPR and TTR conditions should fall within the solid and dashed lines for sideline and cutback noise measurements, respectively.

A sample of 18 milliseconds of far-field acoustic data acquired from the 5.1 cm nozzle ($1/20^{th}$ scale) at the LOW condition is presented in Figure 5-13.

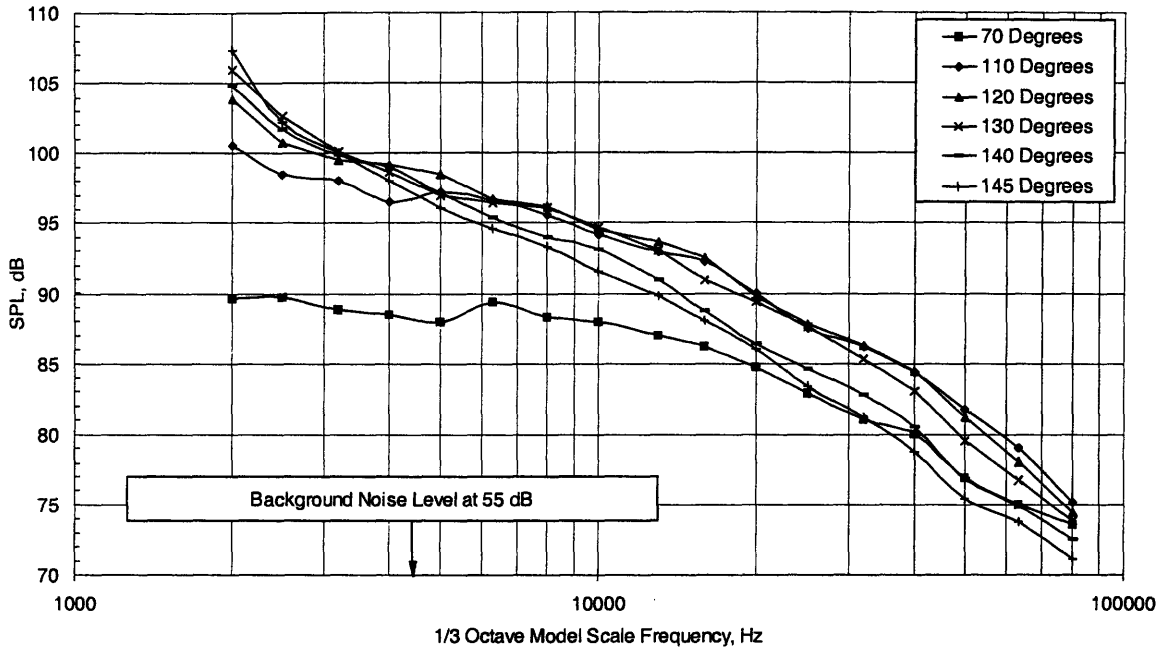

Figure 5-13: As-measured 1/3-Octave SPL versus frequency

The plot shows sound pressure level versus frequency for each of the six microphones, corresponding to directivity angles from 70 to 145 degrees, located on a constant radius arc, R_{mic}, 3.7 m from the nozzle exit plane. The data, which were acquired in narrow-band, can then be extrapolated to any nozzle size, distance from the observer, or ambient condition, as was discussed in Section 2.3. Figure 5-13 was plotted against 1/3-Octave frequencies for clarity. The plot shows several of the distinguishing characteristics typical of circular jet noise measured at constant radius, as were discussed in Sections 5.1.1 and 5.2.1. It can be seen that the aft directivity angles peak at a lower frequency and roll off faster in the high frequency regime. Also present is the distinctive cross-over of the extreme aft directivity angle over the more forward angles with increasing frequency.

Facility repeatability on a run-to-run and day-to-day basis for the ASME nozzles was ascertained by examining the full-scale extrapolated data. For each of the tests presented in Table 5.3, the run-to-run repeatability was found to be better than ± 0.5 dB. On a series of tests on the same nozzle and jet condition, the repeatability over the course of a six week period was on the order of ± 1 dB.

5.2.2.2 Use of Multiple Runs to Reduce Uncertainty of Acoustic Measurements

Acoustic data from a series of runs at the same jet conditions were statistically analyzed to determine if data from multiple shock tube shots can be used to reduce the uncertainty associated with the transient measurements. Analysis of multiple runs shows convergence within the analytical prediction described in

Section 4.3, with two to three shock tube shots typically required before convergence is achieved to within systematic run-to-run error limitations.

Figure 5-14 shows a comparison of the 120 degree directivity angle from the 1/20th scale ASME nozzle at the LOW condition with the 90% confidence intervals shown for 12 and 48 milliseconds of data. The figure shows SPL versus 1/3-Octave full-scale frequency.

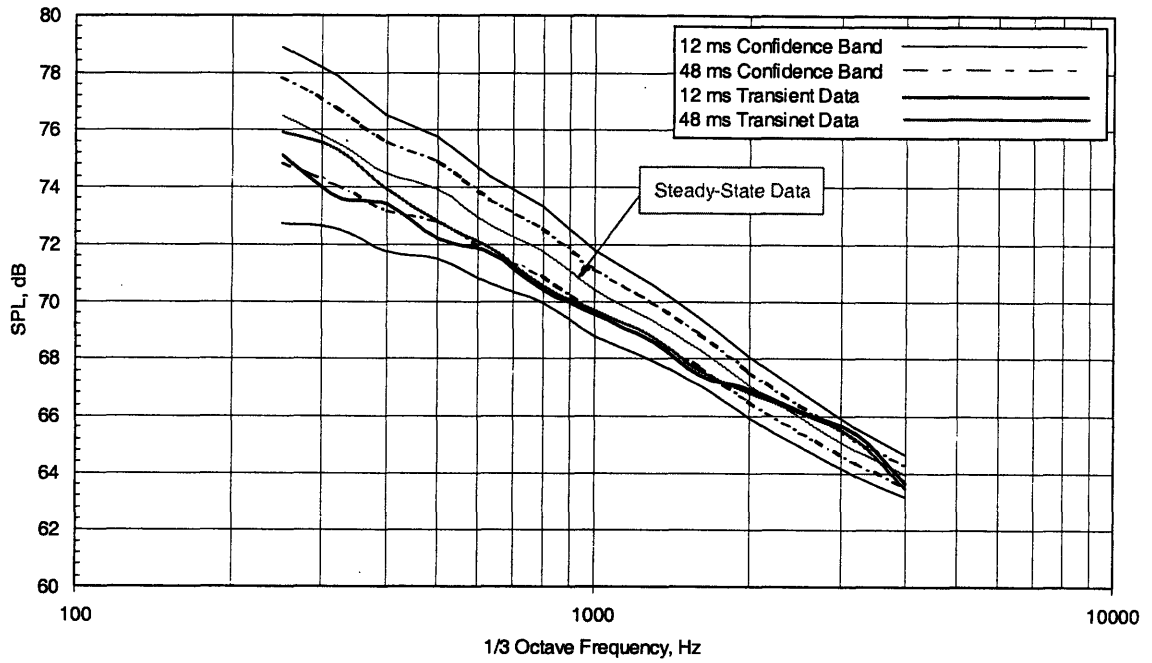

Figure 5-14: Use of multiple runs to decrease the uncertainty of acoustic data

Figure 5-14 shows how the confidence bands around the steady-state data become narrower as the duration of the transient tests increase. Furthermore, in accordance with Section 4.2, the confidence bands can be seen to get narrower for increasing frequency, since less time is required to resolve these frequencies.

Figure 5-14 is typical of each of the runs presented in Table 5.3, in that all angles and test conditions behaved in accordance with the analytically-predicted confidence levels to within systematic and run-to-run repeatability errors. Typically, very little improvement in convergence to steady-state noise data is seen in the high frequency range, with about 1 - 3 dB improvement seen in full-scale frequencies below 500 Hz.

Another way to examine the use of multiple runs to increase the apparent total test time, is to examine the same confidence bands shown in Figure 5-14, as applied to OASPL and PNL curves versus directivity angle. An example of applying these confidence bands for the same nozzle and test conditions, as shown in the previous figure, is presented in Figure 5-15.

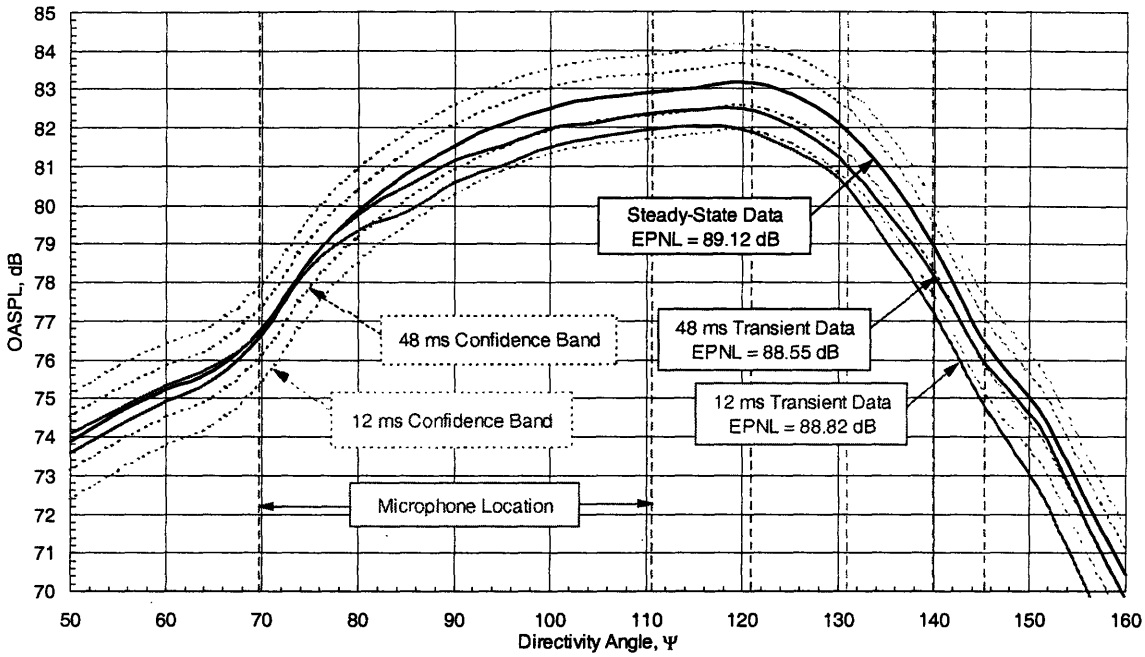

Figure 5-15: 1/20th scale ASME nozzle OASPL and PNL versus directivity angle at LOW condition: Use of multiple runs to decrease the uncertainty of acoustic data, 12 and 48 milliseconds of test time

The figure shows the improvement that can be expected with increasing test time, through the use of multiple runs. In this case, providing additional data beyond approximately 30 milliseconds showed no improvement in convergence to the steady-state values. Typically, it was found that averaging 2 - 3 shock tube shots provided the same acoustic results as averaging 6 - 8 shots. This is due to systematic and run-to-run repeatability errors are on the order of the expected improvement with 72 milliseconds over 60 milliseconds of data.[15]

5.2.2.3 1/20th Scale ASME Nozzle Comparison

Figure 5-16 shows a comparison of jet noise data from the 5.1 cm diameter nozzle (transient) and the 14.5 cm diameter nozzle (steady-state) at four directivity angles for the LOW condition, NPR = 1.51; TTR = 1.82. Once again both data sets were brought to a full-scale diameter of 101.6 cm, simulating the noise at

[15] The effect of how multiple runs were stacked back-to-back was also examined. In one case, the acoustic samples, corresponding to the quasi-steady pressure regions, were put together independent of the number of data points sampled. In a second study, the number of data points for each acoustic sampling length was correlated to the FFT size selected in DADS, such that the cycle of the FFT would correspond to the break point between back-to-back data sets, and thus eliminate any frequency contribution from the acoustic data combination method. The result of this study was that the second method provided no noticeable benefit, so multiple runs in subsequent figures are assembled independent of the data size.

496.5 m from an observer when the source is directly overhead. The transient data consists of three shock tube shots at the same condition, combined back-to-back, to give a total of 48 milliseconds of test time.

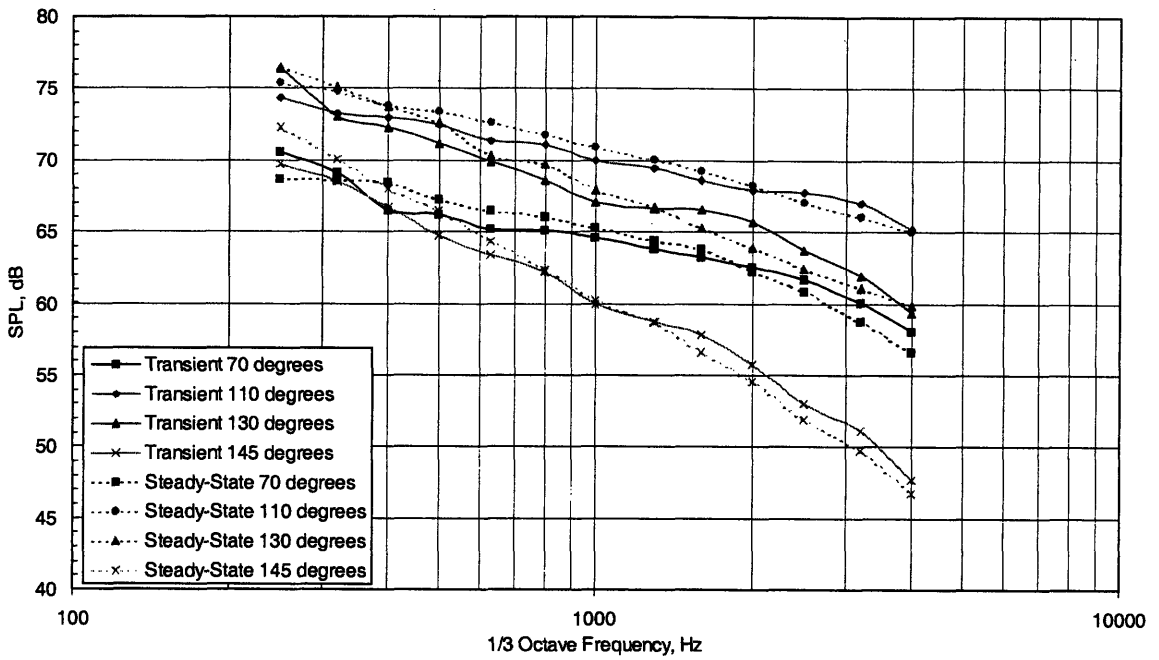

Figure 5-16: Extrapolated data comparison 5.1 cm ASME nozzle, NPR =1.51, TTR = 1.82

The four angles compared in the figure, one forward and three aft, are at 70, 110, 130 and 145 degrees, with a full-scale frequency range of comparison between 250-4000 Hz. The transient data exhibits agreement within 1 - 2 dB in magnitude over the entire frequency range. Directivity trends are also seen to be in agreement for all six angles. Note that the 120 and 140 degree angles have been omitted from this plot for clarity, however, these two angles also exhibit the same agreement with the steady-state noise data.

The corresponding static fly-over data for the $1/20^{th}$ scale ASME nozzle, showing both OASPL and PNL versus directivity angle, was presented in Figure 5-15. OASPL and PNL measurements from the transient data agree to within ± 1 dB in magnitude, show comparable behavior with directivity angle and peak noise at around 120 degrees.

Figure 5-17 shows a comparison of noise data from the 5.1 cm diameter nozzle (transient) and the 14.5 cm diameter nozzle (steady-state) at four directivity angles for the MID condition, NPR = 2.48; TTR = 2.43. The figure shows a general agreement with the steady-state data to within ± 3 - 4 dB on the 120 and 130 degree angles, and around ± 2 dB on the remaining directivity angles. The trends with directivity can be seen between the two sets of data, although the peaking on the 120 degree transient tests is not as defined as in the steady-state test.

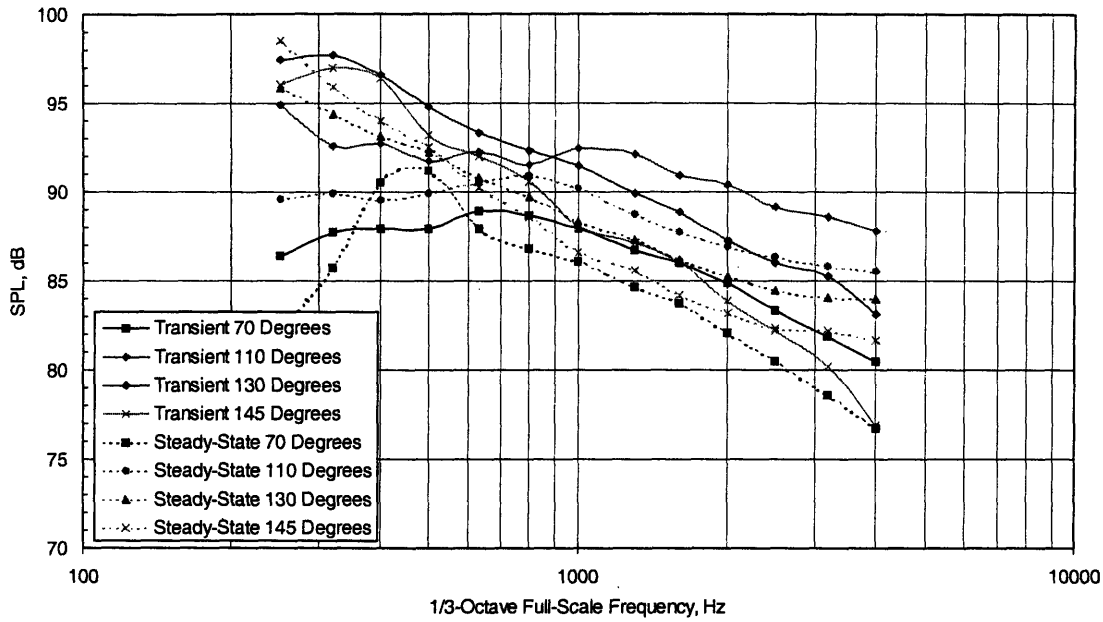

Figure 5-17: Extrapolated data comparison 5.1 cm ASME nozzle, NPR =2.48, TTR = 2.43

Figure 5-18 shows a comparison of noise data from the 5.1 cm diameter nozzle (transient) and the 14.5 cm diameter nozzle (steady-state) at four directivity angles for the HIGH condition, NPR = 3.43, TTR = 2.91.

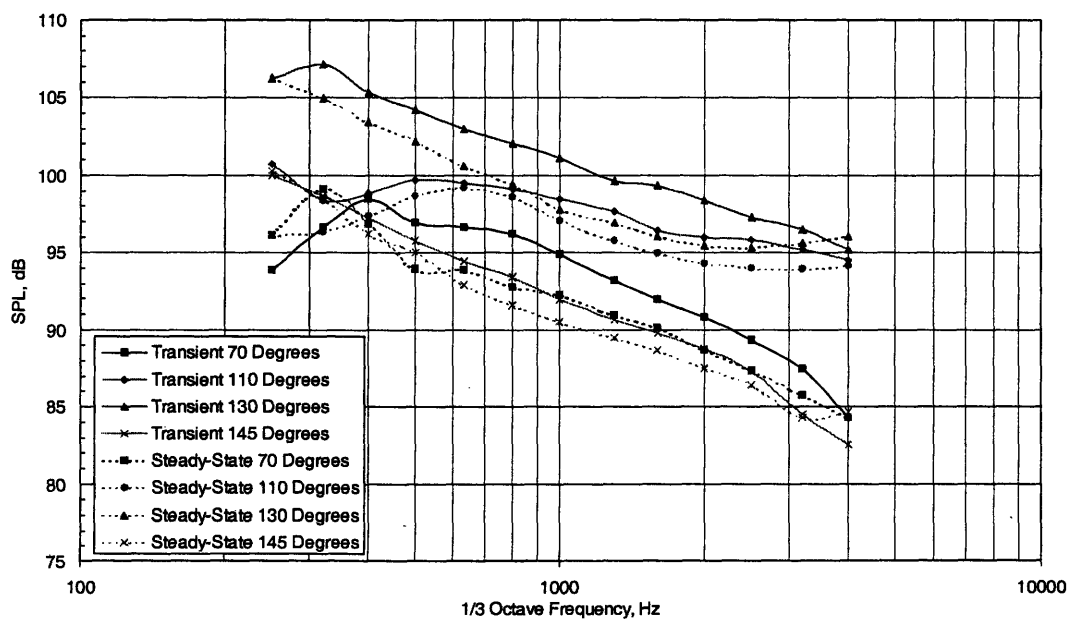

Figure 5-18: Extrapolated data comparison 5.1 cm ASME nozzle, NPR = 3.43, TTR = 2.91

This figure also shows an agreement in the directivity pattern and magnitude between the transient and steady-state data sets. All transient data angles agree to within ± 2 - 3 dB of the steady-state. In contrast to the MID case, the peaking of the 120 degree directivity angle is apparent in the transient data. Also visible is the distinctive cross-over of the most aft directivity angles across the more forward directivity angles.

The corresponding OASPL and PNL versus directivity angle plot for the 1/20th scale ASME nozzle at the HIGH condition is shown in Figure 5-19.

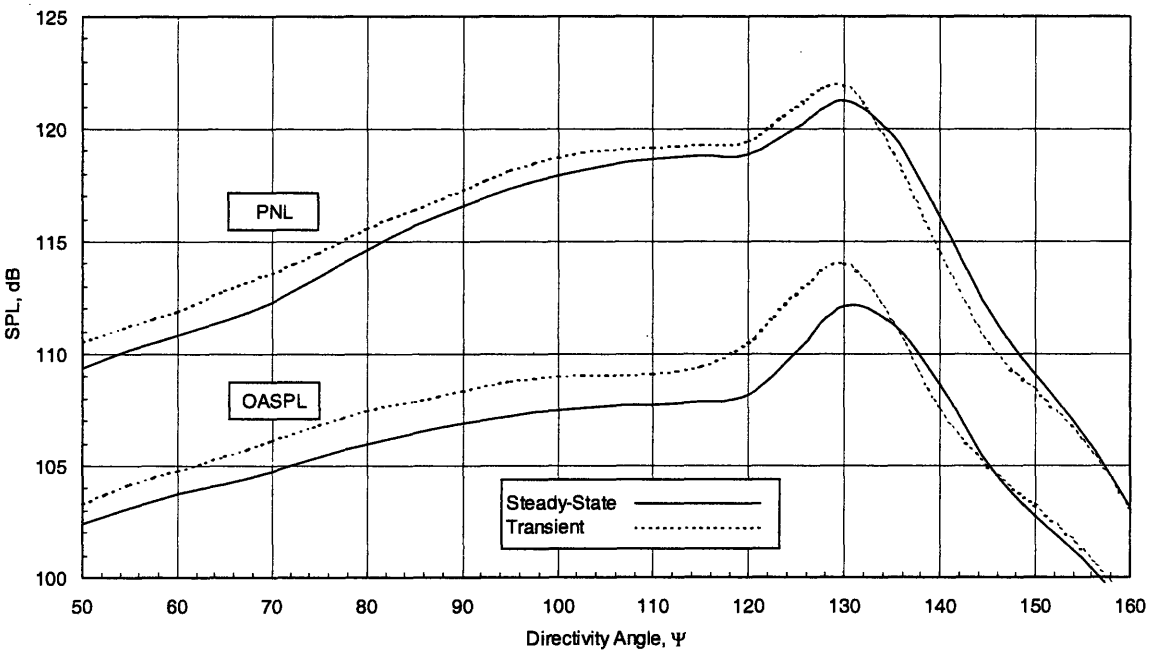

Figure 5-19: OASPL and PNL versus directivity angle comparison for 5.1 cm ASME nozzle

This figure shows that the transient tests duplicated the general trends of the steady-state data at the six microphone locations. Particularly visible is the peak noise at around 130 degrees. Comparing to Figure 5-15, which showed the LOW condition OASPL and PNL versus directivity angle plots, the displacement of the noise peak to more aft directivity angle is captured by the transient tests.

5.2.2.4 1/15th Scale ASME Nozzle Comparison

This section provides the same types of comparisons that were shown for the 1/20th scale nozzle in sub-section 5.2.2.3, but for a slightly larger 1/15th scale ASME nozzle. A comparison between the steady-state and transient data is provided in Figure 5-20 for the MID size nozzle at the MID condition. The figure shows a general agreement between the transient and the steady-state data to within ± 2 dB at 5 of 6 directivity angles, and ± 3 dB at the 110 degree angle.

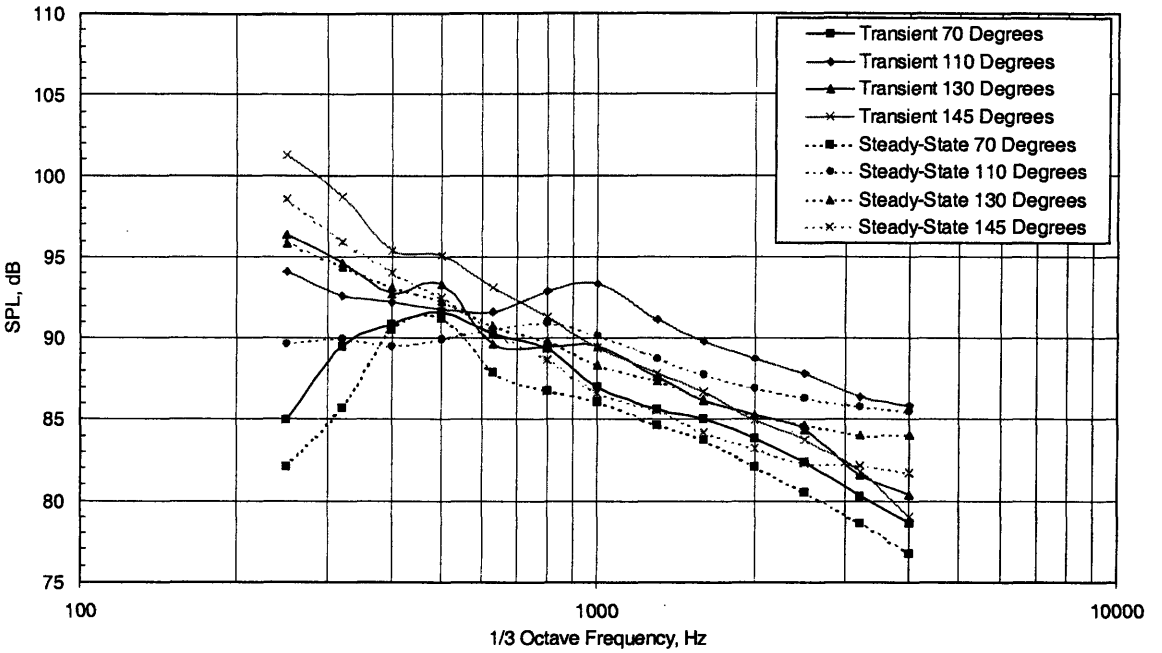

Figure 5-20: Extrapolated data comparison 6.8 cm ASME nozzle, NPR = 2.48, TTR = 2.43

Once again the cross-over of the aft angles can be seen across the more forward angles, and the peaking at the 70 degree angle in the transient data is clearly visible. The plot shows a total of 37 milliseconds of transient data acquired over three shock tube tests at the same NPR and TTR. This section only shows this single NPR and TTR case comparison for the 1/15th scale ASME nozzle. The LOW condition was not tested for the 1/15th scale nozzle, and the HIGH condition exhibited agreement with SPL versus frequency to within ± 2 - 3 dB on all directivity angles. The corresponding plots for OASPL and PNL versus directivity angle for the 1/15th scale ASME nozzle will be shown in Section 5.2.2.6. Also shown in Section 5.2.2.6 will be the 1/10th scale ASME nozzle OASPL and PNL results as compared to the 1/15th scale nozzle results.

5.2.2.5 1/10th Scale ASME Nozzle Comparison

This section provides the same type of comparison for the largest ASME nozzle, 1/10th scale (10.2 cm exit diameter), as was performed in the preceding two sections. A comparison between the steady-state and transient data is provided in Figure 5-21 for the largest nozzle size tested in the transient facility, 10.2 cm exit diameter. The figure shows a comparison of transient and steady-state SPL versus full-scale frequency at the LOW condition, NPR = 1.51 and TTR = 1.82. This figure shows that the transient agrees to the steady-state noise data to within ± 2 dB on 4 of the 6 directivity angles measured. The 110 and 120 degree angles experienced the most deviation of ±3 and ± 4 dB, respectively.

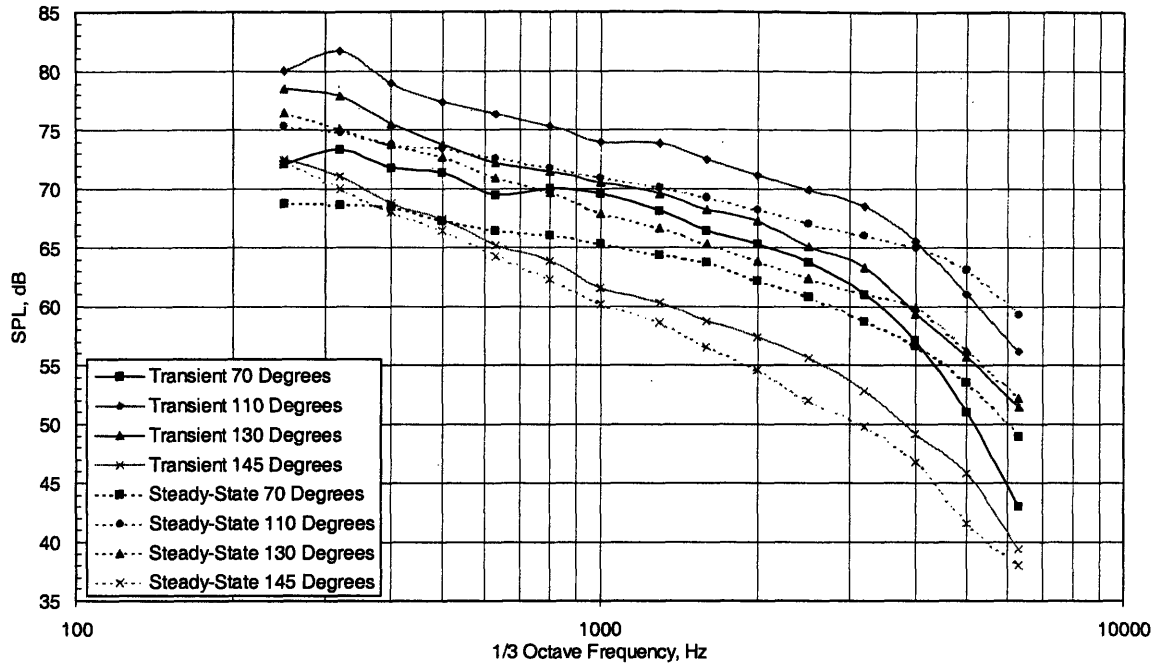

Figure 5-21: Extrapolated data comparison 10.2 cm ASME nozzle, NPR = 1.51, TTR = 1.82

The figure shows that the trends with magnitude and directivity are present for each of the angles. It is also interesting to note that the transient data is consistently higher than the steady-state noise data. If the transient data is shifted down 2 dB in magnitude, the two data sets would lie within ± 1 - 2 dB of each other over the frequency range shown in the figure.

Another interesting aspect to examine is the influence of which portion of the quasi-steady pressure region is used to select the acoustic sampling interval. The purpose of this study is to answer questions like, is the jet 'more developed' further into the quasi-steady pressure region, and hence will exhibit differing acoustic behavior, and does the acoustic signature of the jet vary based on where it is sampled over the quasi-steady region? The results of such an analysis should also help to confirm the jet starting models that were described in Section 4.2.1. Figure 5-22, shows a comparison of parsing the quasi-steady pressure region into a front and back half, and comparing the resultant acoustic signatures for the largest nozzle operating at the LOW NPR and TTR conditions.

As can be seen from the figure, there is less than a ± 1 dB deviation between the acoustic behavior of the jet, depending on whether its signature is based on the first half of the quasi-steady region or the back half. Similar studies were conducted by examining the last quarter of the quasi-steady pressure region versus the earliest quarter. In all such studies, the jets behavior was never deviant by more than ± 1 dB over the course of the quasi-steady pressure region. These results support the jet development times predicted in Section 4.3, that were on the order of 4 - 5 milliseconds. Since the quasi-steady pressure

region does not begin to plateau within this time, due to the overshoot and decay process described in Reference [39], the jet is taken to be fully-developed at the beginning of the quasi-steady pressure region.

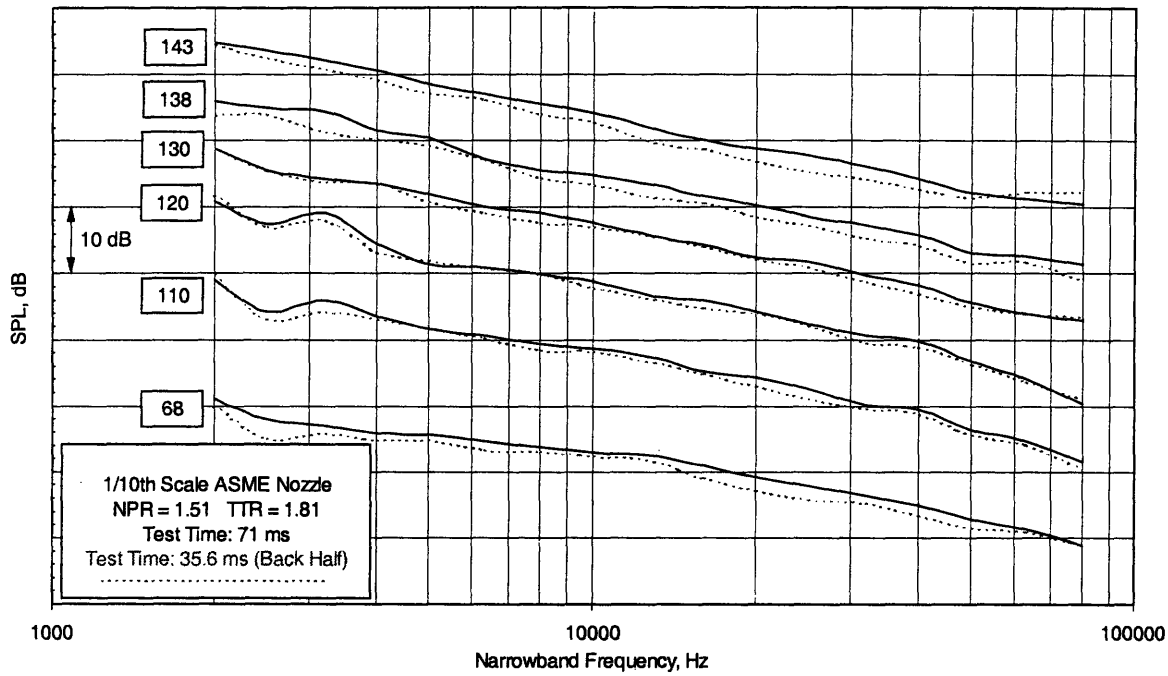

Figure 5-22: Comparison of front end versus back end of the quasi-steady pressure region

Another comparison between the steady-state and transient data is provided in Figure 5-23 for the largest nozzle size tested in the transient facility, 10.2 cm exit diameter. The figure shows a comparison of transient and steady-state SPL versus full-scale frequency at the MID condition, NPR = 2.48 and TTR = 2.43. The transient data contains a total of 52 milliseconds of data from four shock tube firings at the same jet conditions. The addition of more transient data did not show a significant improvement in convergence to the steady-state value. Once again from the figure, the agreement between the transient and steady-state data is around ± 2 dB in magnitude between a full-scale frequency range of 500-6300 Hz. For frequencies lower than 500 Hz, limitations on jet development time, as well as the possibility of interference from the plug that initially seals the driven section from the ambient air, may be important. These two possibilities were taken into account when the full-scale low frequency limit was set to 500 Hz for the 10.2 cm nozzles. Once again, the upper limit on the full-scale frequency is set by microphone frequency response.

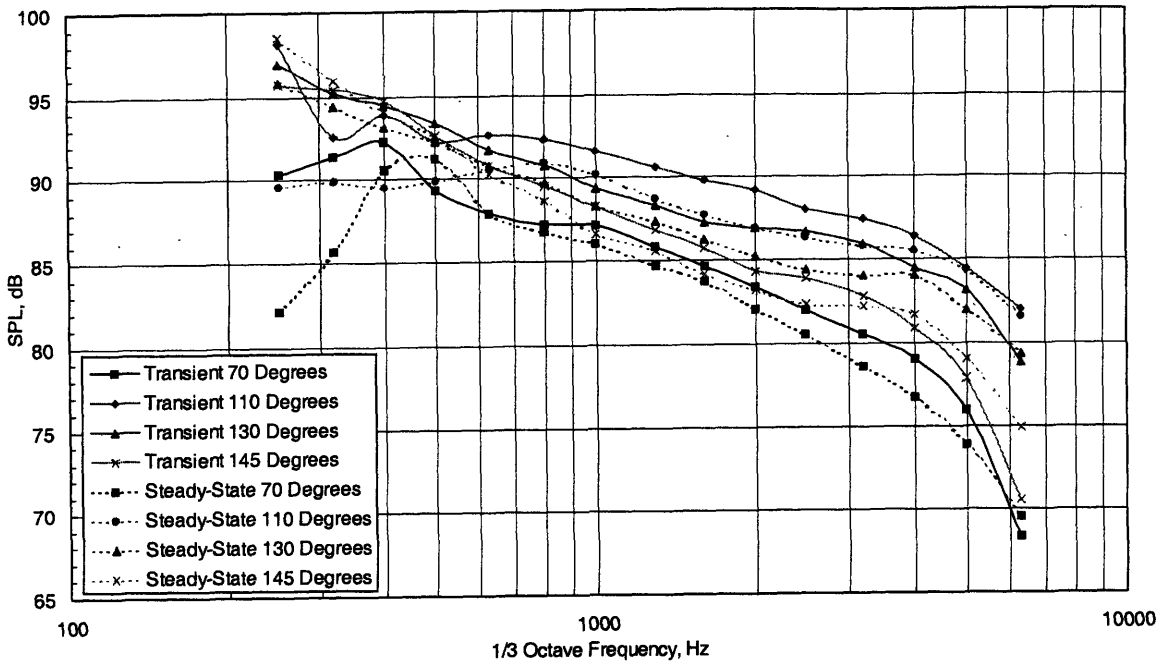

Figure 5-23: Extrapolated data comparison 10.2 cm ASME nozzle, NPR = 2.48, TTR = 2.43

The final comparison between the steady-state and transient data is provided in Figure 5-24 for the largest nozzle size tested in the transient facility, 10.2 cm exit diameter.

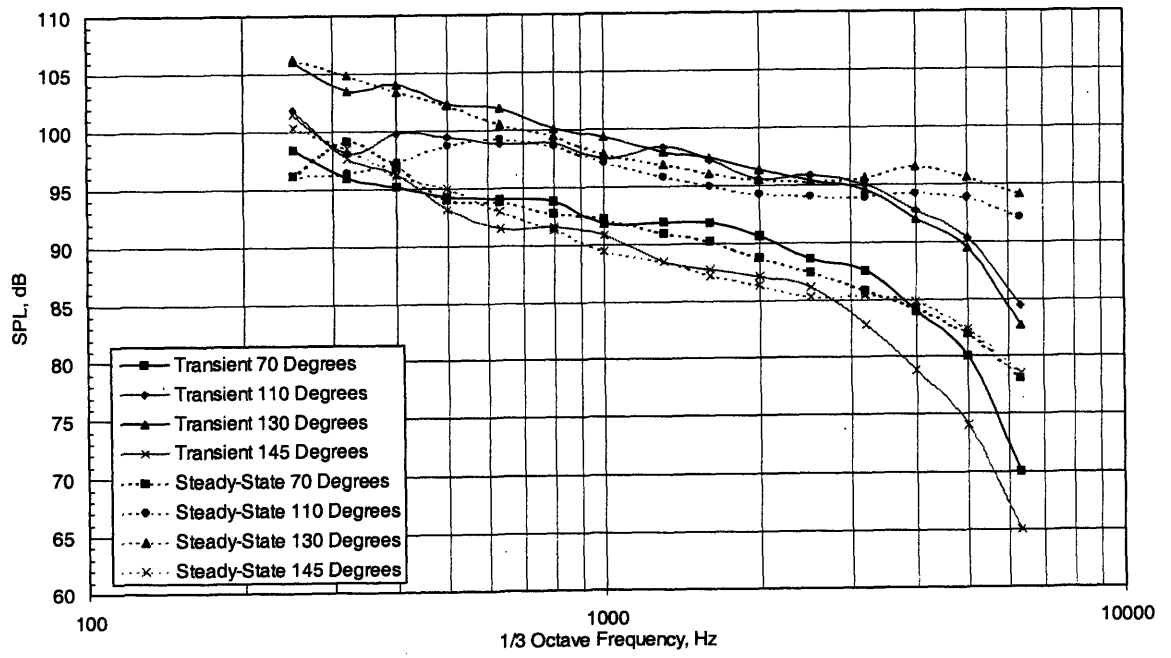

Figure 5-24: Extrapolated data comparison 10.2 cm ASME nozzle, NPR = 3.43, TTR = 2.91

The figure shows a comparison of transient and steady-state SPL versus full-scale frequency at the MID condition, NPR = 3.43 and TTR = 2.91. Once again agreement to within ± 2 dB is observable on all directivity angles between the transient and steady-state data over the frequency range presented. It appears in Figure 5-24 that there is more deviation as the frequency increases between the transient and steady-state noise data. However, the tailing up of the steady-state data for frequencies above 2 kHz on the 110, 120 and 130 degree directivity angles is the result of an interaction with the noise floor. If the acoustic signatures are fared out accordingly, with results seen at other conditions, good agreement is achieved. This noise floor interaction in the steady-state facility was also seen in Figure 5-18. The figure also demonstrates particularly good agreement to within ± 1 dB at the low frequency range (f = 500 to 2000 Hz) for the 1/10th scale ASME nozzle versus steady-state noise data.

5.2.2.6 OASPL and PNL Comparison

Full-scale extrapolated OASPL and PNL versus directivity angle data for all three conditions on the 1/10th scale and 1/15th scale ASME nozzles are shown in Figure 5-25.

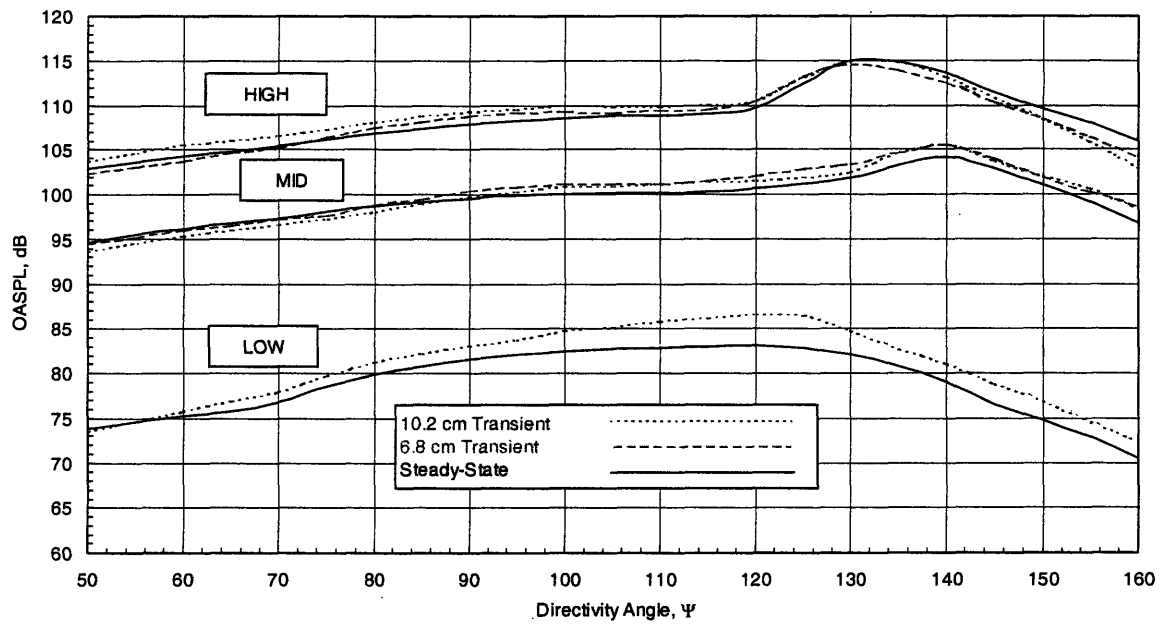

Figure 5-25: Extrapolated OASPL Data Comparison, 6.8 cm and 10.2 cm Nozzles

The HIGH condition contained 46 and 54 milliseconds of test time and the MID condition contained 61 and 64 milliseconds of test time for the 1/10th and 1/15th scale nozzles, respectively. The LOW condition was investigated for the 10.2 cm nozzle and contained 52 milliseconds of transient data.

The figure demonstrates that the transient data taken on 10.2 and 6.8 cm nozzles replicates the directivity pattern of the steady-state data at the HIGH and MID conditions with peaks at 130 and 140

degrees, respectively. In contrast to the 5.1 cm nozzle, the 10.2 cm nozzle deviates by approximately 3 - 4 dB on the LOW condition at the 110 and 120 degree directivity angles, while the other angles show better agreement. The overall appearance of the OASPL versus directivity angle plot exhibits the same general shape and peak noise at around 120 degrees. The achieved NPR of 1.53 for the 10.2 cm nozzle on the LOW condition was also slightly higher than the desired values of 1.51. An additional explanation for the deviation at this one condition may be error due to the jettisoned plug interfering with jet development, which will be discussed in Section 5.4.

5.2.2.7 Summary of Transient versus Steady-State Data Comparison

Table 5.4 presents a summary of the test conditions described in Table 5.3 and an assessment of the agreement between the transient and steady-state noise data.

Table 5.4: Performance comparison between transient and steady-state facilities

Nozzle	NPR & TTR	Full-Scale Frequency Range	Comparison with Steady-State Assessment: SPL versus Full-Scale Frequency
1/20th	LOW	250 - 4000 Hz	± 2 dB on all directivity angles
1/20th	MID	250 - 4000 Hz	± 2 dB on 4 of 6 angles, ± 3-4 dB on 120° and 130°
1/20th	HIGH	250 - 4000 Hz	± 2 dB on 5 of 6 angles, ± 3 dB on 130°
1/15th	MID	300 - 5300 Hz	± 2-3 dB on all directivity angles
1/15th	HIGH	300 - 5300 Hz	± 2 dB on 5 of 6 angles, ± 3 dB on 110°
1/10th	LOW	500 - 6000 Hz	± 2-3 dB on 3 of 6 angles, ± 3-5 dB on 110°, 120° and 130°
1/10th	MID	500 - 6000 Hz	± 2-3 dB on all directivity angles
1/10th	HIGH	500 - 6000 Hz	± 2-3 dB on all directivity angles

Each of the transient nozzles tested exhibited the same overall trends in magnitude and directivity as the steady-state noise data. The 1/20th scale nozzle exhibited better than ± 2 dB agreement on each test condition, except for the 120 and 130 degree angles on the MID and HIGH cases, which deviated by around 3 dB. The 1/15th scale nozzle agreed to within ± 2 dB at the MID and HIGH cases and to within ± 3 dB on the 110 degree angle on the HIGH case. Finally, the 1/10th scale nozzle agreed to within ± 2 dB on the MID and HIGH cases and had the worst agreement of any nozzle at the LOW condition, deviating by 3 - 5 dB at 110, 120 and 130 degrees. All transient tests showed agreement with the steady-state data trends with OASPL and PNL versus angle.

A possible explanation for the deviation at certain conditions and directivity angles is the interference of the diaphragm-plug used as a seal between the nozzle and ambient air. When the incident shock wave arrives at the nozzle, this plug is blown from the end of the shock tube by the ensuing jet and momentarily remains in the flow path. At the LOW condition, high speed video footage (500 frames per second) revealed that for the 5.1 cm nozzle the plug was approximately 12 - 15 exit diameters away from the nozzle exit when the acoustic data acquisition commenced. For the larger 10.2 cm nozzle the plug was

approximately 7 - 10 exit diameters away from the nozzle exit. The plug may still have been sufficiently within the flow field to cause extraneous sound reflections and/or interference with the jet development. A secondary diaphragm section, located between the driver and the test nozzle, was installed to curtail any detrimental effects attributable to the jettisoned plug concept for future shock tube tests.

An additional metric used to quantify the performance of steady-state and transient data is the Effective Perceived Noise Level (EPNL), which is an internationally recognized unit for describing the noise of aircraft operation.[16] To ensure proper comparison, the EPNL values for both the steady-state and transient tests were computed using DADS over the same full-scale frequency range, as shown in Table 5.4, for each of the ASME nozzle sizes. Table 5.5 summarizes this parameter for the conditions and nozzle scales investigated during the ASME nozzle assessment.

Table 5.5: ASME conic nozzle EPNL summary (EPNdB)

NPR	Steady-Steady 14.5 cm	Transient 10.2 cm	Transient 6.8 cm	Transient 5.1 cm
1.51	89.1	92.5	N/A	88.6
2.48	111.1	112.9	113.8	112.4
3.43	118.3	119.6	118.9	118.8

Transient nozzle-to-nozzle tests agreed within approximately 1 dB EPNL for the MID and HIGH cases. Each of the nozzles exhibited a higher value of EPNL, by about 1 - 2 dB, than the steady-state data at the MID condition. Once again the 5.1 cm nozzle displayed the best agreement, with EPNL matched to within 0.5 dB for the LOW and HIGH conditions, and approximately 1 dB for the MID condition. It should also be noted that due to the noise floor interaction of the steady-state data at the HIGH condition, as was discussed in sub-section 5.2.2.5, the steady-state EPNL at this condition is probably somewhat higher than it should be, making the deviation between the transient and steady-state EPNL values somewhat greater than what is portrayed in Table 5.5.

5.3 Implementation of a Secondary Diaphragm Section

The comparison of transient versus steady-state ASME nozzle noise data was completed in Section 5.2 Prior to presenting the results of the LSMS mixer-ejector comparison, this section presents a modification that was made to the shock tunnel facility after completing the initial ASME nozzle validation tests. This section presents an overview of the design and implementation of a secondary diaphragm section to eliminate the jettisoned plug concept described in Section 2.5, which was used to acquire the acoustic data

[16] An overview of the EPNL metric was discussed in Section 4.3.1 and more details can be found in Reference [48].

presented in Section 5.2. To ensure that the secondary diaphragm section posed no significant effects to the acoustic data, a series of diagnostic tests were conducted on 0.64 cm and 5.1 cm exit diameter ($1/20^{th}$ scale) conic nozzles and compared to earlier results to ensure that the section did not alter the acoustic signature of the jet.

5.3.1 Overview and Motivation

A secondary diaphragm section was installed on the nozzle end of the shock tube for two primary purposes:

1. To eliminate the jettisoned plug concept
2. To act as a seal between the evacuated driver section and the atmosphere

Figure 5-26 shows a simple schematic of the shock tube with the location of the secondary diaphragm section between the driven section and the nozzle.

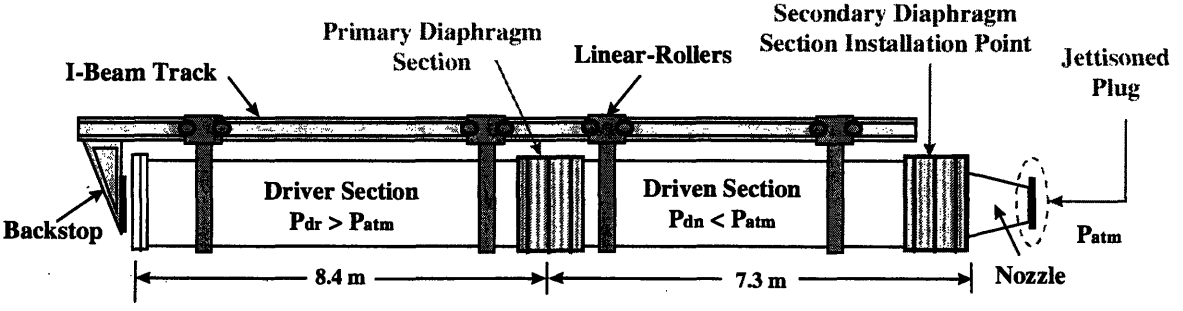

Figure 5-26: Shock tunnel schematic showing the location of the secondary diaphragm section

The plastic plug may interfere in jet development, causing extraneous reflections and/or broadband noise when it is blown off the end of the shock tube. High speed video images revealed that the plastic plug used as a seal between the driven section and the atmosphere, remained in the flow field while acoustic measurements were being made. Figures 5-27 and 5-28 shows that the plastic plug was at approximately 10 - 15 L/D at the start of acoustic data acquisition and at approximately 17 - 25 exit diameters away at the end of the steady-state pressure region. Figure 5-29 correlates these locations to the quasi-steady pressure region within the driven section of the shock tunnel, which selects the section of acoustic data that is processed[17] as was described in Section 2.2.3.

[17] The high-speed camera system, which produced the pictures shown in Figures 5-27 and 5-28, is triggered off a TTL from the incident shock wave that is shown in Figure 5-29 and labeled as incident shock passage.

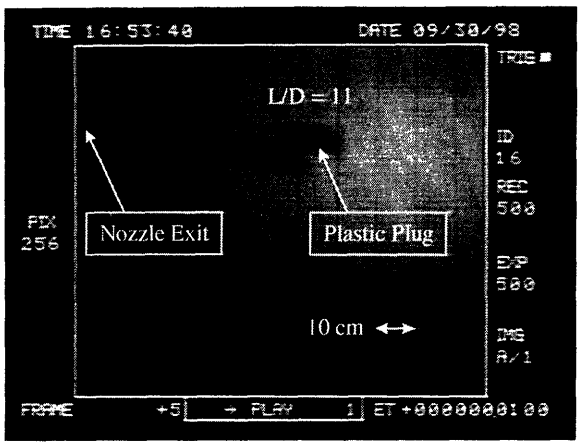

Figure 5-27: Jettisoned plug location at 10 milliseconds after test initiation

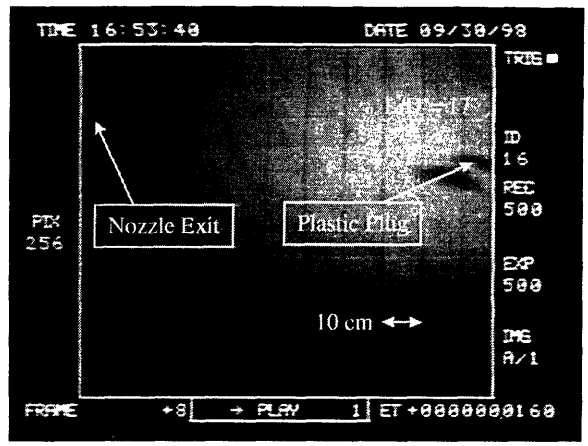

Figure 5-28: Jettisoned plug location at 16 milliseconds after test initiation

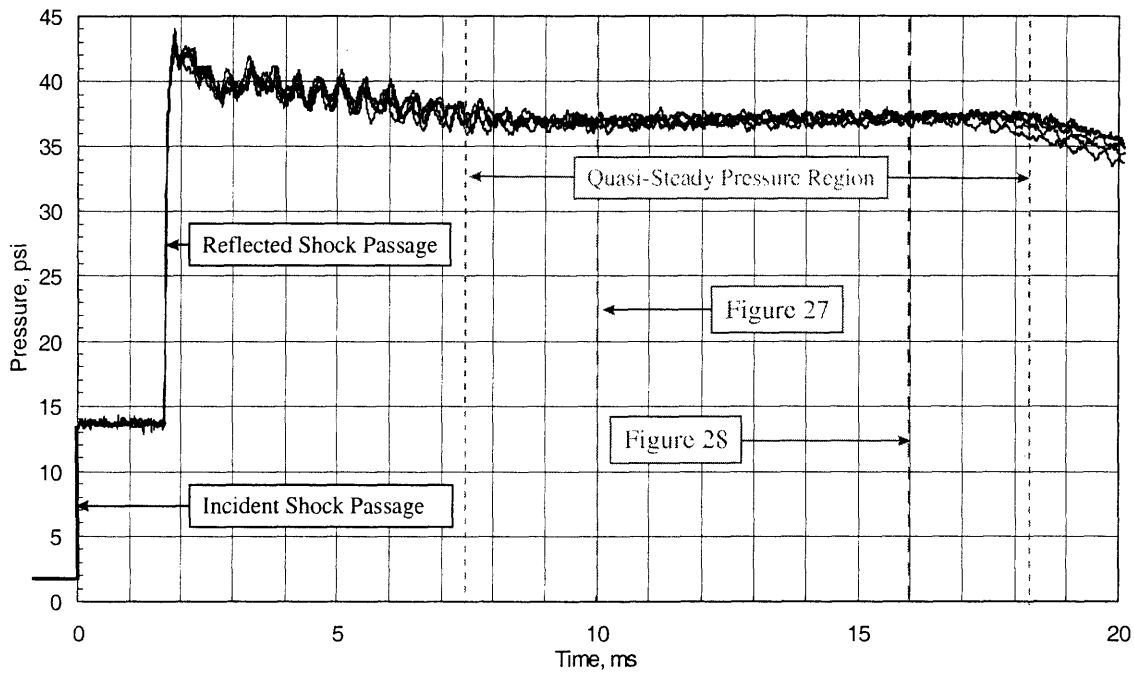

Figure 5-29: Steady-state pressure signature within driven section of shock tube

The plot of jet noise effective source distribution, as was shown in Figure 4-4 of Chapter 4, is another way to examine the influence of the plug flight on the developing jet structure. Figure 4-4 shows that the high-frequency end of the far-field spectrum is generated almost entirely from turbulence in the initial mixing region, whereas the low frequencies are generated over a large region of the jet extending downstream. Although the source of any given frequency will not be a discrete point, but rather a distribution over a finite volume of the jet, we can use such a plot to get a first approximation of what frequencies are being most heavily influenced by the plug's presence, as well as to obtain an approximation for the amount of

time it takes for the plug to be sufficiently out of the flow field before acoustic data acquisition should begin. The results of this are shown in Figure 5-30.

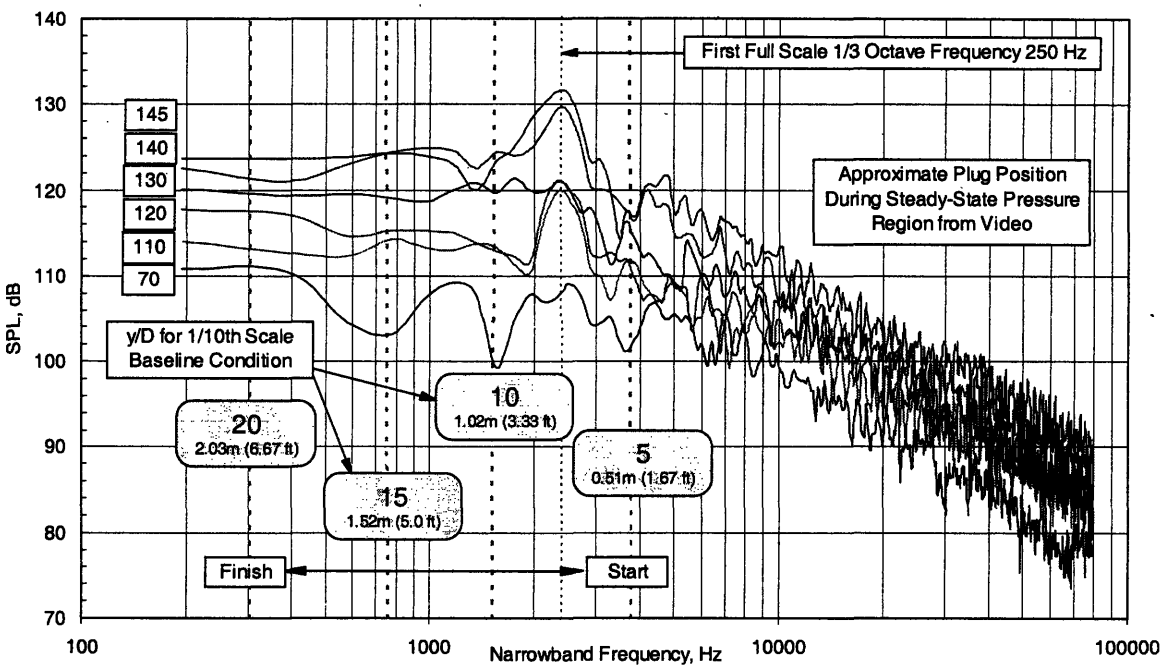

Figure 5-30: As-measured acoustic data for 1/10th scale ASME nozzle

The start and finish boxes in Figure 5-30 show the plug location within the jet during the quasi-steady pressure region, corresponding to 5 and 20 exit diameters, respectively. Full-scale peak frequencies from 30 - 300 Hz are most heavily effected by the plug's presence.

A second advantage to the secondary diaphragm section is to improve upon sealing between the driven section and the atmosphere prior to each test. Using the jettisoned plug concept, the plastic diaphragm had a tendency to wrinkle and distort prior to the firing of the tunnel, and thus to allow some of the ambient air to leak into the driven section. To overcome this, the pressure in the driven section had to be manually monitored and corrected to the desired set condition prior to firing the tunnel. With the secondary diaphragm section in place, the aluminum diaphragm and o-ring combination provide an air-tight seal that did not allow any leakage of the ambient air into the driven section, making the set conditions in the driven section easier to maintain. Furthermore, as the complexity of the nozzle geometry increases, it becomes more difficult to design a plastic or rubber seal to act as an air-tight diaphragm between the driven section and ambient air. LSMS model testing, for example, has a complicated and intricate nozzle exit plane profile that would make sealing the nozzle very difficult using the jettisoned plug concept. Additionally, since the LSMS model has an ejector section attached to it, the plug may not have had sufficient time to exit the section and vacate the developing flow field within the short test time.

Employing the secondary diaphragm section resolves both of these issues in that sealing the section is significantly easier and the jettisoned plug concept is eliminated all together.

5.3.2 Description of the Secondary Diaphragm Section

A mechanical drawing of the secondary diaphragm section is showed in Figure 5-31. The section is 35.56 cm (14 inches) long and has a constant cross-sectional area of 172.2 cm^2 (26.7 in^2) which features a circular to square to circular transition duct. The purpose of the square cross-section was to provide for the best geometry for a diaphragm rupture. The cross-sectional area of the section was kept constant to avoid boundary-layer separation due to the adverse pressure gradient associated with an expansion, [12].

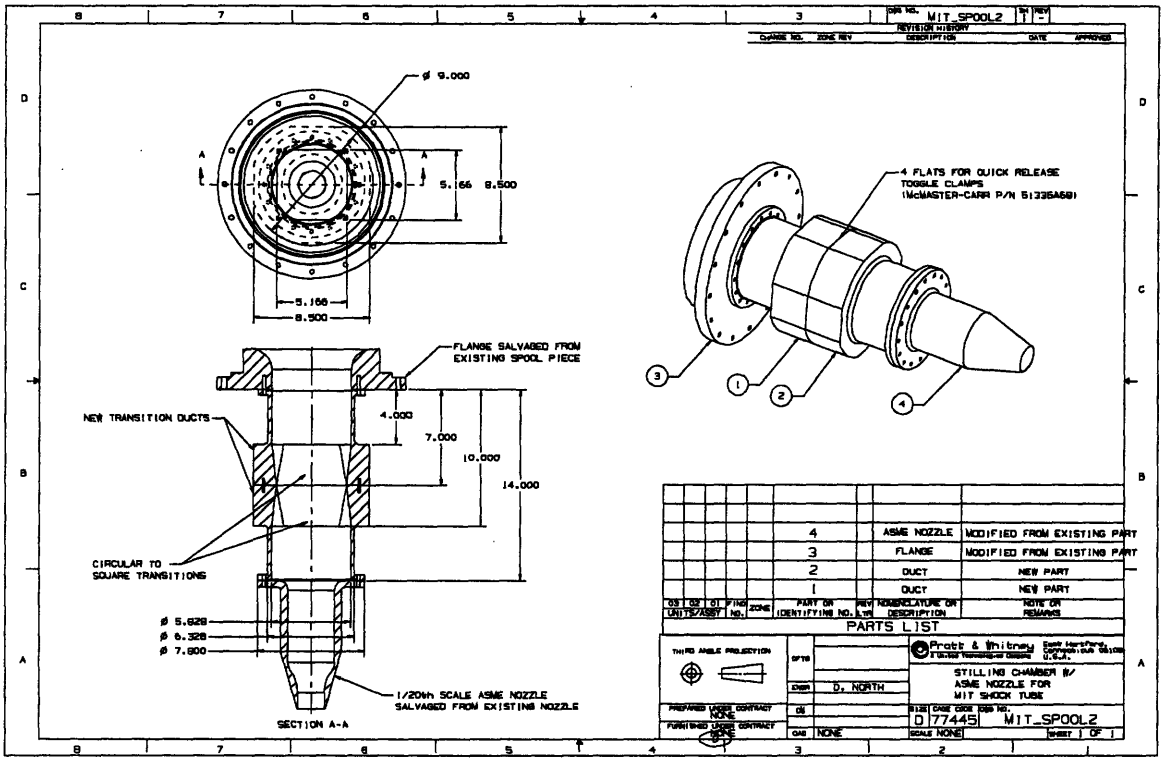

Figure 5-31: Mechanical drawing of the secondary diaphragm section installed on the shock tube

Several digital pictures of the section installed on the shock tunnel are shown in figures 5-32 and 5-33. Figure 32 shows an orthogonal view of the section with the 1/20th scale ASME nozzle in place. Figure 5-33 shows the section open at the location where a 0.01 inch thick scored aluminum diaphragm is placed. This figure also shows the square cross-section at this point in the duct, as was discussed above. Also

visible in both figures are the quick-action toggle clamps, which speed up the diaphragm replacement process between subsequent tests.[18]

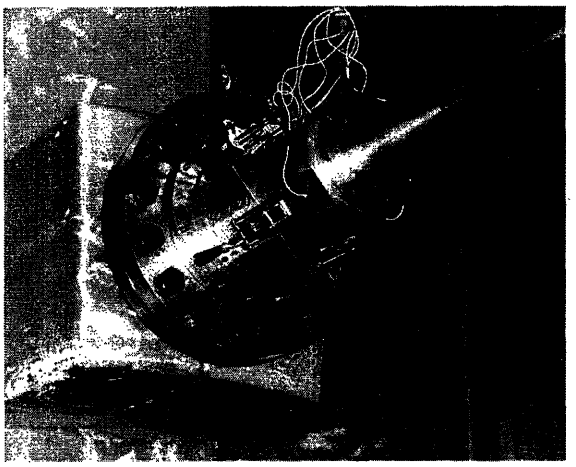

Figure 5-32: Orthogonal view of secondary diaphragm section with 5.1 cm ASME nozzle

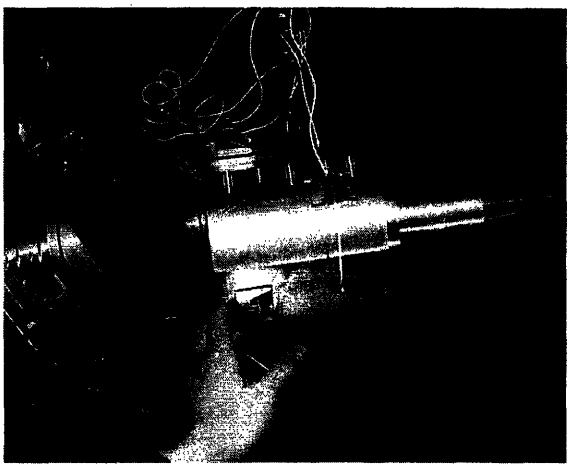

Figure 5-33: Open secondary diaphragm section showing square transition region

A consideration in performing acoustic tests using the secondary diaphragm section is the change in directivity angle that results from the displaced nozzle exit plane location due to the additional length of the section. Since the tube is suspended from a linear roller assembly, the tube can be moved back to a position that allows the elongated section to be positioned such that the nozzle exit plane lines up with the original reference location prior to the installation of the section. Unfortunately, the tube was already rolled back to a position where the backstop (as shown in Figure 5-26) could no be moved any further. Table 5.6 represents the change in directivity angle as a result of testing with the elongated section.

Table 5.6: Change in directivity angle associated with secondary diaphragm section length

Position	Mic 1	Mic 2	Mic 3	Mic 4	Mic 5	Mic 6
Original	70	111	121	131	137	146
Displaced	63	103	113	124	130	140

The change in directivity angle associated with the new secondary diaphragm section posed no problem in the acoustic performance assessment because the DADS processing script interpolates between angles and extrapolates an OASPL and PNL versus directivity angle file for a range from 50 to 160 degrees.

5.3.3 Acoustic Performance Assessment

A series of shock tunnel tests were conducted using the 5.1 cm exit diameter ($1/20^{th}$ scale) ASME nozzle to ensure that the secondary diaphragm section did not detrimentally effect acoustic measurements of the supersonic jet flows.

[18] A modification to replace four - eight bolts that hold the main diaphragm section together with similar

Prior to testing the 5.1 cm exit diameter nozzle, a series of tests was conducted to attempt to ascertain if the shock tube flow was in any way inhibited or altered due to the secondary diaphragm section itself. The steady-state tunnel flushing air was run through a 0.64 cm (¼ inch) exit diameter nozzle and the results compared with acoustic measurements taken on the nozzle prior to the installation of the new section. The tests were both cold flow, at NPR = 2.2 and TTR = 1.0, and exhibited agreement to within ± 1 - 2 dB for directivity angles from 63 to 140 degrees. Additionally, measurements were taken on the 0.64 cm nozzle with the secondary diaphragm section, and compared to the steady-state flushing air flow results. The results of these tests are shown in Figure 5-34 for the 63 and 140 degree angles.

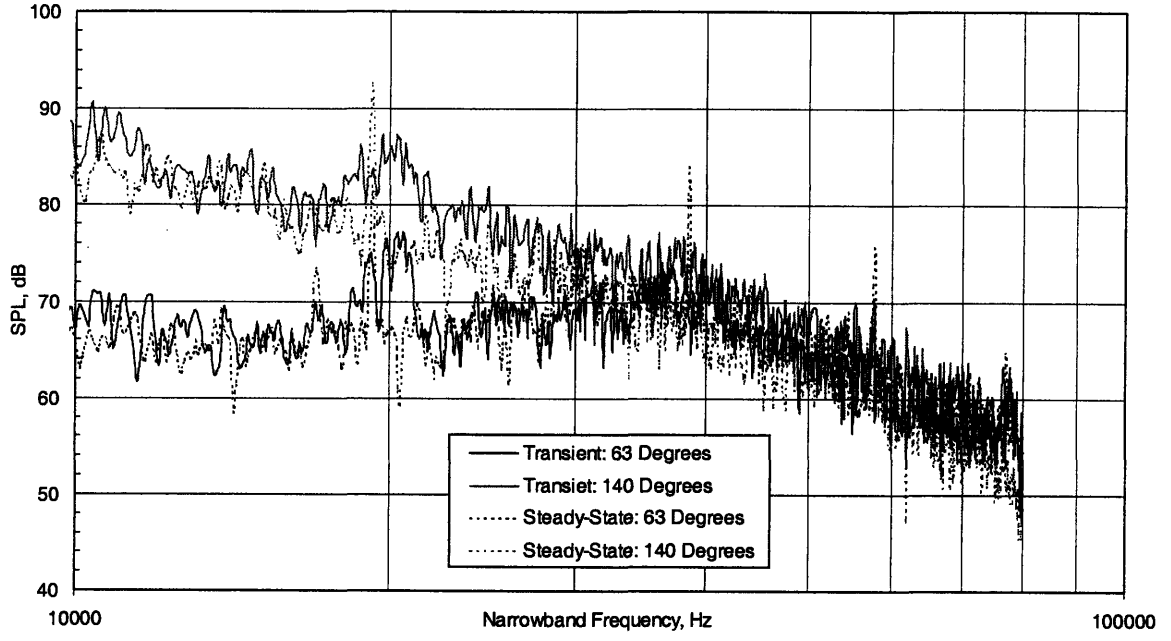

Figure 5-34: 0.64 cm exit diameter nozzle comparison transient versus steady-state with secondary diaphragm section in place

Next a similar assessment was conducted on the 5.1 cm nozzle to gauge the influence of the secondary diaphragm rupture versus the jettisoned plastic plug concept. The plastic plug was used as a seal between the driven and atmosphere with the secondary diaphragm section in place, but with no metal diaphragm used. The acoustic signature of this test was compared to a test using the aluminum diaphragm within the new section. Both tests were conducted at the MID condition and are summarized in Table 5.7.

Table 5.7: Comparison summary for jettisoned plug versus secondary diaphragm section tests

Nozzle	Driven/Atmos. Seal	# of Tests	NPR	TTR	Assessment
5.1 cm	Plastic Plug	2	2.48	2.4	Agreement to within
5.1 cm	Aluminum Diaphragm	4	2.43	2.43	± 1 dB over 250-4000 Hz

quick-action toggle clamps is under consideration as of the writing of this thesis.

A comparison of using the secondary diaphragm as opposed to the plastic plug is shown in Figure 5-35.

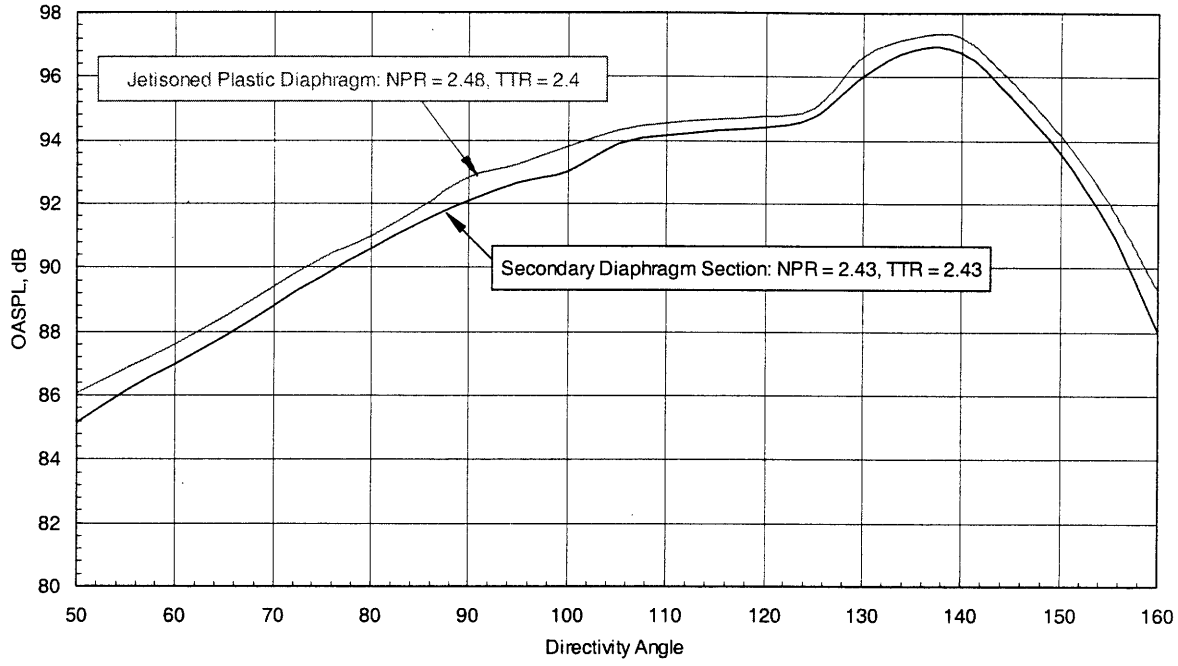

Figure 5-35: Secondary diaphragm section: secondary diaphragm versus jettisoned plastic plug

The figure shows agreement between the two types of diaphragms to within ± 1 dB for OASPL versus directivity angle. In general, the acoustic results from using the secondary diaphragm as opposed to the plastic plug tend to be slightly smoother, suggesting that some variation in acoustic signature may have resulted from the flight or broadband noise associated with the jettisoned plug.

To fully assess the performance of the secondary diaphragm section using the aluminum diaphragm, a complete series of acoustic tests over the range of NPR and TTR, for which the facility is to be used for mixer-ejector testing, was completed. These tests were conducted at the same conditions as a series of steady-state tests conducted at LSAF and prior tests conducted using the jettisoned plastic plug concept without the secondary diaphragm section in place. Table 5.8 summarizes the conditions tested with the secondary diaphragm section in place.

Table 5.8: Summary of acquired data for secondary diaphragm section diagnostics

		LOW			MID			HIGH		
Test Type	**D_e**	**NPR**	**TTR**	**Test Time**	**NPR**	**TTR**	**Test Time**	**NPR**	**TTR**	**Test Time**
Steady-State	14.2	**1.51**	**1.82**	1 sec/angle	**2.48**	**2.43**	1 sec/angle	**3.43**	**2.91**	1 sec/angle
Plastic Plug	5.1	1.53	1.82	75 ms	2.57	2.45	60 ms	3.48	2.93	50 ms
Secondary	5.1	1.54	1.83	64 ms	2.43	2.43	42 ms	3.44	3.02	29 ms

To ensure that the steady-state and transient data are compared over the same frequency range, the desired frequency bands, for input into DADS, are given by the band numbers, BN:

$$BN = 10\log_{10}(frequency) \qquad 5.1$$

Table 5.9 summaries the frequency range and band numbers input into the processing code. A FFT order of 11, corresponding to 2048 points, was used in each of the cases.

Table 5.9: Summary of frequency range of comparison and associated band numbers

Nozzle Scale	Model Scale Frequency Range	Full Scale Frequency Range	First Band Model	Last Band Model	First Band Full	Last Band Full
1/8	2000-32000	250-4000	33	45	24	36
1/20	5000-80000	250-4000	37	49	24	36

5.3.4 ASME Nozzle Acoustic Results

This section presents a comparison of the results for the 1/20th scale ASME nozzle using the jettisoned plug concept, as well as with the secondary diaphragm section in place. The comparison between the two concepts, versus the steady-state noise data, is similar to that presented in sub-section 4.2.2.3 and 4.2.2.6.

5.3.4.1 LOW Condition: Jettisoned Plug and Secondary Diaphragm versus Steady-State

Figures 5-36 and 5-37 show the results for the 1/20th scale ASME nozzle at the LOW condition as SPL versus frequency and OASPL and PNL versus directivity angle, respectively.

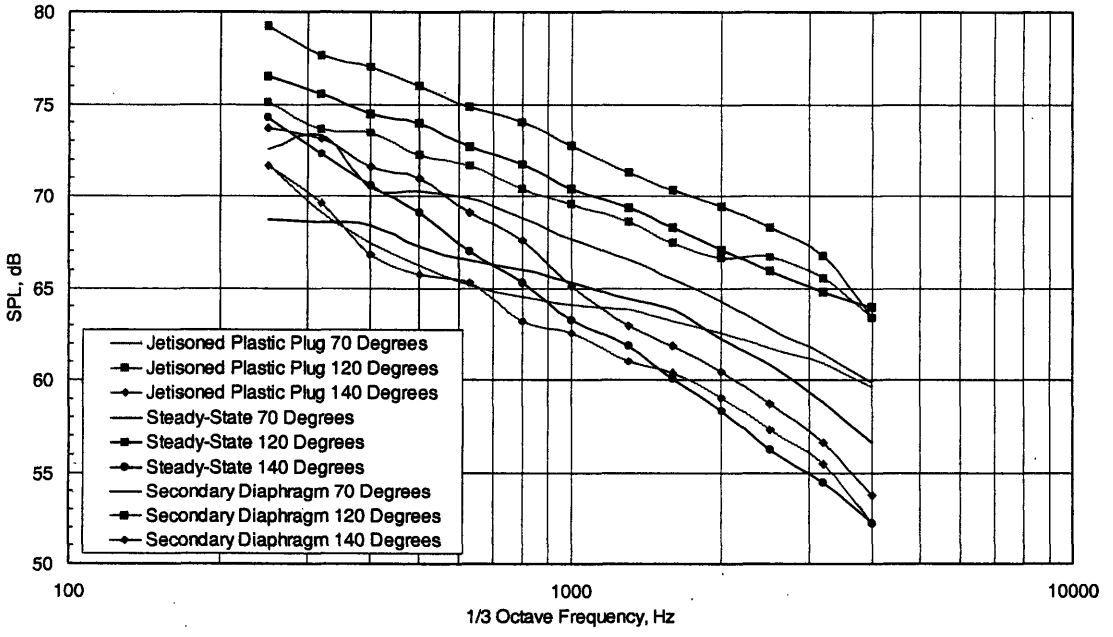

Figure 5-36: SPL versus 1/3-Octave frequency for LOW condition

In both cases it can be seen that the jettisoned plug versus the secondary diaphragm section agree to within about ± 1 - 2 dB. For the LOW condition the secondary diaphragm section did not show an improvement in the acoustic results.

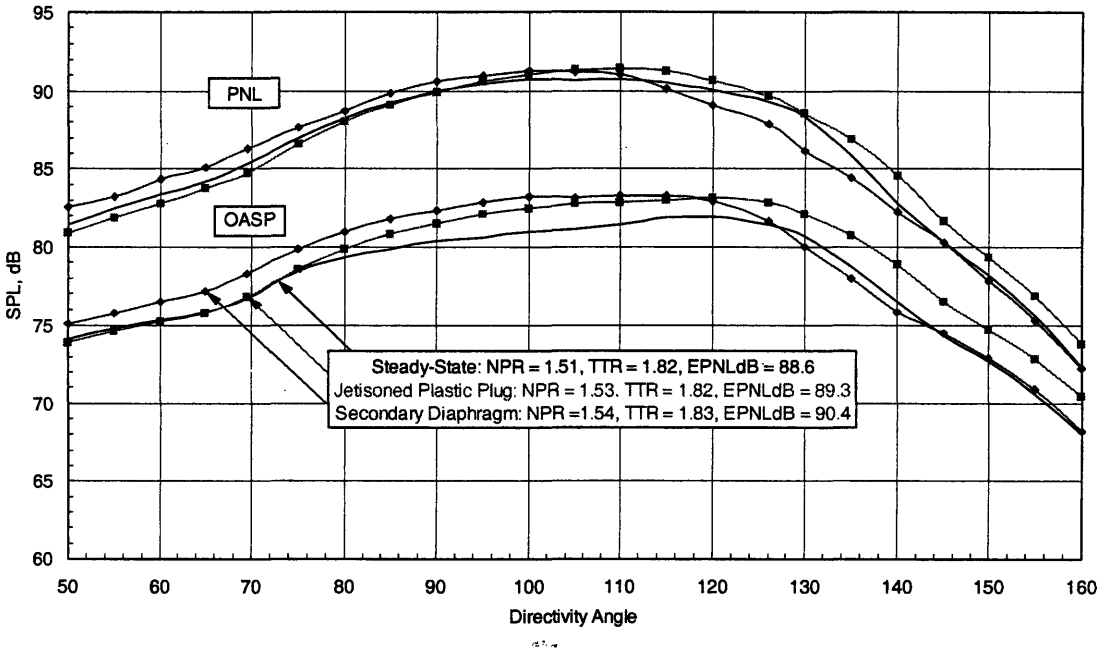

Figure 5-37: OASPL and PNL versus directivity angle for LOW condition

A possible explanation for this is that at the LOW condition, the most test time is acquired, as can be seen in Table 4.3. This suggests that the influence of the jettisoned plug was minimal. The overall trends in magnitude and directivity angle, using the jettisoned plug concept, are on the order of the agreement described in sub-section 5.2.2.3.

5.3.4.2 MID Condition: Jettisoned Plug and Secondary Diaphragm versus Steady-State

This section performs the same type of comparison described in the previous section, but at the MID condition. Figures 5-38 and 5-39 show the 1/20th scale ASME nozzle transient noise data for both the jettisoned plug and secondary diaphragm section tests versus the steady-state data. Once again these tests are at a nozzle pressure ratio of 2.48 and total temperature ratio of 2.43.

Once again, as was seen on the LOW condition, there is no significant improvement in the acoustic data as a result of employing the secondary diaphragm section. The OASPL and PNL curves are in somewhat better agreement to the steady-state data because the NPR and TTR conditions on these tests were closer to the desired values than the jettisoned plug test conditions. The jettisoned plug transient tests were at an NPR of 2.57, whereas the secondary diaphragm section tests were closer to the desired 2.48 at

an NPR of 2.43. The agreement seems to be somewhat better on directivity angles forward of 140 degrees, whereas the 145 degree angle deviated more than the jettisoned plug noise measurement at that point.

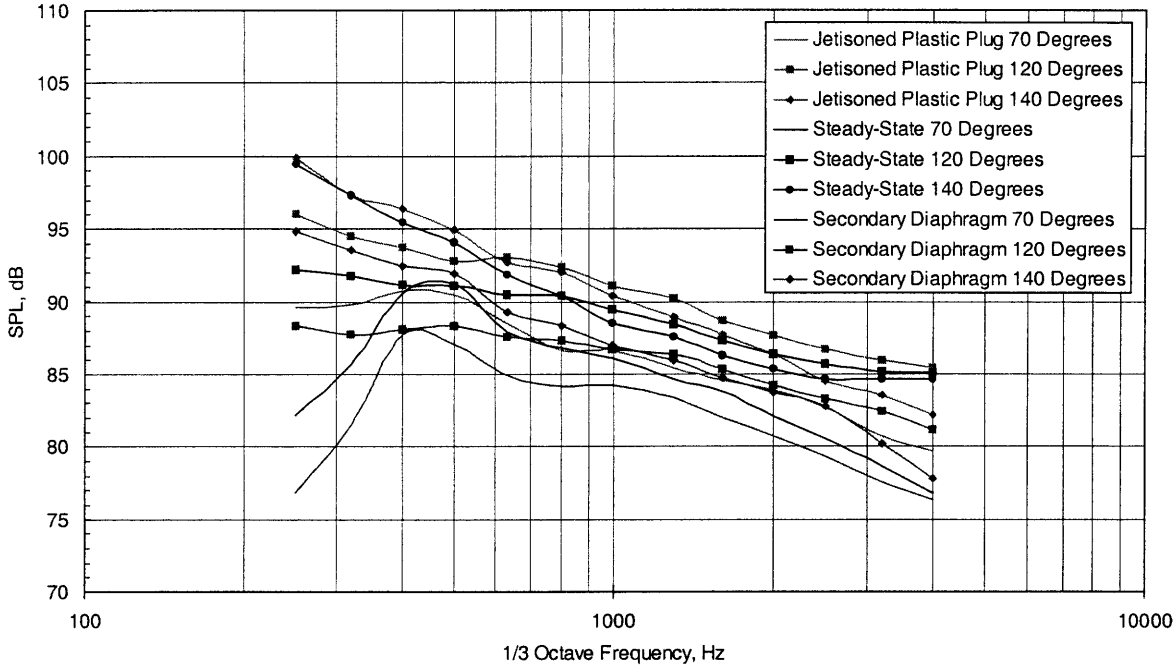

Figure 5-38: SPL versus 1/3-Octave frequency for MID condition

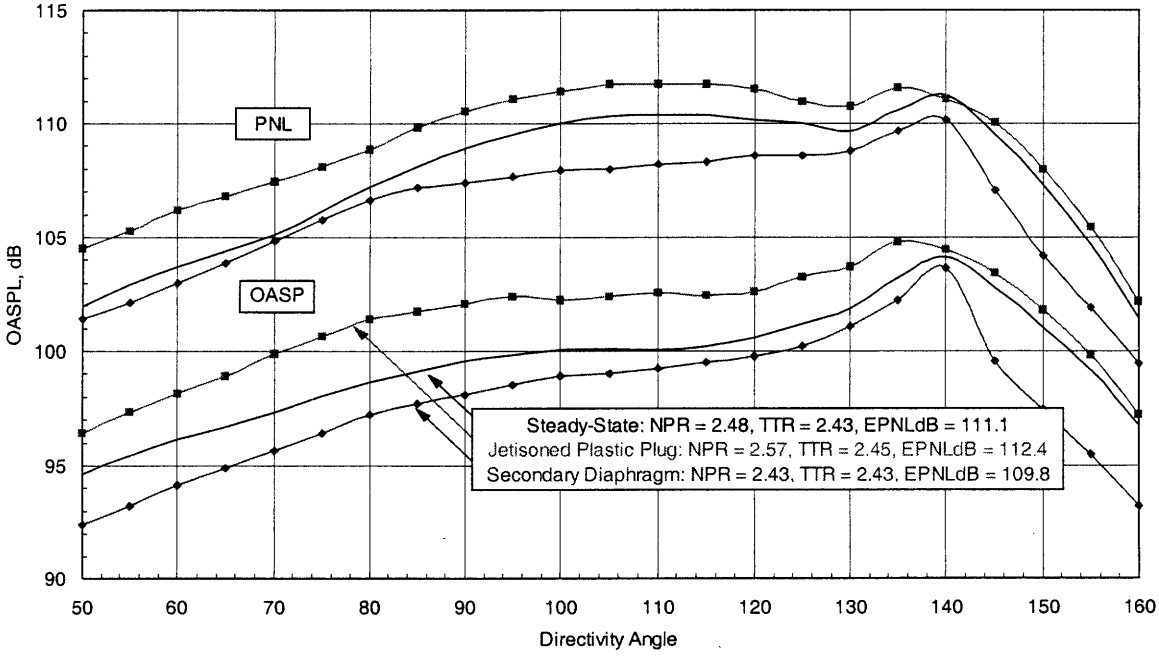

Figure 5-39: OASPL and PNL versus directivity angle for MID condition

5.3.4.3 HIGH Condition: Jettisoned Plug and Secondary Diaphragm versus Steady-State

The results of the 1/20th scale ASME nozzle at the HIGH condition tests are shown in Figures 5-40 and 5-41 as full-scale SPL versus frequency, and OASPL and PNL versus directivity angle.

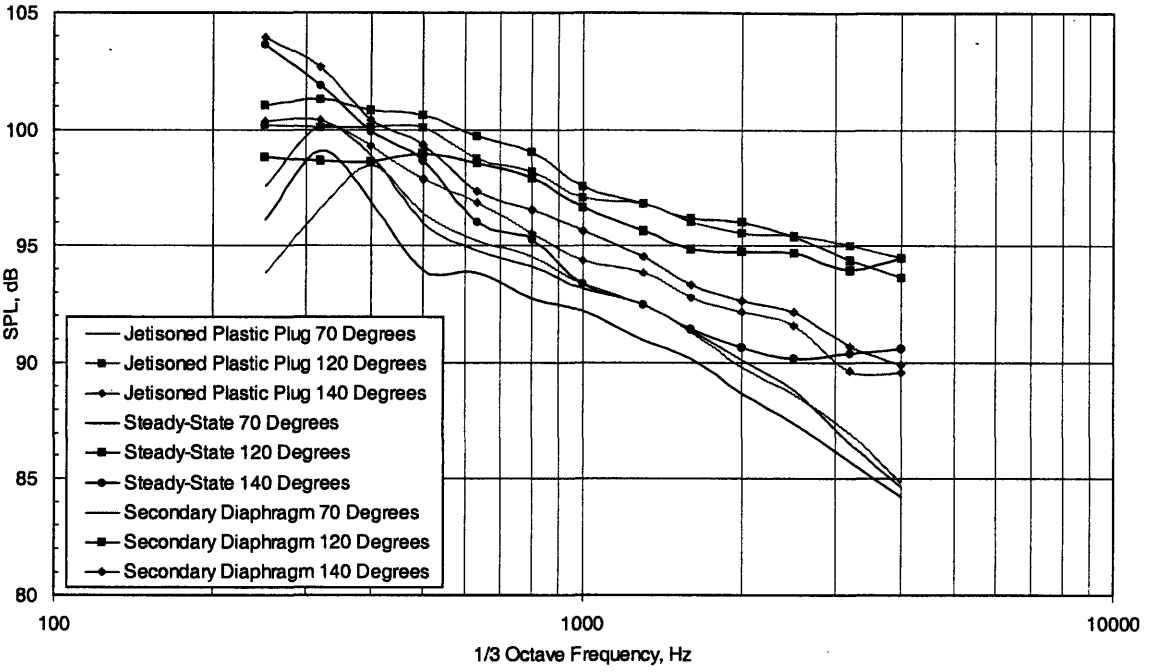

Figure 5-40: SPL versus 1/3-Octave frequency for HIGH condition

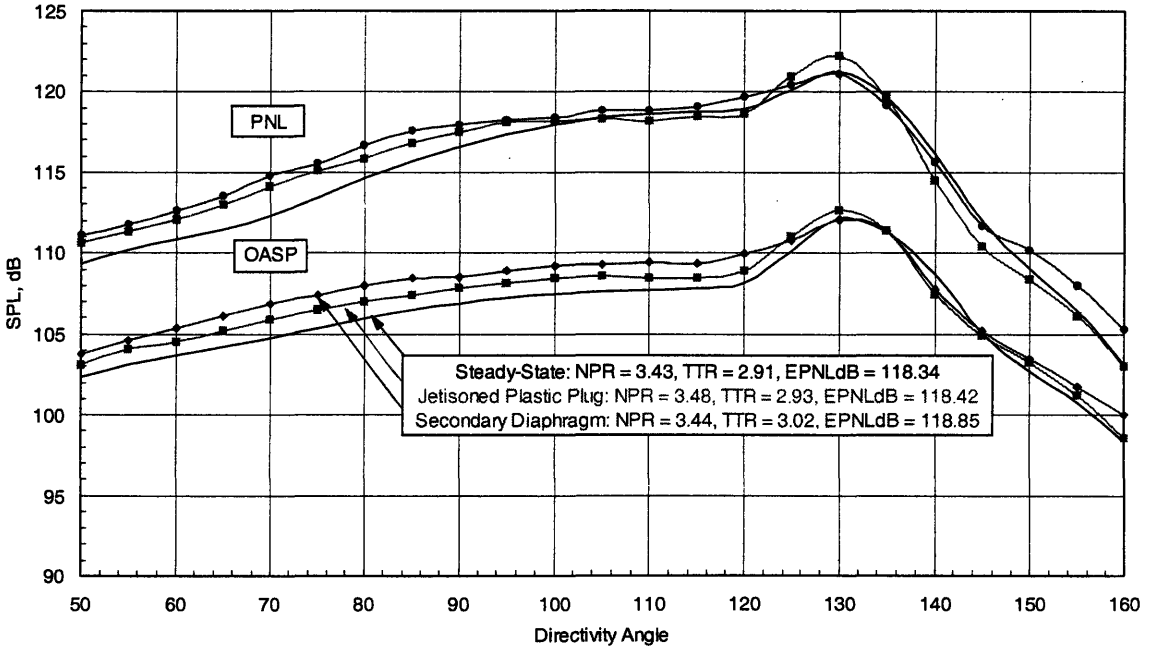

Figure 5-41: OASPL and PNL versus directivity angle for HIGH condition

As can be seen from these two plots, the secondary diaphragm data exhibits somewhat of an improvement over the jettisoned plug concept data. However, judging by the results of the two previous sub-sections, as well as the slight improvement in condition matching to the steady-state noise data, it is likely that this deviation is within the systematic run-to-run error, and not a result of the interference of the plug with the developing jet. The overall trends with magnitude and directivity are present in both plots, and the agreement with the steady-state data is on the order of that discussed in sub-section 5.2.2.3.

Although the installation of the secondary diaphragm section did not result in any substantial improvement in the acoustic data, the section will be beneficial in sealing the driven section off from the ambient in the LSMS tests. An important result, shown in Section 4.3, was that the implementation of the secondary diaphragm section did not cause any detrimental effects to the flow field, and the acoustic signatures from the small scale round nozzle and the $1/20^{th}$ scale ASME nozzle remained in agreement with the steady-state noise data. Most importantly, it does not appear that the addition of the secondary diaphragm section altered the flow within the tube significantly enough to cause any major changes to the acoustic signature from the ASME nozzles.

5.4 HSCT LSMS Mixer-Ejector Acoustic Data Results

With the secondary diaphragm section in place, a nozzle relevant to HSCT application was studied. The large scale model similitude, or LSMS mixer-ejector nozzle, was described in Section 2.1.2.3. Within this section a comparison will be made between transient noise data acquired from the LSMS using the shock tunnel facility and steady-state data acquired from a larger version of the nozzle. The comparison will be made in a manner similar to that completed for the ASME nozzles in Section 5.2. However, the LSMS nozzle is a limited exclusive rights (LER) piece of hardware. Therefore, this section will present more of a qualitative description of the acoustic results obtained from the facilities. Noise results will be shown on relative instead of absolute SPL axes. Nonetheless, it is the intent of this section, without providing detailed SPL, OASPL, PNL, and EPNL values, to provide a definitive answer as to the usefulness of employing a transient testing technique to acquire noise data from geometrically complicated nozzles.

The repetitiveness of testing multiple nozzle scales, as was done for the ASME nozzles in the transient investigation, is somewhat alleviated because only one LSMS nozzle size, a $1/12^{th}$ scale version of the full-size, was tested at the MIT facility. However, the mixer-ejector model has a mixer area ratio, or MAR, that was also investigated. At the steady-state facility, a series of noise measurements were taken at three MAR cases, which will be referred to as LOW, MID and HIGH, and NPR and TTR conditions, which are somewhat analogous to the LOW, MID and HIGH cases described in Section 5.2, for the ASME nozzles. The MAR classification corresponds to the HIGH case being the largest ratio of exit area to

primary throat area, the LOW MAR condition corresponds to the smallest ratio of exit area to primary throat area that was tested, and the MID MAR ratio case is somewhere in between. Suppressor area ratio, or SAR, was not investigated using the LSMS model.

In contrast to the ASME test articles, the LSMS is not an axisymmetric nozzle, and hence variations in azimuthal angle, which correspond to sideline and take-off measurements as depicted in Figure 2-19 of Section 2.3, were also investigated. Table 5.10 summarizes the conditions and configurations that were studied to characterize relevant portions of the LSMS acoustic signature.

Table 5.10: Summary of steady-state tests that will be duplicated at the transient MIT facility using the cast aluminum chute rack

Test Battery	NPR and TTR	MAR	Azimuthal Angle	Shots
1	LOW	LOW, MID, HIGH	90°	9
2	MID	LOW, MID, HIGH	90°	9
3	HIGH	LOW, MID, HIGH	90°	9
Rotate the Shock tube in accordance with Figure 2-30 for azimuthal angle studies				
4	LOW	LOW, MID, HIGH	24°	9
5	MID	LOW, MID, HIGH	24°	9
6	HIGH	LOW, MID, HIGH	24°	9

At approximately three shock tube shots at each of the conditions shown in Table 5.10, a total of 54 shots is required to complete this test matrix. With several preliminary shots used to identify initial set values versus realized jet conditions and microphone gain settings, as well as taking into account shock tube shots that miss-fire, in reality approximately 70 tests were required to complete this matrix. Thus, at nine shots a day, a preliminary assessment of the acoustic performance of a chute rack can be characterized in just over one week. In future work, described in Section 7.3, the test matrix shown in Table 5.10 will be repeated to ascertain the performance of a plastic stereo-lithography, SLA, chute rack, as was described in Section 2.1.2.3.

5.4.1 Summary of Steady-State LSMS Noise Data

This section presents an overview of the steady-state LSMS data in a similar fashion to the overview for the ASME nozzles presented in Section 5.2.1. One of the most insightful ways to study the steady-state LSMS noise data is to examine plots of SPL spectra versus full-scale frequency for each of the combinations that was studied in the transient facility. The next eighteen plots will summarize all of the testing combinations that are presented in Table 5.10. For each NPR and TTR and MAR combination, the 90 and 24 degree azimuthal angle comparisons are shown side by side. The sequence of spectral plots examine each of the three NPR and TTR combinations while varying MAR over each case. Since this is a significant number of plots to keep track of, Table 5.11 will be of help to the reader as a summary. The spacing between adjacent lines on the sound pressure level axis, for this set of figures, is 10 dB. Also note that the frequencies are plotted on a log scale.

Table 5.11: Summary of SPL versus full-scale frequency for LSMS testing combinations

Figure Number	MAR	NPR and TTR	Azimuthal Angle
5-42	LOW	LOW	90°
5-43	LOW	LOW	24°
5-45	MID	LOW	90°
5-46	MID	LOW	24°
5-47	HIGH	LOW	90°
5-48	HIGH	LOW	24°
5-49	LOW	MID	90°
5-50	LOW	MID	24°
5-51	MID	MID	90°
5-52	MID	MID	24°
5-53	HIGH	MID	90°
5-54	HIGH	MID	24°
5-55	LOW	HIGH	90°
5-56	LOW	HIGH	24°
5-57	MID	HIGH	90°
5-58	MID	HIGH	24°
5-59	HIGH	HIGH	90°
5-60	HIGH	HIGH	24°

Figures 5-42 and 5-43 shows SPL versus frequency for the LOW MAR case at 90 and 24 degree azimuthal angles at the LOW NPR and TTR condition. Several features are noticeable from these plots including the roll-off of the spectra at high frequency, the peak noise for both the 90 and 24 azimuthal angles occurs at the 110 and 120 degree directivity angles, and that the 110 degree directivity angle crosses the 120 degree angle at the 24 degree azimuthal angle. Also worth noting is that the spectra for the 70 degree angle is relatively flat over the frequency range and that the 140 and 145 degree angles display a similar profile.

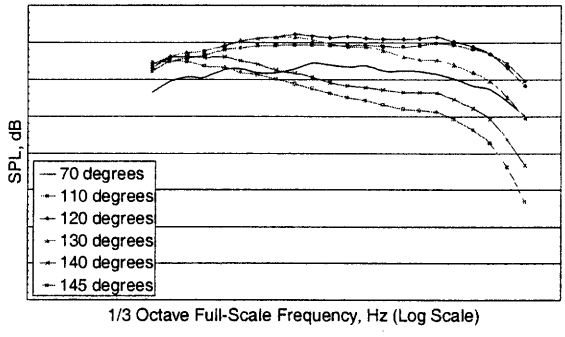

Figure 5-42: LOW MAR, LOW NPR, 90 azimuthal

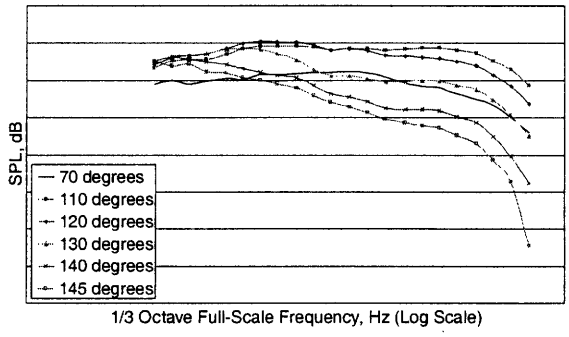

Figure 5-43: LOW MAR, LOW NPR, 24 azimuthal

Figures 5-44 and 5-45 show SPL versus frequency for the MID MAR case at 90 and 24 degrees azimuthal angle at the LOW NPR and TTR condition. Once again the roll-off with high frequency is present and the

cross-over of the 110 degree directivity angle over the 120 degree angle is present in the 24 degree azimuthal angle case. In contrast to the LOW MAR case, the 70 degree angle displays more variation with frequency, and the peaking of the 110 and 120 degree directivity angles are more pronounced at the MID MAR condition at 24 degree azimuthal angle.

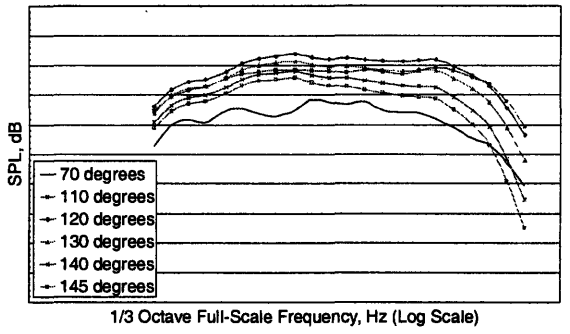

Figure 5-44: MID MAR, LOW NPR, 90 azimuthal

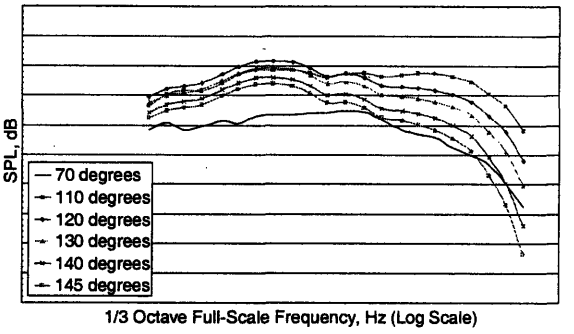

Figure 5-45: MID MAR, LOW NPR, 24 azimuthal

Figure 5-46 and 5-47 show SPL versus frequency for the HIGH MAR case at 90 and 24 degrees azimuthal angles at the LOW NPR and TTR condition. In contrast to the deviations between the MID and LOW MAR conditions, the spectral results from the MID and HIGH conditions are virtually identical, with the acoustic signatures of each of the directivity angles being less the ± 0.5 dB apart. The trends with frequency at each directivity angle are identical.

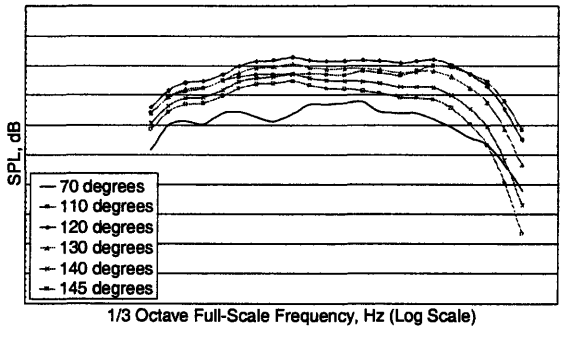

Figure 5-46: HIGH MAR, LOW NPR, 90 azimuthal

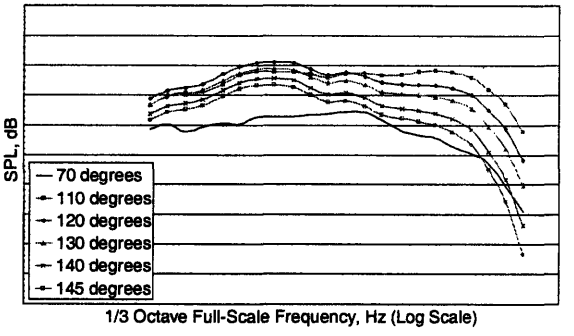

Figure 5-47: HIGH MAR, LOW NPR, 24 azimuthal

The deviation between the LOW and MID/HIGH MAR conditions is also pronounced through each of the next set of comparisons. Figures 5-63 - 5-68 will show this more clearly. As of the writing of this thesis it is not yet clear if this effect is the result of some flow phenomena occurring within the mixer-ejector or a

systematic processing error that took place in the data reduction associated with the LOW MAR condition.[19]

Next, the same six types of plots are examined, but at the MID NPR and TTR condition. Figures 5-48 and 5-49 show SPL versus frequency for the LOW MAR case at 90 and 24 degrees azimuthal angle at the MID NPR and TTR condition. Once again some of the noticeable features of these plots are the relative broadband flatness of the 70 degree directivity angle, the cross-over of the 110 degree directivity angle over the 120 degree angle at the sideline azimuthal angle, the high frequency roll-off, and the correspondence between the 140 and 145 degree directivity angle spectra.

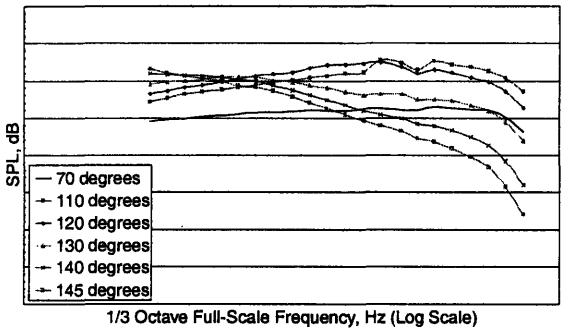

Figure 5-48: LOW MAR, MID NPR, 90 azimuthal

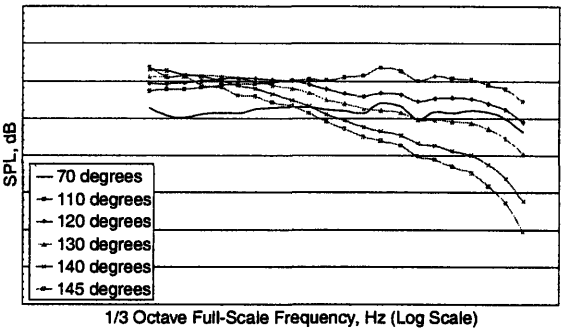

Figure 5-49: LOW MAR, MID NPR, 24 azimuthal

Figure 5-50 and 5-51 show SPL versus full-scale frequency for the MID MAR case at 90 and 24 degrees azimuthal angle at the MID NPR and TTR condition.

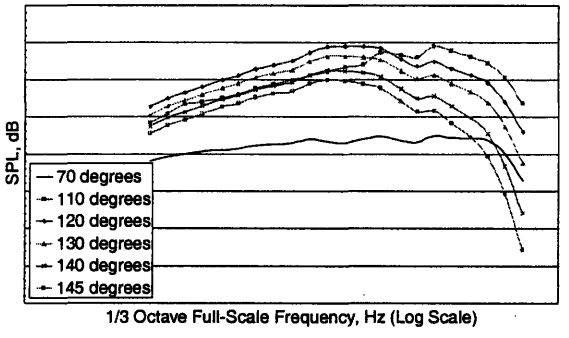

Figure 5-50: MID MAR, MID NPR, 90 azimuthal

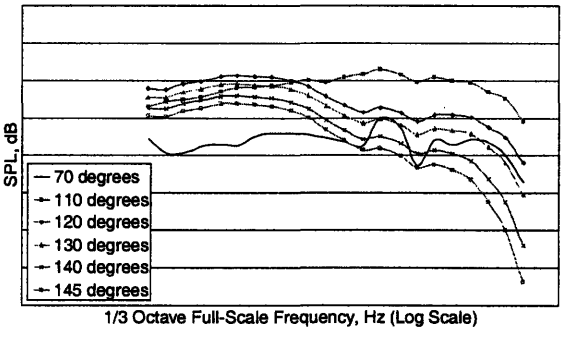

Figure 5-51: MID MAR, MID NPR, 24 azimuthal

Here the cross-over of the 110 degree directivity angle over the 120 degree angle is pronounced in both the fly-over and sideline azimuthal angle. The spectra for the 90 degree and 24 azimuthal angles exhibit self-similarity, with the 70 degree directivity angle remaining relatively flat over the full-scale frequency

[19] It is hoped that the next generation of steady-state noise tests on the LSMS nozzle, which are in progress as of the writing of this thesis, will clarify this behavior.

range shown. For this condition, the peak noise is also concentrated around the 110 - 120 degree directivity angles, which is in contrast to the ASME nozzles for the MID condition, where the peak noise was concentrated around the 130 - 140 degree directivity angles. Another noticeable difference from Figure 5-9 is that spectra for the LSMS model tend to be more flat than the corresponding spectra for the ASME nozzles at conditions somewhat close to the NPR and TTR jet conditions shown in the figure.

Figures 5-52 and 5-53 show SPL versus frequency for the HIGH MAR case at 90 and 24 degrees azimuthal angle at the MID NPR and TTR condition.

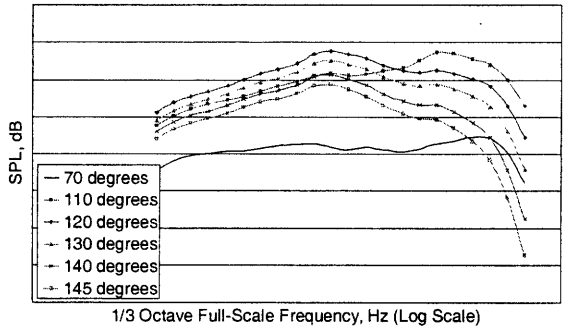

Figure 5-52: HIGH MAR, MID NPR, 90 azimuthal

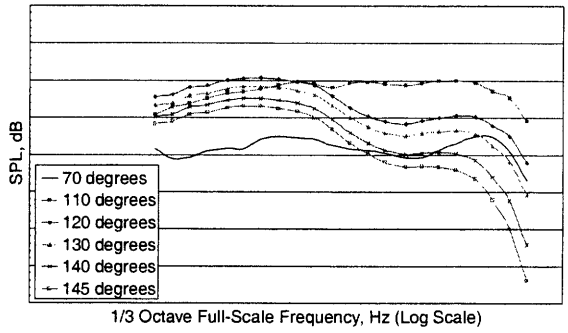

Figure 5-53: HIGH MAR, MID NPR, 24 azimuthal

Once again, the variation at the MID NPR and TTR jet conditions for the MID and HIGH MAR cases is less than ± 0.5 dB over the full-scale frequency range for all directivity angles.

As the last group of plots in the SPL versus full-scale frequency study, the same type of plots are presented but now at the HIGH NPR condition for each of the MARs. Figures 5-54 and 5-55 show SPL versus full-scale frequency for the LOW MAR case at 90 and 24 degrees azimuthal angle at the HIGH NPR and TTR condition.

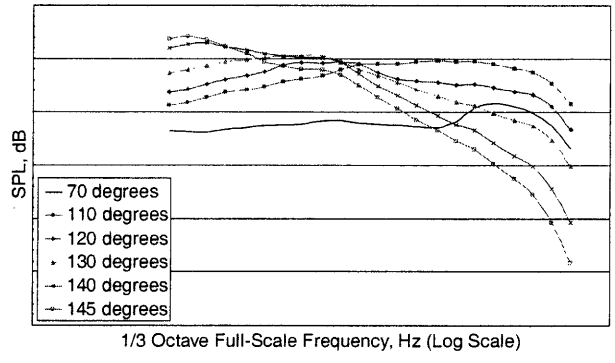

Figure 5-54: LOW MAR, HIGH NPR, 90 azimuthal

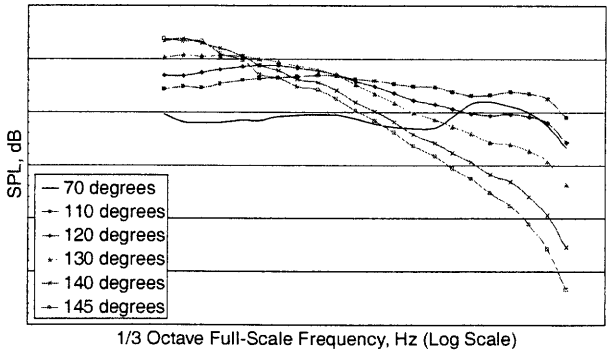

Figure 5-55: LOW MAR, HIGH NPR, 24 azimuthal

These figures show the cross-over of the 110 degree directivity angle over the 120 degree angle in both the fly-over and sideline cases. The 70 degree directivity angle shows a distinct peaking, were as in the LOW and MID NPR and TTR jet conditions the spectra remained relatively flat. Once again the roll-off with high frequency is present for each of the directivity angles, and the 140 and 145 degree directivity angles show a similar profile, but are off-set by about 3 - 5 dB.

Figures 5-56 and 5-57 show SPL versus frequency for the MID MAR case at 90 and 24 degrees azimuthal angle at the HIGH NPR and TTR condition.

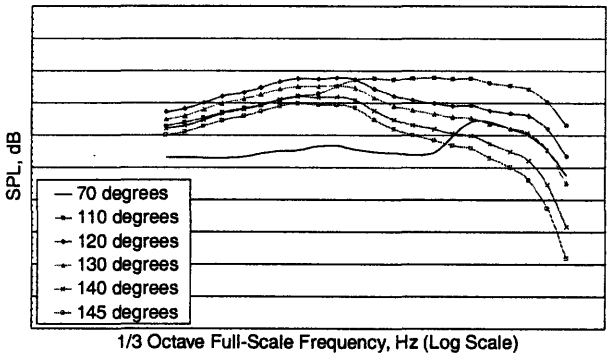

Figure 5-56: MID MAR, HIGH NPR, 90 azimuthal

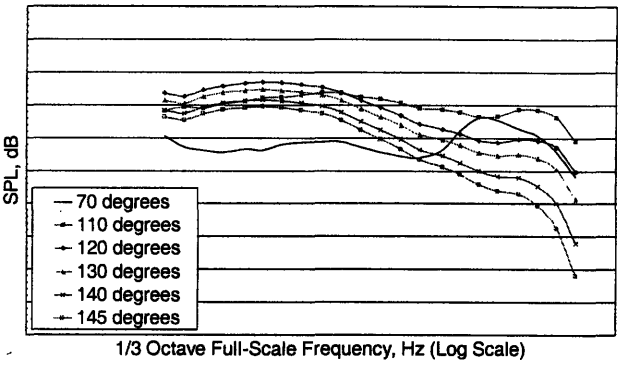

Figure 5-57: MID MAR, HIGH NPR, 24 azimuthal

At this MID MAR condition, the peaking of the 70 degree directivity angle is again noticeable, as well as the cross-over of the 110 degree directivity angle over the 120 degree angle in both the 90 and 24 degree azimuthal angle cases. Comparing Figure 56 to Figure 10, which showed the acoustic signature of the ASME nozzle at somewhat comparable conditions, once again the peak noise shift to more forward directivity angles is observable. The ASME nozzle at the HIGH NPR and TTR condition showed peak noise around 130 - 140 degrees, whereas the LSMS nozzle at conditions close to these show peak noise around the 110 - 120 degree directivity angles.

Finally, Figures 5-58 and 5-59 show SPL versus frequency for the HIGH MAR case at 90 and 24 degrees azimuthal angle at the HIGH NPR and TTR condition. Once again, there is a strong resemblance between the MID and the HIGH MAR acoustic signatures at this HIGH NPR and TTR condition. The peaking of the 110 degree directivity angle is most pronounced at the 90 degree azimuthal angle for this condition. Also the 70 degree forward flight angle shows a pronounced peak, and the cross-over between the 110 and 120 degree directivity angles is present.

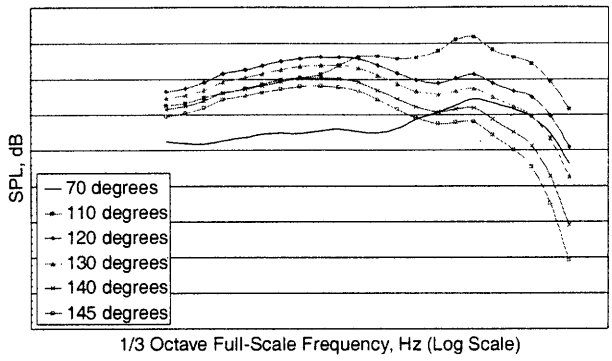

Figure 5-58: HIGH MAR, HIGH NPR, 90 azimuthal

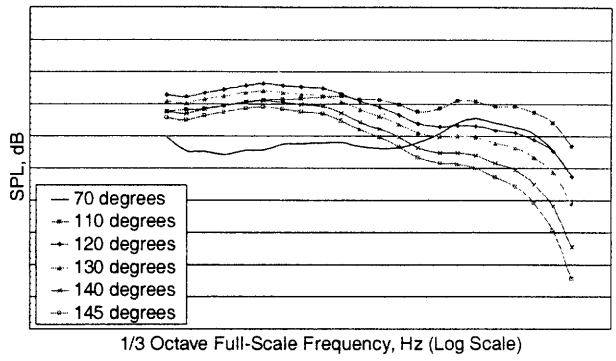

Figure 5-59: HIGH MAR, HIGH NPR, 24 azimuthal

Another way to examine the LSMS steady-state data is to look at OASPL and PNL versus directivity angle curves. This will be done in two ways so that variations with NPR and TTR, as well as with MAR, can be investigated. Once again, since there are a fair amount of figures in this section, Table 5.12 summarizes the OASPL and PNL versus directivity angle comparisons that will be shown.

Table 5.12: Summary of OASPL and PNL versus directivity angle for LSMS testing combinations

Figure Number	MAR	NPR and TTR	Azimuthal Angle
5-60	LOW	LOW, MID, HIGH	90°, 24°
5-61	MID	LOW, MID, HIGH	90°, 24°
5-62	HIGH	LOW, MID, HIGH	90°, 24°
5-63	LOW, MID, HIGH	LOW	90°
5-64	LOW, MID, HIGH	LOW	24°
5-65	LOW, MID, HIGH	MID	90°
5-66	LOW, MID, HIGH	MID	24°
5-67	LOW, MID, HIGH	HIGH	90°
5-68	LOW, MID, HIGH	HIGH	24°

First variations with NPR and TTR conditions at constant MAR values will be discussed for the steady-state LSMS noise data. Examples of this are shown in Figures 60 - 62. Figure 60 shows OASPL and PNL versus directivity angle for all NPR and TTR combinations tested at the LOW MAR condition for both the fly-over and sideline azimuthal angles.

One of the most pronounced features of this plot is the difference in spectra between the 90 and 24 degree azimuthal angles. The plot shows that in each of the NPR and TTR combinations, the 24 degree azimuthal angles shows a more rapid drop off in OASPL and PNL at more aft directivity angles. Furthermore it can be seen that the peak noise at the HIGH condition is located about 10 degrees more aft than in the LOW and MID NPR and TTR jet conditions.

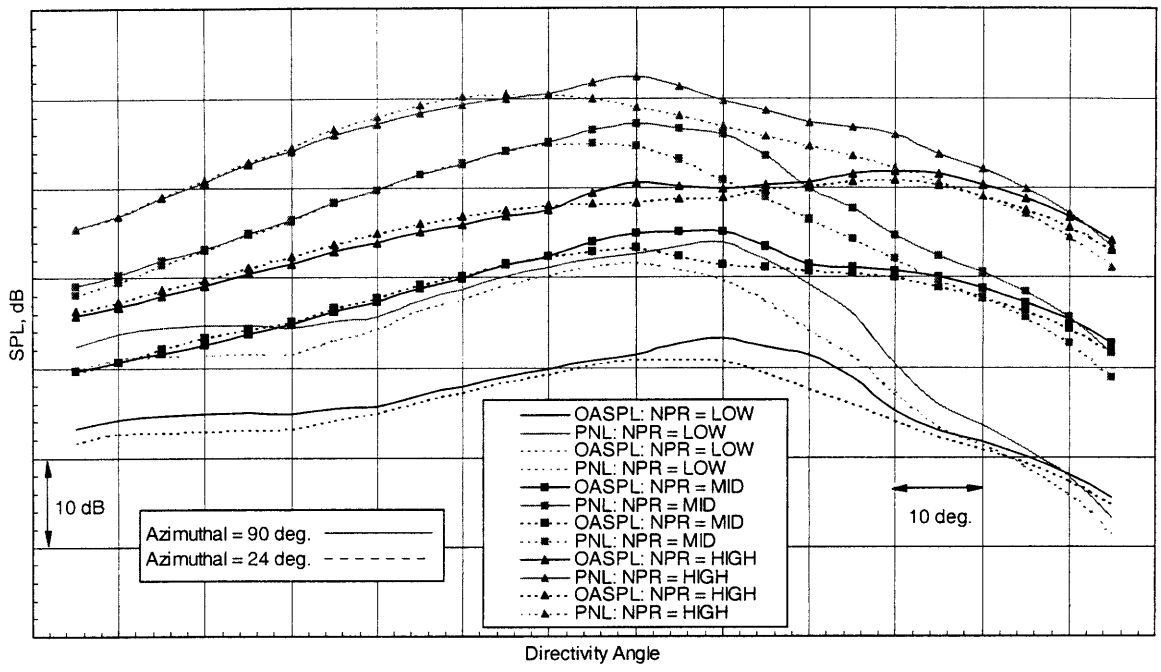

Figure 5-60: Steady-State OASPL and PNL Summary for LOW MAR

Figure 5-61 shows the same type of plot, but at the MID MAR condition. Once again the most noticeable feature of this plot is the variation with azimuthal angle.

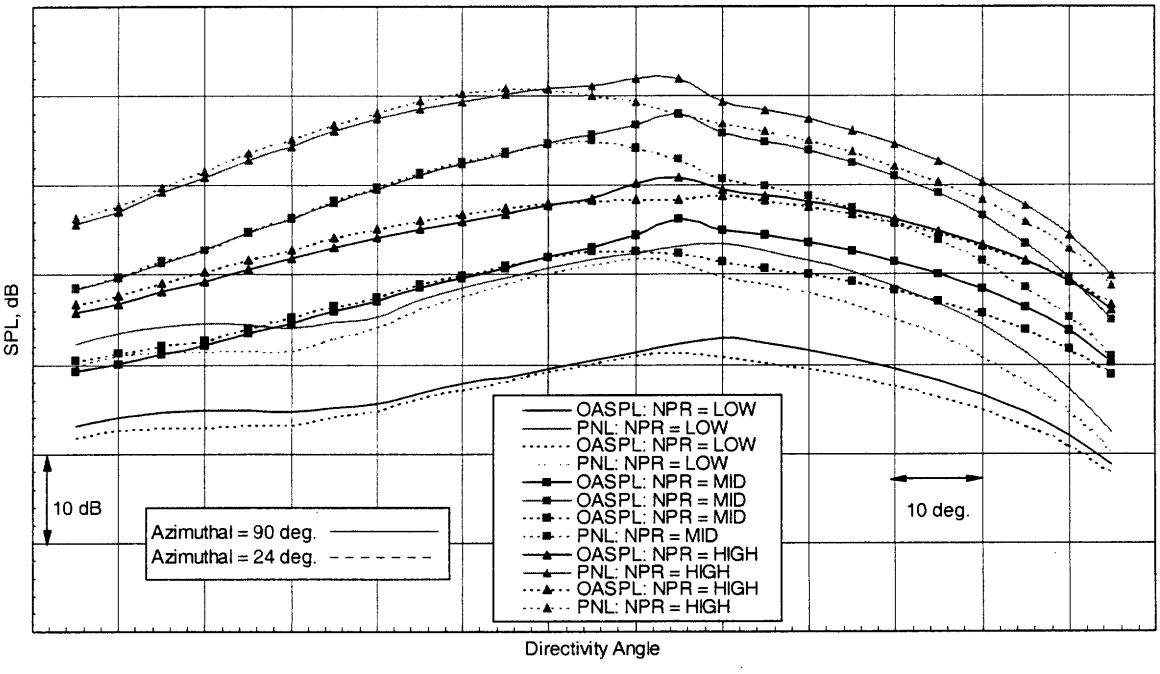

Figure 5-61: Steady-State OASPL and PNL Summary for MID MAR

The 24 degree azimuthal angle falls off more rapidly at more aft directivity angles than the 90 degree azimuthal angle case. The agreement between the two azimuthal angles is within ± 1 - 2 dB on the forward directivity angles.

The last set of plots in this group is shown in Figure 5-62. This figure shows all the NPR and TTR combinations investigated at the HIGH MAR condition.

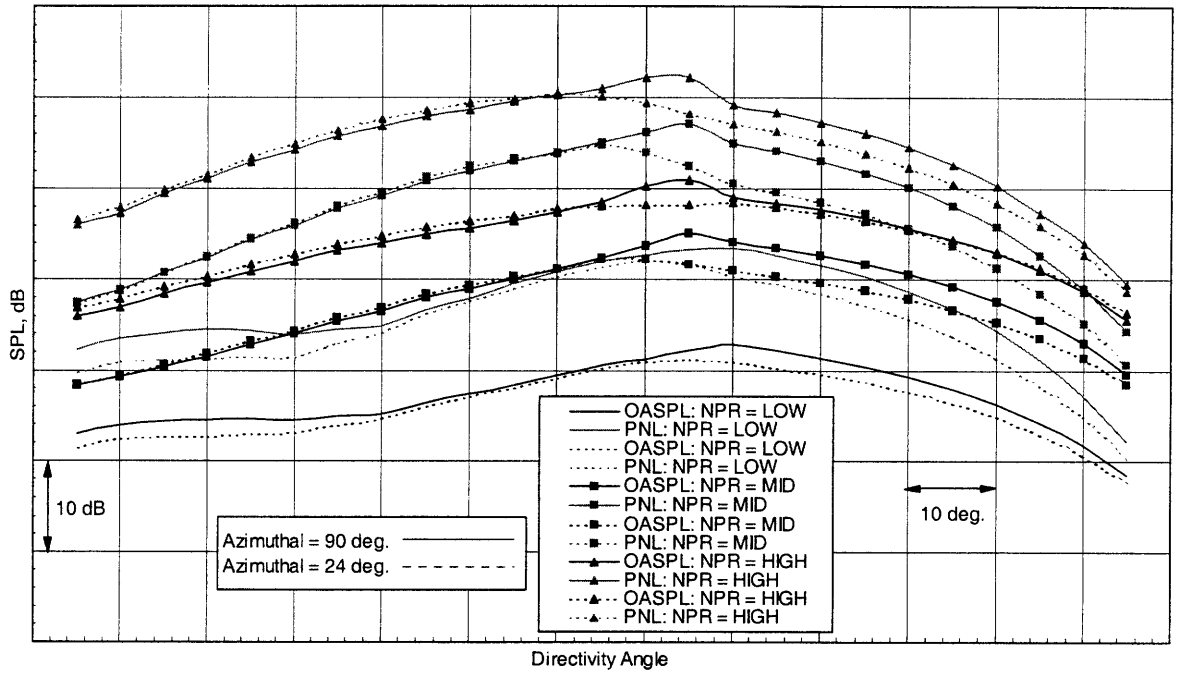

Figure 5-62: Steady-State OASPL and PNL Summary for HIGH MAR

Once again the variation with azimuthal angles is visible, but is less definitive than the LOW and MID MAR cases. Furthermore the directivity angle of the peak noise does not exhibit the same shift in the MID and HIGH MAR cases, as was seen in the LOW MAR case of Figure 5-60.

The last set of Figures, Figures 5-63 - 5-68, show variation with MAR at the same NPR and TTR conditions. From these figures, which once again show fly-over and sideline azimuthal angles in a left - right configuration, respectively, the large variation between the LOW and MID/HIGH MAR conditions can clearly be seen. The LOW MAR condition shows a drop off of about 10 dB at aft directivity angles.

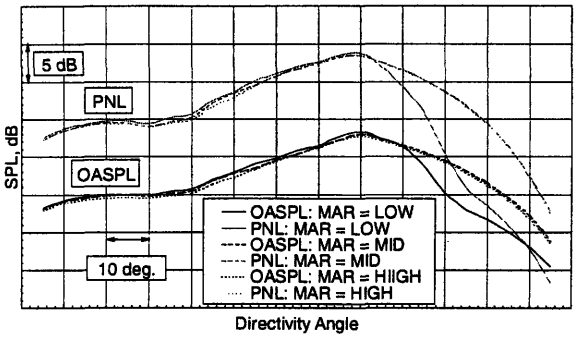

Figure 5-63: Steady-State OASPL and PNL Summary for LOW NPR and TTR, 90 azimuthal

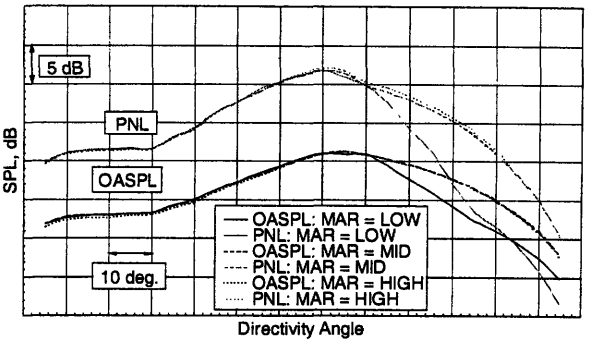

Figure 5-64: Steady-State OASPL and PNL Summary for LOW NPR and TTR, 24 azimuthal

Figures 5-65 and 5-66 show the variation with MAR at the MID NPR and TTR condition. Of the three cases, the MID jet conditions exhibit the least variation with MAR.

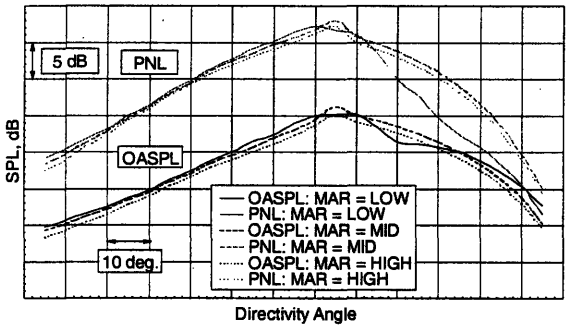

Figure 5-65: Steady-State OASPL and PNL Summary for MID NPR and TTR, 90 azimuthal

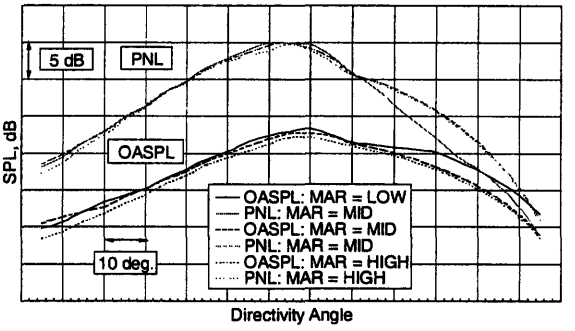

Figure 5-66: Steady-State OASPL and PNL Summary for MID NPR and TTR, 24 azimuthal

The figures show only about 1 - 3 dB deviation between MAR conditions at the MID NPR and TRR condition. However, it is worth noticing that the LOW MAR condition, which exhibits the most deviation in Figures 5-63, 5-64, 5-67, and 5-68, is the MAR condition that shows the most deviation in Figures 5-65 and 5-66. The LOW MAR condition is not as smooth as the acoustic signatures for the MID and HIGH MAR conditions.

The final two figures of the steady-state LSMS noise data are shown in Figures 5-67 and 5-68, which show OASPL and PNL versus directivity angle at the HIGH NPR and TTR jet conditions for the HIGH MAR case. The figures once again show a very pronounced deviation between the LOW and MID/HIGH MAR conditions. As opposed to Figures 5-63 and 5-64, where the LOW MAR condition was significantly lower than the MID and HIGH MAR cases, at the HIGH NPR and TTR conditions, the LOW MAR case is around 10 dB above the MID and HIGH cases at the aft directivity angles.

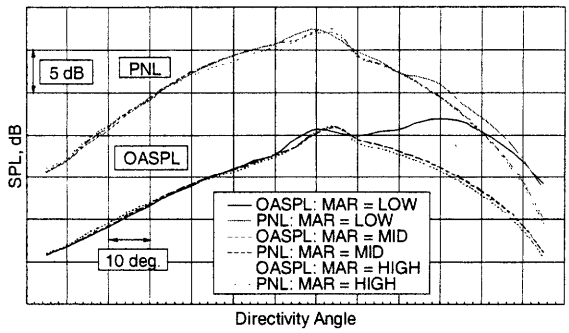

Figure 5-67: Steady-State OASPL and PNL Summary for NPR and TTR = HIGH, 90 azimuthal

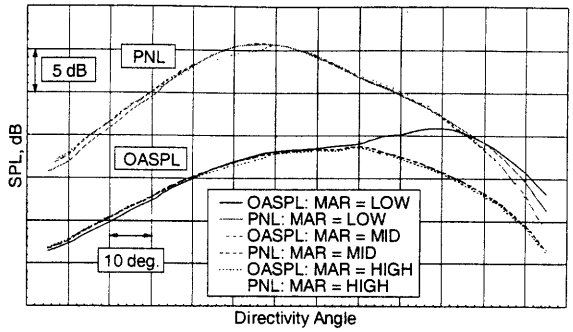

Figure 5-68: Steady-State OASPL and PNL Summary for NPR and TTR = HIGH, 24 azimuthal

The MID and HIGH MAR cases once again exhibit strong agreement with each other in magnitude and directivity over the entire range of directivity angles shown in the figures. Once again, at the writing of this thesis, it is not known whether this behavior with MAR is a result of some unidentified fluid dynamic phenomena occurring within the model, or is the result of an unknown acoustic data processing error. The next generation of steady-state acoustic tests on the LSMS model should provide insight into this deviation at the LOW versus MID and HIGH MAR conditions.

5.4.2 Comparison of Transient and Steady-State LSMS noise data

As of the writing of this thesis, the test matrix shown in Table 5.10 has not yet been completed. This section compares results from transient and steady-state tests performed on the LSMS model that have been obtained thus far.[20]

Figure 5-69 shows a comparison of transient noise data and steady-state data at the HIGH MAR and LOW NPR and TTR condition at 90 degree azimuthal angle. As can be seen from the figure, trends with magnitude and directivity angle are captured using the transient shock tube tests. Deviation between the steady-state noise data and the transient is typically on the order of 3 - 4 dB for this test condition. The transient data has a tendency to roll-off faster on the 110, 120, and 130 degree directivity angles than the steady-state noise spectra. Also present is the cross-over between the 110 and 120 degree directivity angles that was discussed in the previous section.

[20] The MID and HIGH conditions at 24 degree azimuthal angle are currently under investigation.

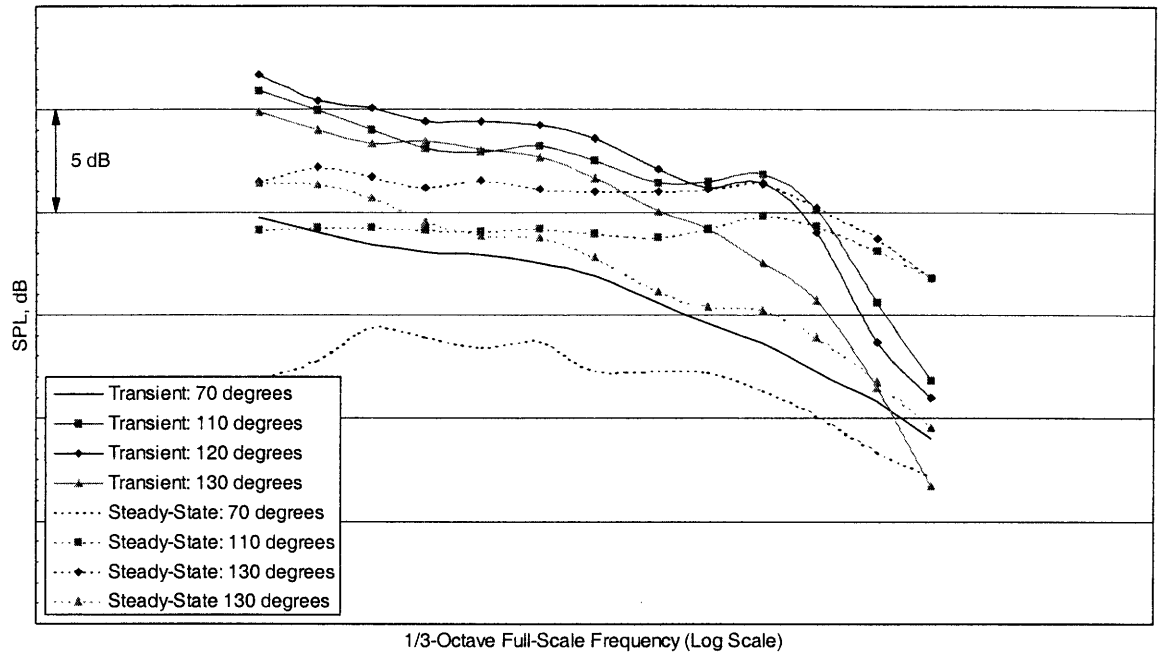

Figure 5-69: SPL versus full-scale frequency, LOW NPR and TTR, HIGH MAR, 90 azimuthal

The corresponding OASPL and PNL versus directivity angle data at the LOW NPR and TTR condition is shown for the LOW and HIGH MAR cases in Figure 5-70.

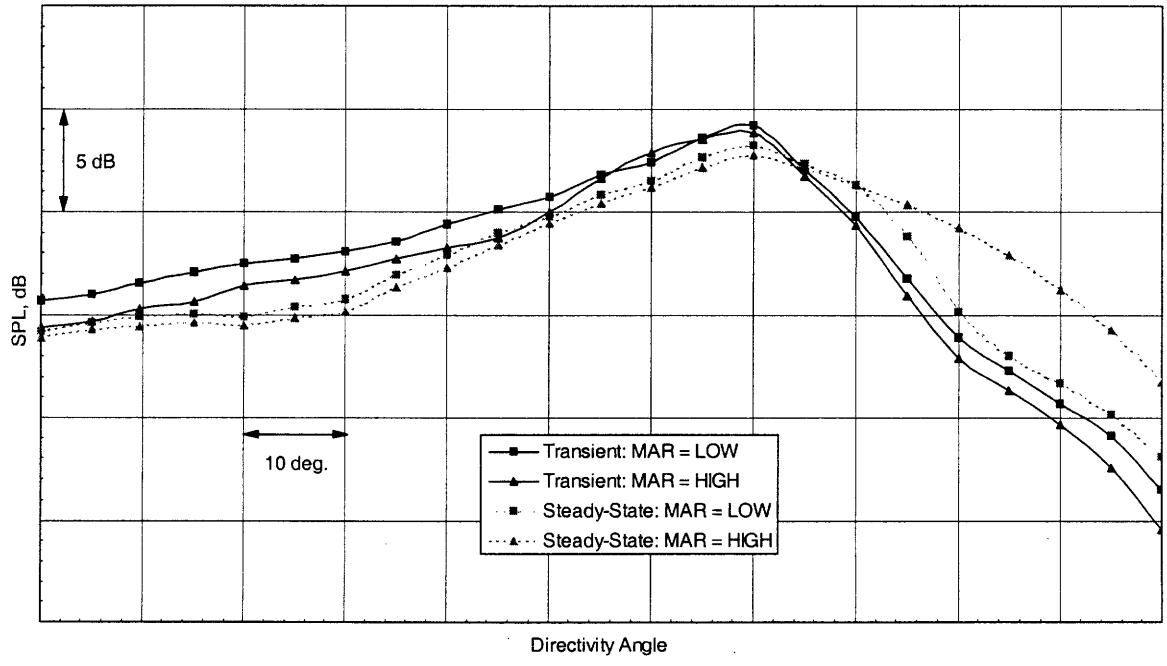

Figure 5-70: OASPL and PNL versus directivity angle, LOW NPR and TTR, 90 azimuthal

This figure shows that the transient data captures the noise peak at the same directivity angle as the steady-state data. The transient data tends to follow the LOW MAR condition in both cases and has a faster drop-off than the steady-state data at the HIGH MAR condition. The transient data also tends to show more variation with MAR than the steady-state data at the forward flight angles. Once again the large deviation in the steady-state data between the LOW and HIGH MAR conditions is unexplained. This deviation was discussed and shown in Section 5.4.1.

At the LOW NPR and TTR condition, the variation with azimuthal angle was also studied. Figure 5-71 shows SPL versus frequency for the LOW NPR and TTR condition at the LOW MAR case for the 24 degree azimuthal angle.

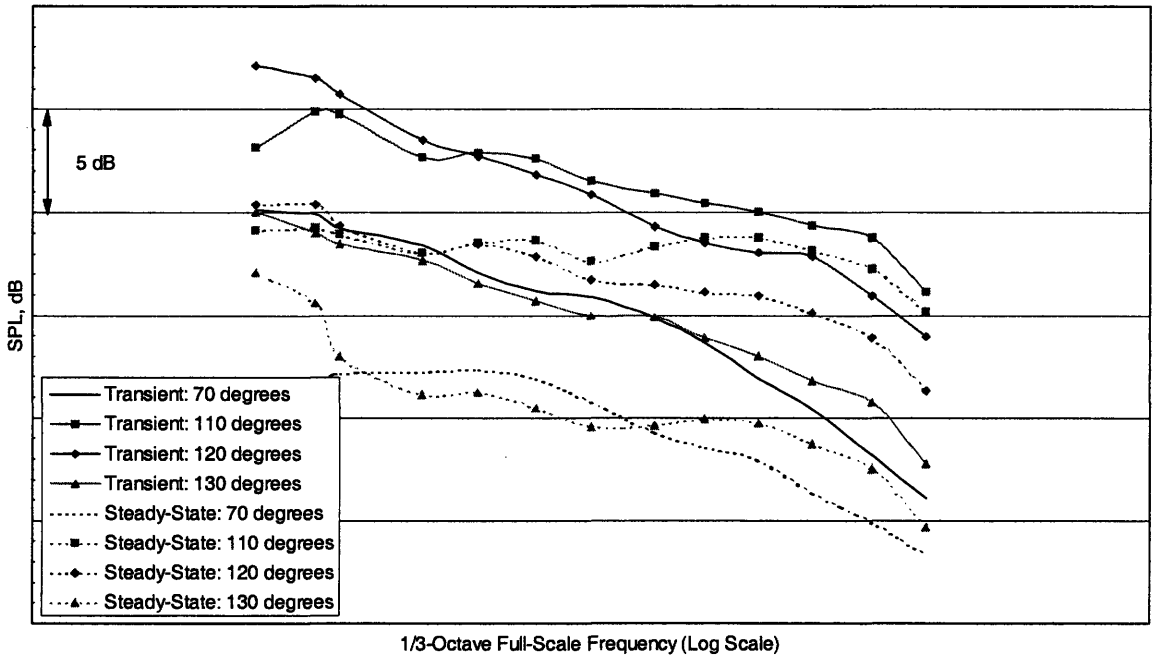

Figure 5-71: SPL versus full-scale frequency, LOW NPR and TTR, LOW MAR, 24 azimuthal

In this case, there is more deviation between the steady-state and transient noise data. As can be seen from the figure, most directivity angles deviate by 4 - 5 dB over the frequency range shown. The transient data does exhibit the same trends with frequency as the steady-state data, but is consistently higher.

Figure 5-72 shows SPL versus full-scale frequency at the LOW NPR and TTR condition, but now showing the HIGH MAR case. Once again, the deviation between the steady-state and transient data is on the order of 3 - 4 dB over the frequency range shown. The transient data exhibits the same trends with directivity angle, but once again the transient data is consistently higher than the steady-state, as was the case at the 90 degree azimuthal angle.

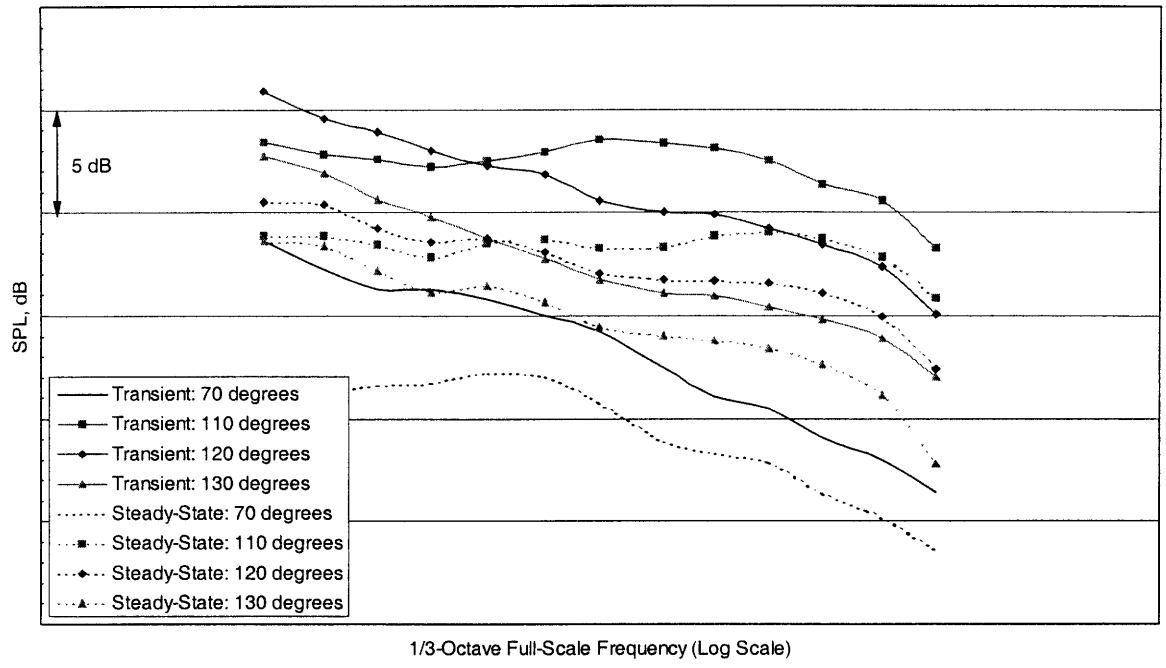

Figure 5-72: SPL versus full-scale frequency, LOW NPR and TTR, HIGH MAR, 24 azimuthal

The corresponding OASPL and PNL versus directivity angle plots for Figures 5-70 and 5-71 are shown in Figures 5-73 and 5-74.

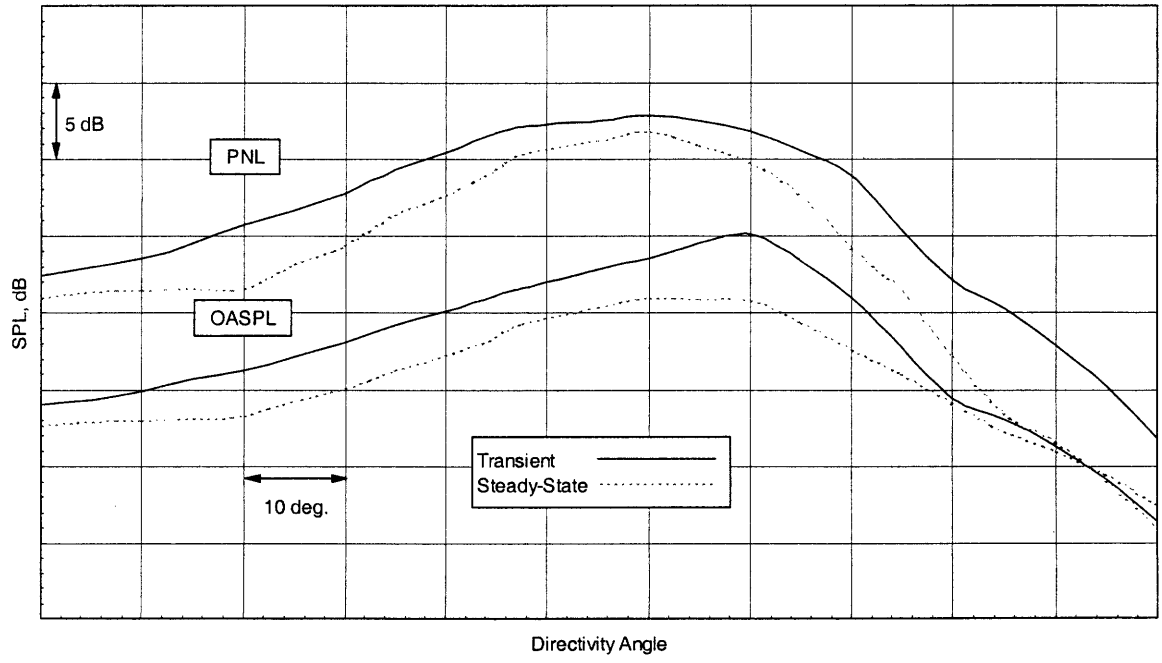

Figure 5-73: OASPL and PNL versus directivity angle, LOW NPR, LOW MAR, 24 azimuthal

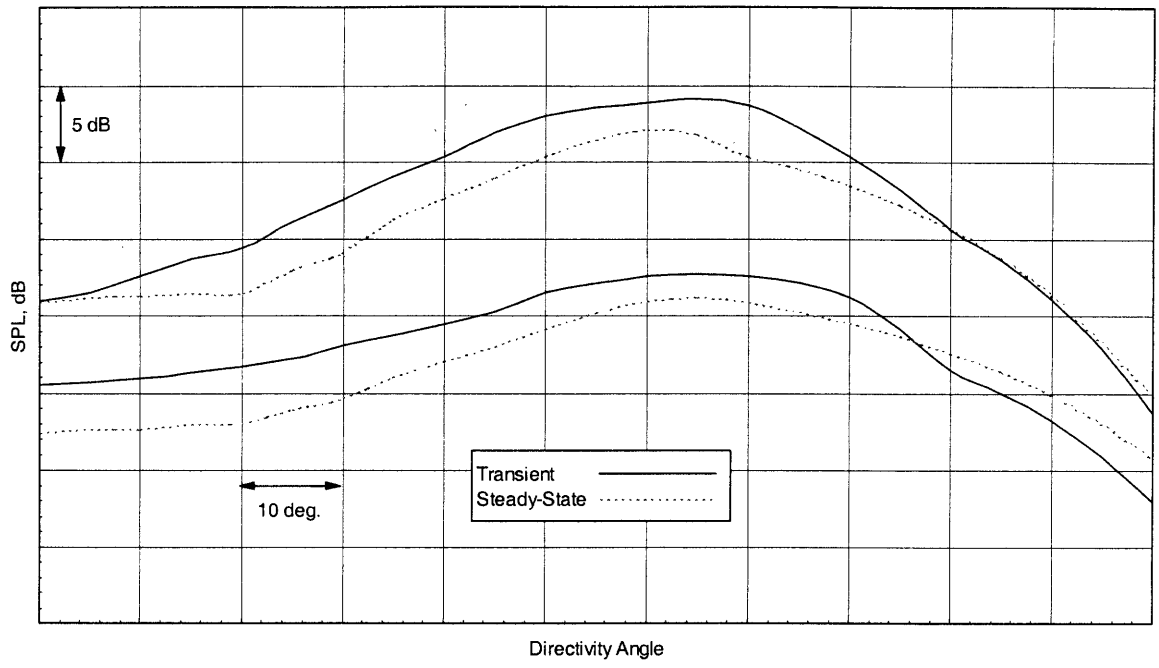

Figure 5-74: OASPL and PNL versus directivity angle, LOW NPR, HIGH MAR, 24 azimuthal

As can be seen from Figures 5-73 and 5-74, the transient data shows the same peak noise directivity angle as the steady-state data. The deviation between the transient and steady-state data for each case is about 3 - 4 dB. Comparing Figures 5-73 and 5-74 with Figure 5-70, it can be seen that the transient data exhibited more of a drop off with aft flight angles in the 24 degree azimuthal angle case compared with the 90 degree azimuthal angle measurement. This is in agreement with the azimuthal angle trends that were presented in Section 5.4.1. EPNL values for both the 90 degree and 24 degree azimuthal angles are about 2 - 3 EPNdB apart, with the transient values being higher. The difference in the steady-state EPNL, between the 90 degree and 24 degree azimuthal angles, is around 3 - 4 ENPdB. This is in agreement with the difference in EPNL values between the two azimuthal angles in the transient investigation. Further azimuthal angle tests are in progress at the MID and HIGH NPR and TTR conditions, over the entire range of MARs presented here. These remaining tests will help determine how well the facility can capture noise variation between the fly-over and sideline cases.

SPL versus directivity angle at the MID NPR and TTR condition at the HIGH MAR condition is shown in Figure 5-75. The MID NPR condition shows agreement with frequency of 2 - 3 dB over the frequency range shown for the aft flight angles, and about 4 dB deviation between the transient and steady-state on the 70 degree directivity forward angle. Once again, the transient data is consistently higher than the steady-state. The transient data appears to exhibit trends in magnitude and directivity with the steady-state noise data.

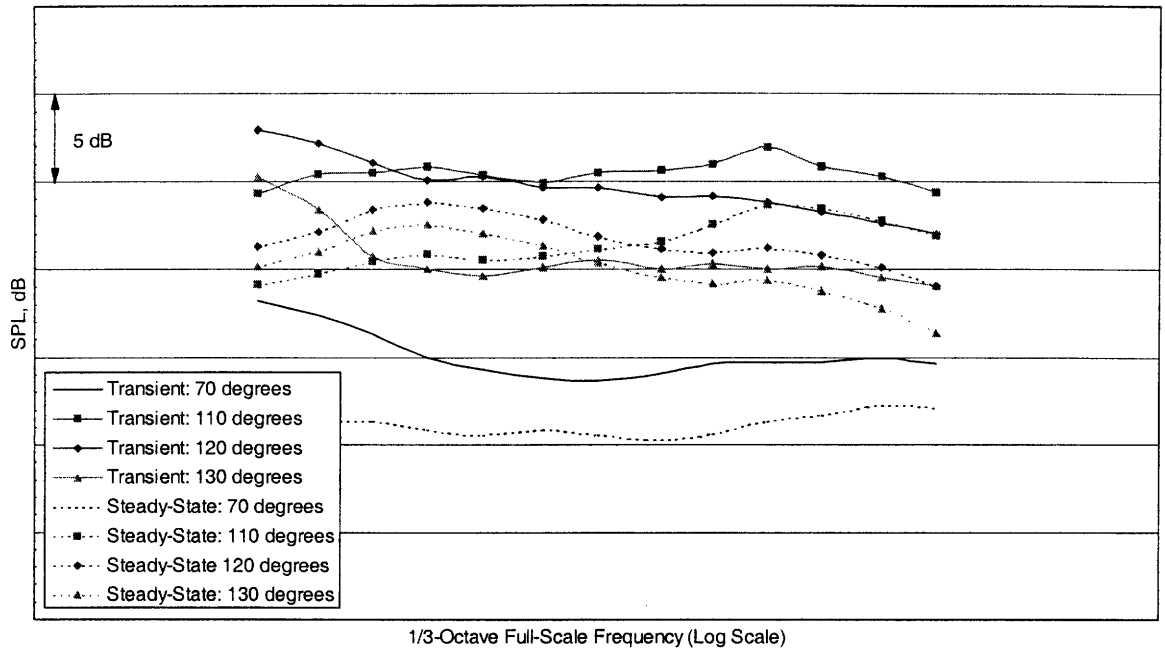

Figure 5-75: SPL versus full-scale frequency, MID NPR and TTR, HIGH MAR, 90 azimuthal

The corresponding OASPL and PNL versus directivity angle at the LOW NPR and TTR condition for each of the MAR cases studied is shown in Figure 5-76.

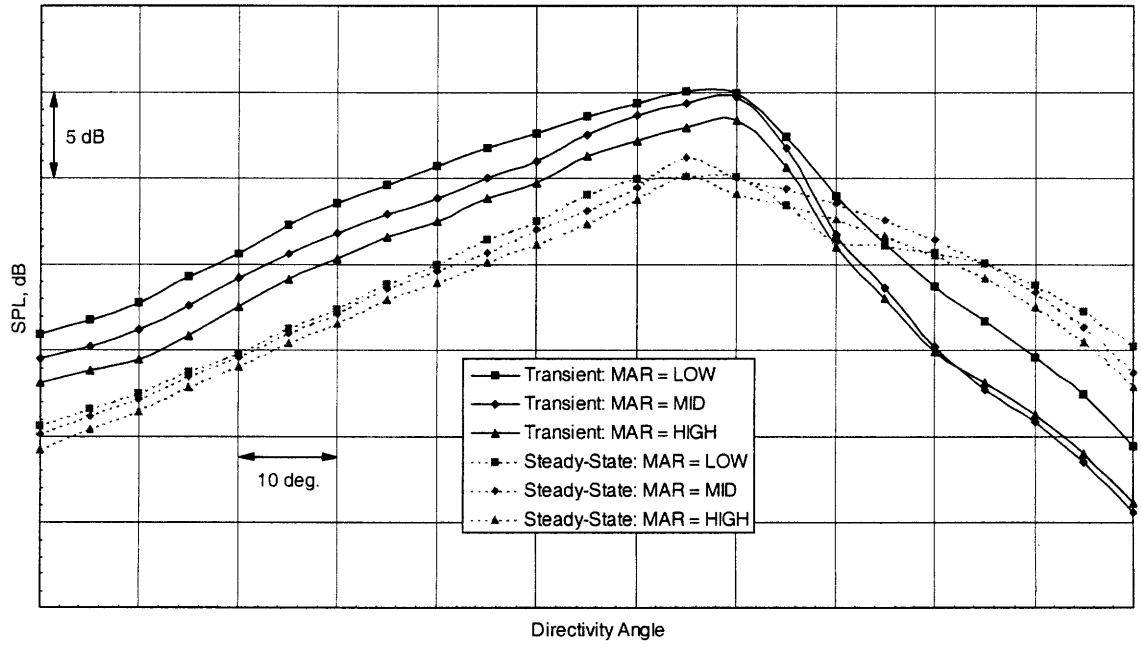

Figure 5-76: OASPL and PNL versus directivity angle at LOW NPR condition, 90 azimuthal

Once again, the transient data is consistently higher than the steady-state noise data by about 2 - 3 dB. At the MID NPR and TTR condition, as was seen at the LOW jet conditions, the transient data tends to fall-off more rapidly than the steady-state noise data at aft directivity angles. Variations with MAR are also over-accentuated in the transient data. The variation with MAR between cases is on the order of 2 dB, whereas for the steady-state data the variations with MAR are on the order of 1 dB between the LOW, MID, and HIGH cases. Both the transient and steady-state data exhibit the same noise peak with directivity angle. In this case, transient data agrees to within around 2 - 3 dB on the 70, 110 and 120 degree directivity angles and shows the most deviation, of around 4 dB on the most aft, or 130 degree directivity angle.

SPL versus frequency at the HIGH NPR and TTR condition is shown in Figure 5-77 at the LOW MAR condition. Once again it is worth noting that the steady-state LOW MAR case at the HIGH NPR and TTR condition shows deviation on the order of 10 dB with the MID and HIGH MAR cases. This is shown in Figure 5-67 for the 90 degree azimuthal angle case. Figure 5-77 shows that the agreement with steady-state and transient data is on the order of 2 - 3 dB for the directivity angles that are shown. Whereas the transient data is typically above the steady-state data in magnitude, it can be seen that for the 130 degree directivity angle case, the steady-state data is now above the transient. This effect takes place in the aft directivity angle region where the steady-state data is substantially higher at the LOW MAR case than corresponding steady-state data at the MID and HIGH MAR cases.

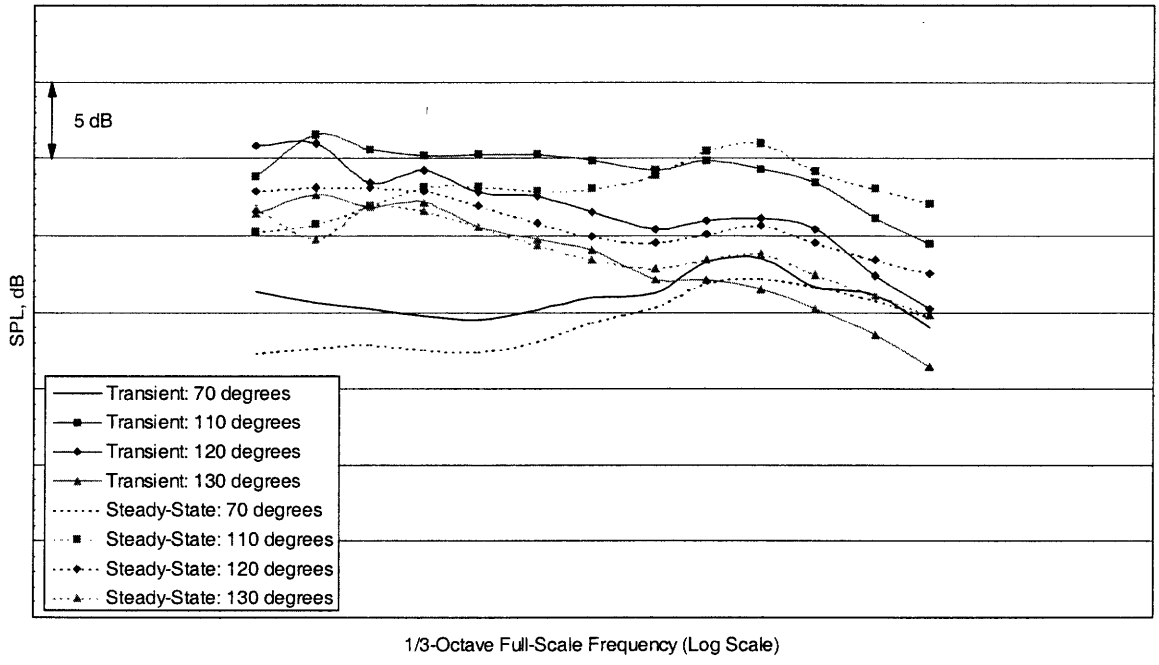

Figure 5-77: SPL versus full-scale frequency, HIGH NPR and TTR, LOW MAR, 90 azimuthal

SPL versus frequency at the HIGH NPR and TTR condition is shown in Figure 5-78 at the HIGH MAR condition. Figure 5-78 shows agreement between the steady-state and transient noise data to within 2 - 3 dB on all directivity angles. Agreement with magnitude is also present.

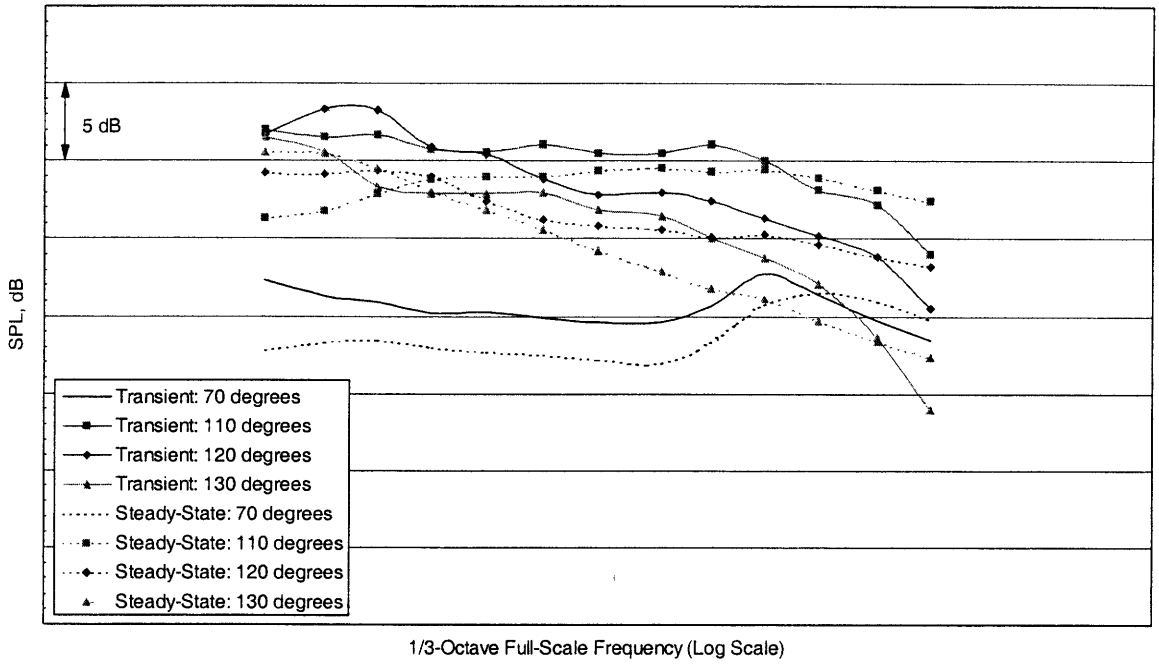

Figure 5-78: SPL versus full-scale frequency, HIGH NPR and TTR, HIGH MAR, 90 azimuthal

Also apparent in the transient data is the cross-over between the 110 and 120 degree angles that was discussed in Section 5.4.1. Thus far in the LSMS investigation, the HIGH NPR and TTR condition at the HIGH MAR case, has shown the best agreement with the steady-state noise data.

The corresponding OASPL and PNL versus directivity angle plots for Figures 5-77 and 5-78 are shown in Figures 5-79 and 5-80. In Figure 5-79, the transient and steady-state noise data exhibit the same peak noise directivity angle. However, at more aft directivity angles, the steady-state data at the LOW MAR cases deviates significantly from the transient noise data. In contrast to the LOW NPR condition, where the transient data tended to follow the spurious LOW MAR case, at the HIGH NPR condition, the transient data does not follow the LOW MAR trends of the steady-state data, but exhibits a more rapid roll-off with aft directivity angles analogous to that seen on the LOW NPR condition.

Once again, it is interesting to notice that as in the LOW and MID NPR and TTR conditions, the transient data at the more aft directivity angles falls off faster than the steady-state data. From the corresponding frequency plots it was shown that the transient data rolled-off faster with frequency than the steady-state data at these angles, explaining the behavior of the OASPL and PNL curves at these angles. This is consistent with all cases examined thus far.

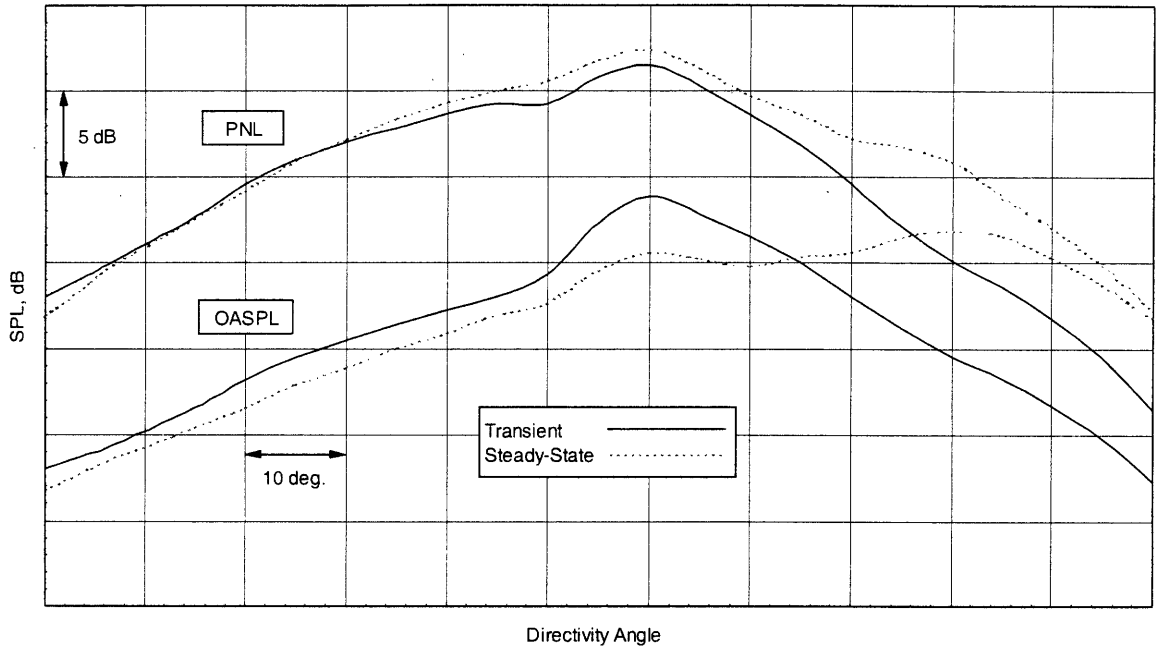

Figure 5-79: OASPL and PNL versus directivity angle at HIGH NPR, LOW MAR, 90 azimuthal

Figure 5-80 also shows that the transient and steady-state noise data peak at around the same directivity angle, and the transient data shows agreement in directivity on OASPL to around 2 - 3 dB at each angle.

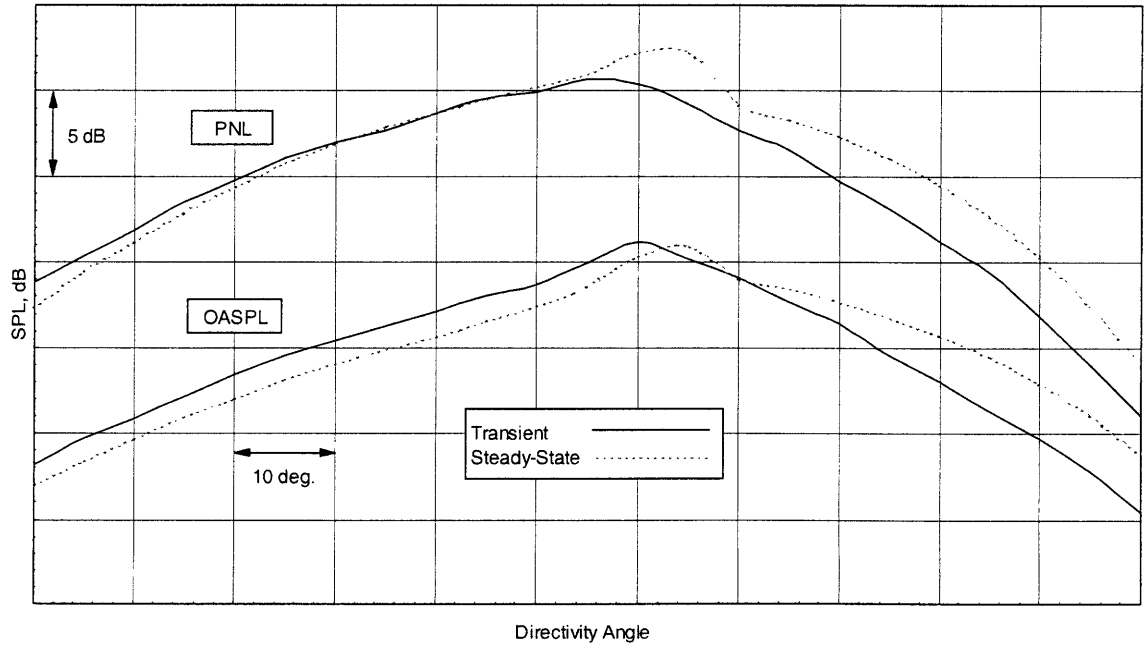

Figure 5-80: OASPL and PNL versus directivity angle at HIGH NPR, HIGH MAR, 90 azimuthal

5.4.3 Summary of LSMS Acoustic Investigation and Facility Assessment

This section summarized the LSMS acoustic performance over the range of frequencies, nozzle pressure ratios, total temperature ratios, MARs, and azimuthal angles relevant to the development of the HSCT mixer-ejector nozzle. The LSMS results obtained thus far should still be considered preliminary, in that issues associated with the complex fluid mechanic behavior of the device are still under investigation. Some of the results of the preliminary comparison between transient and steady-state noise data for the LSMS nozzle are summarized below:

- The transient and steady-state noise data agree to within 2 - 5 dB on SPL versus full-scale frequency, for all NPR and TTR, MAR and azimuthal angles studied thus far.
- The transient data tends to drop-off faster than the steady-state data at aft directivity angles, but on the whole is high, by about 2 - 3 dB over the steady-state noise data.
- Variations with MAR are more pronounced in the transient data. Variations with MAR were typically found to be on the order of 2 dB, whereas the steady-state data shows variation of around 1 dB. It is hoped the enigmatic acoustic behavior associated with the LOW MAR condition will be clarified during future LSMS steady-state tests.
- Transient and steady-state data peaked at nearly the same directivity angle for all cases tested.
- Variation of azimuthal angle with directivity for the transient data was in agreement to the steady-state trends.
- EPNL values were typically 2 - 4 EPNdB higher for the transient data as compared to the steady-state noise data. The difference in EPNL values between the LOW, MID and HIGH NPR and TTR conditions showed agreement to about 1 - 2 EPNdB between the transient and steady-state data. Transient EPNL values were also in agreement with trends in MAR and azimuthal angle seen in the steady-state noise data.
- The use of multiple runs was found to reduce the uncertainty associated with making transient acoustic measurements and was found to be beneficial for convergence to the steady-state noise data for up to 30 - 35 milliseconds of data, or 2 - 3 shock tube shots, depending on desired jet conditions.
- Run-to-run repeatability was on the order of 1.0 dB on a test-to-test basis, somewhat of a poorer repeatability performance than the ASME nozzles, which exhibited better than 0.5 dB on a run-to-tun basis.

Deviations between the transient and steady-state noise may be the result of a number of effects. Mixer-ejectors, such as the LSMS nozzle, are complicated fluid mechanical devices that are very sensitive to small changes in geometry and operating condition. Differences in throat area, Reynolds number, lobe

trailing edge thickness[21] and separation effects, may play a role in the differences seen between the transient and steady-state noise data. Further investigation is underway to study the sensitivity of these parameters.

5.5 Chapter Summary

The underlying purpose of Chapter 5 is to provide an answer to the thesis question, as to whether or not a transient shock tunnel facility can be utilized to acquire useful acoustic data at conditions relevant to the HSCT mixer-ejector development program. The answer to this question was determined by performing a series of comparisons to steady-state noise data that were obtained both at the MIT facility for small-scale nozzles and at Boeing LSAF for larger ASME conic nozzles and LSMS mixer-ejector nozzles. Some selected results are summarized below:

- The first comparisons that were made involved small-sized ¼ to ¾ inch exit diameter nozzles, which were sized to be run at steady-state as well as under transient shock tube conditions. The results from these nozzles indicated that over a given full-scale frequency range of around 63 - 1250 Hz, the acoustic signatures between transient and steady-state tests exhibited agreement to within ± 2 dB.
- The ASME nozzles provided the first test as to the transient shock tunnel facility's viability to capture frequencies relevant to the HSCT over a range of nozzle pressure ratios and total temperature ratios that were investigated at the steady-state facility. Generally, the transient noise data agreed to within ± 2 - 3 dB over most directivity angles, and demonstrated agreement with the steady-state noise data in both magnitude and directivity on OASPL and PNL versus directivity angle plots. Also shown was that multiple runs could be used to reduce the uncertainty associated with making transient acoustic measurements in accordance with Section 4.3.
- Transient testing of the LSMS model did capture many of the trends associated with the steady-state noise data. SPL versus frequency results were typically on the order of agreement of 2 - 5 dB between the transient and steady-state noise data. In general, the results of the transient tests for the LSMS mixer-ejector model do not compare as well as the transient versus steady-state ASME conic nozzle noise signatures. However, these results should still be considered preliminary, as the several issues associated with the complex fluid mechanic behavior of the mixer-ejector model are still being resolved.

[21] The thickness of the lobe trailing edges on the LSMS model tested in the transient facility is approximately twice as thick as those tested in the steady-state. This is associated with robustness and manufacturing of the scale of the nozzle tested in the transient facility.

- Given a new or radical lobe design or ten different chute racks, it appears that transient testing can be employed as a rapid way to ascertain which are the most promising chute racks, or whether or not that radical concept provided significant noise reduction.
- Repeatability of acoustic measurements was on the order of ± 0.5 dB on a test-to-test basis for the small-scale and ASME conic nozzles, and ± 1.0 dB on a test-to-test basis for all LSMS nozzle.

The facility can serve as a valuable tool for conducting jet noise research, with the cost of performing high temperature jet noise experiments being reduced by an order of magnitude. The short duration of the test time enables the nozzles to be made from inexpensive, rapid-prototyping methods and materials. Parametric testing can therefore be performed more economically and faster than in steady-state facilities.

Chapter 6

Synopsis of Mixing Measurement and Thrust Diagnostics

This chapter presents a brief discussion of two transient diagnostic systems that are currently being developed for the MIT shock tunnel facility. The systems are designed for optical flow mixing measurement and thrust measurement for the study of mixer-ejector type nozzles as shown in Figures 2-6, 2-7 and 2-8. More details of these systems can be found in Reference [13].

6.1 Optical Mixing Diagnostics

This section contains a discussion of an optical flow mixing measurement system under consideration for the MIT shock tunnel facility. Figure 6-1 shows some of the details associated with the mixing of two co-flowing streams in a typical lobed mixer application.

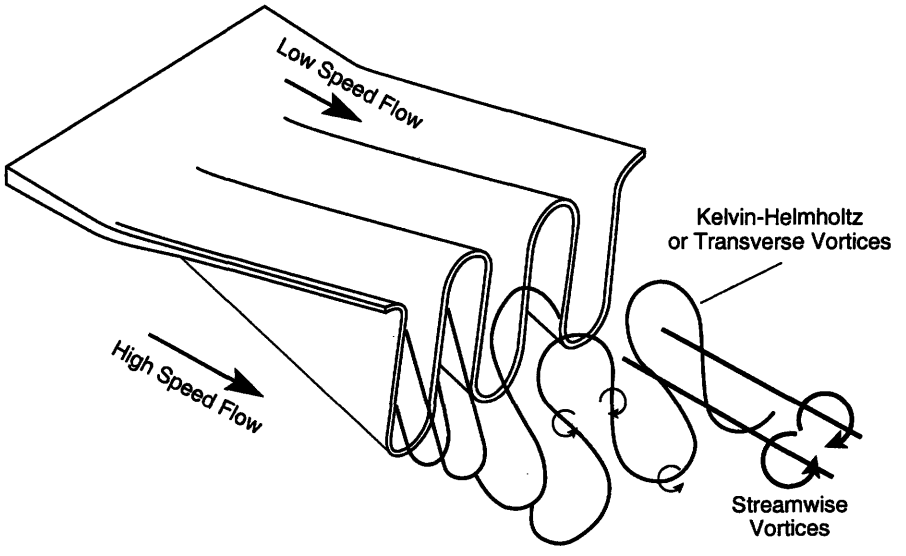

Figure 6-1: Schematic of mixing process associated with a typical lobed mixer

Much of the acoustic and fluid dynamic performance of a mixer-ejector nozzle is closely related to the details of this complex mixing process. A summary of the mixing processes associated with such lobed

mixers was presented in Section 1.1, with many more details found in References [51], [52]. A measurement system based upon Mie-scattering was judged to be most suitable for optical mixing measurements in the transient facility. The proposed system is estimated to deliver density measurements to within 5% with an optical resolution on the order of 5 - 10 mm, dependent upon imaging area, for a cost on the order of $100,000.

6.1.1 Theoretical Background

The basic idea of flow tracer imaging methods is to seed the flow of interest with particles that will follow the motion of the flow and be visible to the imaging apparatus. To accomplish this, the tracers must fulfill three conditions:

1. small enough to follow the motion of the flow
2. sufficiently numerous to allow measurements throughout the flow field
3. visible to the imaging system

Previous experience has demonstrated that a particle diameter of less than 2 microns is necessary to strictly follow the turbulence found in a 20 m/s flow, [3]. In transonic flow, the particles must have a diameter on the order of 0.2 microns to precisely follow the flow field, [53].

Mie-scattering occurs whenever light is incident on particles with a diameter similar to or greater than the wavelength of the incident light. In such a case, the incident light is scattered in all directions, though not with uniform intensity. All wavelengths are scattered in all directions through Mie-scattering. Visualization may be improved if the measured intensity can be made independent of particle velocity. This is accomplished by shortening the exposure time of the imaging device so that the seeded particles appear motionless, i.e. are contained within one pixel of the image. Shortening the exposure time requires an associated increase in the intensity of the light source. However, through such a method the presence and qualitative characteristics, primarily density, of the seeded flow may be determined, thus allowing useful mixing measurements to be made on the flow field.

6.1.2 Attempted Techniques

In the course of evaluating the feasibility of optical measurements for the MIT shock tunnel, three different imaging methods were evaluated: focused-Schlieren, shearing interferometry, and a Mie-scattering imaging system. The Mie-scattering system was found to be most suitable for the mixing measurements to be made on the shock induced nozzle flows. The focused-Schlieren system was used to develop the triggering system necessary for the other diagnostics and to confirm the development of nozzle flow starting. The shearing interferometer was designed to give density field measurements for a low cost and system complexity, and was also used to diagnose the triggering system. This section will discuss the focused-Schlieren and the Mie-scattering systems.

6.1.2.1 Focused-Schlieren System

The focused-Schlieren system uses the deflection of light rays due to changes in index of refraction. A detailed description of the focused-Schlieren system, as well as its relation to traditional Schlieren systems, is given in References [53], [54], [55]. Light is projected through a large Fresnel lens, a source grid of equally spaced lines, and then through the flow field to be imaged. If changes of refractive index exist within that flow field, some of the light will be deflected from its original path. On the other side of the flow field, an imaging lens directs light from a specific plane within the flow, onto a cut-off grid created from the source grid, which removes undeflected light. This allows only the deflected light to continue into the imaging plane.[1] A schematic of the focused-Schlieren setup used in this investigation is shown in Figure 6-2.

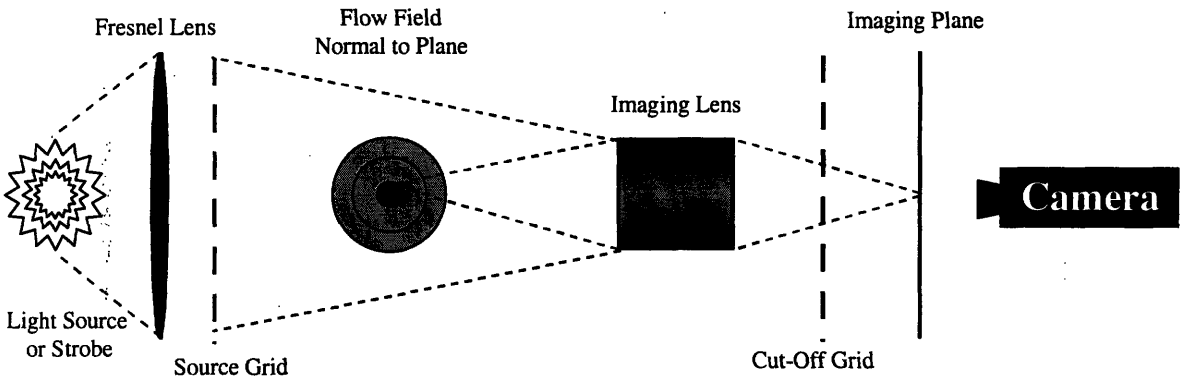

Figure 6-2: Focused-Schlieren system schematic, [54]

Due to the nature of the system, the focused-Schlieren method requires large changes in the refractive index to produce clear images. This effect is accentuated in the focused-Schlieren system because the image is drawn from deflections which occur within a plane of the flowfield, whereas the traditional Schlieren system creates an image from the bending of the light experienced throughout the flowfield. Thus the change in refractive index must be large within a narrow plane rather than across the entire jet. Due to this effect, shock waves are the most readily distinguishable flow features using a focused-Schlieren system.

A ¼ inch diameter axisymmetric nozzle[2] was used with images acquired during both steady-state and transient operation. The results of the focused-Schlieren diagnostics are presented in Figures 6-3 and 6-4.

---

[1] In practice, there is always some inaccuracy or misalignment between the source and cut-off grids, but this is a minor problem because the refracted light merely appears as relative lightening/darkening of the background illumination

[2] These nozzles are described in Section 2.1.2.1.

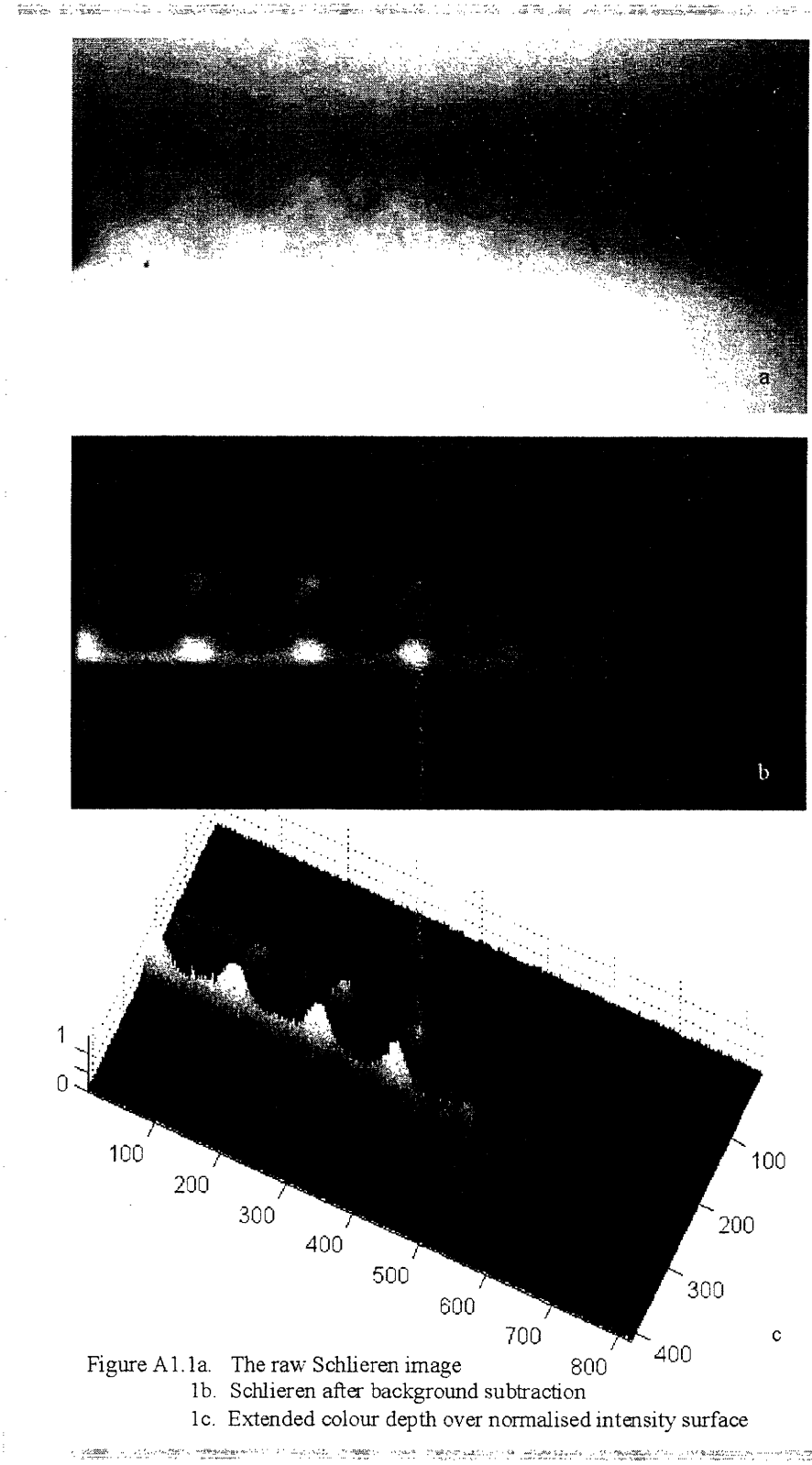

Figure A1.1a. The raw Schlieren image
1b. Schlieren after background subtraction
1c. Extended colour depth over normalised intensity surface

Figure 6-3: Steady-State: a) raw Schlieren image, b) Schlieren after background subtraction, and c) extended color depth over normalized intensity surface

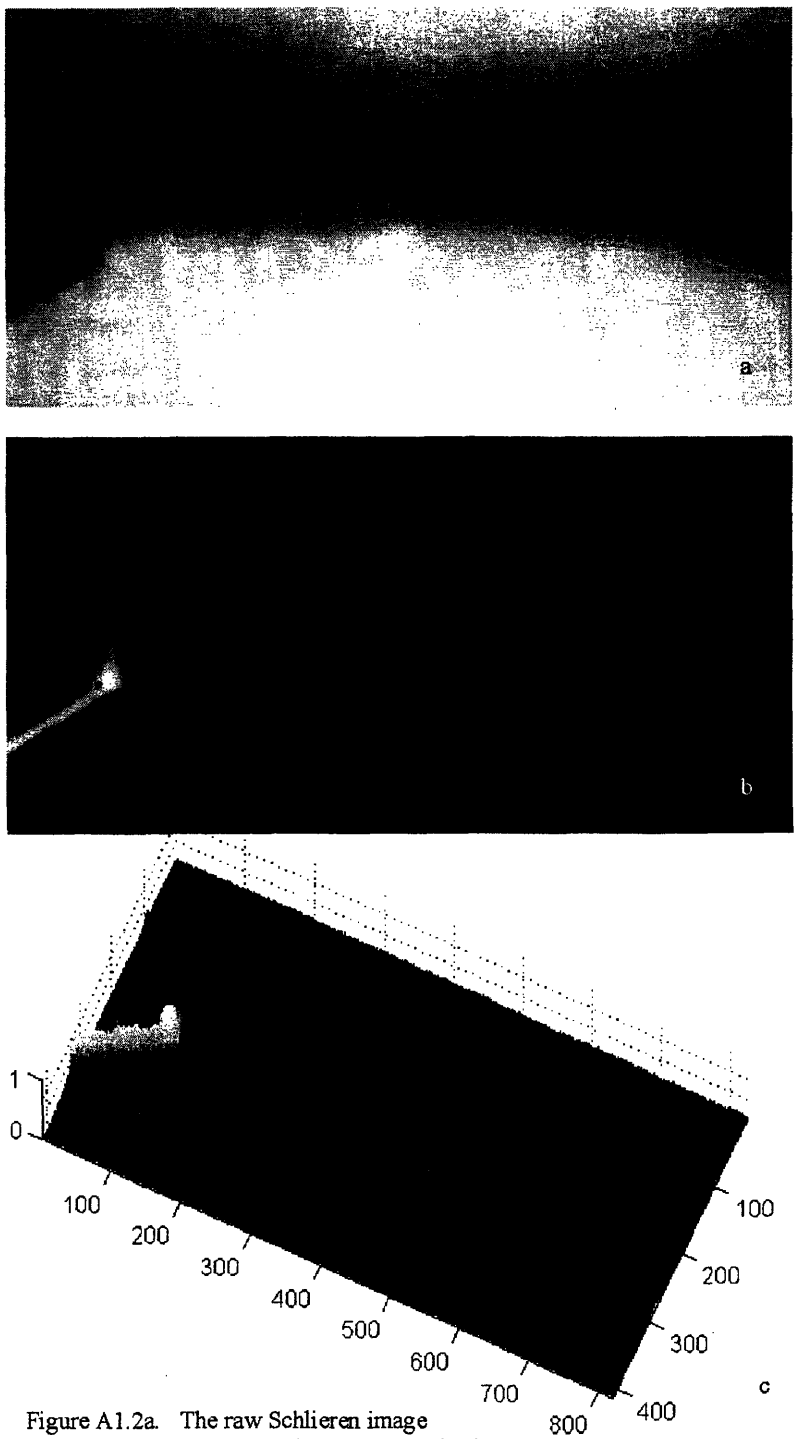

Figure A1.2a. The raw Schlieren image
2b. Schlieren after background subtraction
2c. Extended colour depth over normalised intensity surface

Figure 6-4: Transient: a) The raw Schlieren image, b) Schlieren after background subtraction, and c) extended color depth over normalized intensity surface

The shock structure is the most apparent feature obtained during the steady-state tests, which gives an idea of the capabilities presented by the focused-Schlieren method. The transient image is less defined, although the shock structure is still visible. This is partially due to the fact that there is a less pronounced difference between the refractive index of the transient jet and the surrounding atmosphere than in the steady-state case. The steady-state jet is at a NPR of approximately 3.0, but a TTR of unity.[3] This gives a total density ratio of approximately 3.0 between the jet and the surrounding air. The transient case is tested at a NPR and TTR of approximately 2.5. This leads to a total density ratio of approximately 1.0 between the jet and the atmosphere. This difference in the density gradient between the two flows makes it impossible to make use of the images as a comparison tool between the steady-state and transient methods of testing.

6.1.2.2 Mie-Scattering System

The theoretical basis for mixing measurements made utilizing Mie-scattering was presented in Section 6.1.1 The experimental set-up of such a system is shown in Figure 6-5.

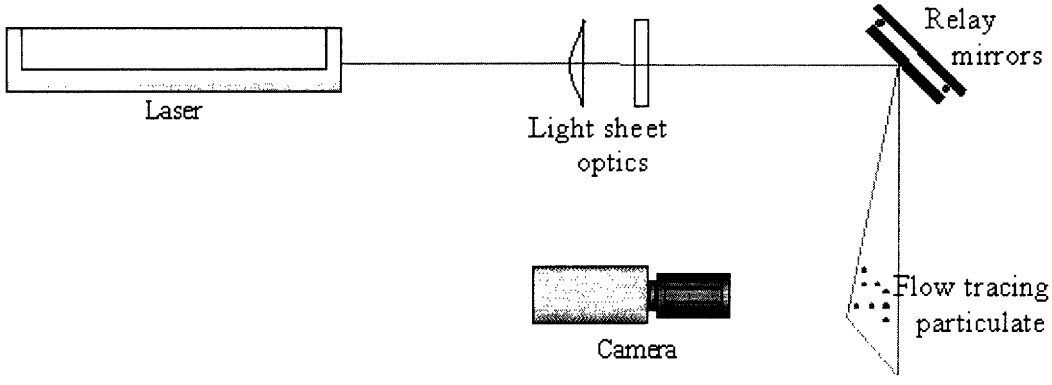

Figure 6-5: Mie-Scattering system schematic

The seed selected for these tests was 0.4 micron diameter styrene particles suspended in water. As mentioned above, seed with a diameter on the order of 0.2 microns, is required to precisely follow the flow through a shock system. The 0.4 micron seed was used for initial proof-of-concept testing since it was more readily available. Seeding was accomplished in two stages to ensure sufficient seed density. First, the driven section was seeded while still at atmospheric pressure until the seed had begun to leak from the nozzle at a sufficient density. Compressed air was bled through a TSI six-jet seeder and into the driven section. This was accomplished through a tap in the wall of the driven section located about 6 m from the nozzle end of the tunnel. Once sufficient seed density had been obtained in this way, preparation for the transient tests began. The driven section was pumped down to 10% below its final value to allow for the

[3] Once again, no heat transfer occurs during the steady-state nozzle operation, thus TTR = 1.0.

secondary seeding to occur. The secondary seeding was begun immediately before the tunnel was ready to be fired, and more seed was added as air leaked through the seeder and into the shock tunnel to bring the driven pressure up to its prescribed value. In this way, the seed densities necessary for testing were consistently achieved.

6.1.2.3 Argon-Ion Laser and Digital Imaging Equipment

A continuous-wave, 10 W all-lines Argon-Ion laser was used to illuminate the flow in the experimental effort. The image was captured by a 30 Hz, digital, 8-bit camera coupled to a shuttered and gated image intensifier. The image intensifier utilized a 60 mm 1:2.8 Nikon lens to focus upon the light sheet. A theoretical gain of 100,000 is possible with this image intensifier, but the practical gain limit is on the order of 1,000. Based upon a single electronic TTL trigger, the image intensifier may be programmed for up to 63 independent exposures, each with a minimum duration of 20 nanoseconds and a minimum separation of 10 nanoseconds. The digital camera used was a 1,000 x 1,000 triggerable, progressive scan digital camera operating at 30 Hz. This operating requirement limited the images that the image intensifier could be programmed to acquire, as only one frame could be acquired by the digital camera during the test time, with one exception. The digital camera, while generally operating at 30 Hz, has the ability to take a single, separate exposure of ¼ millisecond duration immediately following the trigger, followed by the standard, 30 millisecond frame. Thus after a single trigger, a pair of images may be obtained. However, the utility of this feature is limited because the gain on the image intensifier may not be adjusted in the microsecond or less between the frames.

The image intensifier and camera were mounted at 90 degrees to the light sheet, at standoff distances ranging from 2 inches to 32 inches for nozzle sizes from ¼ inch to 4 inches, respectively. A beam-stop was added to prevent the light sheet from causing extraneous reflections. To minimize background illumination, a matte-black screen was placed behind the light sheet in the field of view. Furthermore, the light-sheet was trimmed to prevent reflections off the nozzle being tested. Additionally, the nozzles were also spray-painted black to eliminate reflections, as can be seen in figure 2-4. The triggering system was based upon the passage of the incident shock wave through the test section of the shock tunnel. As the shock wave passed, pressure transducers detected the rapid pressure rise, which initiated a TTL trigger to the imaging system.

6.1.3 Results of Mie-Scattering Experiments

Four sets of images were obtained using the argon-ion laser set-up: ¼ inch nozzle at steady state, ¼ inch nozzle transient test, 0 - 1 diameters downstream for the $1/10^{th}$ scale ASME nozzle transient test, and 1 - 3 diameters downstream for the $1/10^{th}$ scale ASME nozzle transient test. In each case, an instantaneous image of 30 microseconds exposure and a time-average image of 5 milliseconds exposure were obtained.

The ¼ inch nozzle, steady-state images were obtained by utilizing the tunnel flushing air. The jet may be seen exiting the small-scale nozzle in Figure 6-6. Maximum intensity is achieved several diameters downstream after the flow has expanded. This counter-intuitive result is explained by the fact that the intensity is not the result of illuminating the styrene seed, but is rather reflection from water vapor. The compressed air used to maintain the steady-state jet is not heated, so this jet has a TTR of approximately 1.0. As the jet expands and reaches atmospheric pressure, the temperature within the jet drops along with the pressure accordingly, causing condensation within the jet.

In Figure 6-7, the transient ¼ inch nozzle tests support this conclusion, as the maximum intensity is realized within the jet before the expansion and mixing process occurs. The nozzle is being supplied in this case by test gas at NPR = 2.35, TTR = 2.35. While it is a useful diagnostic tool, the ¼ inch nozzle is far from the model scales desired for HSCT testing. The 4 inch exit diameter nozzle, $1/10^{th}$ scale, is more representative of mixer-ejector nozzle models to be tested in terms of scale and exit area. The 5 millisecond time-average exposure in Figure 6-8 shows the jet profile exiting the nozzle. These optical diagnostics demonstrated that a Mie-scattering system is a feasible and effective way to obtain mixedness measurements of the flow in the ejector portion of a mixer-ejector model. As can be realized from the above discussion, several difficulties still remain to be addressed in the implementation of such a system. A system which addresses these shortcomings is described in detail in Reference [13].

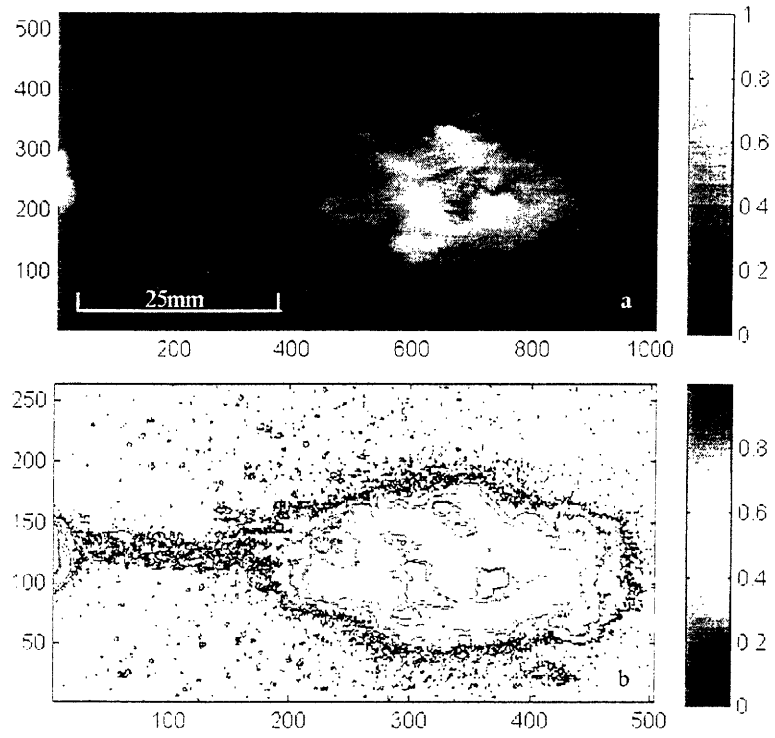

Figure A2.1a.b. 30 μs exposure. Normalised grayscale and contour plots respectively.

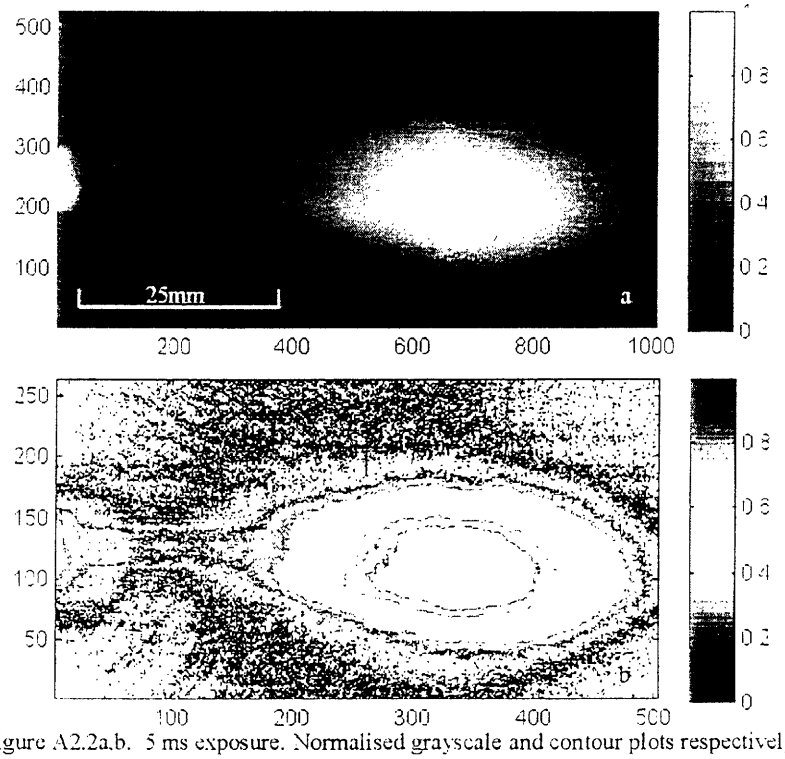

Figure A2.2a.b. 5 ms exposure. Normalised grayscale and contour plots respectively

Figure 6-6: ¼ inch nozzle exit plane: 30 microseconds and 5 milliseconds exposure. Normalized gray-scale and contour plots, respectively

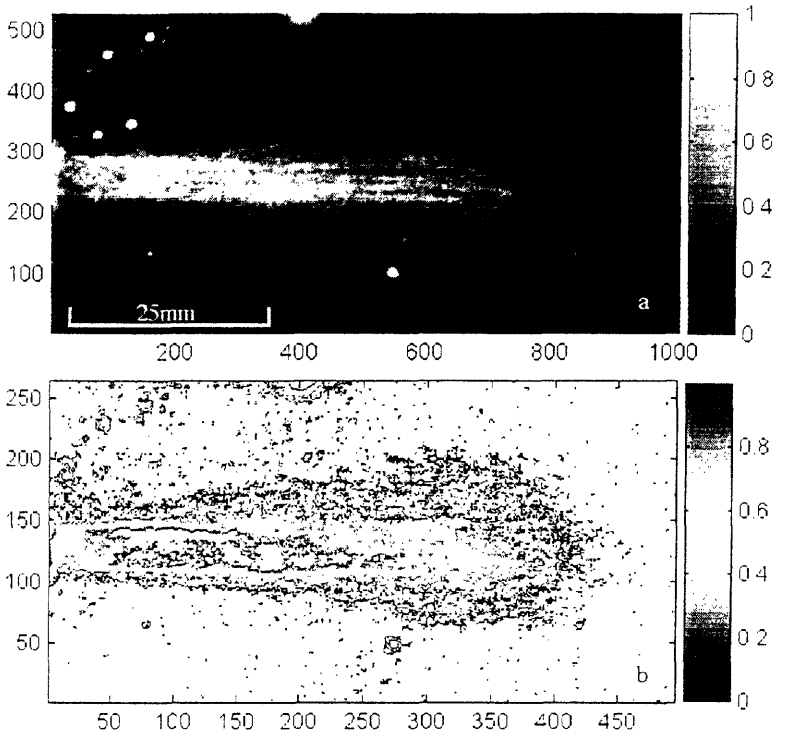

Figure A2.3a,b. 30μs exposure. Normalised grayscale and contour plots respectively.

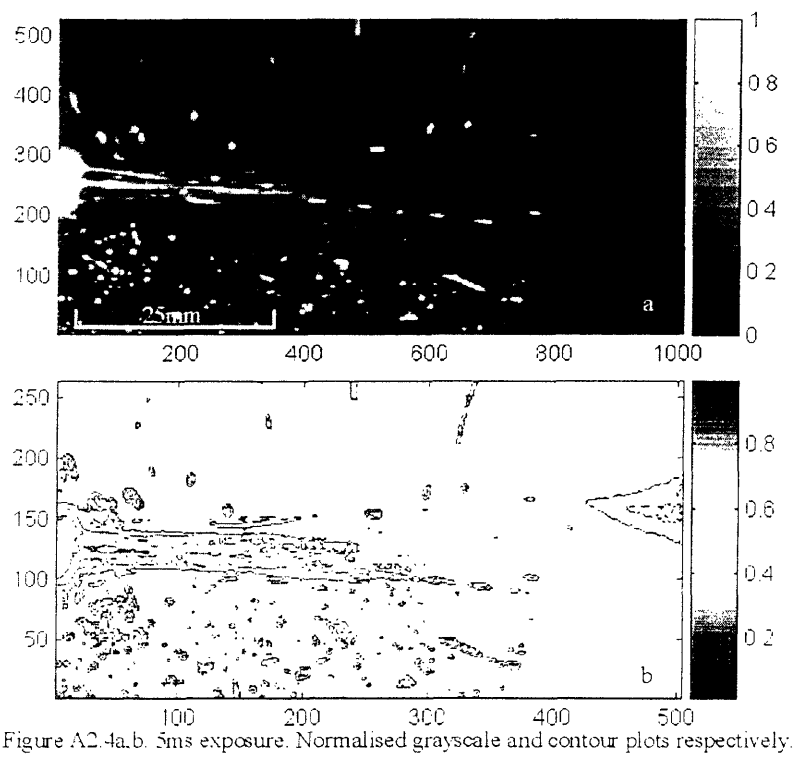

Figure A2.4a,b. 5ms exposure. Normalised grayscale and contour plots respectively.

Figure 6-7: ¼ inch nozzle downstream: 30 microseconds and 5 milliseconds exposure. Normalized gray-scale and contour plots, respectively

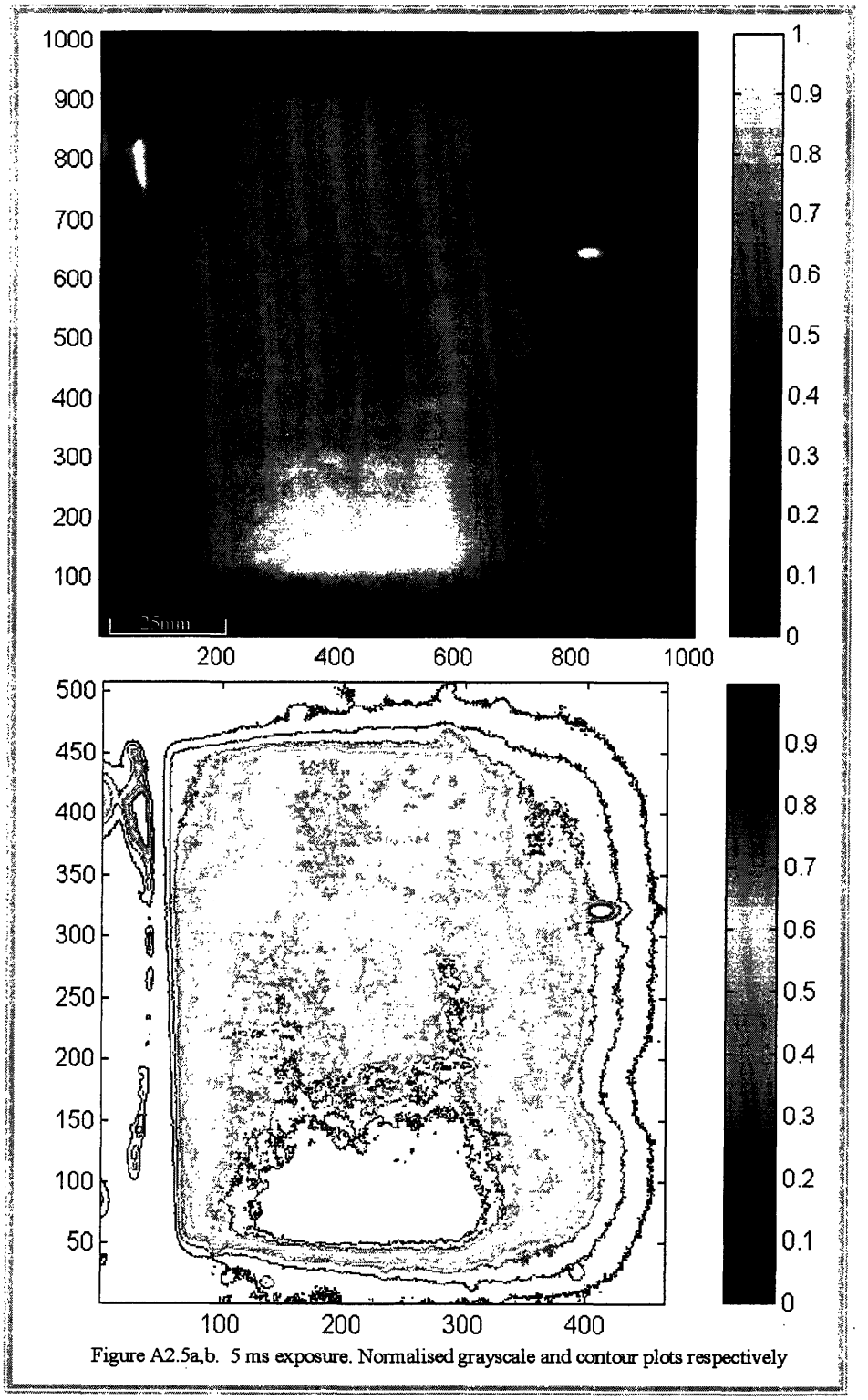

Figure A2.5a,b. 5 ms exposure. Normalised grayscale and contour plots respectively

Figure 6-8: 1/10th Scale ASME: 5 milliseconds exposure. Normalized gray-scale and contour plots, respectively

6.2 Thrust Measurement System

The goal of the thrust measurement system is determination of thrust coefficient with an absolute uncertainty of better than 1%, recognizing that trends may then be resolved with an uncertainty less than or equal to the absolute uncertainty. Additionally, thrust measurements must be made to a reasonable degree of accuracy using a limited number of supporting instruments so as not to interfere with the acoustic capabilities of the facility.

6.2.1 Design Rationale

Because forces acting upon the shock tunnel are at least equal to, and often an order of magnitude greater than the thrust force, measuring the force exerted by the entire shock tunnel on the backstop and then subtracting the endwall pressure forces would lead to a higher than desired uncertainty. Thus, a system was designed to measure the thrust produced by the nozzle utilizing force links at the interface between the test article and shock tube secondary diaphragm section flanges. The idea behind the resultant system developed by Creviston in Reference [13], can be understood by examining the control volume shown in Figure 6-9.

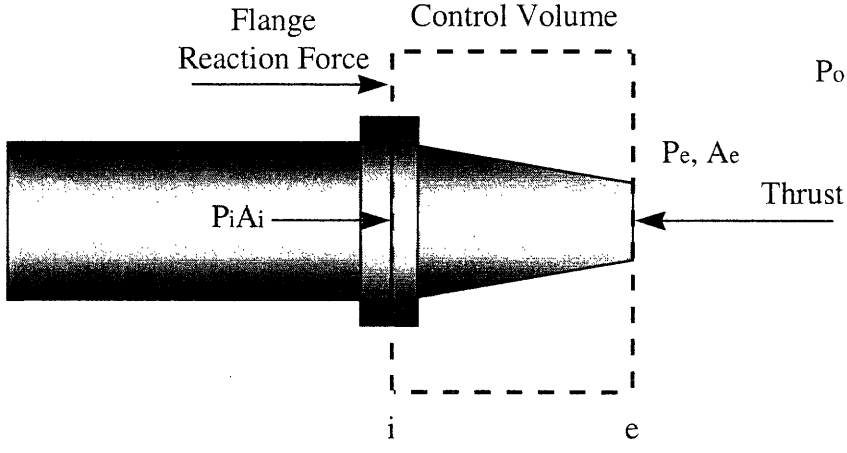

Figure 6-9: Shock tube nozzle force balance schematic

For this control volume the force balance can be written as

$$\left(P_i - P_o\right)A_i - \left(P_e - P_o\right)A_e + F_{reaction} = \dot{m}_e U_e - \dot{m}_i U_i \qquad 6.1$$

For this particular application, equation 5.1 can be re-cast as, [13]

$$Thrust = F_{reaction} + \dot{m}_i U_i + P_{i,gage} A_i \qquad 6.2$$

This formulation presents thrust as a function of the external or flange reaction force, incoming momentum flux, and the pressure force at the control surface. It should be noted that these quantities are constant for the duration of the transient test duration.

6.2.2 Proposed Thrust Measurement System

A schematic diagram of the proposed system is shown in Figure 6-10. The thrust measurement system is designed to measure the force between the secondary diaphragm section and the test article directly using three force links. An elastomeric gasket will cover the flange, with cut-out sections for the force links. The gasket will maintain the seal between the two flanges while carrying only a small fraction of the load. The linear bearing system is necessary to isolate the loading experienced by the force links in the axial direction. The bearing system will support the weight of the test article and prevent any shear forces or moments from being transmitted to the force links, while remaining nearly frictionless and hence transparent in the axial direction.

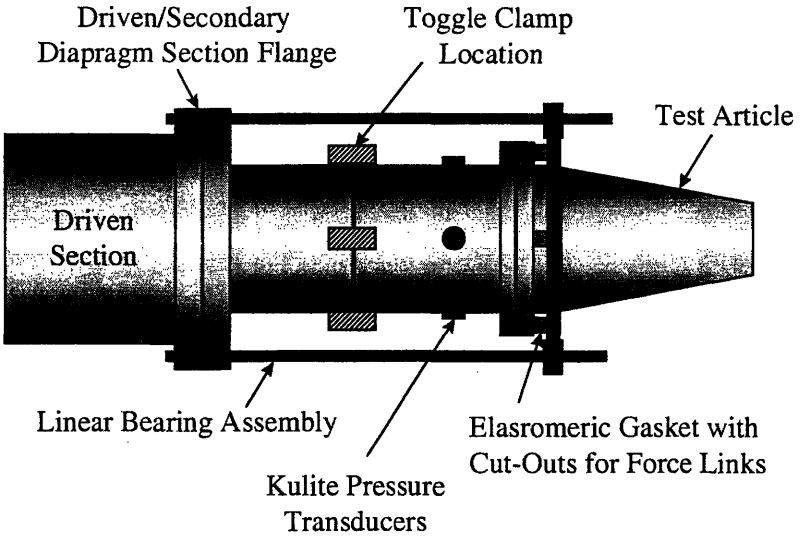

Figure 6-10: Proposed thrust measurement system schematic

$F_{reaction}$, in equation 6.2, is measured directly by the three force links. A_i is only a function of the geometry of the stilling chamber. P_i is a static pressure measurement within the stilling chamber. This measurement will be made by 4 Kulite pressure transducers with high dynamic response. The four transducers will be arrayed circumferentially around the stilling chamber and then averaged to lower the uncertainty in the static pressure measurement. The momentum flux entering the metric section will be

determined as follows. The mass flow will be calculated at the throat using knowledge of basic flow features and a knowledge of $C_{dp}*A_t$, provided by an independent calibration over the Reynolds number range of interest performed at a steady-state, cold-flow facility. Cold-flow calibration should accurately capture the throat area since the short test times experienced with the shock tunnel prevent model heating and expansion. Mass flow at the throat will be calculated according to

$$\dot{m} = C_{dp} A_t \left(\frac{\rho}{\rho_t}(M=1) \right) \rho_t \sqrt{\gamma R \left(\frac{T}{T_t}(M=1) \right) T_{tp}} \qquad 6.3$$

The density and temperature ratio at choked conditions are well-known values. The shock tunnel is already equipped to accurately measure nozzle pressure ratio and total temperature ratio, which provides the stagnation flow quantities needed. The velocity entering the metric section will then be obtained from mass flow, density, and C_d*A_i, the latter of which will also be quantified through independent calibration in a cold flow calibration facility. This provides measurement of the average velocity entering the stilling chamber to within 1%.

6.2.2.1 Dynamic Modeling Analysis

A stiff load cell design is essential to satisfy the dynamic response requirements on the measurement of F_{act}, and is achieved by the choice of piezoelectric force links, which will experience a deflection of less than 100 micro-inches under a thrust load of 1,000 lb. A lumped parameter model was developed to evaluate the requirements for the stiffness of the force links and to facilitate the choice of elastomer material. The results of the dynamic modeling analysis suggested the selection of a force link with spring constant on the order of 5 million psi and a damping constant on the order of 3000 lb. The stiffness of this thrust measuring system will yield a natural frequency of around 1,300 Hz, which is sufficient for the thrust measurements on interest. The dynamic modeling of the system indicated that the vibrations of the system were negligible 5 milliseconds after the quasi-steady thrust level was attained, [13].

6.2.2.2 Uncertainty Analysis

An uncertainty analysis was performed using standard theory for uncertainty propagation according to the equation

$$\sigma_A = \sqrt{\left(\frac{\partial A}{\partial X} \sigma_X \right)^2 + \ldots \left(\frac{\partial A}{\partial Y} \sigma_Y \right)^2} \qquad 6.4$$

where A is a function of (X...Y). The details of this analysis can be found in Appendix B of Reference [13]. The uncertainty goal for thrust measurements in the MIT shock tunnel is 1% of nozzle thrust coefficient, which is defined as

$$C_{T,D} = \frac{F_{actual}}{F_{ideal,primary}} \tag{6.5}$$

This method of uncertainty propagation analysis predicts an uncertainty in the nozzle thrust coefficient of 0.008 based on a nozzle pressure ratio and total temperature ratio of 2.48 and 2.43, respectively. The uncertainty in thrust coefficient is predicted to be 0.011 for NPR = 1.51 and TTR = 1.82, and 0.008 for NPR = 3.43 and TTR = 2.91. The analysis concludes that the force measurement is not the primary source of uncertainty. Uncertainties in effective nozzle throat area, stilling chamber static pressure, and primary total pressure have contributions to the system uncertainty that are an order of magnitude greater than the expected uncertainty in the force measurement itself.

6.2.2.3 Acoustic Measurement Considerations

Whereas it is unlikely that acoustic measurements could be made simultaneously with the mixing measurements described in Section 6.1, due to the required support structure and instrumentation within the acoustic chamber, it may be possible to acquire acoustic noise data and thrust data simultaneously. Obvious benefits of making thrust and acoustic measurements at the same time would be to correlate the steady-state acoustic sampling period with the period over which nozzle thrust is measured. The thrust system shown in Figure 6-10 should be encased in a fiberglass coating, in the same manner as the portion of the driven section of the shock tube that extends into the acoustic chamber, is covered. For the shorter ASME nozzles, the additional acoustic baffling may make it difficult to capture forward directivity angles because of line-of-sight interference with the absorber. This detrimental effect is shown in Figure 6-11, when an over-sized baffling of 4 ft radius was applied 6 inches behind the 1/20th scale ASME nozzle[4].

As can be seen from the figure, the forward flight angle is most significantly attenuated due to the presence of the baffling. The 68 degree directivity angle experiences as much as 10 dB of noise attenuation due to the presence of the absorber. However, the LSMS model should not pose a problem in this regard due to its relatively long ejector duct length, which should provide for a clear line-of-sight from the nozzle exit plane to the microphone location. Refraction effects from the corner of the baffle should be studied by comparing as-measured data for several encasement sizes, as was done in Figure 6-1, until the effect of the acoustic absorber encasement is negligible.

[4] The peaking of the acoustic signatures at frequencies above 60 kHz shown in Figure 11 are an interaction with a noise floor, and not associated with the presence of the baffling or real jet noise effects.

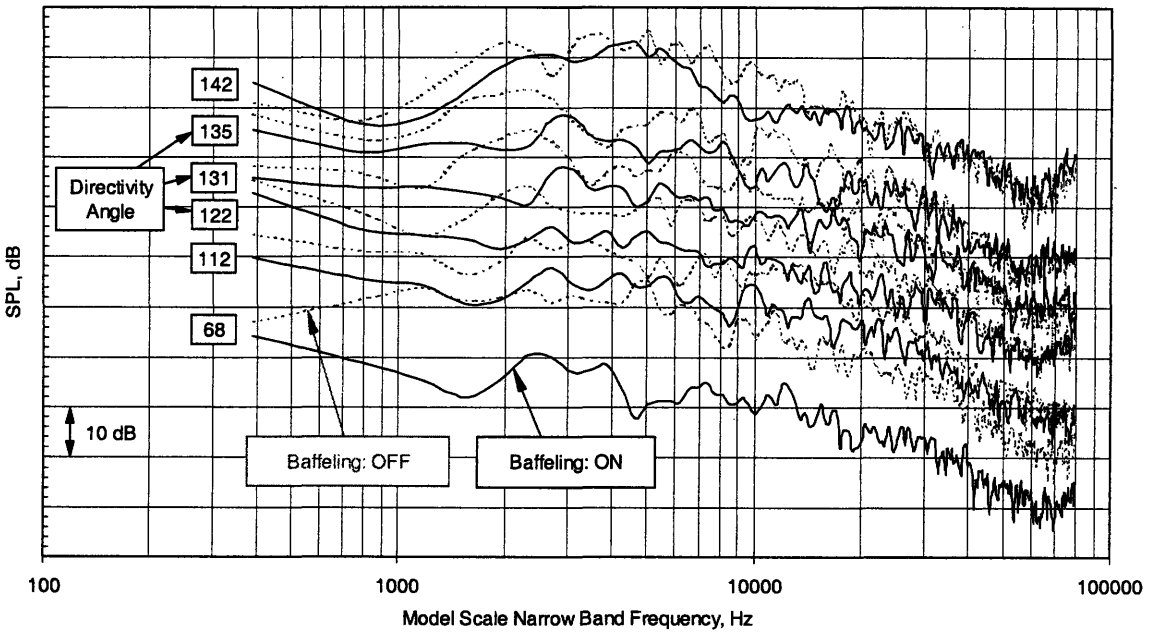

Figure 6-11: Effect of large diameter baffling placed 6 inches behind 1/20th scale ASME nozzle

6.3 Chapter Summary

This chapter presented two additional diagnostics, mixing and thrust measurements, that can be employed to study scaled nozzle flows at the MIT shock tunnel facility. Many more details of the topics covered in this chapter can be found in Crevistion [13].

In the course of evaluating the feasibility of optical measurement using the MIT shock tunnel, three types of systems were considered: focused-Schlieren, shearing interferometry, and Mie-scattering visualization. The latter is best-suited to the objectives of mixing measurements in the shock tunnel facility. The potential of the Mie-scattering method is shown by the results of the Mie-scattering tests. While more development is required, it appears that the Mie-scattering is promising for this application.

The goal for the thrust measurement system is determination of thrust coefficient with an absolute uncertainty of better than 1%, recognizing that trends may then be resolved with an uncertainty less than or equal to the absolute uncertainty. A system was designed to measure the thrust produced by the nozzle utilizing force links at the interface between the nozzle and shock tunnel flanges. The uncertainty in the nozzle thrust coefficient was estimated to be 0.008 based on a nozzle pressure ratio and total temperature ratio of 2.48 and 2.43, respectively. The uncertainty in thrust coefficient is predicted to be 0.011 for NPR = 1.51 and TTR = 1.82, and 0.008 for NPR = 3.43 and TTR = 2.91, which correspond to the LOW and HIGH cases for the ASME nozzles presented in Section 5.2.2.

Chapter 7

Closure

An assessment of the usefulness of a transient testing technique for the study of jet noise was presented. A shock tunnel facility was utilized to generate high pressure and temperature supersonic air jets on which acoustic measurements of scaled nozzle flows can be performed.

7.1 Facility Rationale and Summary

Such a facility has a number of strengths; it is mechanically simple, versatile, has low operating costs, and as shown in this thesis, can be used to generate acoustic and fluid dynamic data comparable to that of steady-state facilities. In addition, a shock tube has a number of inherent advantages over its steady-state counterparts:

- Total temperature and pressure profiles at the nozzle inlet are uniform as a result of shock heating, thus the jet noise does not contain the core noise often present in steady-state, vitiated air facilities.
- The short run times allow for heat sink nozzles to be employed, as opposed to test articles that must be robust enough to withstand elevated temperatures for an extended period of time. Relatively inexpensive stereo-lithography or cast aluminum models can be tested at realistic flow conditions. The use of rapid-prototyping methods, particularly for the SLA models, enables parametric testing to be performed more economically and faster than at a steady-state facility.
- The operation of the facility is inexpensive, requiring a minimal support staff of 1-2 operators, three aluminum diaphragms per test, and approximately 4 m^3 of helium per test.
- Tests can be completed rapidly, with the duration between shock tube shots being on the order of 20 and 60 minutes for the low and high NPR conditions, respectively.

7.2 Summary of Experiments and Results

To assess the usefulness of transient testing to acquire noise data that is comparable to results obtained from continuous facilities, acoustic measurements were acquired on a series of scaled nozzles.

7.2.1 Small-Scale Round Nozzles

The use of a compressed air feed into the shock tube, enables steady-state testing of small-scale nozzles, 0.64 - 1.9 cm exit diameter, at cold flow conditions. Transient tests can be performed at virtually the same jet conditions for an in-house comparison of transient versus steady-state jet noise. Measurements on the scaled nozzles demonstrated:

- Transient testing can be used to acquire acoustic data on scaled nozzles that are in good agreement with the acoustic signatures acquired from steady-state tests over a specified frequency range based on nozzle size, test duration and desired confidence level.
- Steady-state and transient data agreed to within ± 1 - 2 dB over a full-scale frequency range of 60 - 1250 Hz over all six directivity angles measured (70, 110, 120, 130, 140, and 145 degrees).
- The repeatability of acoustic measurements was found to be better than ± 0.5 dB on a test-to-test basis and on the order of ±1.0 dB on a day-to-day basis.

7.2.2 1/20th, 1/15th, and 1/10th Scale ASME Conic Nozzles

In order to better assess the performance of the facility, larger conic nozzles were tested so that:

1. Full-scale frequencies of interest to the HSCT mixer-ejector development program, 250 - 6300 Hz, could be resolved using standard microphones at far-field conditions.
2. Reynolds numbers are more closely matched to the nozzle scales tested at steady-state facilities, particularly for the LSMS model discussed in the next section.
3. The acoustic performance of nozzle scales, on the order of the LSMS model, could be assessed.
4. To determine whether or not multiple runs at the same jet conditions could be used to decrease the uncertainty associated with making transient acoustic measurements.

A complete description of the ASME nozzles was presented in Section 2.1.2.2, and sizing considerations for these nozzles was discussed in Section 4.4. The theoretical basis for the use of multiple runs was presented in Section 4.3. Specific conclusions that can be determined from the ASME nozzle testing include:

- Each of the transient nozzles tested exhibited the same overall trends in magnitude and directivity as the steady-state noise data. All transient tests showed agreement with the steady-state noise trends in OASPL and PNL versus angle.
- The 1/20th scale nozzle exhibited better than ± 2 dB agreement on each test condition except for the 120 and 130 degree angles on the mid and high cases, which deviated by around 3 dB. The 1/15th

scale nozzle agreed to within ± 2 dB at the mid and high cases and to within ± 3 dB on the 110 degree angle on the high case. Finally, the 1/10th scale nozzle agreed to within ± 2 dB on the mid and high cases and had the worst agreement of any nozzle at the low condition, deviating by 3 - 5 dB at 110, 120 and 130 degrees.

- Transient nozzle-to-nozzle tests agreed within approximately 1 dB EPNL for the mid and high cases. Each of the nozzles exhibited a higher value of EPNL, by about 1 - 2 dB, than the steady-state data at the mid condition. The 1/20th scale nozzle displayed the best agreement, with EPNL matched to within 0.5 dB for the low and high conditions, and within 1 dB for the mid condition.
- The use of multiple shock tube shots at the same operating condition was shown to reduce the uncertainty associated with making transient acoustic measurements. Increasing the test time, through combined shock tube shots, demonstrated an improved convergence to the steady-state noise data. Systematic and run-to-run repeatability error prevent convergence to the theoretically achievable levels predicted, with around 30 - 35 milliseconds, or 2 - 3 shock tube shots, required for the best convergence.
- Run-to-run repeatability on jet conditions was found to be better than 1% on NPR and TTR, and within 0.5 dB on SPL versus frequency.

7.2.3 1/12th Scale Large Scale Model Similitude, LSMS, Mixer-Ejector Nozzle

A description of the LSMS mixer-ejector model can be found in Section 2.1.2.3. Noise data from the 1/12th scale LSMS model was obtained at the transient facility and compared to steady-state results obtained at Boeing, over a range of nozzle pressure ratios, total temperature ratios, directivity angles, azimuthal angles, and exit to primary throat area ratios, MARs, relevant to the HSCT mixer-ejector development program. Although, the LSMS data is limited exclusive rights, and hence no detailed numbers concerning the absolute acoustic performance of the model can be revealed, the following observations were noted:

- The LSMS model noise data exhibited agreement with the steady-state noise data to within 2 - 5 dB over a frequency range of 500 - 6300 Hz for all directivity angles and test combinations.
- OASPL and PNL versus directivity angle noise data exhibited agreement with magnitude and directivity to within 1 - 4 dB over each of the cases tested.
- Trends with MAR, NPR and azimuthal angle that are present in the steady-state noise data were revealed using transient testing.
- Repeatability and the use of multiple runs to reduce the uncertainty of the acoustic data were on the same order as the ASME nozzles described above.

- The shock tunnel transient testing facility can be utilized to make acoustic measurements on nozzles with complicated geometries, such as the LSMS, that are in approximate agreement with steady-state noise data.

7.3 Current and Future Work

As of the writing of this thesis, the LSMS mixer-ejector model is still under investigation. Acoustic measurements are being acquired over additional azimuthal angles and jet conditions.

One of the most important questions that still remains is: Can a plastic, stereo-lithography, SLA, model be used as a substitute for the cast aluminum chute rack that is currently being used to acquire acoustic data? A SLA chute rack, identical to the cast aluminum one, has been constructed and is to be tested. The chute rack will be tested at the low nozzle pressure ratio and total temperature ratio condition to ensure that it is robust enough to withstand the impulsively shock-induced flow. Subsequent tests will examine the robustness of the chute rack at more extreme conditions. Additionally, high speed video footage will be conducted on the first series of SLA tests to determine if the model exhibits any fatigue, i.e. significant geometry changes, during the duration of the test. Furthermore, if catastrophic failure should occur, the high speed video should facilitate identifying the failure mechanism so that subsequent SLA models can be made more sturdy in structurally critical regions. Should the SLA chute rack be able to withstand the flow, and give acoustic results that are consistent with the cast aluminum version, a further reduction in cost of the model, as well as the time necessary to fabricate the test articles, can be realized. As was mentioned in Section 2.1.2.3, the cast aluminum chute rack that was tested in these experiments was cast off a plastic stereo lithography chute rack.

7.4 Concluding Remarks

The shock tunnel facility was shown to be an efficient facility for generating and acquiring noise data that are in agreement with steady-state data taken on comparatively sized nozzles. The transient noise data exhibited agreement with steady-state data over a full-scale frequency range, relevant to the HSCT program, to within $\pm$ 2 - 4 dB for a majority of the nozzle and test combinations investigated. The facility can serve as a valuable tool for conducting jet noise research, with the cost of performing high temperature jet noise experiments being retrenched by more than an order of magnitude. The short duration of the test time enables the nozzles to be made from inexpensive, rapid-prototyping. Parametric testing can therefore be performed more economically and faster than in steady-state facilities, making transient shock tunnel testing a valuable tool to serve as a complimentary mode of investigation for jet noise research.

Bibliography

[1] ADTEK Resolution MP II 16 Channel Data Acquisition System, March 1994.

[2] Allen, C.S., Vandra, K., and Soderman, *P.T. Microphone Corrections for Accurate In-Flow Acoustic Measurements at High Frequency*.

[3] Bachalo, W.D., Rudoff, R.C., and Hauser, M.J.. *Laser Velocimetry in Turbulent Flow Fields: Particle Response*. AIAA paper 87-0118, 1987.

[4] Bazhenova, T.V., Eremin, A.V., Kochnev, V.A., and Naboko, I.M. *Test Time Behind Reflected Wave in a Shock Tube with Nozzle*. 9th Shock Tube Symposium.

[5] Brabbs, A., and Belles, F.E. *Contact-Surface Tailoring in Real Shock Tubes*. Page 955. Proceedings of the 5th International Symposium on Shock Tubes and Shock Waves, 1965.

[6] Bridges, J., NASA Lewis Research Center, Personal Communication. 1997-98.

[7] Britan, A.B., Rudintskii A., and Starik, A.M. *Parameter Formation Behind the Reflected Shock Wave in a Shock Tube with a Nozzle*. Journal of Fluid Dynamics, 22:622-628, 1987.

[8] Brüel & Kjær, Instructions and Applications for Quarter Inch Condenser Microphones Type 4135/4136, July 1994.

[9] Brüel & Kjær, Condenser Microphones and Microphone Preamplifiers for Acoustic Measurement, 1992.

[10] Brüel & Kjær, Product Data for Condenser Microphone Cartridges Types 4133 to 4181.

[11] Brüel & Kjær, Technical Documentation for Pistonphone Type 4228, May 1992.

[12] Chimielewski, G.E. *Boundary-Layer Considerations in the Design of Aerodynamic Contractions*. Journal of Aircraft. Volume 11, Number 8. August 1974.

[13] Creviston, D.O. Analysis of Thrust and Mixing Diagnostics for Shock Tube Research. Masters thesis, Massachusetts Institute of Technology, 1999.

[14] Dravet, A., Julliard, J., and Ah-Fa, M. *Jet Noise Experimental Studies of Two Exhaust Concepts for HSCT Application*. Technical Report CEAS/AIAA-95-148, AIAA, 1995.

[15] Drewry, J.E., and Walenta, Z.A. *Determination of Diaphragm Opening-Times and Use of Diaphragm Particle Traps in a Hypersonic Shock Tube*. UTIAS Technical Note No. 90. June 1965.

[16] Forsyth, D.W., The Boeing Commercial Airplane Company, Personal Communication. 1997-98.

[17] Glass, I.I. *Theory and Performance of Simple Shock Tubes*. Technical Report 12, UTIA, 1958.

[18] Hardin, J.C. *Introduction to Time Series Analysis*. Technical Report RP1145, NASA, 1986.

[19] Hartunian, R.A., Russo, A.L., and Marrone, P.V. *Boundary Layer Transition and Heat Transfer in Shock Tubes*. Journal of Aerospace Sciences, 27:587, 1960.

[20] Jaeck, C.L. *Static and Wind Tunnel Near-Field/Far-Field Jet Noise Measurements from Model Scale Single-Flow Baseline and Suppressor Nozzles*. Volume 1: Noise Source Locations and Extrapolation of Static Free-Field Jet Noise Data. Prepared under contact NAS2-8213. Boeing Commercial Airline Co.

[21] Kerrebrock, J.L. Aircraft Engines and Gas Turbines. The MIT Press, 1992.

[22] Kerwin, J.M., Design of a Shock Tube for Jet Noise Research. Master's Thesis, Massachusetts Institute of Technology, 1996.

[23] Kirk, D.R., Creviston, D.O., and Waitz, I.A. *Assessment of a Transient Testing Technique for Jet Noise Research*. 5th AIAA/CEAS Aeroacoustics Conference AIAA 99-1866, Seattle Washington 10-12 May 1999.

[24] Krothapalli, A., Soderman, P.T., Allen, C.S., Hayes, J.A., and Jaeger, S.M. *Flight Effects on the Far-Field Noise of a Heated Supersonic Jet*. AIAA Journal. Vol. 35, No. 6, June 1997.

[25] Liepmann, H.W., and Roshko, A. Elements of Gasdynamics. John Wiley & Sons, Inc., 1957.

[26] Lighthill, M.J. *On Sound Generated Aerodynamically, I. General Theory*. Proceedings of the Royal Society of London, Series A: Mathematical and Physical Sciences, Vol. 211, No. 1107, 1952, p. 564.

[27] Lilly, G.M. *Jet Noise Classical Theory and Experiments*. Technical Report RP-1258, NASA, 1991.

[28] Lord, W.K., Jones, C.W., Stern, A.M., Head, A.L., and Krejsa, E.A. *Mixer Ejector Nozzle For Jet Noise Suppression*. Technical Report AIAA-90-1909, AIAA, 1990.

[29] Louis, Jean F. *A Systematic Study of Supersonic Jet Noise*. Technical Report DOT-TSC-142-1, Department of Transportation, 1971.

[30] Lush, P.A. *Measurement of Subsonic Jet Noise and Comparison with Theory*. Journal of Fluid Mechanics, Vol. 46, part 3, pages 477-500, 1971.

[31] Herman, M. *The Interaction of a Reflected Shock Wave with the Boundary Layer in a Shock Tube*. Journal of Aeronautical Sciences, pages 304-306, 1957.

[32] Martin, W.A. *An Experimental Study of the Boundary Layer Behind a Moving Plane Shock Wave*. Technical Report 47, UTIA, 1957.

[33] Mirels, H. *Attenuation in a Shock Tube Due to Unsteady Boundary-Layer Action*. Technical Report RP-1333, NACA, 1957.

[34] Mirels, R., and Kyser, J. *The Reflection of Shock Waves from an Orifice at the End of a Duct*. Technical Report 72-996, AIAA, 1972.

[35] Oertel, Herbert. *Jet Noise Research by Means of Shock Tubes*. In Modern Developments in Shock Tube Research, page 488. Proceedings of the 10th International Symposium on Shock Tubes and Waves, 1975.

[36] Otens, R.K. Digital Times Series Analysis. John Wiley & Sons, Inc, 1972.

[37] Powell, C.A., and Fields, J.M. *Human Response to Aircraft Noise*. Technical Report RP-1258, NASA, 1991.

[38] Rothkopf, E.M., and Low, W. *Diaphragm Opening Process in Shock Tubes*. The Physics of Fluids, Volume 17, number 6. June 1974.

[39] Rudinger, G. *The Reflection of Shock Waves From an Orifice at the End of a Duct*. NR-098-038, 1957.

[40] SAE Committee A-21, *Aircraft Noise Measurement, Standard Values of Atmospheric Absorption of High Frequency Noise and Application to Fractional-Octave Bands* . NASA CR 2760, 1977.

[41] Schlichting, H. Boundary-Layer Theory. McGraw-Hill Inc., 1995.

[42] Seiner, J.M., NASA Langley Research Center. Personal Communication, 1998.

[43] Seiner, J.M., and Krejsa, E.A. *Supersonic Jet Noise and the High Speed Civil Transport*. AIAA 25th Joint Propulsion Conference. AIAA-89-2358, Monterey, California, July 10-12, 1989.

[44] Seiner, J.M., McLaughlin, D.K., and Liu, C.H. *Supersonic Jet Noise Generated by Large-Scale Instabilities*. NASA Technical Paper 2072. September 1972.

[45] Seiner, J.M., and Norum, T.D. *Experiments of Shock Associated Noise on Supersonic Jets*. AIAA 12th Fluid and Plasma Dynamics Conference. AIAA-79-1526. Williamsburg, Virginia, July 23-25, 1979.

[46] Shields, F.D., and Bass, H.E. *Atmospheric Absorption of High Frequency Noise and Application to Fractional-Octave Bands*. NASA CR 2760, 1977.

[47] Simpson, C.J.S.M., Chandler, T.R.D., and Bridgman, K.B. *Effect on Shock Trajectory of the Opening Time of Diaphragms in a Shock Tube*. The Physics of Fluids, Volume 10, Number 9. September 1967.

[48] Smith, M.J.T. Aircraft Noise. Cambridge Aerospace Series, Cambridge University Press, 1989.

[49] Soderman, P.T., and Allen, C.S. *On the Scaling of Small-Scale Jet Noise to Large Scale*. DGLR/AIAA 14th Aeroacoustics Conference, DGLR/AIAA-92-02-109, May 1992.

[50] Tam, C.K.W., *Supersonic Jet Noise*. Annual Review of Fluid Mechanics, Vol. 27, 1995, p.17.

[51] Tew, D.E. A Computational Study of Mixing Downstream of a Lobed Mixer with a Velocity Difference Between Co-Flowing Streams. Master's thesis, Massachusetts Institute of Technology, 1992.

[52] Tew, D.E. Streamwise Vorticity Enhanced Compressible Mixing Downstream of Lobed Mixers. Ph.D. thesis, Massachusetts Institute of Technology, 1997.

[53] Thomas, P.J. *A Numerical Study of the Influence of the Basset Force on the Statistics of LDV Velocity Data Sampled in a Flow Region with a Large Spatial Velocity Gradient.* 1997, Exp. In Fluids, Vol. 23. Pp. 48-53.

[54] Weinstein, L.M. *Large Field High-Brightness Focusing Schlieren System*. AIAA Paper 91-0567.

[55] Weinstein, L.M. *Designing and Using Focusing Schlieren Systems.* NASA Langley Research Center paper, Feb. 1992.

[56] Westley, R., and Lilly, G.M., *An Investigation of the Noise Field from a Small Jet and Methods for its Reduction*. College of Aeronautics, Rept. 53, Cranfield, England, UK, 1952.

[57] White, F.M. Viscous Fluid Flow. McGraw-Hill, Inc., 1974.

[58] http://www.lerc.nasa.gov/WWW/HSR/HSROver.html

[59] http://www.boeing.com/assocproducts/noise/airports.html

[60] http://www.boeing.com/assocproducts/techsvcs/boeingtech/bts_acoub.html

[61] http://www.boeing.com/assocproducts/aircompat/hsct.htm

[62] http://www.vislab.usyd.edu.au/photonics/fibres/fizzz/scattering2.html

Appendix A

1-D Inviscid Shock Tube Gas Dynamic Model

A detailed set of the equations used to describe the 1-D inviscid shock tube gas dynamic model can be found in References [17], [25]. A 1-D gas dynamic model was also derived by Kerwin in Reference [22]. The model described here makes used of the nomenclature described in Table 3.1, and shown in Figures 3-1 and 3-2. The ideal gas-dynamic model of the shock tube was derived using a number of simplifying assumptions. Most of these assumptions are valid for the temperature and pressure ranges that are employed in the MIT facility. Some of the non-ideal effects, however, are significant over the operating range of interest so corrections can be made to the results from the ideal model. The ideal modeling assumptions are:

- The diaphragm removal is assumed to be instantaneous, resulting in a step discontinuity in pressure between the two sections at t=0. Any effects due to the diaphragm curvature of finite bursting time are neglected.[1]
- It was assumed that there is no mixing between the driver and driven gases such that distinct contact surface exists at the interface between the two regions.
- The flow was assumed to be inviscid[2], except across the shock. This is generally a poor assumption so corrections for the boundary layer must be made to study effects such as shock attenuation and contact surface acceleration.
- One-dimensional flow was assumed throughout the tube.
- Real-gas effects were ignored and the ratio of specific heats was assumed to be constant for each of the driver and driven gases.

The speed of sound in regions (1) and (4) is found from:

---

[1] In actual shock tubes, the diaphragm bursting process is highly three-dimensional and requires a finite period of time for the diaphragm to burst and fold out of the ensuing flow field. As a result there will not be a distinct shock front but rather an irregular distribution of compression waves. These waves, however, will overtake each other as they travel downstream, resulting in a steepening compression front. Within a few tube diameters, the waves coalesce into a distinct shock front and exhibit close agreement with the idealized one-dimensional model.

[2] This restriction is removed in Section 3.4

$$a_1 = \sqrt{\gamma_1 R_1 T_1} \qquad \text{A.1}$$

$$a_4 = \sqrt{\gamma_4 R_4 T_4} \qquad \text{A.2}$$

where the assumption is made that T1 = T4. Furthermore γ4 and R4 are found from:

$$\gamma_4 = \gamma air(1-\chi He) + \gamma He(\chi He) \qquad \text{A.3}$$

$$R4 = Rair(1-\chi He) + RHe(\chi He) \qquad \text{A.4}$$

The pressure ratio across the incident shock wave, P2/P1, can be found as a function of the initial conditions:

$$\frac{P1}{P4} = \frac{P1}{P2}\left[1-\left(\frac{P2}{P1}\right)\sqrt{\frac{((\gamma_4-1)/2\gamma_4)(C_v T)_1/(C_v T)_4}{(\gamma_1+1)/(\gamma_1-1)(P2/P1)+1}}\right]^{\frac{2\gamma_4}{(\gamma_4-1)}} \qquad \text{A.5}$$

This equation indicates that the shock pressure ratio, P2/P1, is a function of the diaphragm pressure ratio, P4/P1, the internal energy ratio across the diaphragm, and the specific heat ratios of the gases in the driver and driven sections. For convenience, equation A.5 can be re-cast as:

$$\frac{P4}{P1} = \frac{P2}{P1}\left[1-\frac{(\gamma_4-1)(a_1/a_4)(P2/P1-1)}{\sqrt{2\gamma_1}\sqrt{2\gamma_1+(\gamma_1+1)(P2/P1-1)}}\right]^{-\frac{2\gamma_4}{(\gamma_4-1)}} \qquad \text{A.6}$$

The remaining quantities can be found as a function of the pressure ratio across the incident shock. The temperature ratio across the shock can be found the Rankine-Hugonoit relation:

$$\frac{T2}{T1} = \frac{\frac{P2}{P1}\left(\frac{(\gamma_1+1)}{(\gamma_1-1)}+\frac{P2}{P1}\right)}{1+\frac{(\gamma_1+1)}{(\gamma_1-1)}\left(\frac{P2}{P1}\right)} \qquad \text{A.7}$$

Since T2=(T2/T1)*(T1), the speed of sound in region (2) can be found from:

$$a_2 = \sqrt{\gamma_1 R_1 T_2} \tag{A.8}$$

The speed of the shock can be found from:

$$U_s = \sqrt{\gamma_1 R_1 T_1}\sqrt{\left(\frac{\gamma_1 - 1}{2\gamma_1}\right) + \left(\frac{\gamma_1 + 1}{2\gamma_1}\right)\frac{P2}{P1}} \tag{A.9}$$

and the shock Mach number is given by:

$$M_s = \frac{U_s}{a_1} \tag{A.10}$$

The velocities of regions (2) and (3) can also be found as a functions of the pressure ratio across the shock:

$$U_2 = a_1\left(\frac{P2}{P1}\right)\sqrt{\frac{2\gamma_1}{(\gamma_1 + 1)(P2/P1) + (\gamma_1 + 1)}} \tag{A.11}$$

$$U_3 = \frac{2a_4}{(\gamma_4 - 1)}\left[1 - \left(\frac{P3}{P4}\right)^{\left(\frac{(\gamma_4 - 1)}{2\gamma_4}\right)}\right] \tag{A.12}$$

where P3/P4 can be found from:

$$\frac{P3}{P4} = \frac{(P2/P1)}{(P4/P1)} \tag{A.13}$$

The temperature in region (3) and consequently the speed of sound in the region from:

$$T3 = T4\left(\frac{P3}{P4}\right)^{\frac{(\gamma_4 - 1)}{\gamma_4}} \tag{A.14}$$

$$a_3 = \sqrt{\gamma_4 R_4 T_3} \tag{A.15}$$

The Mach number in region (3) is given by:

$$M_3 = \frac{U_3}{a_3} \qquad \text{A.16}$$

Imposing the condition that U5 = 0, the reservoir temperature and pressure ratios are simple functions of the incident shock Mach number:

$$\frac{T5}{T1} = \frac{\left[2(\gamma_1 - 1)M_s^2 + (3 - \gamma_1)\right]\left[(3\gamma_1 - 1)M_s^2 - 2(\gamma_1 - 1)\right]}{(\gamma_1 + 1)^2 M_s^2} \qquad \text{A.17}$$

$$\frac{P5}{P1} = \left[\frac{2\gamma_1 M_s^2 - (\gamma_1 - 1)}{(\gamma_1 + 1)}\right]\left[\frac{(3\gamma_1 - 1)M_s^2 - 2(\gamma_1 - 1)}{(\gamma_1 - 1)M_s^2 + 2}\right] \qquad \text{A.18}$$

The equations appear as 3.1 and 3.2 in Chapter 3, and can be used to determine the nozzle pressure ratio and total temperature ratio. Furthermore these equations provide the necessary starting point to calculate the shock attenuation that will be described in Appendix B. Additional details of the derivation of the shock tube model can be found in Reference [22], including a discussion of:

- The parameters behind the reflected shock including nozzle effects
- Interaction of the reflected shock with the contact surface
- Conditions across the centered expansion
- Time-distance history of the centered expansion
- Shock-expansion interaction

Appendix B

Shock Wave Attenuation and Contact Surface Acceleration Analysis and Calculations

The attenuation of the incident shock wave can be predicted by modeling the boundary-layer as a distribution of mass sources along the wall of the tube, as done by Mirels in Reference [13]. It is assumed that the boundary-layer is thin relative to the tube diameter and induces one-dimensional longitudinal pressure waves whose strength are proportional to the vertical velocity at the edge of the boundary-layer. The pressure perturbations can then be integrated along characteristic lines to determine the variation in shock strength with position.

Consider one-dimensional uniform flow in a tube of constant cross-sectional area. Assume that weak mass sources, uniformly distributed across each station are present and perturb the flow. Net perturbation quantities (from the uniform flow conditions) are denoted by Δ. The equations of motion become:

Continuity:

$$\frac{\partial \Delta\rho}{\partial t} + \rho\frac{\partial \Delta u}{\partial x} + u\frac{\partial \Delta\rho}{\partial x} = m \qquad \text{B.1}$$

Momentum:

$$\rho\left(\frac{\partial \Delta u}{\partial t} + u\frac{\partial \Delta u}{\partial x}\right) = -\frac{\partial \Delta p}{\partial x} \qquad \text{B.2}$$

Isentropic Flow:

$$\Delta p = a^2 \Delta\rho \qquad \text{B.3}$$

where m=m(x,t) is the rate of mass addition per unit cross-sectional area per unit length x. The presence of these sources generate waves. The following convention, summarized in Table B.1, is used for the generated perturbations:

Table B.1: Summary of perturbation directionality

Sign	Perturbation directionality
+	Perturbation moving in the +x direction (as denoted in Figure B.X)
-	Perturbation moving in the -x direction (as denoted in Figure B.X)

The solution for the net perturbation at any point x,t may be expressed as:

$$\Delta P \equiv \Delta P^{+} + \Delta P^{-} \qquad \text{B.4a}$$

$$\Delta u \equiv \Delta u^{+} + \Delta u^{-} = \frac{1}{\rho a}\left(\Delta P^{+} + \Delta P^{-}\right) \qquad \text{B.4b}$$

$$\Delta \rho = \frac{1}{a^{2}} \Delta P \qquad \text{B.4c}$$

The variables, ζ and τ, are adopted as integration variables for x and t, respectively, and thus,

$$\Delta P^{+} = \frac{a}{2(1+M)} \int_{-\infty}^{x} m\left(\xi, \frac{x-\xi}{a+u}\right) d\xi \qquad \text{B.5a}$$

$$\Delta P^{-} = \frac{a}{2(1-M)} \int_{x}^{\pm\infty} m\left(\xi, \frac{x-\xi}{a-u}\right) d\xi \qquad \text{B.5b}$$

where m is m(x,t) as specified. The above integrals are conducted along the characteristic lines

$$\tau = t - \frac{(x-\xi)}{(a+u)} \qquad \text{B.6a}$$

$$\tau = t - \frac{(x-\xi)}{(a-u)} \qquad \text{B.6b}$$

in the ζ,τ plane. Note: The upper limit on the integral in equation M.5b is +infinity if M<1, and -infinity if M>1. The tube can be modeled to have "flexible walls" so that a small radial velocity can be generated normal to the core flow. The result of this velocity is equivalent to mass entering the walls of the tube at a rate per unit distance x of:

$$\frac{m}{dx} = \oint \rho v dl \qquad \text{B.7}$$

where the integral is taken around the perimeter of the tube. Once again considering the flow as one-dimensional, the equivalent source strength is:

$$m = \frac{\rho v l}{A} = \frac{4\rho v}{d} \qquad \text{B.8}$$

where d is the hydraulic diameter of the tubes cross-section, and v = v(x,t), thus maintaining m = m(x,t). Combining equations M.4a, M.5a, M.5b, and M.8, the expression for ΔP can be written as:

$$\frac{\Delta P}{P} = \frac{2\gamma}{ad}\left[\frac{1}{1+M}\int_{-\infty}^{x} v\left(\xi, t - \frac{(x-\xi)}{(a+u)}\right)d\xi + \frac{1}{1+M}\int_{x}^{\pm\infty} v\left(\xi, t - \frac{(x-\xi)}{(a-u)}\right)d\xi\right] \qquad \text{B.9}$$

where v is the normal velocity at the edge of the boundary layer. The following convention applies:

Table B.2: Summary of velocity directionality and associated waves

Vertical velocity directionality	Type of wave generated
positive v (v3)	compression waves
negative v (v2)	expansion waves

Equation B.9 can be applied to find the attenuation in a shock tube. The characteristic lines over which this integral will be evaluated is shown in Figure B-1. As can be seen in Figure B-1, it is assumed that the characteristic lines are straight and that the expansion fan can be considered as an "expansion shock" or an expansion wave of zero thickness moving with velocity a4 into region (4). The point d with coordinates (x,t) is assumed to be on the shock wave characteristic.

The problem is to find the net pressure perturbation behind the shock (Δp2,d). This requires an integration of equation B.9 along all characteristic lines which contribute to the net pressure perturbation. Because of entropy discontinuities, there are an infinite number of line segments along which the integration must be conducted. However, the major contributions to the pressure perturbation behind the shock can be attributed to lines **ab**, **cb** and **bd**. Integrating along these lines, equation B.9 can be expressed as:

$$\frac{1}{F}\frac{a_2 d}{2\gamma_2}\frac{\Delta p_{2,d}}{p_2}\left[\frac{1}{1+M_2}\int_{\xi_b}^{x} v_2 d\xi + \frac{C}{1-M_2}\int_{\xi_c}^{\xi_b} v_2 d\xi + \frac{\gamma_3/\gamma_2}{a_3/a_2(1+M_2)} D\int_{\xi_m}^{\xi_b} v_3 d\xi\right]\left(1 - CE\frac{\Delta p_{2,c}}{\Delta p_{2,d}}\right)^{-1} \qquad \text{B.10}$$

The term:

$$CE\frac{\Delta p_{2,c}}{\Delta p_{2,d}}$$

represents the contribution to the net pressure perturbation behind the shock of all the characteristic lines other than bd, bc, and ab. The terms C and D are reflection and transmission coefficients for the contact surface, respectively. The terms E and F are reflection and transmission coefficients for the incident shock wave.

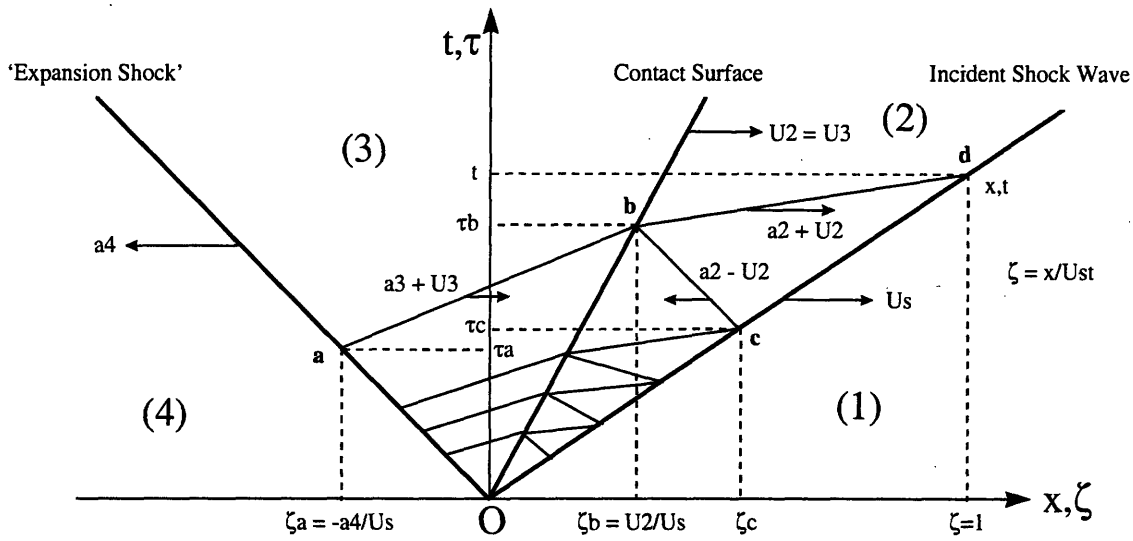

Figure B-1: Characteristic lines over which equation B.9 is to be integrated

The following table presents a summary of the slope of each line.

Table B.3: Summary of line slopes for Figure B-1

Line	Slope ($d\tau/d\xi$)
Ocd	1/Us
Ob	1/U2
Oa	-1/a4
ab	1/(a3+U3)
bc	-1/(a2-U2)
bd	1/(a2+U2)

Weak pressure waves are assumed to interact with the contact surface and the incident shock wave. The strength of the reflected (C,E) and transmitted (D,F) waves can be readily determined. Consider the contact surface which separates region (3) from region (2) as shown in Figure B-2

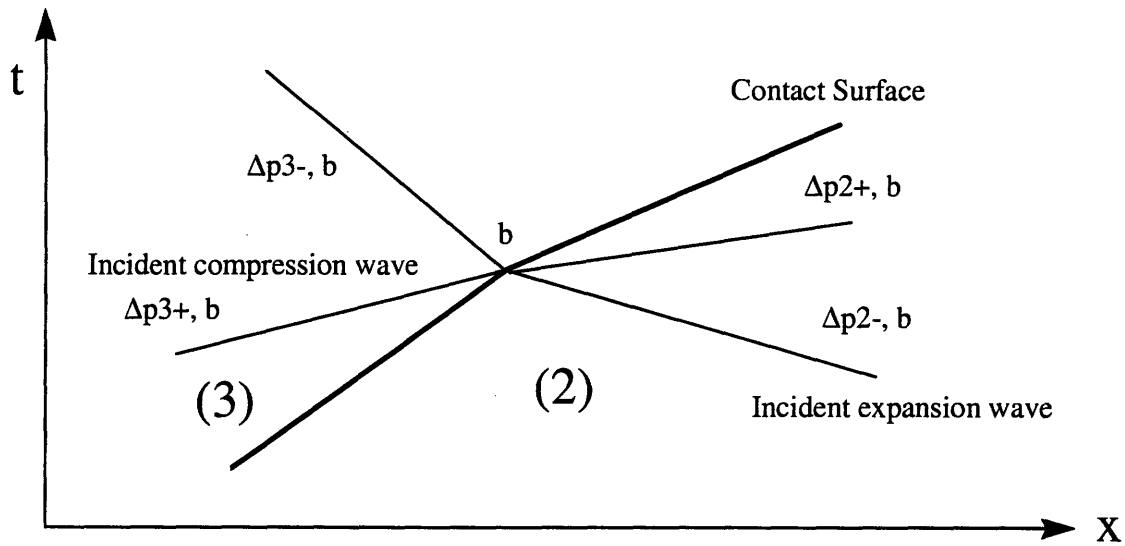

Figure B-2: Incident waves on the contact surface due to boundary-layer effects

At a certain instant in time, known incident waves Δp3+,b and Δp2-,b intersect the surface. The problem here is to find the final waves Δp3+,b and Δp2+,b. From the isentropic flow relations:

$$\Delta p^{+} = \rho a \Delta U^{+} \qquad \text{B.11a}$$

$$\Delta p^{-} = -\rho a \Delta U^{-} \qquad \text{B.11b}$$

The boundary conditions across the contact surface can be written in conservation form as:

$$\Delta U^{+}_{2,b} + \Delta U^{-}_{2,b} = \Delta U^{+}_{3,b} + \Delta U^{-}_{3,b} \qquad \text{B.12a}$$

$$\Delta p^{+}_{2,b} + \Delta p^{-}_{2,b} = \Delta p^{+}_{3,b} + \Delta p^{-}_{3,b} \qquad \text{B.12b}$$

From the above equations, the expression for Δp+2,b and Δp-3,b become:

$$\Delta p^{+}_{2,b} = C\Delta p^{-}_{2,b} + D\Delta p^{+}_{3,b} \qquad \text{B.13a}$$

$$\Delta p^{-}_{3,b} = \left(\gamma_3 / \gamma_2\right)\left(a_2 / a_3\right) D\Delta p^{-}_{2,b} - C\Delta p^{+}_{3,b} \qquad \text{B.13b}$$

where C and D are the reflection and transmission coefficients for the contact surface, which can be solved for:

$$C \equiv \frac{\left(\gamma_3/\gamma_2\right)\left(a_2/a_3\right)-1}{\left(\gamma_3/\gamma_2\right)\left(a_2/a_3\right)+1} \qquad \text{B.14a}$$

$$D \equiv \frac{2}{\left(\gamma_3/\gamma_2\right)\left(a_2/a_3\right)+1} \qquad \text{B.14b}$$

Similarly a shock wave can be considered moving with velocity, Us, into region (1) which is stationary. The conditions across the shock wave can be found from the normal-shock relations. Figure B-3 depicts this situation.

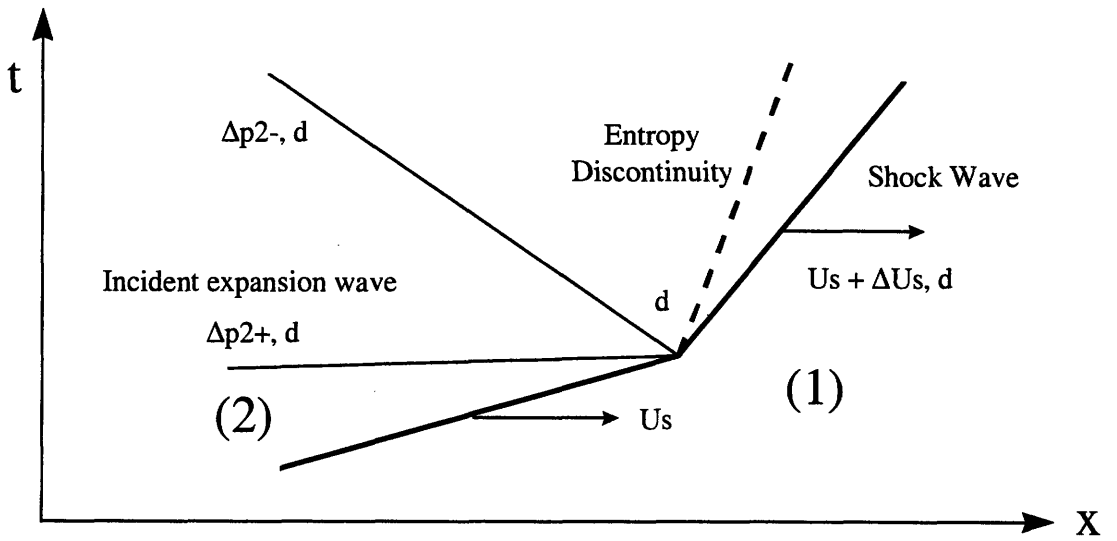

Figure B-3: Incident waves on the shock due to boundary-layer effects

At a certain instant, a known wave Δp2+,d intersects the shock. Using the above analysis, the reflection and transmission coefficients can be shown to be:

$$E \equiv \frac{2\left(\rho_1/\rho_2\right)\left(a_1/a_2\right)\dfrac{M_s^3}{M_s^2+1}-1}{2\left(\rho_1/\rho_2\right)\left(a_1/a_2\right)\dfrac{M_s^3}{M_s^2+1}+1} \qquad \text{B.15a}$$

$$F \equiv \frac{4\left(\rho_1/\rho_2\right)\left(a_1/a_2\right)\dfrac{M_s^3}{M_s^2+1}}{2\left(\rho_1/\rho_2\right)\left(a_1/a_2\right)\dfrac{M_s^3}{M_s^2+1}+1} \qquad \text{B.15b}$$

For either a turbulent or laminar boundary-layer it can be shown that the vertical velocity at the edge of the boundary-layer in regions (2) and (3) can be expressed as:

$$v_2 = -L_2\left[\frac{U2^2/Us}{1-(U_2/U_s)}\right]^{1-n_2}\left(\frac{\nu_2}{U_s\tau-\xi}\right)^{n_2} \qquad \text{B.16a}$$

$$v_3 = L_3\left[\frac{U3^2/a_4}{1-(U_3/a_4)}\right]^{1-n_3}\left(\frac{\nu_{32}}{a_4\tau-\xi}\right)^{n_3} \qquad \text{B.16b}$$

where L2 and L3 are functions of the boundary-layer thickness. Appendix B summarizes the development of the boundary-layer model. The turbulent boundary-layer thickness in region (2) was obtained from a Karman-Pohlhausen-type integral solution. Considering conditions along the characteristic lines depicted in Figure B-1, the maximum boundary-layer thickness occurs at point b of region (2), which is at the location of the contact surface. The following values for n2 and n3 are used to describe whether the boundary layer is laminar or turbulent in regions (2) and (3):

Table B.4: Coefficient summary and physical representation

Coefficient	Value	Physical Representation
n2	**0.5**	Wholly laminar boundary-layer in region (2)
n2	**0.2**	Wholly turbulent boundary-layer in region (2)
n3	**0.5**	Wholly laminar boundary-layer in region (3)
n3	**0.2**	Wholly turbulent boundary-layer in region (3)

Various combinations of boundary-layer types can be introduced into equation B.10 and integrated to calculate the attenuation due to the unsteady-boundary-layer in that region. Using n2 = n3 = 0.2 equation B.10 can be expressed as:

$$\left(\frac{U_s}{U_2}\right)^{7/5}\left(\frac{d}{x}\right)^{4/5}\left(\frac{a_2 d}{\nu_2}\right)^{1/5}\frac{\Delta p_{2,d}}{p_2} = \qquad \text{B.17}$$

$$\frac{-2.5\gamma_2 L_2 F\left(\dfrac{U_s}{a_2}\right)^{3/5}}{\left[1+\dfrac{1-(U_s/a_2)}{M_2}\right]^{3/5}}\left\{1+C\frac{\xi}{x}-\frac{D(\gamma_3/\gamma_2)M_2}{(a_3/a_2)}\frac{\left[1+\dfrac{1-(U_s/a_2)}{M_2}\right]}{1+M_3+(a_4/a_3)}\left(\frac{\nu_3}{\nu_2}\right)^{1/5}\frac{L_3}{L_2}\right\}\left[1-CE\left(\frac{\xi}{x}\right)^{4/5}\right]^{-1}$$

This equation gives the net pressure perturbation behind the incident shock due to the turbulent boundary-layer. Although relatively daunting in appearance, an examination of the terms within the { } reveals that these are merely the relative contributions to the net attenuation from characteristic lines **bd**, **ab**, and **bc**. The final term in the [ ] represents the contribution of all other characteristic lines in Figure B-1 other than lines bd, ab, and bc. The other perturbation quantities behind the incident shock can be found from equation B.17 and the normal shock relations, these are summarized below:

$$\frac{\Delta U_{2,d}}{U_2} = \frac{2\gamma_1 M_s^2 - (\gamma_1 - 1)}{4\gamma_1 M_s^2}\left(\frac{M_s^2 + 1}{M_s^2 - 1}\right)\left(\frac{\Delta p_{2,d}}{p_2}\right) \qquad \text{B.18}$$

$$\frac{\Delta \rho_{2,d}}{\rho_2} = \frac{2\gamma_1 M_s^2 - (\gamma_1 - 1)}{\gamma_1 M_s^2\left[(\gamma_1 - 1)M_s^2 + 2\right]}\left(\frac{\Delta p_{2,d}}{p_2}\right) \qquad \text{B.19}$$

$$\frac{\Delta T_{2,d}}{T_2} = \left(\frac{\Delta p_{2,d}}{p_2}\right)\left(1 - \frac{2\gamma_1 M_s^2 - (\gamma_1 - 1)}{\gamma_1 M_s^2\left[(\gamma_1 - 1)M_s^2 + 2\right]}\right) \qquad \text{B.20}$$

The resulting perturbation of the shock Mach number can also be found in terms of the net pressure perturbation behind the shock:

$$\frac{\Delta M_{s,d}}{M_s} = \frac{\gamma_1 + 1}{4\gamma_1}\frac{\left(p_2 / p_1\right)}{M_s^2} F\left(\frac{\Delta p_{2,d}^+}{p_2}\right) \qquad \text{B.21}$$

We can examine two limiting cases: (1) the incident shock Mach number approaching unity and (2) the incident shock Mach number approaching infinity:

Ms =1

$$\frac{\Delta p_{2,d}^-}{\Delta p_{2,d}^+} = 0 \qquad \text{B.22a}$$

Ms = infinity

$$\frac{\Delta p_{2,d}^-}{\Delta p_{2,d}^+} = \frac{2\sqrt{\frac{\gamma_1 - 1}{2\gamma_1}} - 1}{2\sqrt{\frac{\gamma_1 - 1}{2\gamma_1}} + 1} = -0.14 \qquad \text{B.22b}$$

For the limit where the incident shock Mach number approaches infinity the reflected wave is relatively small and is of opposite sign of the incident wave.

Additional Equations of Interest to the Calculation

The preceeding was a summary of the shock wave attenuation calcualtion, with the resulting attentuation parameters summarized in equations B.18 - B.21. This section presents a set of additional equations that can be used to caluclate the boundary-layer thickness and vertical velocity at the edge of the boundary layer. It is shown that the vertical velocity at the edge of the turbulent boundary-layer can be expressed as:

$$v_2 = -L_2\left[\frac{U_2^2/U_s}{1-(U_2/U_s)}\right]^{1-n_2}\left(\frac{v_2}{\left(\frac{1+M_2-U_s/a_2}{1+M_2}\right)\left(1-\frac{U_2}{U_s}\right)x}\right)^{n_2} \qquad \text{B.23}$$

where L is a function of the boundary-layer thickness, displacement thickness, and momentum thickness and n is 0.2 for the fully turbulent case. L can be shown to be:

$$L_2 = 0.0460\frac{\delta_2^*\left[(U_2/U_s-1)\right]}{\delta_2(U_2/U_s)}\left\{\varphi_2\frac{\delta_2(U_2/U_s)}{\theta_2\left[(U_2/U_s-1)\right]}\right\}^{4/5} \qquad \text{B.24}$$

where the following substitutions can be made to evaluate the above expression:

$$\frac{\delta_2^*\left[(U_2/U_s-1)\right]}{\delta_2(U_2/U_s)} = \frac{U_s}{U_2}\left[\left(\frac{T_2}{T_{2,w}}+\frac{U_2}{U_s}-1\right)\left(1-7\frac{T_2}{T_{2,w}}I_{2,7}\right)-7\left(\frac{T_{2,r}}{T_2}-1\right)\left(\frac{T_2}{T_{2,w}}\right)^2\left(I_{2,7}-I_{2,8}\right)\right] \qquad \text{B.25a}$$

$$\frac{\theta_2\left[(U_2/U_s-1)\right]}{\delta_2(U_2/U_s)} = \frac{T_2/T_{2,w}}{1-(U_2/U_s)}\left[\left(1-7\frac{T_2}{T_{2,w}}I_{2,7}\right)-7\left(\left(\frac{T_{2,r}}{T_2}-1\right)\left(\frac{T_2}{T_{2,w}}\right)+\frac{U_2}{U_s}\right)\left(I_{2,7}-I_{2,8}\right)\right] \qquad \text{B.25b}$$

$$\varphi_2 = \left(\frac{\mu_{2,m}}{\mu_2}\right)^{1/4}\left(\frac{T_2}{T_{2,m}}\right)^{3/4} \qquad \text{B.25c}$$

To determine the viscosity of the air in regions (2) and (3) of the shock tube, the Sutherland relation is employed

$$\frac{\mu}{\mu_1}=\left(\frac{T}{T_1}\right)^{3/2}\frac{T_1+198.6}{T+198.6} \qquad \text{B.26}$$

where T is in Rankine. The adiabatic recovery temperature and mean temperature can be written as

$$\frac{T_{2,r}}{T_2}=1+\frac{\gamma_2-1}{2}M_2^2\,\mathrm{Pr}_2^{1/3} \qquad \text{B.27a}$$

$$\frac{T_{2,m}}{T_2}=\frac{1}{2}\left(\frac{T_{2,w}}{T_2}+1\right)+0.22\left(\frac{T_{2,r}}{T_2}-1\right) \qquad \text{B.27b}$$

The I2,7 and I2,8 can be evaluated from the integral:

$$I_{2,N}=\int_0^1\frac{z^N}{1+\left(\frac{T_{2,r}}{T_{2,w}}-1\right)z-\left(\frac{T_{2,r}}{T_2}-1\right)\left(\frac{T_2}{T_{2,w}}\right)z^2} \qquad \text{B.28}$$

can be evaluated analytically from:

$$I_{2,7}=\frac{\left[\left(I_{2,7}\right)\beta_2-\left(I_{2,7}\right)\lambda_2\right]}{\sqrt{\left(\frac{T_{2,r}}{T_{2,w}}-1\right)^2+4\left(\frac{T_{2,r}}{T_2}-1\right)\left(\frac{T_2}{T_{2,w}}\right)}} \qquad \text{B.29a}$$

$$I_{2,7}-I_{2,8}=\left[\left(\lambda_2-1\right)\left(I_{2,7}\right)\lambda_2-\left(\beta_2-1\right)\left(I_{2,7}\right)\beta_2\right] \qquad \text{B.29b}$$

where $\lambda 2$ and $\beta 2$ can be written as:

$$\lambda^+{}_2,\beta^-{}_2=\frac{1}{2\left(\frac{T_{2,r}}{T_2}-1\right)\left(\frac{T_2}{T_{2,w}}\right)}\left(\left(\frac{T_{2,r}}{T_{2,w}}-1\right)\pm\sqrt{\left(\frac{T_{2,r}}{T_{2,w}}-1\right)^2+4\left(\frac{T_{2,r}}{T_2}-1\right)\left(\frac{T_2}{T_{2,w}}\right)}\right) \qquad \text{B.30}$$

where the superscript associated with the dependent variables indicates which sign is used prior to the discriminant. It can be shown that for all cases $\beta 2$ is less than zero and $\lambda 2$ is always greater than unity. For ranges outside -1.6 < b2 < 0 and 1 < l2 < 2, the following expansions become useful to analytically evaluate the integral:

$$\left(I_{2,7}\right)\beta_2 = \frac{1}{8\left(1-\beta_2\right)}\left[1+\sum_{m=1}^{\infty}\frac{8!m!}{(8+m)!}\left(\frac{1}{1-\beta_2}\right)^m\right] \qquad \text{B.31a}$$

$$\left(I_{2,7}\right)\lambda_2 = \frac{1}{8\left(1-\lambda_2\right)}\left[1-8\sum_{m=1}^{\infty}\frac{1}{(8+m)(7+m)}\left(\frac{1}{\lambda_2}\right)^m\right] \qquad \text{B.31b}$$

A similar expression can be found for the vertical velocity in region (3). The turbulent-boundary-layer thickness as obtained from an integral Karman-Pohlhausen-type of boundary-layer solution can be shown to be:

$$\delta_2 = 0.0574\left\{\varphi_2\frac{\delta_2\left(U_2/U_s\right)}{\theta_2\left[\left(U_2/U_s-1\right)\right]}\right\}^{4/5}\frac{\left(U_2/U_s\right)^{3/5}}{1-\left(U_2/U_s\right)^{4/5}}\left(\frac{\nu_2}{U_2}\right)^{1/5}\left(\left(\frac{1+M_2-U_s/a_2}{1+M_2}\right)\left(1-\frac{U_2}{U_s}\right)x\right)^{4/5} \qquad \text{B.32}$$

at point b, which corresponds to the location of the contact surface, or region of maximum thickness. Once again a similar expression can be found for the boundary-layer thickness in region (3). The equation was plotted against 3.27, and the results were found to be in agreement to within 20%.